HAL
open science

Scattered light studies for the LISA optical metrology system
Vitalii Khodnevych

▶ **To cite this version:**

HAL Id: tel-03177562

https://theses.hal.science/tel-03177562

Submitted on 23 Mar 2021

THÈSE DE DOCTORAT

Etudes de lumière diffusée pour le système de métrologie optique LISA

Vitalii Khodnevych

Laboratoire ARTEMIS (UMR7250),
Observatoire de la Côte d'Azur

Etudes de lumière diffusée pour le système de métrologie optique LISA

Jury :
Président du jury

Rapporteurs
Thierry Bosch, Professeur, Université Paul Sabatier, Toulouse
Guido Mueller, Professeur, University of Florida

Examinateurs
Thierry Bosch, Professeur, Université Paul Sabatier, Toulouse
Noël Dimarcq, Directeur de recherche, Université Côte d'Azur
Gerhard Heinzel, Professeur, Albert Einstein Institute
Mathilde Hugbart, Chargé de Recherches, Institut de Physique de Nice, Université Côte d'Azur
Zoran Sodnik, Optical Communication Technology Manager in the Govsatcom and Secure Communications Section at ESA-ESTEC.
Peter Wolf, Directeur de Recherches, Observatoire de Paris

Etudes de lumière diffusée pour le système de métrologie optique LISA

Le Laser Interferometer Space Antenna (LISA) est un observatoire spatial d'ondes gravitationnelles, qui est actuellement en phase A. La détection d'ondes gravitationnelles est effectuée par des mesures interférométriques hétérodynes très précises. Si de la lumière, non prise en compte dans la conception (lumière parasite), se couple aux faisceaux destinés aux mesures interférométriques, alors ces dernières seront faussées. La lumière diffusée se distingue des autres types de lumière parasite (comme la diffraction aux ouvertures, la réflexion ou la transmission parasites) dans le sens où elle résulte d'un profil de rugosité inconnu ou d'une distribution de contamination de poussières: aucune évaluation exacte n'est possible. Cette thèse est consacrée à l'étude de l'impact de la lumière diffusée sur les mesures interférométriques.

Lorsqu'une surface rugueuse est éclairée par un faisceau de lumière monochromatique et cohérente, elle diffuse alors la lumière et cette lumière diffusée prend alors une structure granuleuse, appelée tavelures (speckle en anglais). Une structure similaire est également observée dans le cas de la diffusion par une contamination particulaire, ou encore due aux irrégularités dans la structure des fibres optiques. Cette thèse est consacrée à l'étude de la diffusion de lumière cohérente et à la perturbation des signaux en sortie d'un interféromètre perturbé par de la lumière diffusée. Pour ces études de diffusion de la lumière cohérente, j'ai utilisé deux approches: la modélisation numérique et les mesures expérimentales.

J'ai développé un modèle numérique de la diffusion cohérente due à la microrugosité. Il est en accord avec le modèle Harvey-Schack de la fonction de distribution de réflectance bidirectionnelle (BRDF). En outre, il décrit correctement les caractéristiques observées de la diffusion cohérente: amplitude, distribution d'intensité et dimension spatiale d'un grain de speckle.

Un autre modèle numérique, que j'ai développé, est utilisé pour décrire la rétrodiffusion cohérente dans les fibres optiques. Le résultat du modèle coïncide avec celui du modèle conventionnel incohérent. De plus, il décrit correctement les caractéristiques de la diffusion cohérente observées sur une expérience réalisée à l'Institut Albert Einstein à Hanovre: distribution d'intensité et dépendance avec la température.

Deux montages interférométriques fibrés (à $1,55\ \mu m$ et $1,06\ \mu m$) ont été mis en oeuvre pour des études expérimentales de la diffusion cohérente. Ces études sont motivées par la nécessité d'une description précise des effets de diffusion cohérente dans les montage interférométriques fibrés tels que LISA. Les deux configurations ont montré une réponse de type speckle à l'orientation de la surface de l'échantillon. Un algorithme de traitement du signal a été spécialement développé pour mesurer les faibles valeurs de rétrodiffusion des surfaces optiques. Le plancher de mesure de la configuration 1.06 μm atteint 10^{-13} en puissance relative, et $10^{-5}\ /sr$ en BRDF, ce qui correspond à l'état de l'art des diffusomètres.

Les mêmes dispositifs expérimentaux ont été utilisés pour étudier la diffusion cohérente due à la contamination. Les résultats des mesures ont été comparés avec la théorie de diffusion de Mie.

Par ailleurs, j'ai utilisé des méthodes conventionnelles pour étudier la lumière diffusée due à l'impact des micrométéorites. L'impact sur une surface optique par une micrométéoroïde donne naissance à un type spécifique de lumière parasite propre aux instruments optiques spatiaux. La lumière est diffusée pour deux raisons: le cratère d'impact et la contamination par les ejecta. Je propose une méthode d'estimation de la lumière parasite et l'applique au cas du télescope LISA. J'ai ainsi estimé une limite supérieure à la rétrodiffusion pour des durées de mission nominales (4 ans) et étendues (10 ans).

Ce travail apporte un ensemble d'études expérimentales et de modélisations qui améliorent la connaissance des propriétés de la diffusion cohérente de la lumière et de ses conséquences et ses conséquences dans les instruments interférométriques de haute précision.

Scattered light studies for the LISA optical metrology system

The Laser Interferometer Space Antenna (LISA) is a space-based gravitational wave observatory now in Phase A. The measurements of the gravitational waves are performed by precise heterodyne interferometric measurements. If any light, which was not intended into the design (stray light), couples to the interfering beams, the measurements will be perturbed. Scattered light differs from other types of stray light (such as diffraction at apertures, stray reflection or transmission) in that it results from an unknown roughness profile or dust contamination distribution: no exact evaluation is possible. The thesis is dedicated to the studies of the consequences of the scattered light on interferometric measurements.

When a rough surface is illuminated by a coherent, monochromatic beam of light, a scattering process takes place, and the scattered light shows a grainy structure called speckle. A similar pattern is also observed in the case of scattering from particulate contamination, or due to the irregularities in the structure of optical fibers. This thesis is devoted to the study of the scattering of coherent light, and the perturbation of the readout of an interferometer due to the presence of scattered light. For these studies of coherent light scattering, I use two approaches: numerical modeling and experimental measurements.

I have developed a numerical model of coherent scattering due to microroughness. It is in agreement with the Harvey-Schack model of the Bidirectional Reflectance Distribution Function (BRDF). From the other side, it correctly describes the observed features of coherent scattering: amplitude and intensity distribution, the spatial dimension of the single speckle grain.

Another numerical model, which I have developed, is used to describe coherent backscattering in optical fibers. The result of the model coincides with the conventional, incoherent model. In addition to this, it correctly describes the features of coherent scattering observed on an experiment made at the Albert Einstein Institut in Hannover: intensity distribution and temperature change rate.

Two fibered, homodyne interferometric setups (at 1.55 μm and 1.06 μm) were built for experimental studies of the coherent scattering. These studies' necessity is driven by the need for an accurate description of coherent scattering effects in interferometric setups, such as LISA. Both setups have demonstrated the presence of a speckle type response. A signal processing algorithm was specially developed to measure low backscattering values from the optical surfaces. The measurement floor of the 1.06 μm setup reaches 10^{-13} in relative power, and 10^{-5} $1/sr$ in BRDF, which matches modern, state-of-the-art BRDF meters.

The same experimental setups were used to study coherent scattering due to contamination. The results of the measurements were compared with the Mie scattering theory.

Besides this, I have used conventional methods to study scattered light due to micrometeoroid damage. The impact on an optical surface by a micromete-

oroid gives rise to a specific type of stray light inherent only in space optical instruments. This causes a double source of light scattering: the impact crater, and the ejected contamination. I propose a method of stray light estimation and apply it to the case of the LISA telescope. I have estimated upper limits for the backscattering fraction for nominal (4 years) and extended (10 years) mission durations.

This work brings an ensemble of experimental and modeling studies that improve the knowledge of the properties of coherently scattered light, and its consequences in high precision interferometric instruments.

Remerciements

Contents

Chapter 1

Introduction

In this chapter, I will give a short historical overview of gravitational waves (GW), GW searches, and their discovery (see Sec. 1.1). GW are ripples in space-time generated by the acceleration of massive objects. I will justify the possibility of GW detection with free-falling masses and optical interferometry. One of the possible instruments that will use this concept for GW detection is LISA (Laser Interferometer Space Antenna, see Sec. 1.2). Here I will describe the scientific goals of the mission, give a general design overview, and motivate stray light studies for the LISA mission (see Sec. 1.2).

1.1 Gravitational waves

The prediction of GW [11] comes from the most famous physicist of our time - Albert Einstein. He saw that Newtonian gravitational theory also needed a change after he applied a Special Theory of Relativity (STR) to mechanics and electrodynamics. In relativistic physics, the concept of causality is the prohibition of any signal propagation faster than the speed of light. The new theory that describes the gravitational interaction is called the General Theory of Relativity (GTR). Immediately after its creation, GTR was used to explain the shift of the perihelion of Mercury. In 1919, Eddington had checked the prediction that the gravity of the Sun was bending the light of stars. Only in the 1960s, it was confirmed by observations that a clock deep in a gravitational potential appears to run slower for an external observer.

Einstein used the weak field approximation to predict GW in 1916, and then he got the math right in 1918. He demonstrated the possibility of GW in his theory and showed that in systems with accelerating mass distribution would lose energy by the emission of GW. Experimental searches for GW began in the 60s of the 20th century, but the required sensitivity level was achieved only in 2015. Before I dive into the theory of interferometric GW detectors, I would like to present the physical principle of detection [48].

1.1.1   Propagation of the GW

In STR the space-time interval ds is:

$$ds^2 = \eta_{\mu\nu}dx^\mu dx^\nu,\tag{1.1}$$

where $\eta_{\mu\nu}$ is Minkowski metric:

$$\eta_{\mu\nu} = \begin{pmatrix} 1 & 0 & 0 & 0 \\ 0 & -1 & 0 & 0 \\ 0 & 0 & -1 & 0 \\ 0 & 0 & 0 & -1 \end{pmatrix}.\tag{1.2}$$

In GTR, space-time is no longer flat, but curved in order to represent what is called gravitation:

$$ds^2 = g_{\mu\nu}dx^\mu dx^\nu,\tag{1.3}$$

where $g_{\mu\nu}$ contains all the information about space-time curvature. We assume a small perturbation of space-time and so we rewrite the metric in the from:

$$g_{\mu\nu} = \eta_{\mu\nu} + h_{\mu\nu},\tag{1.4}$$

where $h_{\mu\nu}$ are metric's perturbations away from Minkowski space.

Later in the text, we will use a transverse traceless gauge, in which the world lines of free-falling test masses (by definition, objects which don't feel any other influence than gravity) mark out the coordinates. In the weak-field limit and using these coordinates, Einstein's field equations become a wave equation:

$$\left(\nabla^2 - \frac{1}{c^2}\frac{\partial^2}{\partial t^2}\right)h_{\mu\nu} = 0,\tag{1.5}$$

with the solution $h_{\mu\nu} = h(\omega t - \vec{k}\cdot\vec{x})$, where $\omega/2\pi$ is the frequency of the GW and $\vec{k}$ is a wave vector of it. It should also be mentioned that GW has two polarizations usually marked h_+ and $h_\times$.

Gravity in these coordinates is not a force, but a geodetic movement through curved space-time. Therefore, free-falling masses are not accelerated when a GW passes through them, and can, therefore, be used to realize the coordinate system of the space-time .

The next step is to examine how changes in the metric affect the measurable distance between free-falling masses.

1.1.2   Measurements principle of the GW

Let us consider plane GW in single polarization state, which propagates is the x_1 direction:

$$\eta_{\mu\nu} = \begin{pmatrix} 0 & 0 & 0 & 0 \\ 0 & 0 & 0 & 0 \\ 0 & 0 & h(kx_1 - \omega t) & 0 \\ 0 & 0 & 0 & -h(kx_1 - \omega t) \end{pmatrix}.\tag{1.6}$$

The interval between two neighboring events is given by:

$$ds^2 = g_{\mu\nu}dx^\mu dx^\nu = c^2dt^2 - dx_1^2 - (1 + h(kx_1 - \omega t))dx_2^2 - (1 - h(kx_1 - \omega t))dx_3^2. \tag{1.7}$$

Let us put free flying masses at position $x_2 = -L/2$ (light transmitter) and $x_2 = L/2$ (receiver). For the light which propagates between these two masses, we can write a total interval:

$$ds^2 = 0 = c^2dt^2 - (1 + h(kx_1 - \omega t))dx_2^2, \tag{1.8}$$

here was used that fact that speed of light is equal to c in any inertial frame of reference.

The equation can be rewritten as:

$$cdt = \sqrt{1 + h(kx_1 - \omega t)}dx_2, \tag{1.9}$$

as $h \ll 1$, so

$$cdt = [1 + \frac{1}{2}h(kx_1 - \omega t)]dx_2. \tag{1.10}$$

If travel time of light τ is much smaller than period of the GW, then the integral is simple:

$$\tau = \left(1 - \frac{1}{2}h(t)\right)\frac{L}{c}. \tag{1.11}$$

If $h = 0$, so $\tau = \frac{L}{c}$. But, due to presence of the GW, the variation of τ is:

$$\delta\tau = h(t)\frac{L}{2c}. \tag{1.12}$$

In the case of optical phase measurements, the phase shift would be:

$$\Delta\phi = \frac{2\pi c}{\lambda}\delta\tau = \frac{\pi L}{\lambda}h(t), \tag{1.13}$$

where λ is the wavelength of the optical signal used to probe the GW. Optical interferometry is the most appropriate way to measure the travel time between two test masses, and so, to measure GWs.

1.2 Laser Interferometer Space Antenna

Laser Interferometer Space Antenna (LISA) will be the first space-based GW observatory[37]. Since the publication of [11], where Albert Einstein postulated their existence, 99 years have passed until their first observation in 2015 by the ground-based interferometer LIGO[1] in the USA (Nobel Prize 2017). Due to seismic noise, gravity gradient noise, and other effects, ground-based interferometers (LIGO, Virgo) are limited at low frequencies. Significant improvements can be made by the construction of an underground interferometer (Einstein Telescope) on the stable lithospheric plate [12]. However, even underground detectors will be limited to observe the black holes with total masses

of a few hundred solar masses. For thousands of solar masses, ground detection will be impossible. To detect GW at lower frequencies, and detect more massive and slower objects, the detector has to be in space and is likely to be a space interferometer mission such as LISA. The LISA frequency band (0.1 mHz to 100 mHz) will include GW generated by compact objects captured by supermassive black holes in galactic nuclei, compact binaries in our Galaxy and beyond, binary supermassive black holes, and quantum fluctuations in the early universe. The science objectives are to test general relativity with observations, probe new physics and cosmology, explore stellar population and dynamics in galactic nuclei, survey compact stellar-mass binaries, and study the structure of the Galaxy. It also allows us to trace the formation, growth, and merger history of massive black holes[37].

LISA is a GW observatory space mission now in Phase A. It is a constellation of three identical satellites (see Fig. 1.1), forming an equilateral triangle of arms-length L=2.5 million km. The constellation will be placed on heliocentric
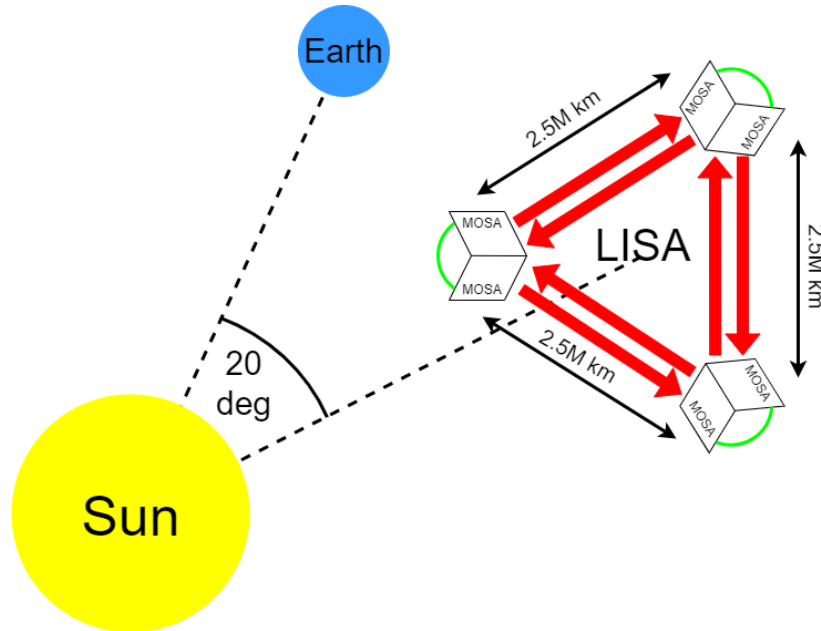
Figure 1.1: Artist's illustration of the LISA constellation (not to scale).

orbit and will follow the Earth at 20 deg separation. The Earth-constellation distance at the starting time of data taking is 50 million km. With time, the constellation will move far away from the Earth, and the distance will reach about 65 million km at the end of 10 years of data taking. Each of the spacecraft will contain two moving optical subassemblies (MOSA), which will point to the distant satellite. Each MOSA includes a telescope, optical bench, test mass, and receives the beam from a frequency-controlled laser beam. The two MOSAs onboard a satellite are linked by an optical fiber to provide cross-referencing of the two optical local oscillators (green curve in Fig. 1.1). Each arm of the triangle forms a double Michelson-like interferometer, in which the test masses define the ends of the arm.

To eliminate the influence of forces of non-gravitational origin, such as light pressure and solar wind on the test masses, each spacecraft is built as a satellite with zero drag. The test mass is in free fall inside the satellite (in the direction to the far satellite) while the spacecraft revolves around it and absorbs all the local non-gravitational forces. In addition to this, capacitive sensors determine the position of the Test Mass (TM) with respect to spacecraft. Then, the information is sent to the Drag Free Attitude Control System (DFACS) that control and maintain the spacecraft position around the TM. This technology was demonstrated with LISA Pathfinder [3].

The continuous measurement of the light path length $L[1 + h(t)]$ between two test masses reveals the presence of the GW $h(t)$. It is performed via six interferometric heterodyne phase measurements (in total) at each end of the triangle arms. In the presence of any light which was not intended to be in the design (stray light), the heterodyne interference can be disturbed. The correct assessment of the stray light, together with the instrument stability, is vital for LISA measurements, which aim at a precision of 10^{-21} in the GW $h(t)$ strain, that is, in the measurement of the fractional change of the light path length $L[1 + h(t)]$.

1.3 Place of the thesis work in the context of the LISA mission

Careful consideration of all noise sources is a crucial step in the LISA instrument. One of the most significant contributors to the noise in interferometric GW measurements is the stray light [37]. The conventional methods to eliminate stray light are discussed in Chapter 2 and work well for most applications with incoherent light, such as imaging or light collection.

Indeed, perturbations by classical, incoherent stray light are likely to be a more or less constant contribution, with slow time dependence, with very little consequence on the phasemeter readout of the heterodyne measurement. However, in heterodyne measurements, coherently scattered light is a more complex issue:

- amplitudes add, not intensities. To keep the perturbation below the 10^{-6} level, for instance, the relative intensity of coherent light must be kept below 10^{-12};

- the perturbation due to scattered light shows a strong dependence on various parameters such as path-length difference, of course, but also incidence angle (see Sec. 6.3), the ambient temperature in the case of light backscattered by an optical fiber (see Chapter 7) as well as the laser wavelength;

- when observing the backscattering and its dependence, the striking feature that shows up is the speckle-type structure: when scanning one of these different parameters, or moving the sample with respect to the laser

spot (see Sec. 5.4.2), the backscattering changes in an unpredictable way, linked to statistical nature of the roughness map of the target surface, similar to the speckle maps observed in the light scattered from a rough surface illuminated by a laser beam.

As a result, perturbations of the LISA interferometers will bring in noise due to a number of parameters, and it is important to see whether the corresponding instability falls into the LISA detection band and whether their magnitude exceeds the allocation.

For this reason, a study of scattered light, both experimental and simulation, is required. It is necessary to provide an understanding of how scattered light affects the readout of an interferometer, in parallel to other studies, underway in the LISA Consortium, devoted to the other type of stray light: ghost beams and diffracted light.

During the thesis work, I built two homodyne interferometric setups for coherent backscattering measurements, with which I could observe that the speckle properties are ubiquitous in all types of measurements. I studied spatial and statistical properties of scattered light and confirmed that these properties could be retrieved under the classical approach of the random phasor sums. I demonstrated that conventional scattering is the limit case of coherent scattering when an average over detection area erases coherent features.

This thesis work provides both the link between the conventional and coherent properties of scattered light and helps understand the limits of the software-embedded routines for the calculation of scattered light in optical systems.

1.4 Content of the thesis

In Chapter 2, I will describe how LISA heterodyne measurements are performed and how they can be perturbed by stray light. I will discuss the potential sources (microroughness, contamination, etc.), key parameters of scattered light description and main mitigation strategies. Particular attention is dedicated to contamination and particle counting as one of the most contributing stray light sources. In Chapter 8 I had designed and built a cleanroom contamination control system based on the Internet of Things (IoT) concept in order to test the idea of using general-purpose particle counter for a clean room application.

During my studies, I used conventional methods to study stray light in LISA but also developed new techniques. For example, In Chapter 3, I used a conventional method but for a new application. In the chapter, I estimate stray light contribution due to micrometeoroid impact. On the other side, coherent scattering has many unique features (see Chapter 4), so it requires a new approach. To study this problem, I built two setups at 1.55 μm and 1.06 μm for studies of coherent scattering from optical surfaces. To explain the experimental results of scattering due to microroughness, I develop a numerical model (see Chapter 4). This model agrees with widely used models, but more

than this, it can correctly describe speckle behavior and explain experimental results.

The experimental setup at 1.55 μm (see Chapter 5) was the first method demonstration setup. It shows the possibility to measure backscattering at a level down to -125 dB, which would be impossible without the signal processing algorithm developed particularly for this setup. I had shown that speckle in interferometric measurements is present, and it changes when the target moves, and it relies on beam properties. The other setup at 1.06 μm (see Chapter 6) qualitatively confirms the achieved results. It is representative of LISA as it works at the same wavelength and performs interferometric measurements as well. The setup demonstrates the possibility to measure BRDF at a level down 10^{-5} $1/sr$ what is the level of modern state-of-art BRDF-meters.

The scattering in LISA will also happen in optical fibers, which would link two MOSA. In Chapter 7, I propose a model of coherent backscattering in an optical fiber. The goal is to show that speckle is present in this kind of scattering and that with my model, I can analyze the experimental data, argue the analysis, and suggest improvements in an experiment.

The setup that I build was used for measurements of coherent backscattering from contamination (see Chapter 8). For this, I had compared the measured backscattering signal with Mie theory. To count the number of spheres on the surface, I had developed image processing algorithms.

In conclusion, the study reaches the understanding of coherent scattering phenomena in interferometric setups, and they are summarized in Chapter 9

Chapter 2

Stray light

As was discussed in the Chapter 1, the gravitational wave signal is encoded in the phase of the interferometric signal. The LISA instrument will perform heterodyne interferometric phase measurements (see Sec. 2.1). These measurements can be perturbed in case of presence of the stray light (see Sec. 2.2). Stray light is considered to be any light in an optical instrument that was not intended in the design. Stray light in LISA includes ghosts, diffraction of the beam, exterior contribution (starlight), and scattering. The complete list of stray-light sources will be given in Sec. 2.3.

This thesis is mainly concentrating on the study of stray light due to scattering. In section 2.4, I will present the key concept of the description of scattered light – Bidirectional Scattering Distribution Function (BSDF). I will also explain the link between surface microroughness and BSDF. Another important scattering source is contamination, and this will be discussed in Sec. 2.5. In that section, I will give an overview of contamination classification and sources, transfer methods, optical effects, and prevention/mitigation strategy. Particular attention will be dedicated to contamination particle counting (see Sec. 2.5.2).

In Section 2.6, I discuss possible mitigation strategies of the stray light in the LISA instrument. Throughout the chapter, I will highlight my contributions to these studies.

2.1 LISA heterodyne phase measurements

The phase measurements in the LISA instrument will be performed by a heterodyne schema. Heterodyne means that the two beams involved in the interferometric measurements have a shift in optical frequency. This shift is not constant in time and in LISA case, it slowly varies in the range 5-25 MHz. The discussion of all the advantages and necessity of the heterodyne measurements is beyond this document's scope [19], but one of the reasons will be exposed in Sec. 2.2. However, in section 2.2 I will describe the positive impact of it on stray-light rejection.

To demonstrate the principle of heterodyne interferometric measurements, let us assume that two beams with amplitude a_i, phase ϕ_i, and optical fre-

quency Ω_i are superimposed on the detector surface. The complex amplitude of each beam in this case is:

$$B_i = a_i e^{j\phi_i + j\Omega_i t}.$$ (2.1)

The intensity of superposition of these beams is:

$$I = |a_1 e^{j\phi_1 + j\Omega_1 t} + a_2 e^{j\phi_2 + j\Omega_2 t}|^2 = a_1^2 + a_2^2 + 2a_1 a_2 \cos((\Omega_1 - \Omega_2)t + (\phi_1 - \phi_2)) =$$
$$= (a_1^2 + a_2^2)(1 + \frac{2a_1 a_2}{a_1^2 + a_2^2} \cos(\Omega t + \Delta\phi)) = J[1 + C\cos(\Omega t + \Delta\phi)], \quad (2.2)$$

where $J = (a_1^2 + a_2^2)$ is averaged intensity and C is constant. The interference pattern is not constant in time but oscillates at the frequency $\Omega/2\pi$, where $\Omega = (\Omega_1 - \Omega_2)$. The path length difference ΔL of two beams is encoded in the phase of the interference:

$$\Delta\phi = \phi_1 - \phi_2 = \frac{2\pi}{\lambda}\Delta L.$$ (2.3)

The current of the photodiode is linearly proportional to the optical power, which arrives on its surface S. This power is integral over S of the derived above intensity:

$$P = \int_S I dx dy = \overline{P}[1 + C\cos(\Omega t + \Delta\phi)],$$ (2.4)

where $\overline{P}$ is averaged power, which arrives on the photodiode and C is some constant.

The photodiode current is converted to a voltage with a trans-impedance amplifier. To extract the phase from the measured signal, the LISA phasemeter is used. The basic principle of it is based on lock-in detection. For this the measured signal $2A\cos(\Omega t + \Delta\phi)$ is multiplied on the reference signal $\cos(\Omega t)$ of the same frequency:

$$2A\cos(\Omega t + \Delta\phi) \times \cos(\Omega t) = A\cos(\Delta\phi) + A\cos(2\Omega t - \Delta\phi).$$ (2.5)

The low pass filter filters the high pass component at the frequency 2Ω. The result of filtering is the in-phase component:

$$I = A\cos(\Delta\phi).$$ (2.6)

The same procedure is performed with a shift of 90 deg for the reference signal. The result of demodulation, in this case, is a quadrature component:

$$Q = A\sin(\Delta\phi).$$ (2.7)

The combination of the in-phase and quadrature components provide the phase of the interferometric signal:

$$\Delta\phi = arg(I + jQ).$$ (2.8)
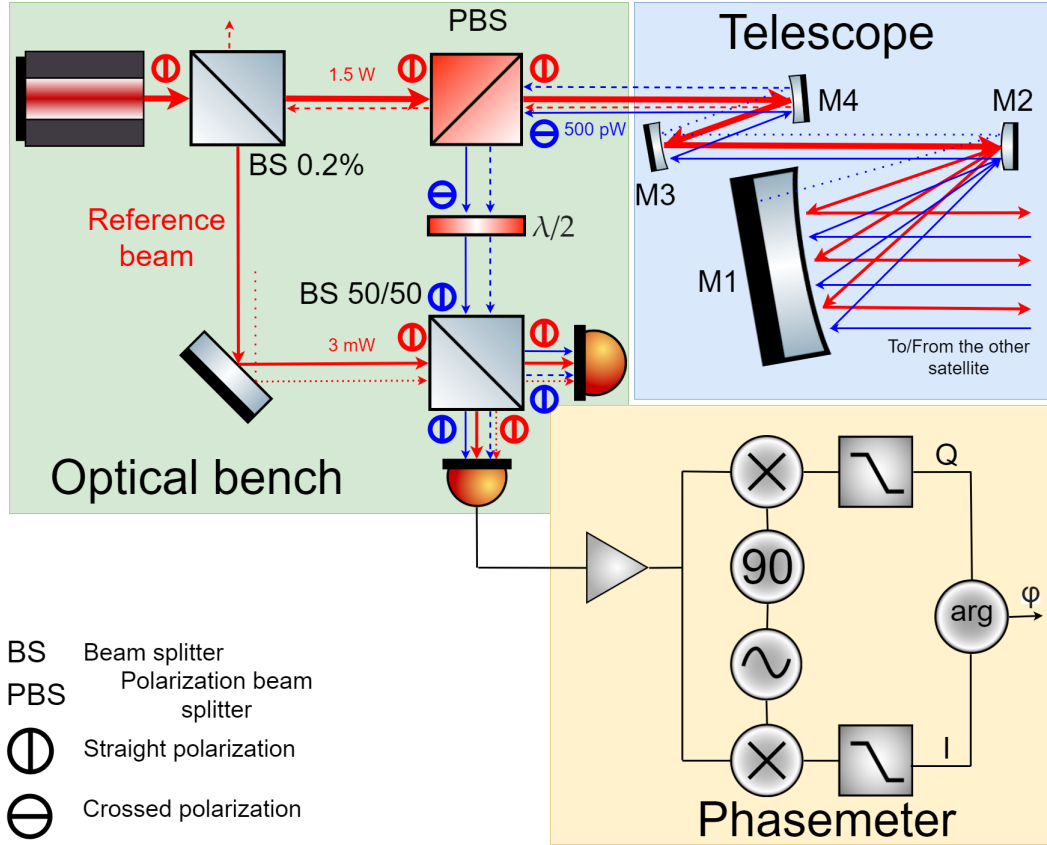
Figure 2.1: The simplified schema of the "long-arm" LISA heterodyne interferometer. In green: the "long arm interferometer area of the LISA optical bench. In blue: the telescope area. In yellow: the phasemeter. The blue and red lines represents the difference in frequency of the two beams. The dashed lines display the stray-light beams.

The more detailed schema of the satellite-satellite ("long-arm") LISA heterodyne interferometric measurements is shown in the Fig. 6.3. A powerful beam (1.5W), called the "Transmit" beam, or Tx beam, is sent to the telescope (thick red line in Fig. 6.3) and then transmitted to the distant satellite. Simultaneously, the same telescope receives the much lower power beam emitted by the distant satellite in the orthogonal polarization and shifted in optical frequency (thin blue line). This beam is called the "received beam", or Rx beam. A polarization beam splitter (PBS) is installed to avoid the mixing of the two beams of different polarizations. A small fraction (0.2%) of the transmitted beam is pinched out to create the reference beam. That and the received beam (after $\lambda/2$ plate to turn the polarization by 90°) interfere at the two-quadrant photodiodes. The measured signal is amplified, demodulated, and analyzed by a phase meter. The phase ϕ contains information about the GW.

2.2 Stray light in LISA

In the presence of stray light, the phase measurements can be disturbed. Stray light is an additional beam (dashed lines in Fig. 6.3), which can perturb a heterodyne measurement – provided that it has the same polarization and wavelength as one of the two nominal beams of the heterodyne interference. So, even if many sources of stray light exist in the system, they are generally eliminated by the phasemeter, because the signal is outside the detection range. The main parameter for these properties is the optical frequency difference between two interfering beams $\Omega/2\pi$, where $\Omega = \Omega_1 - \Omega_2$. The demodulation is performed at the frequency $\Omega/2\pi$ frequency, so only in this case, the phase of the beat interference signal will be measured. The second property is linked with the polarization distribution in the system. To make the interference possible, the two beams that arrive on the photodiode should be in the proper polarization. However, the transmitted and received beams are in crossed polarization. The polarizing beam splitter highly rejects the scattered Tx beam of the straight polarization, and the $\lambda/2$ plate rotates the polarization vector in the straight orientation (see Fig. 6.3). The combination of these two factors highly reduces the dependence of the instrument to stray light.

Let us look closer to this stray-light rejection feature of the LISA instrument. For this, let us build a simple model and list all interferences possible in the system and discover which of them affect the measurements. All the beams considered in the model are listed below:

- Tx beam on the optical bench $B_{Tx}^B(\Omega_1)$.

- Stray Tx beam in the straight polarization $B_{TxS}^B(\Omega_1)$.

- Received beam $B_{Rx}(\Omega_2)$ in cross polarization.

- Stray received beam in the cross polarization $B_{RxS}(\Omega_2)$.

- Stray transmitted beam in crossed polarization $B_{TxS}(\Omega_1)$.

For the reference polarization, I take the polarization of the reference beam ("local oscillator" beam in the interferometer). The cross polarization means that the polarization vector is rotated on 90 deg with respect to reference one. The cross polarization of the stray transmitted beam is possible not only due to the scattering process but also due to rotation of the polarization vector (in PBS, for example) of the transmitted beam before the scattering. I neglect the effect of possible system perturbation by the stray transmitted beam on the optical bench, as this $B_{TxS}^B(\Omega_1)$ beam does not directly reach the photodiodes.

The polarization vector of the received beam $B_{Rx}(\Omega_2)$ and two stray beams ($B_{RxS}(\Omega_2)$, $B_{TxS}(\Omega_1)$) is rotated on 90 deg by $\lambda/2$ plate before they reach the recombining beam splitter (see Fig. 6.3). So all the beams reach photodiodes in aligned straight polarisations. Also, I consider here that amplitude of interference contribution in crossed polarization at the surface of the photodiode is negligible.

The intensity on the photodiode (after the half-wave plate has switched the received beam polarization to align it parallel to the reference beam polarisation) is the square modulus of the sum of all the superposed beams:

$$I = |B_{Tx}^B(\Omega_1) + B_{TxS}^B(\Omega_1) + B_{Rx}(\Omega_2) + B_{RxS}(\Omega_2) + B_{TxS}(\Omega_1)|^2. \qquad (2.9)$$

The variable (AC) part of the interferometric intensity is:

$$
\begin{aligned}
I_{AC} = & B_{Tx}^B B_{TxS}^B \cos(\phi_1) + & [1] \\
& B_{Tx}^B B_{Rx} \cos(\Omega t + \phi_2) + & [2] \\
& B_{Tx}^B B_{RxS} \cos(\Omega t + \phi_3) + & [3] \\
& B_{Tx}^B B_{TxS} \cos(\phi_4) + & [4] \\
& B_{TxS}^B B_{Rx} \cos(\Omega t + \phi_5) + & [5] \\
& B_{TxS}^B B_{RxS} \cos(\Omega t + \phi_6) + & [6] \\
& B_{TxS}^B B_{TxS} \cos(\phi_7) + & [7] \\
& B_{Rx} B_{RxS} \cos(\phi_8) + & [8] \\
& B_{Rx} B_{TxS} \cos(\Omega t + \phi_9) + & [9] \\
& B_{RxS} B_{TxS} \cos(\Omega t + \phi_{10}) + & [10].
\end{aligned}
\qquad (2.10)
$$

From this equation, it is clear that the terms 1,4,7,8 (green) will not contribute to the signal, as their beat frequency is not Ω. The term 2 (blue) is the nominal one. It is the interference of the received and Tx beams. Only terms 3, 5, 6, 9, 10 (red) will contribute to perturbation of the phase measurements. Each of the contributions has its optical path difference phase ϕ_x, which is a phase difference of two beams. If this phase were stable, the phasemeter would see a constant shift, which would not affect the LISA measurements. However, the phase shift may change due to the pointing of the telescope and thermo-vibrational movements of the optical components. This will cause noise in phase measurements, so it is critical to make the instrument components and optical system from a highly thermally stable material, such as Zerodur. Temperature stability of the telescope and at the optical bench is one of the different ways to mitigate the consequences of the coupling of stray light in the LISA measurements [24].

Balanced detection [19] can reduce the impact of stray light as well. For this, the signals of two photodiodes on both outputs of the recombination beam splitter are subtracted. This causes the suppression of the common stray light signal.

On a general basis, a stray light analysis consists in studying the different characteristics of stray light:

- the amplitude of the stray light field reaching the photodiode (more precisely the fractional amplitude);

- the noise in the phase difference between the stray light and the nominal light;

- possibly the noise in the stray light amplitude (will be considered in Sec. 4.1.1) ;

- the polarization of the stray light (with respect to the nominal polarization);

- the overlap between the stray light field and the nominal beam mode (will be considered in Sec. 4.1.2);

and the study can be made experimentally or by simulation. Using Eq. 2.10, one can identify the contribution that dominates. This result should be included in the general model of the impact of stray light on LISA measurements, but it will not be used in the thesis.

Stray light to phase coupling

Another approach (see Ref. [24]) to stray light consists in considering the phasor sum [1] of the nominal beam and the stray light contribution. We consider, in the complex plane, the phasors that correspond to each of the two beams. If we can assume that the stray light field is small and brings only a small perturbation of the nominal beam, then Taylor's expansion of the vector sum allows us to get a convenient expression for the link between stray light and heterodyne phase perturbation. To first order in the fractional stray light amplitude epsilon, one gets:

$$\Phi \approx \varepsilon \cdot \sin \phi, \qquad (2.11)$$

where ε is field amplitude fraction of the stray light, and ϕ is the phase difference between stray and nominal light (see Fig. 2.2).
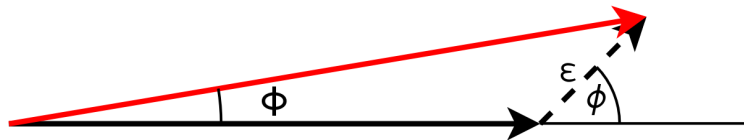
Figure 2.2: Illustration to stray light to phase coupling. If the nominal beam (solid black vector) contains the stray light contribution (dashed vector), the amplitude and phase Φ of the measured vector (red solid vector) is perturbed.

I will use this approach to derive statistical properties in the study of coherent scattering (see Sec. 4.2)

---

[1]In the complex plane, a phasor, oriented at an angle theta, is a graphical representation of a harmonic signal $\sin(\Omega t + \theta)$, and the convenient aspect of it is that the sum of two harmonic signals at frequency $\Omega/2\pi$ is readily represented by the vector addition of the two corresponding phasors. It is to be noted that, implicitly, the phasor representation is valid for signals at frequency $\Omega/2p\text{ß}$: signals at a different frequency $\Omega'/2\pi$ will rotate in the complex plane, at frequency $(\Omega' - \Omega)/2\pi$.

2.3 Potential sources of stray light in LISA

A wide range of phenomena contribute to the stray light in the LISA instrument, which can be classified in four types: celestial stray light (this stray light is incoherent), ghost beams, diffraction, and scattering.

Ghosts are parasitic beams that occur:

- on the front side of a mirror, reflection should be total, but a small fraction of the power is transmitted;

- on the rear side of a beam splitter: reflection due to an imperfect anti-reflection coating, or because of a film due to molecular contamination;

- reflection at apertures.

Ghosts occur on the optical bench as well as in the telescope. Beams with slightly wrong polarization also can be treated as ghosts.

Multiple apertures in the LISA instrument will limit the beam size. This causes undesired diffraction effects and so stray light.

The impact of the celestial sources of stray light (sun, planets, stars) for the constellation acquisition sensor (CAS) was analyzed in Ref. [7]. CAS is the system that is looking for light from the distant satellite. This study concludes that celestial sources are unlikely to produce perturbing effects on the CAS during regular operation.

Scattering is one of the most significant contributors to the stray light in the LISA instrument. The origin of scattering is a wide range of phenomena: microroughness, contamination, cosmetic defects (digs, scratches, micrometeoroid damage) and scattering inside the medium (inside optical fibers, inside lenses, etc.).

There has recently been performed scattering calculations using FRED and Zemax optical software for scattering issues in LISA telescope [41]. Scattering is an issue not only for the interferometer but also for the CAS. Coherent scattering can make the pointing of the satellite impossible. Scattering in optical fibers is under study at the Albert Einstein Institute (AEI) [21].

This thesis is mainly focused only on the scattering aspect of the stray light. The thesis provides the studies for a wide range of scattering sources: micrometeoroids (Chap. 3), microroughness (Chap. 4, 5, 6), contaminations (Chap. 8), fiber backscattering (Chap. 7).

2.4 Key parameters of scattered light description

The central concept in the scattered light description is the Bidirectional Scattering Distribution Function (BSDF). But before introducing it, I would like to remind the reader of some fundamental radiometric quantities.

The flux (power) $d\Phi$ is the number of photons per second. Irradiance E is the radiant flux $d\Phi$ received by a surface per unit area dA:

$$E = \frac{d\Phi}{dA}.$$ (2.12)

The irradiance is used to describe the illumination of the surface (see Fig. 2.3a). The radiance L (see Fig. 2.3b) is the emitted, reflected or transmitted flux $d^2\Phi$ by the surface per projected area of the source $dAcos(\theta)$ into the differential solid angle $d\Omega$:

$$L = \frac{d^2\Phi}{dAcos(\theta)d\Omega},$$

(2.13)

where θ is an emission angle counter from normal of the surface (polar angle in spherical coordinates) and Ω is a collecting solid angle. A surface whose

(a)   *(b)*
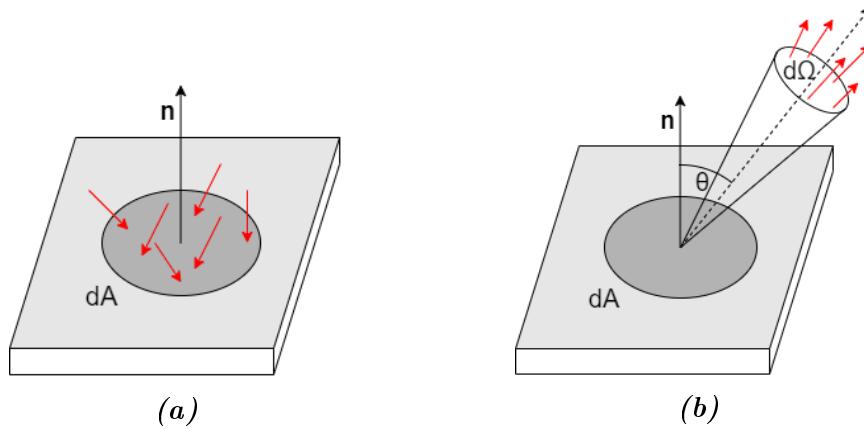
Figure 2.3: Illustrations of irradiance (a) and radiance (b).

radiance is constant concerning the emittance angle θ is said to be Lambertian.

Using these quantities, we can determine the BSDF as the radiance of a scattering surface, normalized by the irradiance incident of the surface.

$$BSDF(\theta_i, \phi_i, \theta_s, \phi_s) = \frac{dL(\theta_i, \phi_i, \theta_s, \phi_s)}{dE(\theta_i, \phi_i)},$$

(2.14)

where the index i indicates the incident direction and the indexes s indicates the scattered direction. ϕ is azimuthal angle in spherical coordinates and $d\Omega_s$ is scattering solid angle. Or in the other terms:

$$BSDF = \frac{d\Phi_s/d\Omega_s}{(d\Phi_i)cos\theta_s}.$$

(2.15)

Depending on the transmittance or reflectance, BSDF is divided on Bidirectional Transmittance Distribution Function (BTDF) and Bidirectional Reflectance Distribution Function (BRDF). In the next chapters, I will mainly use BRDF.

A commonly used quantity is the Angle-Resolved Scatter, which is basically $BRDF(\theta_s, \phi_s) \times \cos\theta_s$. Another widely used quantity is the Total Integrated Scatter (TIS):

$$TIS = \int_0^{2\pi} \int_0^{\pi/2} BSDF \sin\theta_s \cos\theta_s d\phi d\theta_s.$$

(2.16)

For a Lambertian scatterer $BSDF = TIS/\pi$. TIS is an easily measurable quantity because the only light source, an integrating sphere and detector are required to measure it. In the case of BRDF measurements, special instrumentation with synchronous detection and precise rotation mechanisms for the detector are required. When measuring BRDF in high quality, weakly scattering optics, a trade-off may have to be done between the detector size (the bigger size – more flux) and angular resolution. When the scattering is low (low contamination level, super-polished surfaces under testing), measurements are complicated or even impossible with this approach. In Chapters 5 and 6, I will describe a new state-of-art interferometric setup for backscattering measurements from optical surfaces, constructed for the research presented in this thesis.

When simulating the scattering properties, each source of scattering is treated separately, and it is described by its BSDF (the names of the corresponding most used models are in the brackets):

1. Surface micro-roughness (ABC, Harvey-Shack, ABg);

2. Particulate contamination (Mie, Spyak & Wolfe (Lallo & Petro), Dittman);

3. Cosmetic defects: digs, scratches (Peterson).

The total scattering is the sum of BSDF's from all the contributors. In Chapter 4, I will use the Harvey-Shack theory to verify my numerical model. In Chapter 3, I will use the Peterson model to estimate the scattering due to micrometeoroid damage, and in chapter 8, I will use Mie theory to compare it with experimental results.

2.4.1 Scattering due to microroughness

The scattering from optical surfaces due to microroughness is straightforward to describe. It is caused by the phase fluctuation in the reflected wavefront (see Fig. 2.4). If the surface height fluctuation $z(x, y)$ are small compare to wavelength, so the phase fluctuation can be approxiamted [5]:

$$P_{surf}(x, y) = exp(j\frac{4\pi}{\lambda}\cos(\theta_i)z(x, y)) \approx 1 + j\frac{4\pi}{\lambda}\cos(\theta_i)z(x, y). \qquad (2.17)$$

For optical quality surfaces, two terms expansion is sufficient to describe the scattering outside the specular core. The second term is responsible for scattering due to microroughness.

In this case, the optical surface is treated as the sum of figure profile and surface roughness profile $z(x, y)$. The figure profile determines image forming properties, and the surface roughness profile determines the amplitude and angular distribution of light scattered from it [16]. Figure profile includes aberrations also. Aberrations are in between reflection and scattering, as it does not give rise to scattering, but it is not nominal either.
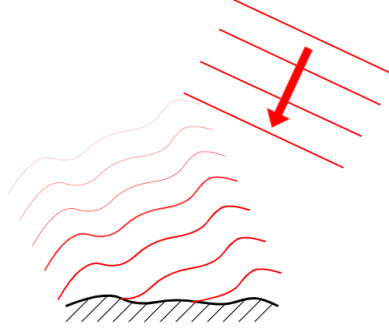
Figure 2.4: The wavefront of the incident plane wave in a moment after reflection after reflection from a rough surface follow the surface roughness profile (up to constant).

BSDF of a rough surface

The perturbative (Rayleigh-Rice) theory shows, in the weak scattering limit, that a rough surface can be understood as a collection of diffraction gratings. It claims that the relationship between Power Spectrum Density (PSD) and BSDF ("Golden rule") can be determined in the case of small roughness ($\ll \lambda$):

$$BSDF(\theta_i; \theta_s, \phi_s) = \frac{4\pi^2 \Delta n^2}{\lambda^4} \cos(\theta_i) \cos(\theta_s) Q S_2(f_x, f_y), \qquad (2.18)$$

where Δn is the difference in refractive index across the boundary of the scattering surface (equal 2 for mirrors), and Q is the polarization factor, and it is approximately equal to the specular reflectance or transmittance of the surface. The term $S_2(f_x, f_y)$ is PSD of the rough surface will be discussed later in this section.

The most used BSDF models of surface microroughness are the K-correlation (ABC), ABg, and Harvey-Shack models. In K-correlation model, the BSDF is:

$$BSDF(|\sin\theta_s - \sin\theta_i|) = \frac{4\pi^2 \Delta n^2}{\lambda^4} \cos\theta_i \cos\theta_s Q \times A[1 + (Bf)^2]^{-C/2}, \quad (2.19)$$

where the coefficients A, B, C will be discussed in the next section. In the 3-parameter Harvey-Shack model, the BSDF is:

$$BSDF(|\sin\theta_s - \sin\theta_i|) = b_0 \left[1 + \left(\frac{|\sin\theta_s - \sin\theta_i|}{l}\right)^2\right]^{s/2}, \qquad (2.20)$$

where the b_0 coefficient defines the level of scattering close to the forward direction, l parameter sets the position of the knee in PSD, and s represents the slope of high-frequency part of it.

The ABg model is similar to Harvey-Shack model:

$$BSDF = \frac{A}{B + |\sin\theta_s - \sin\theta_i|^g}, \qquad (2.21)$$

where the A, B and g coefficients can be computed from the Harvey-Shack coefficients [16].

The goal for all the models is to describe scattering correctly, so they all give a good approximation of the PSD of the surface roughness and no matter which one to use. So, to describe the scattering from the surface, only three parameters are required, which is convenient. Some of these parameters can be calculated from the optics manufacture data; others depend on the type of polishing and can be predicted. The origin of these parameters will be discussed in the next section.

Roughness characterization

The power spectral density (PSD) of the surface roughness profile is:

$$S_2(f_x, f_y) = \lim_{L \to \infty} \frac{1}{L^2} \left| \int_{-L/2}^{L/2} \int_{-L/2}^{L/2} z(x,y) exp[-2\pi j(f_x x + f_y y)] dx dy \right|^2, \quad (2.22)$$

where L is the size of the measured profile and f_x, f_y are the spatial frequencies.

When the roughness is significantly lower than $\lambda/(4\pi)$ (optical-quality surface), the PSD of surface roughness can be approximated by the curve of type:

$$S(f) = A[1 + (Bf)^2]^{-C/2}, \quad (2.23)$$

where A,B,C are model coefficients and the frequency is $f = (f_x^2 + f_y^2)^{1/2} = |\sin\theta_s - \sin\theta_i|/\lambda$. A surface whose scattering varies as a function of $|\sin\theta_s - \sin\theta_i|$ is said to be shift invariant.

The shape of this curve is given in Fig. 2.5. The three parameters for this
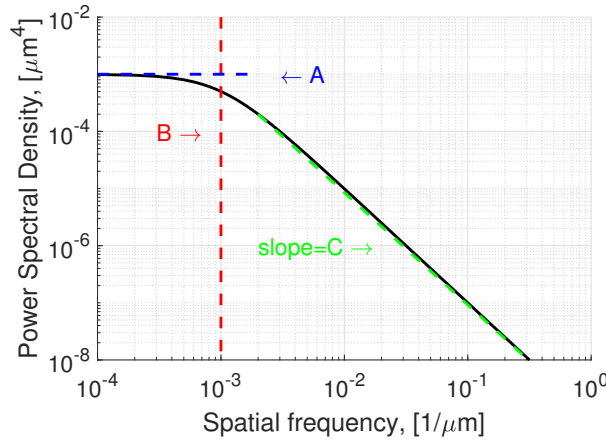
Figure 2.5: *The PSD in K-correlation model:* $A = 1e - 3 \ \mu m^4$, $B = 1e + 3 \ 1/\mu m$, $C = 2$.

curve model have the following meaning:

- A is the magnitude of the PSD at low frequencies;

- $1/B$ is the spatial frequency at which "roll-off" occurs;

- C is the slope of the PSD at frequency $> 1/B$.

This curve is not unique to describe the PSD of similar shape. This set of coefficients is used in the K-correlation (ABC) model. A very similar result can be obtained with the ABg or Harvey-Shack model. There exists a relationship between parameters of this models [16].

Another important parameter in the roughness description is the RMS roughness:

$$\sigma = \lim_{L \to \infty} \frac{1}{L^2} \left\{ \int_{-L/2}^{L/2} \int_{-L/2}^{L/2} [z(x,y)]^2 dx dy \right\}^2. \qquad (2.24)$$

But in practice what is more useful is the effective surface roughness:

$$\sigma_\lambda^2 = \int_{1/d}^{1/\lambda} S_2(f) df, \qquad (2.25)$$

where d is the dimension of the area under measurement; the integral here is definite because spatial frequency components higher than $1/\lambda$ do not generate optical scatter. Another advantage of using this parameter is that TIS is proportional to σ_λ.

The most significant disadvantages of these models are numerous simplifications made to derive this simple expression for BSDFs. These results that in the case of coherent scattering are models valid only on average (and will be discussed in detail in chapter 4).

2.5 Contamination and scattered light

A contaminant is any unwanted molecular or particulate matter on the surface or in the environment of interest that can affect or degrade the consistent performance or lifetime [10]. In the context of a space mission, contaminations are divided by its nature into three groups:

- Molecular. It is a foreign film matter, droplets of size $\approx 0.1-10 nm$. They play roles essentially in flight but also on the ground. Typical molecular contaminants are phthalates, phenols, polybenzimidazole, aromatic hydrocarbons, etc.

- Particulate. It is a foreign matter of miniature size with observable length, width, and thickness (size: μm).

- Microbiological. This is an entity of microscopic size (bacteria, fungi, viruses). They are essential on the ground, mainly due to human activity.

The key parameters in the contamination affecting a piece of optics are:

- the people in the vicinity, and their activity,

- the nature and choice of the nearby materials,

- manufacturing procedures,

- quality procedures,

- integration procedures.

Chemical contamination is mostly released by structures, resins/varnishes, adhesives, tapes, paints.

Contamination travels from source to critical surface/volume by typical transport mechanisms that are different at each phase of satellite lifetime:

- On the ground: manufacturing, AIVT (assembly integration verification test), transport, storage.

- During launch: outgassing + re-condensation on (cold) optics and detectors, mechanical vibrations, plume effects.

- In-flight: outgassing of polymers, plume effects, aging (under Sun UV, atomic oxygen, radiations, thermal cycling), micrometeoroid, UV enhanced contamination.

The main optical effects of contamination are scattering, loss of transmission, reflection, degradation of thermal coatings, substantial material damage.

To predict, to take precautions and to avoid catastrophic consequences of contamination, several approaches can be attempted at different stages of the satellite life:

- At the early stage: the identification of sensitive/contaminant surfaces, selection of materials with strict criteria, qualification of contamination levels, design (venting ducts, heaters, traps), performance loss studies, contamination modeling (molecular contamination based on outgassing: FEMAP, COMOVA).

- At a later stage: assembly /integration in cleanroom ISO5, covers, purging, contamination control, the appropriate cleaning method, thermal vacuum bakeout, regular inspection of critical points.

Numerous satellites (SCATHA, SMM SBUV, Landsat, HRTS/Sunlab, INSAT 1 B, HST) had problems with contamination [15]. Different reasons caused degradation of the optical performance, but the result was the same for all: significant loss of functionality or complete loss of the instrument. Successive studies (LDEF, FRECOPA) of the behavior of materials in the space environment allowed us to develop several methods to prevent and mitigate the impact of contamination.

In this section, I will describe a basic approach to describe scattering due to contamination (see Sec. 2.5.1) and main types of particle counters (see Sec. 2.5.2), which are used to estimate the cleanliness level.

2.5.1 Scattering due to contamination

Contamination of the optical surface is treated as a sphere of a certain diameter. The scattering of an individual sphere was calculated in Mie's theory. Total BRDF from the contamination on the surface is the sum of the scattering intensities for all particles present on it:

$$BRDF(\theta_s) = \frac{1}{(2\pi/\lambda)^2 \cos\theta_s} \sum_{i=1}^{N} f(D_i) \times$$
$$\times \left[\frac{RI_s(D_i, \theta_s) + RI_p(D_i, \theta_s) + I_s(D_i, \theta_b) + I_p(D_i, \theta_b)}{2} \right], \quad (2.26)$$

where $f(D_i)$ − surface density of particles of the i-th diameter D_i, R − is surface reflectance, I_s, I_p − are scattering intensity in s & p polarization (Mie scatter theory [16]). The angle θ_s is the scattering angle (angle between the surface normal and observation direction) and θ_b is angle between incidence and scattering directions (different from θ_i).

The intensities of the scattering from a sphere are well-known quantities (analytical expressions can be found in Ref. [6]). However, the most significant error in this calculation is the density distribution function $f(D_i)$. The estimate of this function is one of the largest source of uncertainty in this study.

Based on experience, a reasonable approach to describe particle distribution in the cleanroom was developed and summarized in the IEST CC1246 standard. This standard is applied only for a cleanroom environment, and it specifies the number of particles N_p (per 0.1 m^2) whose diameter $\geqslant D$:

$$N_p(S, CL, D) = 10^{|S|[\log_{10}^2(CL) - \log_{10}^2(D)]}, \quad (2.27)$$

where S − is particle distribution slope, $S = -0.926$ (IEST CC1246 standard), $S = -0.383$ (NASA standard), $S = -0.6$ (for particles $> 25\mu m$, Airbus D&S standard). This slope is dependant on the orientation of the surface ($V > 45^o > H+$)). The cleanliness level of the surface is CL and is linked with ISO class of the cleanroom, the orientation of the surface, exposure time, etc.

The typical shape of the N_p as a function of particle diameter for several cleanliness levels is given in Fig. 2.6.

The density function $f(D_i)$ is simply the derivative of $N_p(S, CL, D)$. In this way, the calculations of the scattering due to contamination is easy to proceed, and it is already implemented in optical simulation software such as FRED.

As particles have some physical dimensions and they cover some surface, so it may be useful to characterize cleanliness in terms of the Percent Area Coverage:

$$PAC = 10^{K + |S| \log_{10}^2(CL)}, \quad (2.28)$$

where coefficient $K = -7.245$ for $S = 0.926$ and $K = -5.683$ for $S = -0.383$. It is a convenient quantity, as $PAC/100$ is $\approx$ TIS of the surface due to contamination scatter.

I use the Mie theory in Chapter 8 to estimate the backscattering from samples with deposited spheres.
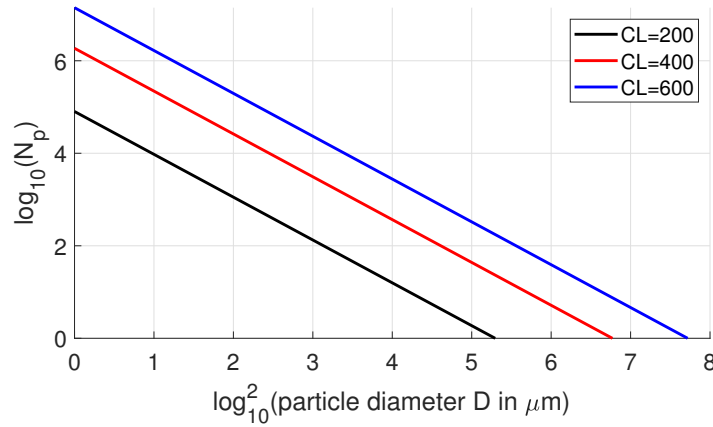
Figure 2.6: Number of particles N_p per 0.1 m^2 whose diameter $\geqslant D$ in accordance to IEST CC1246 standard ($S = -0.926$) for cleanliness levels CL=200, CL=400, CL=600.

2.5.2 Particle counting

To control the cleanliness of the cleanroom, particle counting is used (number of particles of a certain range of diameters in a unit of volume (air contamination) and on a unit of surface (surface-borne contamination)).

In section 2.5.1, I had mentioned two approaches to describe the particles on the surface: by the size distribution, and by the area coverage. Each method uses a different type of particle counting system: air particle counters, microscope imaging, Particle Fall Out (PFO) ppm meters, etc. The link between these types of measurements is not always obvious, and the instruments are not replaceable by each other. Usually, two types of devices are used at once.

Particle counting on surface

The typical instrument to measure surface contamination is the PFO Photometer. The standard unit of measurements is ppm (parts per million). This gives an idea of which surface in mm^2 is covered by particles of m^2 optical surface square. The principle of the measurements of this device is scattering analysis by settled particles from the surface illuminated by light beams nearly parallel to a non-reflective surface under test. Analyzed areas are only 15 mm in diameter, and the substrate can be only smooth dark glass PFO wafers.

As the only information available is ppm, sometimes it may be too little. An alternative method is using an optical microscope with image processing software. In this way, particle distribution is also available. The diversity of substrates is higher, and the tested area can be much larger.

During image processing of the optical surface with particles, these arise the problem of assignation of the size of the particle and comparison of this size with others. Typically particles have an irregular form, but they all are treated as spheres. The diameter of the representative sphere is recovered from the volume, surface area, or a combination of these two. When the dynamics

of the particles are important, the diameter can be retrieved from the Stokes equation[2].

I use this approach in a microscope-type system for particle counting on the optical surface that I had built (see Chapter 8), and in the same chapter, I present a software for image treatment that I had designed.

Particle counting in air

This type of instrument is based on laser light scattering of particles in the air, as each particle gives a pulse of scattered light when it crosses the laser beam. Usually, this particle exploits the amplitude of the pulse to provide size information, in several channels.

The test of the cleanroom class can be performed with these types of counters. A certain amount of air is tested in several locations of the cleanroom following ISO14644-1:2015(E) [27] standard. The same standard specifies the maximum number of particles for each ISO class of the cleanroom. For example, the ISO5 class is the most common standard used during the AIVT phase of the optical space instruments. The experiments described in Chapter 5 and Chapter 6 are performed in a nominally ISO8 cleanroom. However, for the free space optical part of the setup, a home-made enclosure was built to improve cleanliness, and I could measure, in the enclosure, airborne particulate levels corresponding to an ISO5 cleanroom.

Another promising technique to measure particles in the air is based on the "On-the-fly" particle metrology in hollow-core photonic crystal fibre [52]. A particle trapped inside a laser beam is directed to the hollow-core photonic crystal fiber. Inside the fiber, this particle scatters and so decreases the transmission. The duration and the level of transmission drop allow the calculation of the refractive index and particle size with precision down to 18 nanometers. The knowledge of these two parameters will increase the accuracy of models used to calculate scattering due to particle contamination.

As contamination are dangerous not only for optics but also for human lungs, recently, numerous cheap particle counters have appeared on the market. With one of them (SPS30), I designed and built a Clean Room Monitoring System (CRMS) (see Sec. 8.3.1) for continuous monitoring of air cleanliness in the MATISSE cleanroom, in PES building, at Observatoire de la Côte d'Azur.

2.6 Mitigation strategies

In Sec. 2.2, It was discussed the specific methods to reject the stray light influence in the LISA: heterodyne measurements, polarization-based method, temperature stability, and balanced detection. Besides these, there is a standard procedure to mitigate the stray light in an optical instrument. It consists of four steps:

1 Build the model which simulates the optical instrument.

---

[2]www.nte.mines-albi.fr

2 To make a start scattered light simulations of the optical system, assign appropriate BSDF to every surface, and proceed using an optical software in which a module for stray light calculations is embedded.

3 Find the stray light paths. Identify the most critical surfaces.

4 Apply a particular solution to eliminate the stray light: "Move it or block it or paint/coat it or clean it."

Case-by-case solutions are the use of smooth & clean optics (lenses, mirrors, beam dumps, etc.), black coating for structures, baffles, stop design, and smart optical design to avoid ghosts. Stray light simulations, tests, and accurate measurements are a crucial part of this method. A recent trend is to use image correction to reduce stray light.

The key term in the stray light analysis is BSDF. The level of surface polishing or cleanliness can be expressed in terms of this function, which allows us to perform simulation for various optical components in an easy way. However, the laser scattering is a stochastic process, and knowledge of the BRDF allows no prediction of the actual amplitude or phase of the scattered light field, even if BRDF has been measured. There is no software available to describe the scattered light beyond the ray tracing approximation. This creates inconvenience in the application of the method described above in interferometric setups or instruments. In Chapter 4, I had built a bridge model between the classical method of analysis with BRDF and coherent features of scattering in case of microroughness.

The studies on scattered light are performing for different systems (telescope (see chapter 3), optical bench, fibers (see chapter 7)), and different levels (component and optical system). The setup for coherent backscattering measurements from components was built (see Chapter 6).

2.7   Conclusion

In this section, I described how LISA heterodyne measurements are performed and the impact of the stray light in these measurements. I had described the various sources of stray light which are present in the LISA instrument and conventional procedure for stray-light analysis.

In this thesis, I will emphasize the scattering side of the stray light. For my study, I use the conventional methods of scattered light analysis using BRDF (as was described in Sec. 2.6), reuse them for new goals (see Chapter 3) and propose new methods and models (see Chapters 4,7). This is especially important in the case of coherent scattering, which will take place in LISA (see Chapter 4).

Nevertheless, this study is mainly experimental. The two setups were built for homodyne backscattering measurements at 1.55 and 1.06 μm (see Chapters 5 and 6). The installations were mainly devoted to study the scattering due to microroughness of the optical components; however, the experiments

for scattering due to contamination were performed with them as well (see Chapter 8).

In Sec. 2.5.2, I describe the existing particle counting systems. I contribute to this variety of instruments by creating a cleanroom cleanliness monitoring system (see Sec. 8.3.1). Besides this, I constructed the model of coherent backscattering in fibers and applied it to explain the experimental results (see Chapter 7).

Chapter 3

Stray light due to micrometeoroids

Scattering due to micrometeoroid damage is a specific type of stray-light, which is inherent to space instruments with optics exposed to the space environment (like M1 mirror in LISA telescope). Free flying dust particles in space can hit and damage the optical surface. This will cause an increase of stray light in the system. The problem of micrometeoroid damage has been known since the first space flights[8]. However, only a few papers[26, 34] study and provide estimates pertaining to this type of stray light.

In this chapter, I propose a four-step method to estimate light scattering induced by the micrometeoroid damage:

1. Definition of the environmental conditions (Particulates Environmental Model) of the satellite: estimation of the flux and parameters of the particles which arrive at the critical surfaces (see Sec. 3.2).

2. Calculation of the expected damage crater diameter (see Sec. 3.3.1) and ejected mass due to micrometeoroid impact (see Sec. 3.3.2).

3. Calculation of the BSDF that results from the impact craters with the Peterson model [43] (see Sec. 3.4.1). Calculation of the corresponding cleanliness level and slope due to contamination by ejected mass (see Sec. 3.4.2).

4. Optical software (FRED) calculation of the scattered light (see Sec. 3.5).

The solution is general and can be applied for any space optical instrument. In this chapter, I apply the results for the study of stray light due to micrometeoroids to the case of the LISA telescope (see Sec. 3.1). I consider the sun-orbiting LISA trajectory, 50 Mkm away from the Earth, in the micrometeoroid flux estimates. In the following, each step will be described, and the results will be presented.

3.1   NASA design of the LISA telescope

To make the phase measurements between beams from distant satellites possible, an optical telescope is used for transmitting and receiving the beams. The
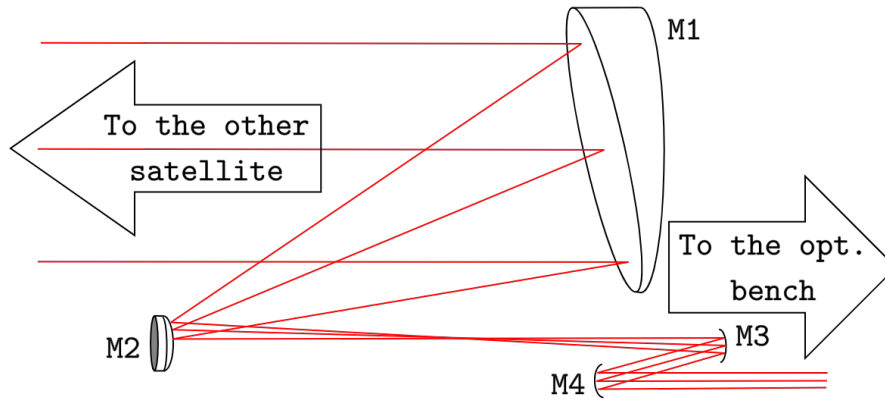
Figure 3.1: Schema of the Cassegrain four mirror telescope designed by NASA for the LISA mission. The same telescope is used to expand the transmitted beam and collect the light of the received beam.

telescope is a part of the MOSA (moving optical sub-assembly), which also includes the optical bench and the gravitational reference sensor. From the optical bench, the transmitted beam propagates and expand through the telescope, and is sent to the distant satellite. A thermal shield will surround the mirrors of the telescope, and we assume that only mirror M1 will be exposed to the space environment.

The scheme of the LISA telescope is given in Fig. 3.1. In the NASA design [55], it is an afocal Cassegrain telescope, which consists of four mirrors. The mirrors are named in sequential order following the beam from the big entrance aperture: M1 (primary mirror), M2 (secondary mirror), M3, and M4. This off-axis design provides better performance in terms of diffracted light, in comparison to the on-axis configuration.

3.2 Environmental conditions: particulates environmental model

The first step of stray light analysis due to micrometeoroid damage is to determine the particulate environment for the satellite. This includes information about the flux, velocity, density, mass, the directivity of the micrometeoroids. In the particular case of LISA, the environment of the satellite is given in the LISA Environment Specification document[39]. Chapter 5 of that document contains information about the micrometeoroid distribution.

The flux-mass model for meteoroids at one astronomical unit from the Sun has been proposed and presented by Grün et al. [9] (see Fig. 3.2). It gives the total average meteoroid flux $\phi_G(m)$ (sporadic+ stream average) in terms of the integral flux (i.e., the number of particles per square meter, per year, of mass larger than or equal to a given mass m, impacting a randomly-oriented flat plate under a viewing solid angle of 2π). Except for Earth shielding and
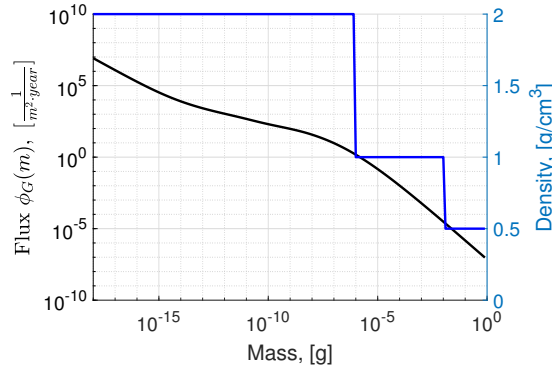
Figure 3.2: *The Grün meteoroid flux-mass model (in black) and the step function of density distribution (in blue)[13]*

gravitational effects (which are negligible at the LISA altitude of 50 Mkm), this flux is omnidirectional. This interplanetary flux is valid for the micrometeoroid mass range of 1×10^{-18} g to 1 g.

For the impact crater calculation, I use a density value of $2.5 \, \text{g/cm}^3$ for all ranges of mass, as was specified in the LISA Environmental model [39]. However, since the mass density of the micrometeoroids is not a measured quantity, an improved assumption should be used instead. Another description of the density is given as a step function [13] (see Fig. 3.2). This function will be used in Sec. 3.5.

As a first approximation, I use the constant value of meteoroid impact velocity of $20 \, \text{km/s}$ for all the masses of micrometeoroids. This value is the typical mean velocity for a micrometeoroid impact with a sun-orbiting body [54], and it is proposed by LISA environmental model[39].

The space debris environment is not considered.

The next step is to apply this model to the investigated surface. For this, some parameters of the mission are required: duration of the mission, nature of the critical surfaces (size, material, orientation, shielding), etc. For the calculation of the number of expected impacts, I use the Grün model[39] and the following parameters:

- Nominal mission duration is four years (extended duration is ten years).

- The primary M1 mirror diameter of the LISA telescope is $0.3 \, \text{m}$. I assume that M1 is the only mirror exposed to micrometeoroids.

Because the mechanical structure is unknown at the moment, no correction is made to account for the shielding by the structure surrounding the telescope. The approach presented in this thesis corresponds to a worst-case scenario.

Since the flux $\phi_G(m)$ is a cumulative flux, to know the number of expected impacts in a certain mass range (one bin), the difference between neighboring bins should be taken into account. The result of the calculation is given in Fig. 3.3. The bin size is uniform in the logarithmic scale. The ratio between the
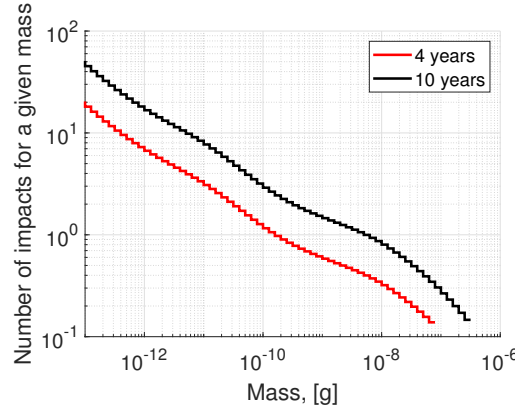
Figure 3.3: The expected number of micrometeoroid impacts on the M1 mirror, calculated according to the Grün Model, as a function of the micrometeoroid mass. The bin size is logarithmically uniform. The total number of micrometeoroid impacts with mass $> 1 \times 10^{-12}$ g is 92 for four years mission and 231 for ten years mission.

neighboring bin size is $10^{1/10}$. The number of expected impacts is a fractional value (different from integer[26]), as it is a statistical quantity. In the mass spectrum of the meteoroid (see Fig. 3.3), I neglect the high mass tail, for which the cumulated flux is lower than $1/e^2$.

3.3   The effect of the micrometeoroids

The hypervelocity impact of the optical surface causes a double effect in terms of scattering. The direct result of the impact is the micro crater. It causes scattering inside of it and diffraction on the border of the crater. From studies of lunar craters and craters in hardware returned from space, it is known that the shape of the damage crater is approximately circular, independent of micrometeoroid shape or incidence angle[26]. This is because hypervelocity impact is an explosive release of energy in which heat diffuses outward from a point. In this chapter, I use a single parameter to describe the impact crater: the Damage Crater Diameter (DCD). Below, I propose several methods to calculate the DCD.

Another effect of the hypervelocity impact is the contamination of the surface by the ejected material. There is experimental evidence that ejection takes place, due to the strength of the hypervelocity impact [20, 42, 53]. I cannot write a definitive account as to whether contamination goes to the mirror, or to the structure around (including other mirrors). The danger with ejected material is that it can contaminate other components in the system, which, for a given contamination level, can generate a higher scattered light contribution to the photodetectors. In principle, the amount of stray light caused by contamination may be of the same order or even larger than that caused by the impact craters. The mechanisms for re-deposition go well beyond the scope of

the thesis, but I can place upper limits by assuming that the impacted mirror receives 100% of the contamination it generates. So, in this thesis, I derive an upper limit for the contamination of the impacted mirror, by considering that all ejected matter is deposited back. After DCD estimates, I give expressions to calculate the total mass ejected for single micrometeoroid impact.

3.3.1 Estimate of the damage crater diameter

To calculate the size of the DCD, I use two different models [14, 26] with seven sets of parameters in total. The Hörz [14] model is based on the analysis of three laboratory experiments performed by independent investigators in order to calibrate the impact of micro craters. The damage crater diameter D [cm] is found to be a function of the mass of the projectile m [g]:

$$D = C \times m^\Lambda.$$ (3.1)

The coefficients C [cm] and Λ are given in Table 3.1. The DCD as a function of mass for these three Hörz models are given in Fig. 3.4.

Table 3.1: $log_{10}C$ and Λ coefficients of the Hörz model[14] and Eq. 3.1. Each set of the coefficients corresponds to an independent experiment.

	$Log_{10}C$	Λ
Hörz 1	1.569	0.37
Hörz 2	1.793	0.396
Hörz 3	1.485	0.377

Another model is based on a damage equation [13], which describes the physics of projectiles impacting a target at high velocities. The damage crater diameter D in this case is given by:

$$D \text{ [cm]} = K_1 K_c d_\mu{}^\zeta \rho_\mu{}^\beta v^\gamma [cos\alpha]^\xi \rho_t^\kappa \ ,$$ (3.2)

where K_1 is a factor characteristic of the model, d_μ [cm] is micrometeoroid diameter, ρ_μ, ρ_t [g/cm^3] are the densities of the micrometeoroid particle and target respectively, v [km/s] is the impact velocity, α is the impact angle, the crater factor K_c is the ratio of the crater radius to the crater depth and it may be as high as 10 for brittle targets (glass) [13].

Various investigations (Gault, Fechtig, McHugh& Richardson, Cour-Palais) have provided different values for the parameters, which are summarized in Ref. [13]. Typical values of the parameters of the Eq. 3.2 are given in the Table 3.2.

As a conservative approach, the value of the impact angle α is set to 0°. In the LISA telescope, the material for the primary M1 mirror will be a Zerodur ceramic with a density of $\rho_t = 2.53$ g/cm^3. Zerodur is a brittle material. I

Table 3.2: Parameters for DCD calculation with Eq. 3.2 in case of brittle targets [13].

Model	K_1	ζ	β	γ	ξ	κ	K_c
Gault	1.08	1.071	0.524	0.714	0.714	-0.5	10
Fechtig	6.0	1.13	0.71	0.755	0.755	-0.5	10
McHugh&Richardson	1.28	1.2	0	2/3	2/3	0.5	10
Cour-Palais	1.06	1.06	0.5	2/3	2/3	0	10
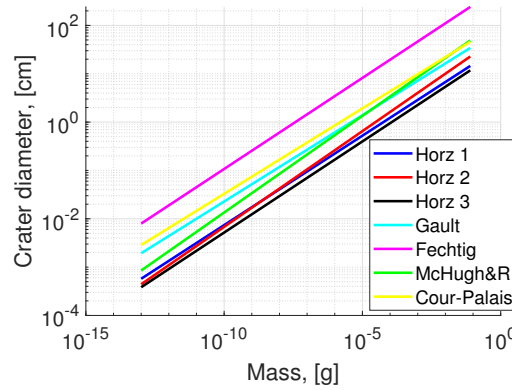
Figure 3.4: Calculated DCD with models listed above for micrometeoroids of mass $10^{-13} - 10^{-2}$ g, impact velocity of 20 km/s and micrometeoroid density 2.5 g/cm^2.

assume that the coating on the mirror does not affect crater formation. I choose $K_c = 10$ as the worst-case scenario.

The results of the different DCD calculations are given in Fig. 3.4. The difference between different models (up to one order of magnitude) can be explained by the variety of the experimental conditions in the study of hyper-velocity impacts, the complexity of the physical phenomena, and the different analytical approaches of the investigations. I assume that some of the used models may overvalue or undervalue DCD for Zerodur material. For this reason, I calculate the BRDF and perform optical simulations for each model separately. In the future, new experimental data might help to make a preference between the various models listed above, or possibly new models.

3.3.2   Estimate of mass ejection

As a micrometeoroid impact is a micro-explosion event, some mass will be ejected and can contaminate surfaces, including the M1 mirror. Here I consider this micro-explosion process and calculate the total amount of ejected mass M_e.

To calculate M_e, I use the equation derived by Gault[20, 53] following the

analysis of a range of experimental data:

$$M_e = 7.41 \times 10^{-6} K (\rho_\mu/\rho_t)^{1/2} E_i^{1.133} (cos\alpha)^2 \; (SI \; units) \,, \qquad (3.3)$$

where E_i – is the projectile kinetic energy in Joule, and α – is the angle of impact. For brittle materials such as Zerodur, the coefficient K depends on the diameter d_μ of the micrometeoroid: $K = 1$ for for > 10 µm and otherwise $K = d_\mu \; [m]/10^{-5}$.

To derive a worst-case value, I assume that all the ejected mass will be deposited on the M1 mirror surface. As a result, using Eq. 3.3, I can calculate the mass ejected for each mass of the micrometeoroid and so to build an appropriate M1 contamination model (see Sec. 3.4.2).

3.4 BSDF Calculations

As was mentioned above, the hypervelocity impact of the mirror surface by a micrometeoroid can cause scattering for two reasons: from the impact crater and ejected contamination. Each of them requires a specific analysis.

3.4.1 BSDF due to crater damage

To calculate $BSDF(\theta)$ (θ is the scattering angle) from damage craters, I use the Peterson model, which is devoted to calculating the BSDF of the scattering due to digs in optical components[43]. I assume that modeling the scattering from a dig can apply to model the scattering from an impact crater of the same diameter. In this model for a crater of a given diameter of D, the scattered light is divided into two contributions:

- "geometric" scattering or backscattering from surfaces inside the crater, considered as a Lambertian scatterer of diameter D

- diffraction of light that passes around the crater, considered as a circular mask of diameter D.

In the Peterson model [43] the digs are considered to be circular, and the intensity of diffracted light from a dig (crater) is calculated using scalar diffraction theory in the Fraunhofer (far-field) limit and Babinet's principle. So, the total BSDF from digs (craters) is calculated as the sum of the geometric and diffraction contributions:

$$BSDF(\theta) = \frac{N_D D^2}{4} \times \left[1 + \frac{\pi^2 D^2}{4\lambda^2} \left(1 + \frac{sin^2(\theta)}{l_D^2} \right)^{-3/2} \right] \,, \qquad (3.4)$$

where N_D is the number of digs per unit area, D is dig (crater) diameter, $\lambda = 1.064$ µm is optical wavelength, and the roll-off angle[43] is $l_D = \left(\frac{4}{\pi^4} \right)^{\frac{1}{3}} \frac{\lambda}{D}$. After integration over the range of micrometeorite masses, the calculated BSDF for different models of DCD is given in Fig. 3.5. The first term in this equation
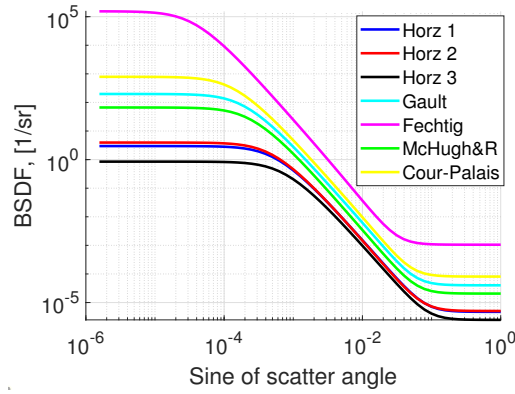
Figure 3.5: *Application of the Peterson model[43] to the scattering from a surface damaged by micrometeoroids. Assumptions: exposition duration is four years, exposition area is a disk with a diameter of* 30 cm, *micrometeoroid flux is given by the Grün model[9]. The names given to the BSDF models are the same as the ones used in Sec. 3.3.1 in the calculation of the DCD.*

is Lambertian scattering inside the crater area, and the second is due to the diffraction of crater boundaries.

I further proceed with FRED optical software in which the "ABg model" of BSDF is embedded. This model is widely used to describe scattering due to microroughness [16, 44] and involves only three parameters: A, B, and g corresponding, respectively to a proportionality factor, to a roll-of angle, and to a slope. To implement this Peterson model in the FRED software, I fit the resulting BRDF (see Fig. 3.5) with the ABg model plus a constant term:

$$BSDF = \frac{A}{B + (sin(\theta))^g} + \frac{R}{\pi},$$

(3.5)

The first term in Eq. 3.5 corresponds to the diffraction of light that passes around the crater, and the second term corresponds to Lambertian scattering of level R inside the crater. The fit of the Peterson BSDF by the ABg model[44] curve was previously used to simulate light scattering by digs in the METIS coronograph [17].

Let us now consider backscattering from the primary mirror of NASA's model of the LISA telescope. The precalculated BSDF for different models of DCD is shown in Fig. 3.5. The contribution to the backscattering fraction due to the diffractive part varies according to the different models from 1.6% to 8.7% (5.4% on average over the seven models). All the rest is due to Lambertian scattering. These values are specific for NASA's design of the LISA telescope. So in this particular case, methods based on percentage area coverage [16] give a reasonable estimate of the scattered light due to micrometeoroid damage.

The total integrated scatter (TIS) is a ratio of the total scattered power to the incident power. TIS for different models and mission duration is given in Table 3.3. The values of TIS due to micrometeoroid damage is significant.

Table 3.3: Total integrated scatter for the nominal and extended mission duration [13, 14]

Model	TIS, 4 years	TIS, 10 years
Hörz 1	2.35×10^{-5}	9.02×10^{-5}
Hörz 2	2.52×10^{-5}	1.02×10^{-4}
Hörz 3	1.23×10^{-5}	4.79×10^{-5}
Gault	2×10^{-4}	7.44×10^{-4}
Fechtig	5.26×10^{-3}	2.05×10^{-2}
McHugh&Richardson	1.03×10^{-4}	4.2×10^{-4}
Cour-Palais	4.04×10^{-4}	1.49×10^{-3}

3.4.2 BSDF due to ejected contamination

To calculate the BSDF due to ejected contamination, I assume that the size distribution of particles can be described with the (IEST)CC1246 standard [46]. It describes the number of particles N_p (per 0.1 m^2) whose diameter is greater than or equal to D_p by:

$$N_p(S, CL, D_p) = 10^{|S|[log_{10}^2(CL) - log_{10}^2(D_p)]} , \qquad (3.6)$$

where S is the slope of particle size distribution, CL is the cleanliness level, D_p is particle diameter in µm.

This is a common way to describe the distribution of the contamination on an optical surface. The model is implemented in FRED optical software and is easy to use as it requires only a few parameters (λ, S, CL, etc.) and relies on the properties of Mie scattering. Here I will calculate the cleanliness level using the definition of the CL parameter (the largest particle [in microns], which can be found on a surface of 0.1 m^2; see Eq. 3.6) and using the following considerations:

- In the regime of hypervelocity micrometeoroid impacts, the largest ejected particle mass is proportional to the total mass ejected [42], with a coefficient of proportionality is of a fraction of one. For simplification, I assume the worst case when the coefficient of proportionality is equal to one: the biggest ejecta carries most of the ejected mass. As a consequence, the biggest mass ejected is from the biggest impact micrometeoroid.

- Ejected mass is mainly target mass (Zerodur) and has the same density as target material. Ejected particles are spherical.

- All the ejected mass deposits back onto the surface.

Using the flux calculated in Sec. 3.2 and ejected mass in Sec. 3.3.2, I find that after four years of exposition, I will have maximum ejected mass equal to 1.14×10^{-4} g, which corresponds to a diameter of a sphere equal to 441 µm, so $CL = 441$.

To find the slope S, I use the mass conservation law. The total mass of particles, which is given by this distribution, should be equal to the total mass ejected over the exposition duration:

$$\sum_{D_p=0}^{\infty} \Delta\Big(N_p(S, CL, D_p)\Big) \frac{S_m}{0.1 \;[\mathrm{m}^2]} \times m(D_p) = \sum_{d_\mu=0}^{\infty} M_e(d_\mu) \times \Delta\Big(\phi_G(m(d_\mu))\Big) \,,$$

(3.7)

where S_m is the M1 mirror area, the mass of the micrometeoroid $m(x)$ is a function of its equivalent sphere diameter x and M_e is the ejected mass given in the Sec. 3.3.2, $\phi_G(m)$ is integrated flux given in Sec. 3.2, Δ is a difference operation between the neighboring bins of the distribution (N_p and ϕ_G are cumulative distributions). On the right side of Eq. 3.7 is the total mass ejected due to all micrometeoroid impacts, and on the left side is the total mass of contaminations, assuming that the distribution of particles on the surface will be given by Eq. 3.6. When the slope parameter S is chosen correctly, these two masses will be equal.

I find that for four years, the absolute value of the slope is equal to $S = 0.8738$, which is quite close to the value of 0.926 used in the CC1246D standard. For ten years of exposition: $CL = 743.2$ and $S = 0.7668$.

Due to thermal emission considerations, the super-polished surface of the M1 mirror will be coated with silver. The silver coating will have a consequence on the amount and type of the ejected material. To estimate the effect, let us consider a limiting case when the ejected material will be only silver. In this case, in Eq. 3.3, the coefficient is $K = 1$ for all diameters of the micrometeoroid. The corresponding S and CL coefficients are $S = 1.2827$ and $CL = 216.6$ for four years of mission duration and $S = 1.0998$, $CL = 365$ for ten years.

3.5 FRED Simulations

The backscattering in the direction of the photodiode of the LISA telescope has been calculated using FRED simulation software. The scattering model has been applied for the M1 telescope mirror only.

3.5.1 Scattering due to impact craters

To calculate scattering due to impact craters in FRED software, I use two embedded BSDF models: Lambertian and ABg. The coefficients of these models were obtained from the fit of total Peterson's BSDF, as was described in section 3.4.1. The calculation results are summarized in the Table 3.4. Despite the high values of the TIS (see Table 3.3), the values of backscattering are low, as the coupling factor of the M1 mirror is low.

To study the impact of micrometeoroid parameters on the final result, I consider a situation when the density of micrometeoroid follows the step distribution given in Fig. 3.2 (blue curve), and I simulate distribution velocities following Taylor's[54], which is a re-evaluation of the Harvard Radio Meteor

Table 3.4: Backscattering fraction (BSF) for the nominal and extended mission duration in the LISA telescope

Model	BSF, 4 years	BSF, 10 years
Hörz 1	3.2e-15	1.2e-14
Hörz 2	3.4e-15	1.1e-14
Hörz 3	1.7e-15	6.4e-15
Gault	2.6e-14	9.5e-14
Fechtig	6.6e-13	2.5e-12
McHugh&Richardson	1.3e-14	5.4e-14
Cour-Palais	5.2e-14	1.9e-13

Project (HRMP) data of about 20000 meteor observations. HRMP is a multi-station radar system that measures the strength of the echo from the ion column of the meteors [25]. The result is summarized in Table 3.5 (third column). For comparison, the second column contains values of backscattering fraction with the assumptions used in the thesis: constant velocity $v = 20$ km/s and density $\rho = 2.5$ g/cm^3 of the micrometeoroid. No qualitative change is observed. The values are slightly lower, as the considered density of micrometeoroids is lower.

Table 3.5: Backscattering fraction for variable density and velocity of the micrometeoroids.

Model	BSF, 4 years Constant ρ, V	BSF, 4 years Variable ρ, V
Gault	2.6e-14	1.7e-14
Fechtig	6.6e-13	5.1e-13
McHugh&Richardson	1.3e-14	1.4e-14
Cour-Palais	5.2e-14	3.7e-14

The FRED divot analysis approach was used by NASA[51] to estimate micrometeoroid damage of the M1 mirror. In their work, the total area occupied by the craters was modeled as a single divot placed on the M1 mirror surface. Depending on the position of the divot on the mirror surface, the BSF obtained in their study is in a range from 1.73e-14 to 3.33e-13, which is compatible with the values obtained in this study.

3.5.2   Scattering due to ejected mass contamination

The FRED calculation of contamination was performed with the embedded 1246C[46] standard. The values of CL and S used in the simulation are listed in the Sec. 3.4.2. The computed values of backscattering are summarised in

Table 3.6. As Zerodur mirror will be coated with silver, it would certainly cause an effect of contamination population, and so the real value of scattering will be in between two limit cases: mirror material is only Zerodur and mirror material in only silver.

Table 3.6: Backscattering fraction due to contamination for a mission duration of four and ten years.

Mirror material	BSF, 4 years	BSF, 10 years
Zerodur	4.93e-13	1.04e-12
Silver	2.16e-12	4.46e-12

These values are compatible with the highest of the scattering data of Table 3.4. So scattering contribution due to ejected mass is dominant under the assumption that 100% of the ejecta contribute to the M1 contamination. The re-deposition of the ejected matter deserves more investigations. The contribution to the scattering of the ejected mass contamination should not be neglected in stray-light estimates caused by micrometeoroid impacts.

3.6 Conclusion

In this chapter, I developed a method for the estimation of the stray-light due to micrometeoroid damage of optical surfaces. It consists of four steps. The first step is the flux calculation based on the satellite environmental model. The second step is the calculation of the damage crater diameter and ejected mass. The third step is the calculation of the corresponding bidirectional reflectance distribution function using the Peterson model and the 1246C standard. The last step is the calculation of the scattering with an optical software, for the particular application to the optical configuration considered. I have applied the method to the simulation of the scattering of light in the LISA telescope, due to the damage to the primary mirror from a micrometeoroid impact. The results suggest that even under the worst-case assumptions the impact craters and the resulting contamination contribute to an acceptable scattering of light to the LISA detectors.

It should be noticed that contamination due to mass ejection gives a significant contribution. It even reaches or exceeds the contribution due to the damage craters. The assumption, used here as a worst-case scenario, that 100% or the ejected mass is collected by the mirror itself, should be evaluated. Processes exist, such as electrostatic processes, that can give rise to re-deposition, but actual re-deposition is probably only partial. Indeed further work should address possible contamination due to ejecta towards mirrors other than the primary mirror.

The main sources of uncertainty are in the modeling of the damage crater diameter and in the distribution of ejected particles (shape and quantity) on the

damaged surface. The modeling presented here should benefit from any future improvements in the experimental data, particularly when optical materials are used as targets for the hypervelocity impact experiments.

The method is straightforward to apply, to modify, and it can be used for any space optical instrument with minor parameter changes. The code is available on GitHub[1]. The model can be used not only for reflective but for refractive optics as well. The final result of the scattered light calculation depends on the optical design of the telescope: in our case, the beam expanding telescope that is required to transmit the emitted beam to the distant spacecraft. This work has been sent to publication in the Journal of Astronomical Telescopes, Instruments, and Systems (JATIS) [30].

---

[1] https://github.com/KVital/BSDF

Chapter 4

Coherent scattering

Coherence is a property of waves that allows stationary (temporal and spatially constant) interference pattern to occur [50]. In the case of scattering from a rough surface, this interference pattern is called speckle.

Speckle was discovered in the early 1960s [23] under the illumination of a rough surface with a laser source of highly coherent light. Speckle is a random interference pattern of a diffraction nature. This grainy structure consists of bright and dark spots as shown in Fig. 4.1.

<div align="center">(a)   (b)</div>
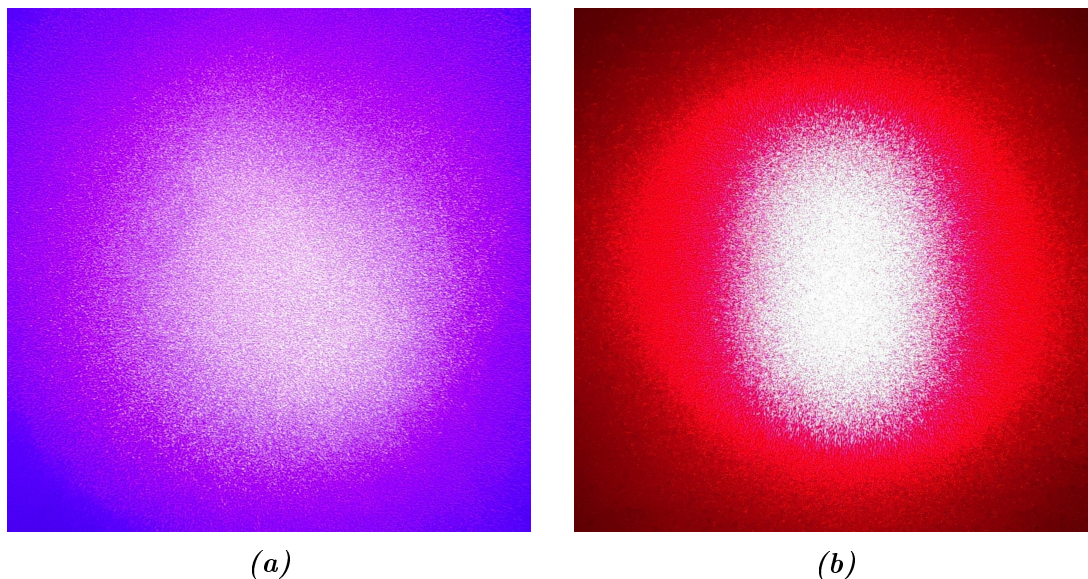
Figure 4.1: Image of the speckle pattern taken under illumination of a white surface with 405 nm (a) and 650 nm (b) laser pointers.

By analogy with the "original" speckle structure of Fig. 4.1, we also call speckle the grainy structures observed in Sec 5.4.1 and Sec. 5.4.2 as they also originate in the random nature.

In this chapter, I will describe the properties of coherent scattering, that is, the properties that show up when coherent light is scattered by a rough surface. In the analysis of stray light from a surface, from a component or an optical system, it is essential to remember these properties. Most of the time,

they contradict our everyday experience, and, as an example, they cannot be described by using the widespread notion of BSDF (bidirectional scattering density function), which applies to coherent scattering only after appropriate averaging is made. In Sec. 4.1.1, I will describe the statistical properties of the speckle, such as amplitudes, phases, and intensities distributions based on the approach of Goodman [23]. The spatial properties of the single speckle grain (lateral, axial sizes) are discussed in Sec. 4.1.3. Sec. 4.2 will show how it is possible to apply this knowledge to LISA heterodyne measurements.

In the rest of the chapter (see Sec. 4.3), I will describe a model of coherent scattering. Basically, it is a generalization of the Harvey-Shack model [32]. The new model uses a minimum of assumptions, and it combines a conventional approach of BRDF for the rough surface with speckle properties of coherent scattering. In Sec. 4.4, I implement the model and test it under various conditions. I will show that even if the distribution of the amplitudes and phases in the speckle is random, the envelope of the mean speckle intensity is defined by the roughness properties of the scattering surface and is compatible with BRDF of the Harvey-Shack model.

To clarify the definition, I would like to emphasize the difference between the coherent backscattering used in this manuscript and other research papers [2, 56]. The backscattering, which I discuss in this and the next chapter, happens on the surface, and it is merely scattering in backward direction in reference to nominal beam propagation direction and in certain solid angle. In Ref. [56], the term coherent backscattering is used to describe scattering, which happens inside the disordered medium and is responsible for weak localization.

4.1   Speckle properties

So far, the best description of the statistical properties of the speckle pattern was given by Goodman [23]. In Sec. 4.1.1, I will provide a short summary of these properties which are essential for the understanding of this and the next chapters. In Sec. 4.1.2 gives a treatment of the particular case when the random field senses the perturbation of a constant, offset field. This case is fundamentally important as it describes the distribution of amplitudes, phases, and intensities that can be directly applied for LISA heterodyne measurements (see Sec. 4.2) and explains the distribution of backscattering intensities in an optical fiber (see Chapter 7). At the end of the section (see Sec. 4.1.3), I will describe how it is possible to derive typical lateral and axial sizes of the single speckle grain.

4.1.1   Single speckle's point statistics

As was mentioned earlier, the scattering of coherent light causes the occurrence of a random interference pattern, called speckle. At each point of the speckle pattern, the amplitude can be treated by a random phasor sum $\mathbf{A}$ (see Fig.4.2a)

of multiple scattering contribution with random amplitude a_n and phase ϕ_n:

$$\mathbf{A} = Ae^{j\Theta} = \frac{1}{\sqrt{N}} \sum_{n=1}^{N} a_n e^{j\phi_n}. \tag{4.1}$$

To derive the probability density function (PDF) of the sum, Goodman[23] uses the following assumptions:

1. The amplitudes and phases a_n and ϕ_n are statistically independent of a_m and ϕ_m provided $n \neq m$.

2. For any n, a_n and ϕ_n are statistically independent of each other.

3. The phases ϕ_m are uniformly distributed on $(-\pi, \pi)$.

If the number of steps N is large, the sum of N independent random variables is asymptotically Gaussian (due to the central limit theorem):

$$p_{\mathcal{R},\mathcal{I}}(\mathcal{R}, \mathcal{I}) = \frac{1}{2\pi\sigma^2} exp\left(-\frac{\mathcal{R}^2 + \mathcal{I}^2}{2\sigma^2} \right), \tag{4.2}$$

where $\mathcal{R}, \mathcal{I}$ are the real and imaginary parts of $\mathbf{A}$ and σ^2 is the second moment of $\mathcal{R}$ (or $\mathcal{I}$, which is the same). After a change of variables from $\mathcal{R}, \mathcal{I}$ to amplitude and phase A, Θ, one obtains:

$$p_{A,\Theta}(A, \Theta) = p_\Theta(\Theta) \times p_A(A) = \frac{1}{2\pi} \times \frac{A}{\sigma^2} exp\left(-\frac{A^2}{2\sigma^2} \right), \tag{4.3}$$

where $p_A(A)$ is Rayleigh density function (see Fig. 4.2b). The probability density for the phase $1/2\pi$ is constant: no preferred phase appears, and the phases are uniformly distributed.

(a) *(b)*
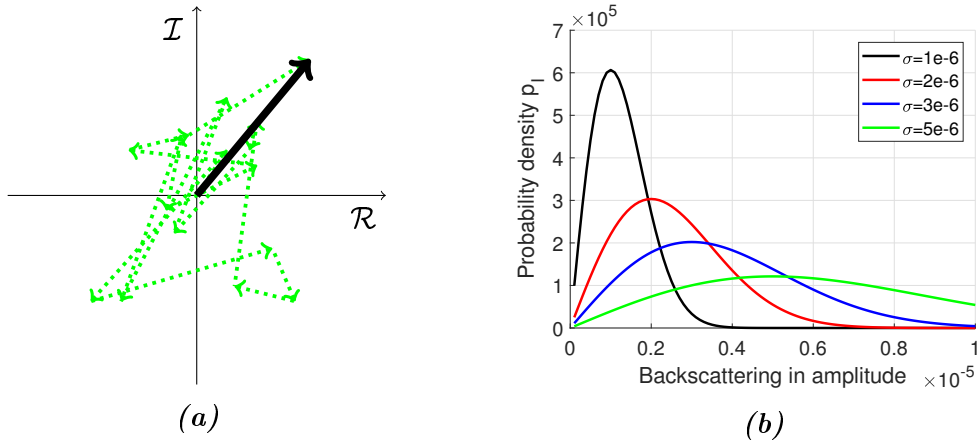
Figure 4.2: Random phasor sum (a − the black arrow is resulting vector A of multiple scattering contributions (green dashed arrows)) and Rayleigh probability density function (b) for different values of the mean value.

The mean of the distribution is:

$$\overline{A} = \sqrt{\frac{\pi}{2}}\sigma. \tag{4.4}$$

The intensity distribution of a random phasor sum can be computed similarly. As the intensity $I = A^2$, so

$$p_I(I) = \frac{1}{\overline{I}} exp\left(-\frac{I}{\overline{I}} \right), \qquad (4.5)$$

where the mean $\overline{I} = 2\sigma^2$. A speckle with this intensity distribution is called *fully developed speckle*. Probability to find intensity larger than $\overline{I}$ is $1/e \approx 0.368$.

The contrast of the speckle is defined as:

$$C = \frac{\sigma_I}{\overline{I}}, \qquad (4.6)$$

where σ_I – is the standard deviation of the intensity pattern, $\overline{I}$ – is the mean intensity. For fully developed speckle $C = 1$. Contrast can be reduced due to polarization or wavelength diversity and can reveal the presence of imperfections in a setup.

4.1.2 Single speckle's point statistics with a constant contribution

The real situation which will be realized in the LISA instrument is the sum of a constant phasor (the nominal beam of an interferometer) and a random phasor sum (stray light). Let us assume that the constant vector A_0 is directed along the real axis. Then the real and imaginary parts can be written:

$$\mathcal{R} = A_0 + \frac{1}{\sqrt{N}} \sum_{n=1}^{N} a_n \cos \phi_n,$$
$$\mathcal{I} = \frac{1}{\sqrt{N}} \sum_{n=1}^{N} a_n \sin \phi_n. \qquad (4.7)$$

Using the same approach [23], it is possible to derive the PDF in amplitude (see Fig. 4.3a) :

$$p_A(A) = \frac{A}{\sigma^2} exp\left\{ -\frac{A^2 + A_0^2}{2\sigma^2} \right\} I_0 \left(\frac{AA_0}{\sigma^2} \right). \qquad (4.8)$$

However, the distribution in phase Θ is not uniform anymore, but it is given by a rather complicate expression:

$$p_\Theta(\Theta) = \frac{e^{-\frac{A_0^2}{2\sigma^2}}}{2\pi} + \sqrt{\frac{1}{2\pi}} \frac{A_0}{\sigma} e^{-\frac{A_0^2}{2\sigma^2} sin^2(\Theta)} \frac{1 + erf\left(\frac{A_0 cos(\Theta)}{\sqrt{2}\sigma}\right)}{2} cos(\Theta), \qquad (4.9)$$

where erf is the standard error function. This distribution for several values of the ratio A_o/σ is given in Fig. 4.3b.

When A_0/σ becomes large, $p_\Theta(\Theta)$ approaches a Gaussian density function:

$$p_\Theta(\Theta) \approx \frac{1}{\sqrt{2\pi}\sigma/A_0} e^{-\frac{\Theta^2}{2(\sigma/A_0)^2}}. \qquad (4.10)$$
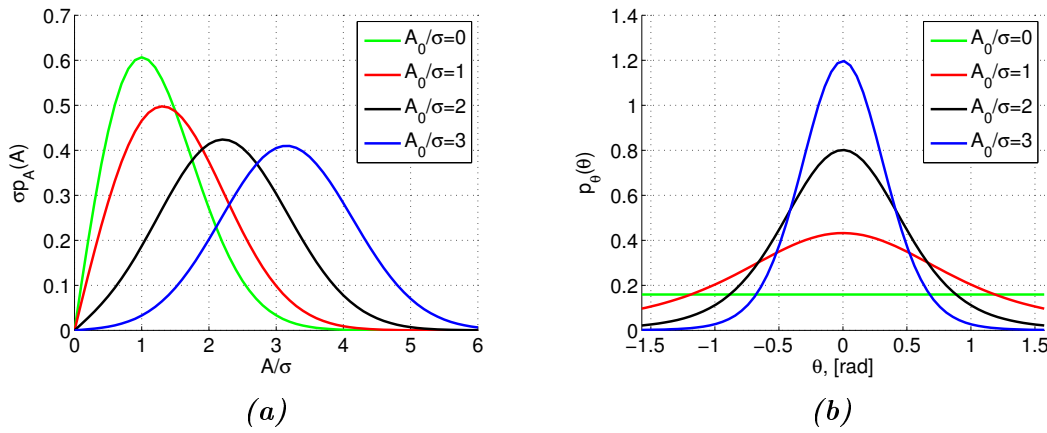
Figure 4.3: The amplitude (a) and phase (b) probability distribution functions in the case of the constant contributor to random phasor sum.

The knowledge of the amplitude distribution provides the error on the phase measurements. In the case of the LISA instrument, the histogram analysis of the signal amplitude distribution will allow us to determine the value of phase error due to stray light. The amplitude of the signal can be retrieved from the in-phase and quadrature signals, as used for phase measurements. This allows us to have an onboard zero mass (zero cost) stray light detector. The acquisition of the amplitude histogram should be taken when the speckle changes over multiple grains. This situation will occur during repointing events of the MOSA or when the satellite is hit by a micrometeoroid, for example.

4.1.3 Spatial dimensions of a speckle grain

The size of a single speckle grain is different in lateral and axial dimensions so that both cases will be studied separately. The derivations of the spatial sizes are based on the consideration presented in Ref. [47].

In this section, I will examine a simple imaging system with a single convex lens (see Figs. 4.4,4.5) of diameter D. The point source P_0, on the rough surface (speckle generation source), is imaged by a lens. The image of the point P_0 is P_0' located at a distance f from the lens. This point is the center of curvature of the emerging wavefront Γ, where all the waves in the wavefront are in phase.

The lateral dimension of a speckle grain

Let us consider a point source P_0 at the rough surface. The image of this point is situated in point P_0' (see Fig. 4.4). A point P is placed in the image plane at a distance y from P_0' (then the ray at the upper edge of the lens, has a different beam path from the lower ray, at the bottom of the lens). The waves, which arrive at P, have a phase difference relative to P_0'. The maximum occurring phase difference is on the sides of the aperture (lens), and it is linked to the size D of the aperture. The corresponding path length difference is:

$$\Delta = D \sin \theta, \tag{4.11}$$

where D is the lens diameter, and θ represents the height of P above the optical axis.
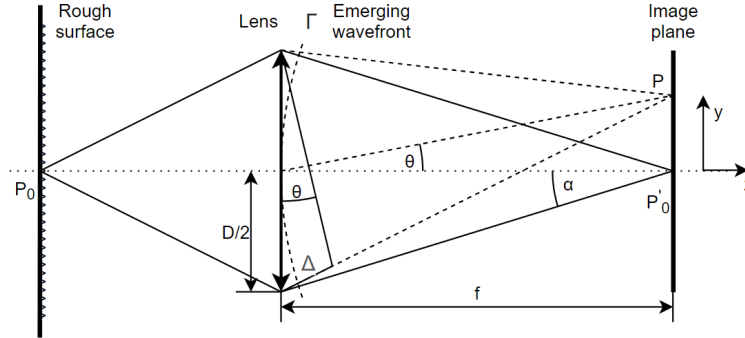
Figure 4.4: Elementary analysis of the lateral dimension of a speckle grain. The point P_0 is imaged in the point P_0' by a lens of diameter D.

We assume that the path length difference reaches a value $\approx \lambda$ for which the intensity in P differs significantly from P_0', that is

$$D \sin \theta \approx \lambda. \tag{4.12}$$

As y is small compared to the image distance f:

$$D \frac{y}{f} \approx \lambda. \tag{4.13}$$

So the lateral extension δ can be defined as:

$$\delta = 2y \approx 2\lambda \frac{f}{D} = \frac{\lambda}{\alpha}, \tag{4.14}$$

where $2\alpha = D/f$ is the aperture of the image-forming objective. Up to a constant factor, the result is consistent with diffraction consideration at a circular aperture.

The axial dimension of a speckle grain

Let us move the image plane π' (screen) on δz along the axis z (see Fig. 4.5). The displaced plane contains an out of focus image P_0'' of the source P_0. We assume that $\delta z \ll f$. Same as in the previous case, P_0' is located at the center of curvature of the wave front Γ, so the waves emerging from it arrive all in phase to P_0'. But in plane π'' they have some phase difference. The corresponding maximal path difference is:

$$\Delta = IP_0'' - OP_0'', \tag{4.15}$$

where I is point on the converging wave front Γ (see Fig. 4.5). The lengths $IP_0' = OP_0' = f$. Using the cosine theorem:

$$(IP_0'')^2 = f^2 + \delta z^2 - 2f\delta z \cos \alpha, \tag{4.16}$$
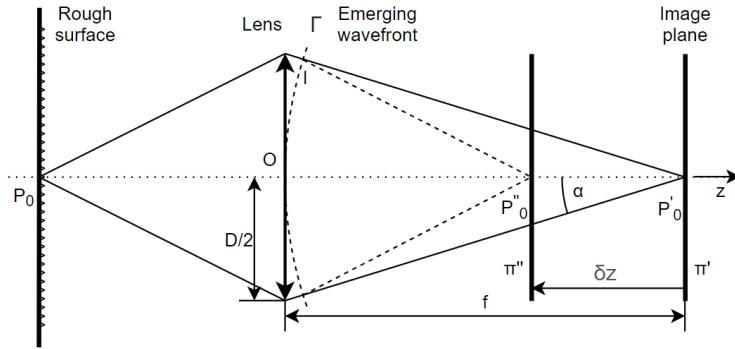
Figure 4.5: Elementary analysis of the axial dimension of a speckle grain under small defocusing condition. The point P_0 is imaged in the point P_0' by a lens of diameter D.

and

$$OP_0'' = f - \delta z. \tag{4.17}$$

This can be rewritten:

$$IP_0'' = f\sqrt{1 + \frac{\delta z^2}{f^2} - 2\frac{\delta z}{f}\cos\alpha} \approx f\left(1 - \frac{\delta z}{f}\cos\alpha\right) = f - \delta z\cos\alpha, \tag{4.18}$$

where was used that $f \gg \delta z$, so:

$$\Delta = f - \delta z\cos\alpha - f + \delta z = \delta z(1 - \cos\alpha) = 2\delta z\sin^2\frac{\alpha}{2}. \tag{4.19}$$

As the aperture of the system α is small, the maximum path difference is

$$\Delta = \delta z\frac{\alpha^2}{2}. \tag{4.20}$$

To give a significant change, the path length difference has to be of the order of a wavelength:

$$\delta z \approx 2\frac{\lambda}{\alpha^2}. \tag{4.21}$$

We consider that the axial dimension of the speckle grain is:

$$\delta z \approx 4\frac{\lambda}{\alpha^2}. \tag{4.22}$$

So the speckle grain is ellipsoidal with typical dimensions δ and δz (see Eq.4.14 and Eq. 4.22 correspondingly $\delta/\delta z = \alpha/4$). The same consideration [47] can be applied for the case of free space propagation (no lens). The speckle grain has a form of a cigar elongated along the propagation axis. So the typical dimension of the speckle grain depends on the numerical aperture of the observation system and on optical wavelength, which again confirms the diffraction nature of this phenomena.

The dimension of a speckle grain under the tilt of a sample

Let us consider a laser beam of diameter 2ω incident of a sample surface with an angle θ_1 (see Fig. 4.6). The speckle pattern will move if the incidence angle is changing $\theta_1 \rightarrow \theta_2$. Practical interest is how fast the change happens or, in other words, what is the single speckle grain in this case.
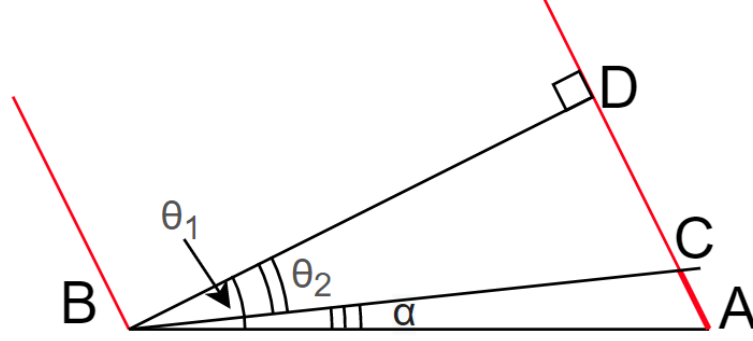
Figure 4.6: Illustration to the derivation of the speckle size under tilt of the sample. The difference in path length is considered between two situations: the beam is incident with an angle theta$_1$ and after tilt, the beam incident with angle theta$_2$. Red lines represent a beam of diameter $BD = 2\omega$.

Let us consider a triangle $\triangle ABC$. The side of the triange $AB = BD / \cos \theta_1$ and $BC = BD / \cos \theta_2$, where BD=2ω. Using cosine theorem:

$$AC^2 = AB^2 + BC^2 - 2AB \cdot BC \cos(\theta_1 - \theta_2). \tag{4.23}$$

The tilt angle $\alpha = \theta_1 - \theta_2$ is small and so $BC \approx BD / \cos \theta_1$ and $\cos(\alpha) = 1 - \frac{\alpha^2}{2}$.To obtain the speckle change, the phase difference between opposite sides of the beam should be in order of 2π or the same $AC = \lambda$. Then from Eq. 4.23 we get:

$$\alpha = \frac{\lambda}{2\omega} \cos \theta_1. \tag{4.24}$$

So when the surface tilted by angle $\frac{\lambda}{2\omega} \cos \theta_1$, we observe full speckle change. This quantity depends on the incidence angle and is compatible with beam divergence $\frac{\lambda}{\pi \omega_0}$, where ω_0 is the beam waist. This result will be used in Sec. 4.4.4, and Sec. 5.4.2 is the analysis of modeled and measured speckle data.

4.2 Consequence of coherent scattering on LISA phase measurements

Let us consider the case of LISA phase measurements in the presence of stray light due to coherent scattering from a rough surface. Two nominal beams with amplitudes A_0 and B_0 will interfere on the surface of the photodiode. What needs to be measured is the angle between A_0 (considered as the reference,

local oscillator) and B_0. However, both of the beams have also stray light contributions. This contribution, in a simple case, can be described by a single vector [24] in the amplitude/phase plane. In two different realizations of a MOSA, the stray light amplitude and phase will be different. The distribution of these successive realizations of the stray light phase and amplitude contributions to nominal beams will be random because two mirrors, for instance, are never identical (their roughness distribution changes from mirror to mirror even if the statistical properties of the roughness profile are reproducible). Due to this fact, I switch to a description of the stray light with a random phasor sum rather than by a single vector. This random phasor sum has certain properties described in section 4.1.2, and its distribution in phase and amplitude can be characterized by a finite amount of parameters (see Eq. 4.9). We label by σ_A and σ_B the parameters of the stray light amplitude distribution of the corresponding beams.

It is important to notice that the addition of a multitude of sums on an amplitude basis has no consequences on the functional form of the statistical distributions [23]. That means that the total sum of scattering from different optical surfaces (each of them has a parameter of distribution σ_i) will also have a Rayleigh distribution on the amplitude basis with parameter:

$$\sigma^2 = \sum_i \sigma_i^2.$$

(4.25)

So each of the beams will have a constant contribution A_0 or B_0 and stray light will be a random phasor sum with parameter σ_A or σ_B respectively. This case was considered in Sec. 4.1.2. A_0 being the reference, local oscillator amplitude. We will label by A (or B) the resulting amplitude and by Θ_A (or Θ_B) the resulting phase. Θ_A and Θ_B are zero mean phase distributions given by Eq. 4.9.

The intensity that results from the recombination of the two beams can be written as:

$$A^2 + B^2 + 2AB \times cos(\Theta_A - \Theta_B + \theta_X + 2\pi F t),$$

(4.26)

where θ_X is the phase difference between nominal beams (desired quantity to measure), F is the optical frequency difference between the two beams (heterodyne frequency), and t is time.

After demodulation at F frequency, the phase meter will measure $\Theta = \Theta_A - \Theta_B + \theta_X$. If $A/\sigma_A \gg 1$ and $B/\sigma_B \gg 1$, the PDF of Θ is:

$$p_\Theta(\Theta) \approx \frac{1}{\sqrt{2\pi}\xi} exp\left[-\frac{(\Theta - \theta_X)^2}{2\xi^2} \right],$$

(4.27)

where the width of the distribution is

$$\xi^2 = \left(\frac{\sigma_A}{A}\right)^2 + \left(\frac{\sigma_B}{B}\right)^2.$$

(4.28)

So if the phase measurements are desired to be precise, the fraction of stray light relative to each of the beams is required to be small, no matter how small the stray light contribution is in absolute units.

4.3 Model of coherent scattering

The goal of this model is to build a bridge between the BRDF description of the properties of scattering and the coherent properties of the scattering on the example of surface microroughness. This unified model should, on one side, describe the observed properties of coherent light when it is scattered by a rough surface, and on the other side have as a limit the Harvey-Schack (or similar) models. For this, the calculation of the scattered field should be done with minimal assumptions and averaging. For example, we do not put any constraints on surface roughness distribution.

The simplicity of my model allows easy modification, and so accelerates the studies of scattering under the different conditions: scattering from curved surfaces, polarization effects, different modes of the illumination beam, etc. However, the down side of this is a high demand for computational resources. But as the goal of this study is purely scientific, we do not concentrate on the practical application of the model code.

The model for scattering presented below considers the problem when a Gaussian beam (section 4.3.1) is collimated using collimator C1 towards the surface under test (see Sec. 4.3.2) as shown in Fig. 4.7. The roughness of the surface causes the perturbation of the beam's wavefront and so the scattering. The scattered field propagates (Sec. 4.3.3) through the lens of a collimator C2, and the fiber is located at the focus of the lens, to collect scattered light. Some parts of the light in this plane couple (Sec. 4.3.4) into the fiber. This coupled intensity will be analyzed in Section 4.4. The model can be used to calculate scattering in any configuration. It can also applies to the case of backscattering, the configuration implemented in Chapters 5 and 6, except for the fact that, in backscattering, the emitting and collecting collimators are the same.
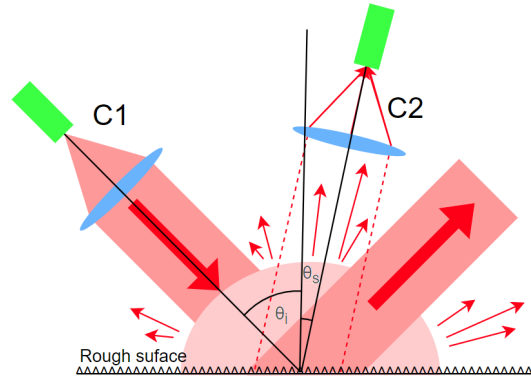
Figure 4.7: Illustration of the physical setup considered in the model. A fibered collimator C1 illuminates the rough surface with a Gaussian beam (the surface is in focus) under angle θ_i. A collimator C2 collects the scattered light under angle θ_s. The collection area is schematically shown by the red dashed line. The scattered light collected by the collimator C2 lens couples in the optical fiber.

I want to mention the alternative model [33], which was developed in the In-

stitut Fresnel and uses a similar approach but a different realization of coherent scattering field computation.

4.3.1 Gaussian beam

Let us consider a Gaussian beam, which propagates in a z direction. The field distribution of the beam in the plane (x, y) which is perpendicular to propagation axis z is given by:

$$E(r, z) = A_0 \left(\frac{2}{\pi \omega(z)^2} \right)^{\frac{1}{2}} exp\left(\frac{-r^2}{\omega(z)^2} \right) exp\left(-j\left(k\left(z + \frac{\pi r^2}{\lambda R(z)} \right) - \psi(z) \right) \right), \quad (4.29)$$

where A_0 is amplitude of the beam, the beam width is $\omega(z) = \omega_0\sqrt{1 + (z/z_R)^2}$, the Rayleigh range is $z_R = \pi \omega_0^2/\lambda$, ω_0 is beam waist, the radius is $r^2 = x^2 + y^2$, the wave vector is $k = 2\pi/\lambda$, the radius of curvature is $R(z) = z(1 + (z/z_R)^2)$ and the Gouy phase is $\psi(z) = atan(z/z_R)$.

The power of the beam is:

$$\int |E|^2 2\pi r dr = A_0^2, \quad (4.30)$$

where the integration takes place in (x, y) plane, that is prependicular to beam propagation axis z.

Nevertheless, if the normal of the target surface is turned at an angle θ_i (incidence angle) with respect to the beam direction, then it is useful to introduce another system of coordinates, rotated by θ_i:

$$\begin{bmatrix} \xi \\ zI \\ \eta \end{bmatrix} = \begin{bmatrix} cos(\theta_i) & sin(\theta_i) & 0 \\ -sin(\theta_i) & cos(\theta_i) & 0 \\ 0 & 0 & 1 \end{bmatrix} \times \begin{bmatrix} x \\ z \\ y \end{bmatrix}, \quad (4.31)$$

where (ξ, η, zI) are coordinates attached to the target surface, and (x, y, z) are the coordinates in the frame attached to the Gaussian beam waist and direction. If the target is in focus before the surface tilt, then $z = 0$ and $\xi = cos(\theta_i)x$, $zI = -sin(\theta_i)x$, $\eta = y$.

Eq. 4.29 allows us to write the amplitude and the phase distribution of the incident beam on the target surface. There is no difficulty in injecting a laser beam in the higher-order modes. As an example, I plot an intensity profile of the Gaussian beam $E(\xi, \eta, zI = 0)$ (see Fig. 4.8a) and phase of the beam (see Fig. 4.8b) under small incidence angle ($\theta_i = 1\ mrad$).

In the model, the surface illuminated with a Gaussian beam works as a complex aperture (the rough surface is larger than the illuminated area).

4.3.2 Target surface

To describe target surface orientation, reflectance, curvature, surface height distribution, the term $p_R(\xi, \eta)$ is used as an effective reflectance in amplitude:

$$p_R(\xi, \eta) = \sqrt{R_{s/p}} \times e^{j\phi_R} \times e^{j\phi_T} \times e^{j\phi_C}, \quad (4.32)$$
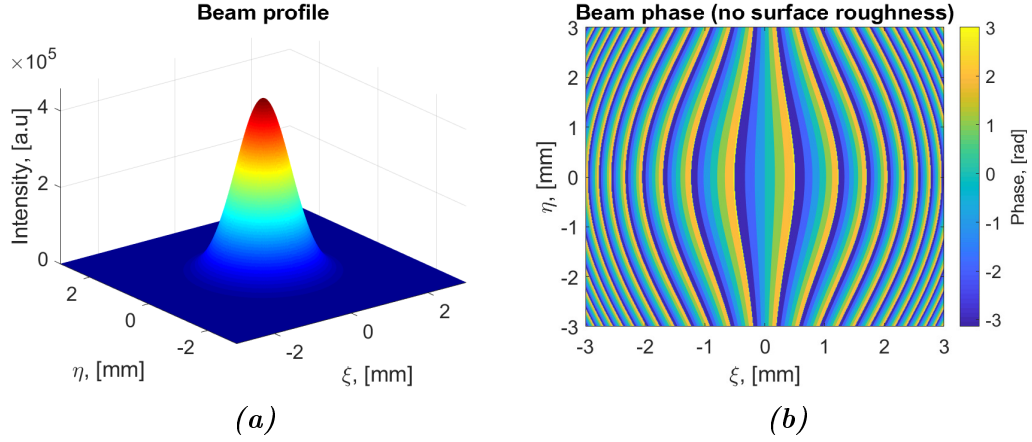
Figure 4.8: *The intensity (a) and phase (b) of the Gaussian beam $E(\xi, \eta, zl = 0)$ on the target surface at incidence angle $\theta_i = 1$ mrad. The wavelength of the beam $\lambda = 1.064$ μm and beam waist $\omega_0 = 1.15$ mm. The small incidence angle was chosen to underline the sequential phase change on the surface (if $\theta_i = 0$, the phase would be plain).*

where $R_{s/p}$ is the reflectance in power. The reflectance depends on the polarization (s or p) of the incident beam:

$$R_s = \left| \frac{n_1 \cos\theta_i - n_2\sqrt{1 - \left(\frac{n_1}{n_2}\sin\theta_i\right)^2}}{n_1 \cos\theta_i + n_2\sqrt{1 - \left(\frac{n_1}{n_2}\sin\theta_i\right)^2}} \right|^2, \qquad (4.33)$$

$$R_\mathrm{p} = \left| \frac{n_1\sqrt{1 - \left(\frac{n_1}{n_2}\sin\theta_i\right)^2} - n_2\cos\theta_i}{n_1\sqrt{1 - \left(\frac{n_1}{n_2}\sin\theta_i\right)^2} + n_2\cos\theta_i} \right|^2, \qquad (4.34)$$

where n_1, n_2 are complex refractive indexes of the air and the target surface. The phase ϕ_T is a phase which accounts for the tilted incidence at a flat surface:

$$\phi_T = \frac{2\pi}{\lambda}\xi sin(\theta_s), \qquad (4.35)$$

where θ_s is the scattering angle (between the normal to the surface and observation direction).

This phase is linked with the orientation of the nominal surface relative to the observer (one part of the surface is above the nominal plane, and the other is below) and it is independent of the beam properties on the surface. The phase ϕ_C is introduced to account for the curvature of the surface and abberations. Phase ϕ_R is introduced due to surface roughness (see Fig. 4.9):

$$\phi_R = \frac{2\pi}{\lambda}OPD, \qquad (4.36)$$

where the optical path difference (OPD) is introduced in a similar way as in
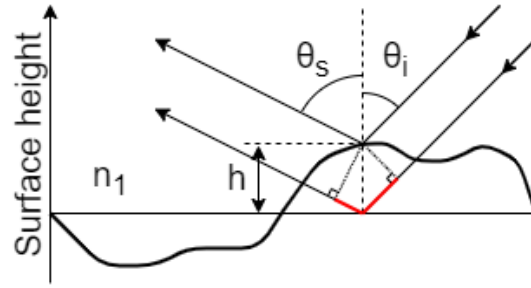
Figure 4.9: Illustration to define the optical path difference (marked in red).

the Harvey-Shack model [32]. For the case of reflection, the OPD is

$$OPD = -n_1(cos(\theta_i) + cos(\theta_s)) \times h(\xi, \eta), \qquad (4.37)$$

where $h(\xi, \eta)$ is a surface roughness profile and n_1 is the refractive index of the medium from which the beam came.

To run the model I need to generate a surface height distribution $h(\xi, \eta)$. To do that I use a method described om mysimlabs.com[1]. In the generation are used two parameters: the RMS surface roughness and the correlation length. The generation is performed in two steps:

1. Random normal distribution with zero mean and desired standard deviation of roughness (height) distribution $S(\xi, \eta)$.

2. Convolution of the achieved distribution with a Gaussian $G(\xi, \eta)$ of a given width (which is proportional to a correlation length).

For the last step, the Convolution theorem of a Fourier transform (FT; IFT is the inverse Fourier transform) is used:

$$h(\xi, \eta) = const \times IFT(FT(S(\xi, \eta)) \times FT(G(\xi, \eta))). \qquad (4.38)$$

An example of the generated surface roughness profile is given in Fig. 4.10a. The perturbed wave front of the reflected from the rough surface beam is given in Fig. 4.10b.

---

[1] www.mysimlabs.com
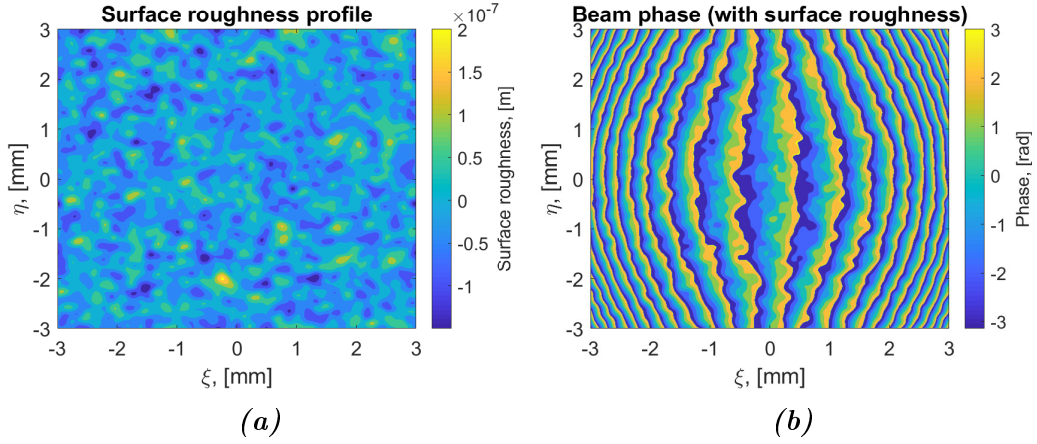
Figure 4.10: Surface roughness profile (a) and the perturbed wave front of the Gaussian beam $E(\xi, \eta)$ on the target surface at an incidence angle of $\theta_i = 1\ mrad$. The surface roughness height RMS is 30 nm, and the correlation length is 100 μm (arbitrary chosen coefficients). The value of roughness is slightly exagerated, but it helps to see the impact of surface roughness on the reflected phase distribution.

4.3.3 Propagation

So just after the reflection from the rough surface, the wavefront of the reflected beam up to constant factor (see Eq. 4.37) will follow the surface height profile. The complex amplitude of the beam at this moment is:

$$t_A(\xi, \eta) = E(\xi, \eta) \times p_R(\xi, \eta). \tag{4.39}$$

To propagate this wavefront to the area of interest (see Fig. 4.11), I use expression (5-20) in p.107 from Goodman [22].
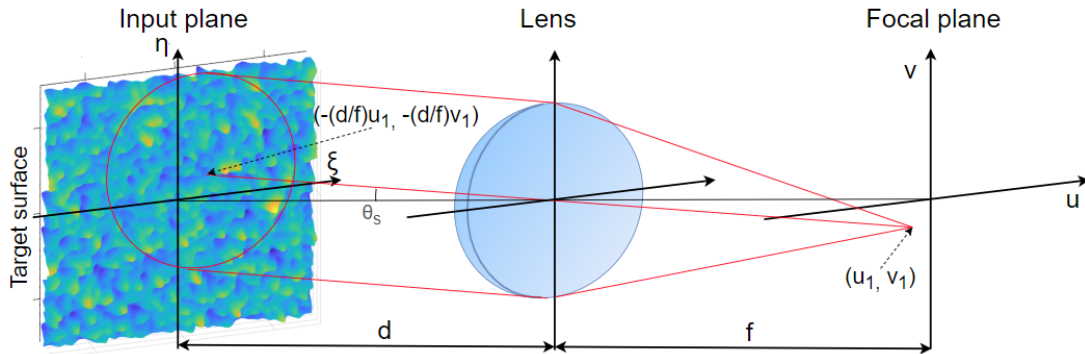
Figure 4.11: Illustration to the propagation of the perturbed wavefront. The input plane contains the target surface, which is observed with a convex lens at distance d from the surface. The image is formed in the focal plane of the lens.

The complex amplitude in the focal plane is:

$$U_f(u,v) = \frac{exp\left[j\frac{k}{2f}\left(1 - \frac{d}{f}\right)(u^2 + v^2)\right]}{j\lambda f} \times$$

$$\int_{-\infty}^{+\infty}\int_{-\infty}^{+\infty} t_A(\xi, \eta)P\left(\xi + \frac{d}{f}u, \eta + \frac{d}{f}v\right)exp\left[-j\frac{2\pi}{\lambda f}(\xi u + \eta v)\right]d\xi d\eta, \tag{4.40}$$

where P is the pupil function (1 inside and 0 outside) which describes the lens of diameter D, f is the focal length, d is the lens-object distance, (u, v) are the coordinates in the focal plane.

An example of the computed diffractograms is given in Fig. 4.12. The diameter of the green dashed circle is equal to the fiber mode diameter. In the case of specular reflection, the diffractogram of the gaussian beam is a Gaussian (see Fig. 4.12a). But in the case of scattering, the speckle pattern is observable (see Fig. 4.12b). Red and black lines are corresponding to zero of the real and imaginary parts of the diffractogram pattern U_f. The crossing of these two lines corresponds to zero scattering power.

(a) $\theta_i = \theta_s = 0^o$ *(b) $\theta_i = 0^o$, $\theta_s = 45^o$*
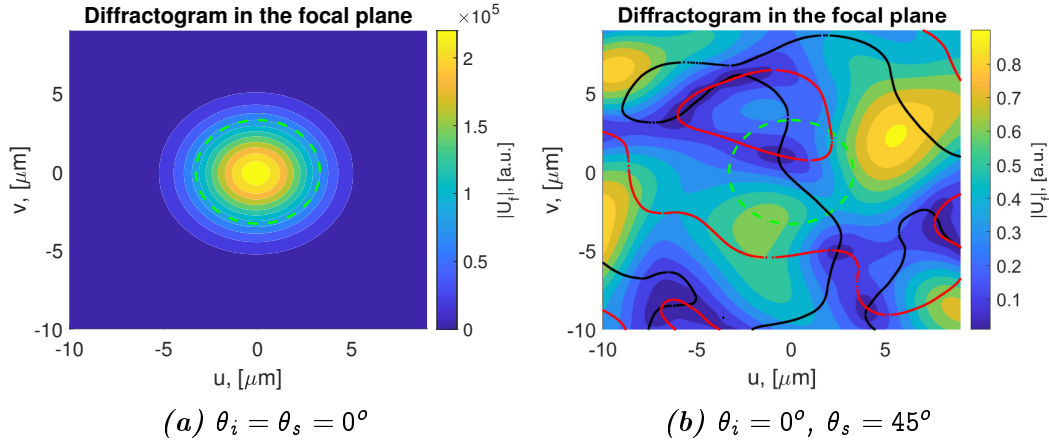
Figure 4.12: The diffractogram patterns under different scattering angles. The RMS surface roughness is 10 nm and the correlation length is 1 μm (arbitrary choosen values). The red and black lines are zeros of real and imaginary parts of the scattered field in the focal plane. The dashed green line is an indication of the fiber core perimeter.

4.3.4 Coupling

At the last step, the field in the focal plane couples into the fiber (see Appendix A). The intensity, which couples into the fiber (ignoring losses due to reflection at the fiber end) is:

$$I_\Omega = \frac{\left|\int\int U_f(u,v) \times F(u,v)^* du dv\right|^2}{\int\int |F(u,v)|^2 du dv}, \tag{4.41}$$

where F is the guided fiber mode (the fiber is assumed to be a single mode fiber):

$$F = \sqrt{\frac{2}{\pi}} \frac{1}{(a_0/2)} exp(-\frac{u^2 + v^2}{(a_0/2)^2}), \tag{4.42}$$

where a_0 is mode field diameter of the fiber.

The calculated intensity can be compared with conventional BRDF, provided a normalization on scattering angle and input intensity is made. The solid angle in which this system receives scattering intensity is:

$$\Omega = \pi(\theta_b)^2, \tag{4.43}$$

where $\theta_b = \frac{\lambda}{\pi \omega_0}$ is beam divergence. For convenience, I set the input amplitude $A_0 = 1$, so:

$$BRDF = \frac{I_\Omega}{\Omega}. \tag{4.44}$$

This value can be compared with the BSDF of the Harvey-Shack model.

4.4 Numerical implementation of the model

As was discussed before, scattering is a diffraction effect caused by the perturbation of the wavefront reflected by the rough surface. In Fig. 4.13a is a diffractogram of the Gaussian beam at normal incidence at a rough (red curve) and ideal (black curve) surface. Without scattering, the diffractogram is quite similar to the Airy function (diffraction by the circular aperture). However, for the latter plot, the diffractogram (the oscillatory structure on the wings) is caused by a limited integration area. While in the presence of scattering, the diffractogram on the periphery is much higher and broader. The width of it depends on the roughness spectrum of the target. Measurements of the scattering as a function of scattering angle is a scan of this diffractogram, as shown in Fig. 4.13b. The change of the scattering angle causes the shift of the diffractogram. As the fiber is in the center of the focusing system, only that part of the light couples into the fiber, which is in the middle of the plot.

So the calculation of the scattering field is equivalent to diffractogram calculation. In this frame, certain precautions (see Sec. 4.4.1) should be taken to avoid introducing errors in the calculation. In Section 4.4.2, I list all the parameters, which were used in the model. The values of these parameters are close to the parameters of the experimental setup (see Chapter 6). In the rest of this section, we will discuss the main achieved results.

4.4.1 Numerical error issues

The implementation of the model described above in a program code causes the need to use a finite limit of integration and nonzero integration step. The main integral to be taken in the model is Eq. 4.40, and it is a Fourier transform. As only half of the frequencies are useful in discrete Fourier transform

(a) Diffractogram without surface roughness
(black) and with (red).

(b) Change of scattering angle θ_s cause a shift of the diffraction pattern.
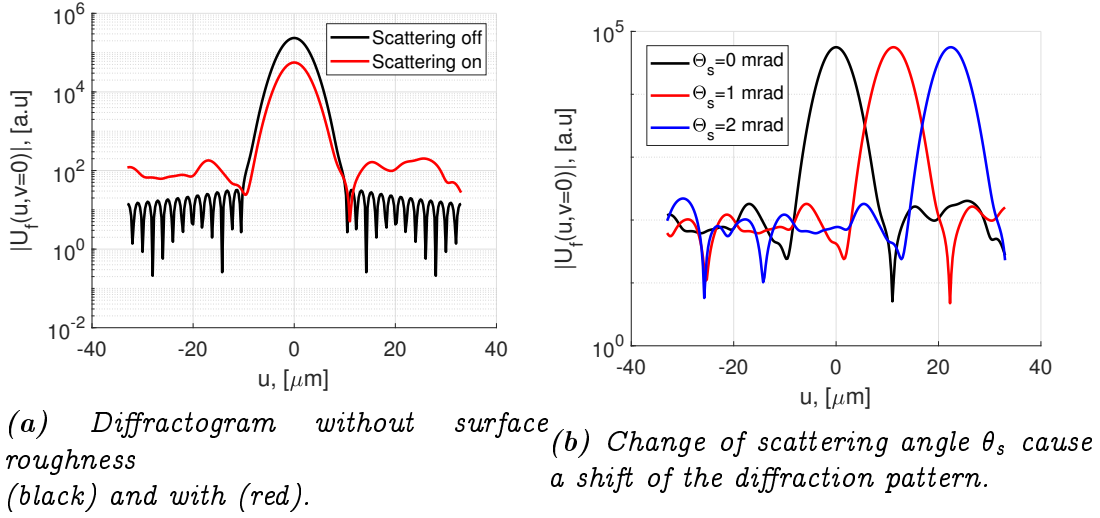
Figure 4.13: Illustration to the discussion

(Nyquist theorem), so the corresponding precautions should be taken to avoid undesirable numerical effects.

Let us consider an imaging system, as shown in Fig. 4.14. Light with wavelength λ is incident on the lens with angle θ. The projection of the wave vector on the x axis corresponds to a wavelength of:

$$\lambda_x = \lambda / \sin \theta. \tag{4.45}$$

The lens is a Fourier transform system that shifts the focus on x_0, proportionally to the spatial frequency of $f_x = 1/\lambda_x$. As the Fourier transform performed
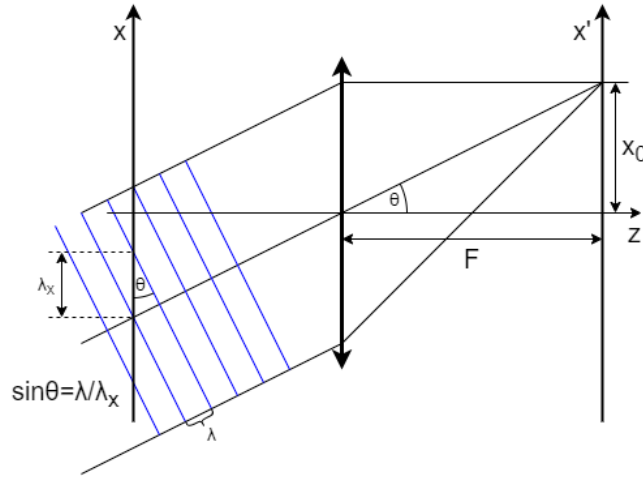
Figure 4.14: Fourier transform system: we assume the monochromatic wave has a wavelength λ in the direction of propagation, and λ_x is a projection of the wavelength along the x axis, the angle between the direction of propagation and z axis is θ. F is the focal length.

by the lens is discrete, so the maximal observable frequency is half of the inverse

sampling step Δx (Nyquist–Shannon sampling theorem), so $f_x = 1/(2\Delta x)$. Sampling step is integration step in Eq. 4.40. Using this and Eq. 4.45, we have:

$$sin(\theta) = \frac{\lambda}{2\Delta x}. \tag{4.46}$$

So, to be able to correctly calculate the scattering at $\theta = \pi/2$, the maximum step of integration in the input plane should satisfy inequality $\Delta x \leq \lambda/2$.

Another problem is rather physical. A Gaussian beam illuminates the surface. This beam has, in principle, an infinite extension in the transverse plane. If the size of the surface is smaller than the size of the beam, the corresponding diffraction pattern will be observable, which is not desirable. In practice, the data about the surface is stored in a matrix. The storage and manipulation with the matrix require physical memory. So the size of the matrix (integration area) should be limited at an acceptable level.

The problem is worse when a nonzero incidence angle is used. In this case, the beam spreads over the target surface and causes an aliasing and parasitic diffraction. This situation will be discussed in Sec. 4.4.5.

Except for pure numerical problems, the model can have human errors. To eliminate them, I use several checkpoints to test the validity of the calculations:

1. In input plane

$$\int \int |E_0|^2 d\xi d\eta = A_0^2. \tag{4.47}$$

   To simplify $A_0 = 1$. In the case of the finite integration borders, this value will be slightly smaller.

2. Due to Parseval's theorem, in the focal plane

$$\int \int |E_0|^2 d\xi d\eta = \int \int |U_f|^2 du dv. \tag{4.48}$$

3. In case of specular reflection (with reflection coefficient $R = 1$), $I_\Omega \approx 1$

4 If in the input plane the aperture is circular with a diameter D, then the first zero of the diffraction pattern in the focal plane is $d_0 = 1.22\frac{\lambda f}{D}$, where f − is the focal distance.

4.4.2 List of the model parameters

The model uses three types of settings: parameters of the optical system, of the surface, and numerical parameters. Their listed names are the same as in the program code. The units (if they exist) are listed on the right of the parameter name. The choice of this set of the model parameters was caused by the desire to describe the results of the experimental setup. Therefore, the numerical values of the parameters of the optical system are as close as possible to the real ones.

Optical system parameters are: the lens diameter $D = 0.027\,[m]$, the object-lens distance $d = 0.82\,[m]$, the (equivalent) focal distance $f = 0.0112\,[m]$,

the fiber core diameter (a_0 is Eq. 4.42) for PM980 fiber is $a\_core = 6.6 \cdot 10^{-6}$ $[m]$, the wavelength $lambda = 1.064 \cdot 10^{-6}$ $[m]$, the Gaussian beam waist $omega\_0 = 0.00115$ $[m]$, the incident angle $Thet\_i$ is usually 0 $[rad]$ if not otherwise mentioned, the scattering angle $Thet\_s$ $[rad]$ is a variable value.

Parameters of the target surface are: the correlation length rc $[m]$ (no fixed value), the RMS surface roughness $sigmaW$ $[m]$ is variable too, $n1$ is refractive index of the area ($n1 = 1$ for air), $n2$ refractive index of the target ($n2 = 1.3763$ for Aluminum at 1.064 μm), $k1$ is extinction coefficient (the imaginary part of the complex optical index) of the area ($k1 = 0$ for air), $k2 = 0$ is extinction coefficient of the target ($k2 = 10.245$ for Aluminum at 1.064 μm), $Polarization = 0$ is polarization of the incident beam (for s $Polarization = 0$, for p $Polarization = 1$).

The numerical parameters are: the integration length in input plane $Lmax = 0.009$ $[m]$ (the integration in Eq. 4.40 is performed in $[-Lmax, \ Lmax]$), the integration step in the input plane $step = 0.5 \cdot 10^{-6}$ $[m]$, this integration area is subdivided in smaller pieces $LB = 0.003$ $[m]$, the integration step in the image plane $stepUV = 1 \cdot 10^{-6}$ $[m]$.

The integration area $Lmax \times Lmax$ in the input plane is divided into smaller pieces $LB \times LB$ due to the high demand for a computer memory resource. For the parameters listed above, the input surface plane is divided into nine submatrices. Each submatrix takes 1 GB hard drive place. The generation of the surface and calculation of the propagation integral is separated on two steps due to RAM issues. The computation of the model is performed on the INRIA cluster with MATLAB code. To achieve fast computation, the code was highly vectorized and optimized for GPU calculation with CUDA.

The crosschecks with the parameters listed above are:

1 In the input plane $\int \int |t_A|^2 d\xi d\eta \approx 0.95023$ (reflection coefficient $R = 0.95023$)

2 In the focal plane $\int \int |U_f|^2 du dv = 0.950227$ (The integration area in the focal plane is limited. The corresponding correction factor = 0.99123)

3 In the case of specular reflection, $I_\Omega = 0.940134$. (coupling factor is 0.989378)

So the cross-checks are satisfied and further modeling is possible.

4.4.3 Comparison with the Harvey-Shack model

The new model described above requires physical verification. One of the possible ways to do this is to compare the output results of it with a well-known, widely used model. As a reference model, I chose a Harvey-Shack model. This model provides the link between BRDF and parameters of surface: roughness and correlation length.

In this section, I perform a comparison of the Generalized Harvey-Shack model [28] with parameters: wavelength $\lambda = 1.064$ $[\mu m]$, refractive index $n1 = 1 = -n2$ (minus sign is due to reflection), variable surface roughness,

correlation length, and scattering angle. In contrast, the incidence angle remains zero ($\theta_i = 0$), unless otherwise. The numerical parameters of the model to compute Harvey-Shack are the number of Gauss points $\mu = 1000$ and number of Fourier expansion terms (20).

For simplicity of comparison, I will call the model described in Sec. 4.3 the coherent scattering model. The comparison between the Harvey-Shack model and the coherent scattering model was made for three values of the surface roughness and constant correlation length of the surface (see Fig. 4.15a) and three values of correlation length and constant surface roughness (see Fig. 4.15b).

(a) Correlation length $rc = 1$ μm

(b) Surface roughness $sigmaw = 10$ nm
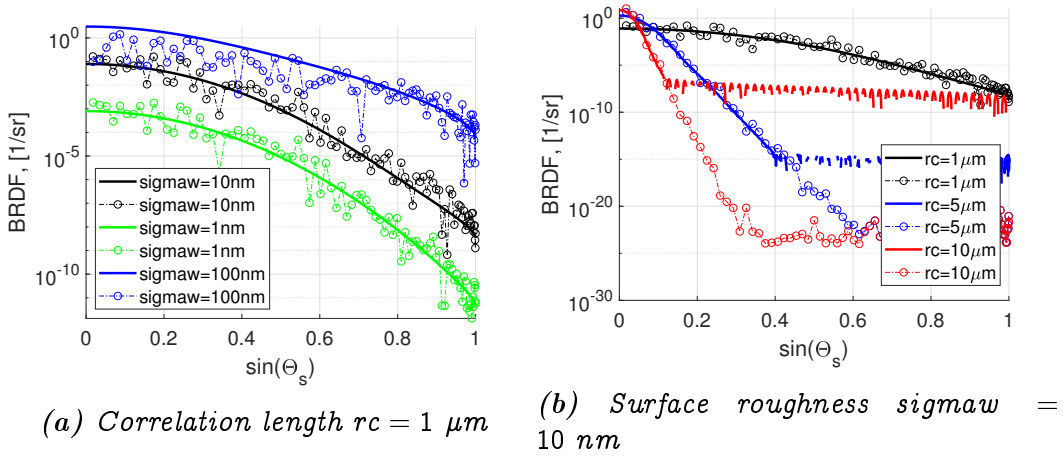
Figure 4.15: Comparison of the scattering distribution given by the Harvey-Shack (solid line) and by the coherent scattering model (circle-dashed line).

As a general rule, the values retrieved under the coherent scattering model show strong dispersion with respect to the Harvey-Shack BRDF because the coherent scattering model is based on a random distribution of the surface profile, and this randomness manifests itself in the random nature of the calculated coupling factor, a property known under the name of speckle (see Sec. 4.1). But agreement is expected (and observed) on average, since the Harvey-Shack model is based on the statistical averages of the surface height profile. The overvalued result of the Harvey-Shack model for RMS surface roughness of 100 nm (see Fig. 4.15a) can be explained by the fact that a 100 nm roughness exceed the domain of validity of the Harvey Shack Model which assumes that the roughness is small compared to wavelength. For this specific case $\lambda/RMS \approx 1/10$, what is probably not sufficient.

The comparison of the averaged BRDF of the coherent scattering model and Harvey-Shack for certain scattering angles is given in Table 4.1.

So based on data given in Fig. 4.15 and Table 4.1, we can conclude that two models are in good agreement.

Table 4.1: Comparison of the averaged values with Harvey-Shack model: sigmaw = 10 nm, rc = 1 μm. The contrast of the speckle is approximately equal to one, so fully developed speckle is observed as expected.

Angle	This model	Harvey-Shack	Contrast
0	11.5×10^{-2}	7.8×10^{-2}	0.99
$\pi/8$	7.6×10^{-3}	5.7×10^{-3}	0.95
$\pi/4$	1.2×10^{-5}	1.13×10^{-5}	0.86
$2.5\pi/8$	10.3×10^{-7}	5.3×10^{-7}	1.02
$2.75\pi/8$	6.4×10^{-7}	1.5×10^{-7}	0.9
$3\pi/8$	21.9×10^{-8}	5.2×10^{-8}	1.03

4.4.4 Coherent properties of the scattered light

From the other side, the coherent scattering model should also describe coherent features of the scattering described in Sec. 4.1. The closer look at the scattering pattern of the coherent scattering model at different angles (see Fig. 4.16) shows a random structure. In this section, I will study this feature and show the similarity with the properties expected for speckle.
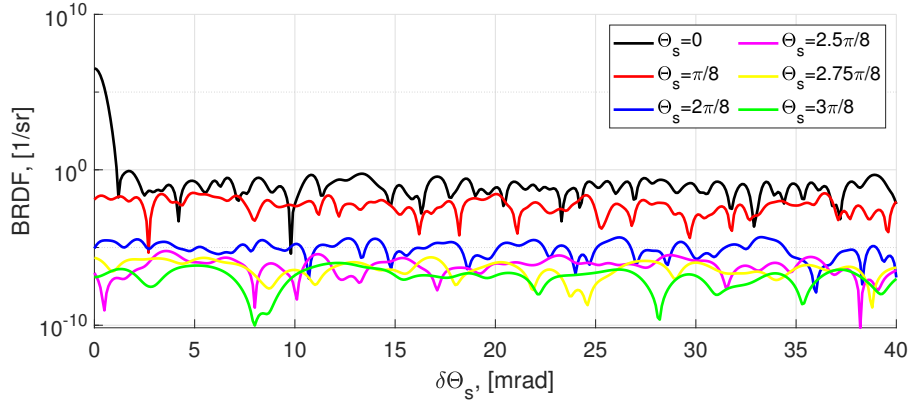
Figure 4.16: BRDF from the coherent scattering model, plotted at high resolution. The scattering angle θ_s is scanned with steps of 100 μradian. At zero angle of the black curve is a reflected beam. Surface properties: sigmaw = 10 nm, rc = 1 μm.

The intensity distribution of the coherent scattering model is given in Fig. 4.17a(red). This distribution can be described by the derived negative exponential distribution 4.5.

The size of the speckle grain was discussed in Sec. 4.1.3, and here I verify the listed consideration for the case of the lateral speckle grain dimension. In Eq. 4.14 it is claimed that this size is proportional to wavelength λ and inversely proportional to the aperture α of the image-forming objective. In the considered case $\lambda = 1.064$ μm and $\alpha = 27$ mm$/(2 \times 11.2$ mm$) = 1.2$, so the lateral size of the speckle grain in the image plane is $\delta \approx \lambda/\alpha = 0.88$ μm. On the other side, I extract the value of the speckle grain in the image plane (before

coupling calculation) from the model. For this, I calculate the 2D autocorrelation function of the speckle pattern using the Wiener-Khinchin theorem [29] and fit the achieved function along u and v axis with Gaussian type function $A \times \exp(-\frac{x^2}{2B^2}) + C$. The value of B gives the size of the single speckle grain in units of length, and it is given in Fig. 4.17b. The size of the speckle grain in the image plane is independent of the scattering angle θ_s and is equal to $\approx 2 \ \mu m$. This value is compatible with one provided by Eq. 4.4.

(a) $\qquad\qquad\qquad\qquad$ (b)
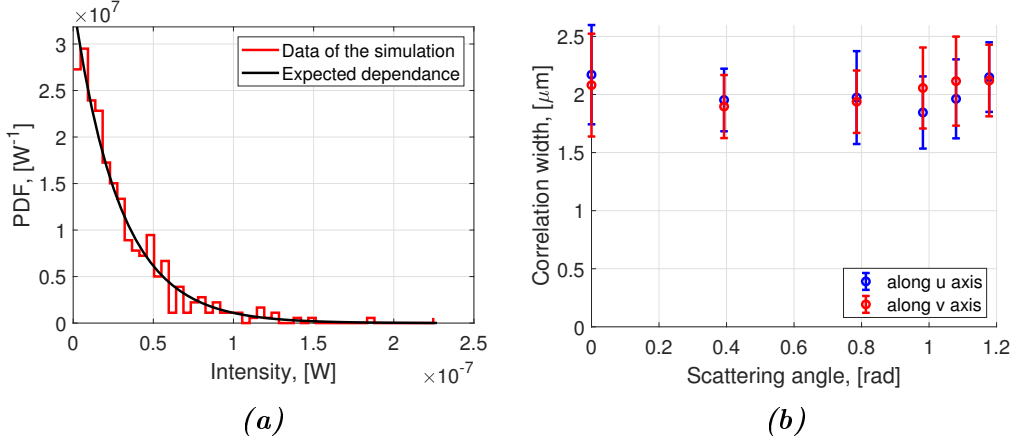
Figure 4.17: Distribution of scattering intensities near zero scattering angle given by the coherent scattering model (a) size of the autocorrelation function of the speckle in the image plane along u and v axes for different scattering angles θ_s (b).

The autocorrelation function of the BRDF in Fig. 4.16 is given in Fig. 4.18a. The half width of the autocorrelation functions HW_{auto} at 0.9, 0.8 and 0.7 of maximum are given in Fig. 4.18b. Speckle size scales with scattering angle θ_s as $HW_{auto}/cos(\theta_s)$ as expected 4.1.3. The values of HW_{auto} for 0.9, 0.8 and 0.7 of maximum are $0.23 \pm 0.02 \ [mrad]$, $0.35 \pm 0.02 \ [mrad]$ and $0.47 \pm 0.02 \ [mrad]$ correspondently. This is compatible with the value of half beam divergence $0.29 \ [mrad]$.

The contrast (see Eq. 6.22b) of all datasets is close to one (see Tab. 4.1), so all patterns given in Fig. 4.16 patterns are fully developed speckles.

The distribution of the uncorrelated amplitudes and phases in the focal plane is shown in Fig. 4.19. It shows good agreement with Eq. 4.3.

These results are in full agreement with the statistical approach of Goodman [23].

4.4.5 Modeling of backscattering

In the case of backscattering studies (see Chap. 6), the incident angle will be of one or several 10s of degrees, then the shape of the beam spot on the target surface will turn to elliptical. After some critical angle, the limits of the integration in the input plane will cause diffraction on the square aperture (due to limits of integration, as shown in Fig. 4.11). In addition to that aliasing will show up. The illustration of this problem is given in Fig. 4.20.
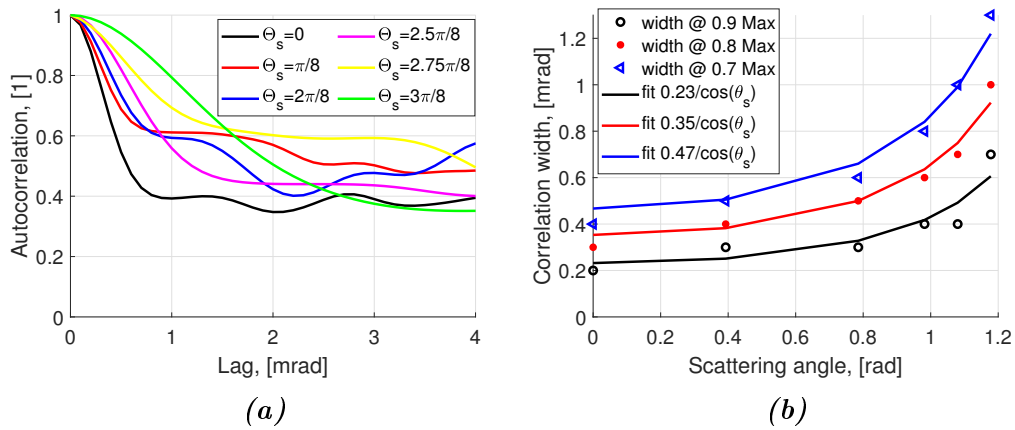
Figure 4.18: Autocorrelation functions as a function of angular separation (Lag) of the same data at different scattering angles (a) and the width of the corresponding functions at 0.9, 0.8, and 0.7 of maximum (b).
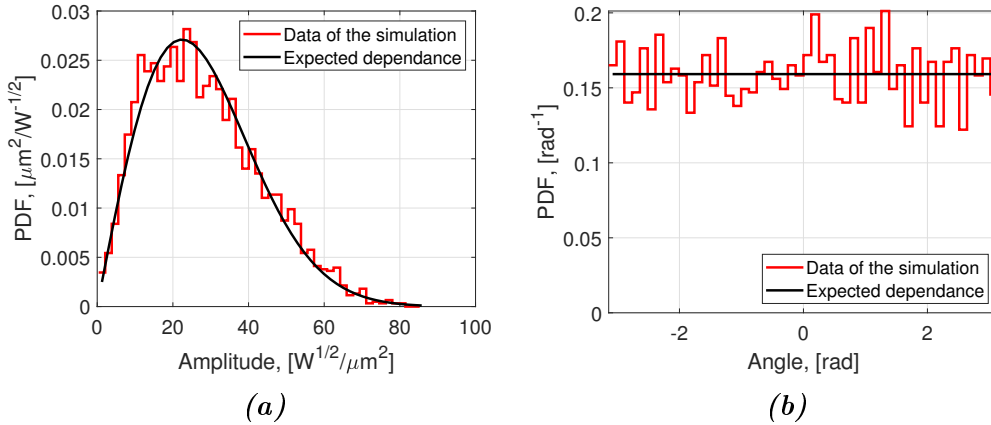
Figure 4.19: Distribution of amplitude (a) and phase (b) in the focal plane near zero scattering angle provided by the coherent scattering model.

The black curve was computed for the case of the ideal surface (zero roughness). In the ideal case, this curve should show an extremely fast decrease (the decrease of the reflected incoming Gaussian beam profile) or be equal to the amplitude of the numerical limit (rounding errors) of the calculation. However, at about 10°, the value of the BRDF calculated under the coherent model starts to rise. This behavior is due to the explained above numerical features of the computation. The red curve is BRDF for the case of the rough surface. The calculation appears to be wrong beyond $\theta_s = 25^o$.

This demonstrates the limit angle for backscattering numerical studies. The numerical parameters should be adjusted if backscattering calculations and large incidence angles are required. However, the incidence angles in the LISA telescope are small (not exceeding 20°), and the observed limit of modeling is more than acceptable. So backscattering studies of coherent scattering in the LISA telescope can be performed with this model, as concerns backscattering due to surface roughness.
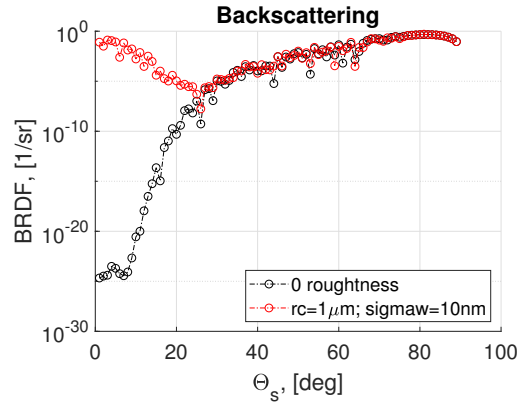
Figure 4.20: Illustration of the limits of the numerical coherent scattering model: calculated back-scattering BRDF as a function of the scattering angle θ_s, with steps of 1 deg, with (red points) and without (black points) roughness on the target surface. The incident angle (in modulus) is equal to the scattering angle (case of backscattering).

4.5 Conclusion

In this chapter I described coherent scattering and its main properties. As was mentioned before, the main feature of coherent scattering is the presence of random interference pattern – speckle. In the first section of the chapter, I gave an overview of the main, known features of speckle: statistical distributions [23] and dimensional sizes [47]. Later, I have applied this to derive the probability density function of the perturbation of the LISA heterodyne phase measurements in the presence of coherent scattering taking place at the surface of the LISA optical bench or telescope optics.

From the other side, a model of coherent scattering was developed and implemented in MATLAB code. This model unites the well-known and widely used approach based on BRDF with features of coherent scattering. The model was tested under different circumstances. Except for the direct calculation of scattering fields, the model explains why the speckle is formed. Also, I had described fine detail of the numerical implementation of the coherent scattering model.

The results of the coherent scattering model show that it agrees with the Harvey Shack model, and it correctly describes the properties of coherent scattering. The parameters of the model are the same as used in the experimental setup described in Chapter 6. The result obtained with this modeling will be applied to explain the experimental results. Moreover, the model can be applied to describe coherent features of scattering in optical components of the LISA instrument.

The coherent scattering model can be extended for scattering from optical coatings and by introducing the effect of the polarization change during the scattering process.

Chapter 5

Experimental setup at 1.55 μm

This chapter is devoted to backscattering, that is, scattering that gives rise to light with a propagation direction opposite to the incoming propagation mode. Back-scattering deserves a specific study because:

- in many photonic applications, "optical return" is a key issue, and if specular reflection can be eliminated or reduced by tilting the optical component, backscattering cannot be eliminated. Two examples can be given: the perturbation of a laser by the retro-injection of its own emission [4], and the role of backscattering in optical gyros [18].

- in the LISA instrument, the backscattering of the Tx beam is the dominant contribution to the perturbation of the heterodyne Tx-Rx interference. The backscattering of the Tx beam in the telescope generates a speckle field that directly overlaps with the Rx beam. Diffusion at an angle will, in general, not produce scattered light, which overlaps with the Rx unless two or three scattering processes take place, so the corresponding probability is very weak (an exception to that is the 90 deg scattering in the polarising beam splitter. Polarization tagging is the only way to attenuate before it reaches the photoreceivers of the long arm interferometer, the Tx light backscattered by the optics to and in the telescope.

This chapter aims at characterizing the properties of backscattering at the component level, particularly the dependence on such parameters as the spot position or the incidence angle.

To measure the properties of coherent backscattering, we built an interferometric setup, as described in this chapter. The setup is based on the Michelson interferometer: in one arm, a mirror, in the other arm, the component under test, tilted, so that only backscattering is measured in the interferometer. It has a simple design and a linear dependence of the amplitude of the interferometric signal on the backscattering amplitude. To be representative of LISA, the wavelength of the interferometer should be 1.06 μm. However, to demonstrate the method, we temporarily used optics and lasers at the telecom 1.55 μm wavelength.

The construction of the setup starts from a fully fibered interferometer (see Sec. 5.1), which does not measure backscattering from free-space optics, but simulates it by an optical attenuator. The goal of this setup is to develop electronics and algorithms for signal processing, discover the limits and possible issues of low-level backscattering measurements. The next step (see Sec. 5.2) is the construction of the free space part of the interferometer and characterization of each component. The measurements of the low backscattering levels from the target optical surfaces face the problem of scattering from other elements in the setup. As a solution, I propose a method of signal processing adapted to the case of multiple-beam interference (see Sec. 5.3). The result of the measurements with the setup at $1.55\mu m$ is summarized in Sec. 5.4.

5.1 Characterization of the fibered setup

To be able to measure the backscattering from the reflective optics, the sample will be inserted in the beamline (see Fig. 5.1) of the Michelson interferometer. The nominal beam will be reflected in the beam dump, while a small fraction of scattered light will scatter back to the setup and interfere with light in the reference arm on the photodiode surface.
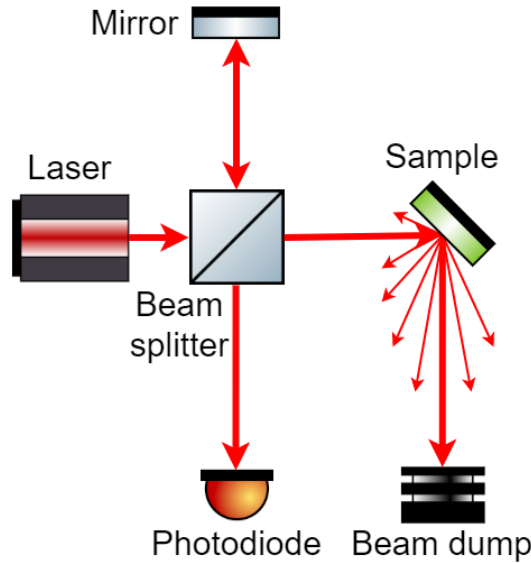
Figure 5.1: The schema of the Michelson interferometer for backscattering measurements

The amplitude of the interferometric signal on the photodiode is proportional to the backscattering fraction in amplitude. Our goal is to build a setup, which can operate under small values of backscattering. However, operations in the desired regime require signal processing routines and a fundamental understanding of all limits of the measurements. To simulate the setup for backscattering measurements in hardware and develop such a method of signal processing, we built a fully fibered interferometer. In one arm of it, we insert a fixed and a variable attenuator to simulate the backscattering.

For low values of the transmission of the attenuators, the measurements of fringe amplitude will be technically complicated and, at some point, impossible. The point at which the reconstructed fringe amplitude will not depend on the transmission defines the measurement floor. We will observe this limit, discover which effects (noise sources) limit these measurements, and will calibrate the setup.

5.1.1 Description of the experimental setup

The schema of the fibered interferometric setup is shown in Fig. 5.2.
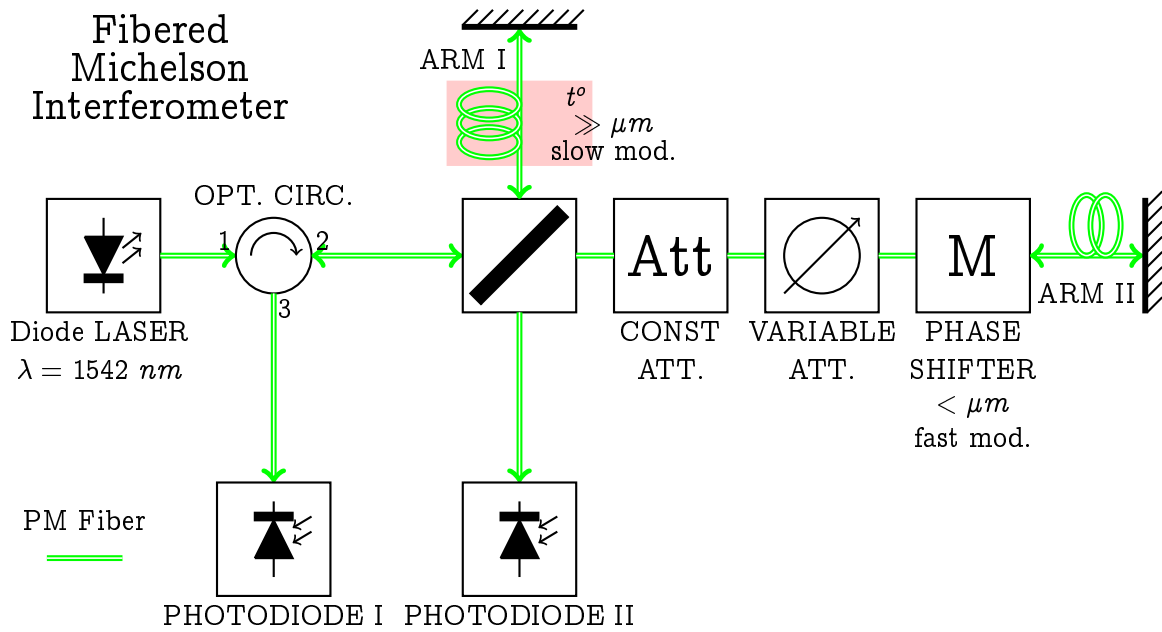
Figure 5.2: The schema of the experimental simulation of the setup for the backscattering measurements

The laser source is an ORION Laser module with a central wavelength of 1542.54 nm and power 9.87 mW. The laser is equipped with an optical isolator, which prevents self-mixing due to the optical return from the Michelson interferometer. Polarization maintaining (PM) panda-style fibers maintain a high polarization extinction ratio in the interferometer, and FC/APC (angled) connectors avoid back reflection on the connector ends.

In the chain after the laser module is placed a PM Fiber Optical Circulator (OPT. CIRC if Fig. 5.2) from AFW technologies. Similar to an electronic circulator, it allows light to travel only in one direction (port 1 → port 2 → port 3) with minimal loss. This device improves the rejection of the optical return to the laser module and also allows to install the second photodiode for the interferometric measurements. The 2 × 2 Polarization-Maintaining (PM) bidirectional Fiber coupler (beam splitter) divides the laser beam with a 50:50 coupling ratio. Arm I of the interferometer is terminated by a golden mirror. The heating of the fiber can be applied for the slow thermal scan of the phase

of the interferometric signal. Arm II contains constant attenuators (*Att*) of 10dB and 20dB, a variable attenuator, and a phase shifter (M – modulator) and is terminated by a golden mirror.

The usage of fixed attenuators allows us to increase the attenuation and decrease the value of the reflected light from the variable attenuator. The PM variable attenuator works down to -50 dB of attenuation. The principle of the operation of this device is quite simple: in between collimating and focusing lenses is inserted a blocking device (blade), which is pushed by a screw. However, back reflection from the blade and so from the variable attenuator is not negligible. For this reason, it is crucial to put modulator after attenuators, else back-reflected light will be modulated, and so it will be detected by the lock-in amplifier (will be discussed later).

The Fiber Phase Shifter from General Photonics (Ref. FPS-001-01-NT-PP-FC/APC) is used for the beam phase modulation. The device is a piece of fiber winded on a piezoelectric crystal. The stretching of the optical fiber causes an optical phase delay in the propagation. Modulation of the piezo is possible only at relatively low frequencies, up to about 7 kHz, where the first resonance takes place. The sound of the parasitic acoustic waves of the piezo can propagate in the air and cause crosstalk to the other fibers of the setup. So reliable shielding of the phase shifter is required.

The EPM650 photodiodes are used to measure the interferometric signal. Due to anti-reflection coating at the detector surface, the optical return at the photodiodes is as low as -40 dB.

The lengths of the two arms were equalized to reduce the coupling of the laser frequency noise.

5.1.2   Theory of operation

In this section, we will link backscattered amplitude with an amplitude of the interferometric signal for the setup described above. We will discuss the effect of the beam path modulation on the response of the interferometric signal and the spectrum of this signal.

Detected intensity

In the Michelson interferometer, a laser beam with intensity I_L is split in two by a beam splitter (see Fig. 5.2). In each arm of the interferometer, the beam is reflected, passes a second time through the beam splitter, and finally interferes at the photodiode surface. If intensities of the interfering beams are I_1 and I_2 and assuming that the polarization is the same for the two beams that interfere, then the result of the interference is:

$$I = I_1 + I_2 + 2\sqrt{I_1 I_2} \times \cos(\frac{2\pi}{\lambda} 2\Delta L), \qquad (5.1)$$

where the optical arm length difference is $\Delta L = n\Delta l$. Here Δl is the geometrical arm length difference and n is the refractive index of the fiber at wavelength λ.

In our setup, and particularly when measuring backscattering from a quality optics, the I_2 intensity will be (much) lower than I_1. But let us first consider the case of the symmetric Michelson interferometer.

a The ideal, symmetric Michelson interferometer

If the laser intensity I_L is divided into equal parts by the beam splitter and there are no losses in the setup, the interfering intensities are $I_1 = I_L/4$, $I_2 = I_L/4$. The interference intensity is:

$$I = I_L/2 + I_L/2 \times \cos(\frac{2\pi}{\lambda}2\Delta L). \tag{5.2}$$

The maximum of interference I_L is obtained on the photodiode when two beams are superposing in-phase ($\frac{2\pi}{\lambda}2\Delta L = 2\pi \times m$, $m \in \mathbb{Z}$). If the beams are superposed with the opposite phase ($\frac{2\pi}{\lambda}2\Delta L = \pi + 2\pi \times m$, $m \in \mathbb{Z}$), so the minimum of intensity is obtained on the photodiode (zero power). In general, when the optical arm length difference ΔL changes, the interferometric intensity I oscillates from zero to full laser intensity I_L, as shown in Fig. 5.3 (blue line). Due to the conservation of energy, the sum of the two intensities at the two photodiodes (see Fig. 5.2) is equal to I_L, due to the fact that the reflection coefficients at the beam splitter follow some antisymmetry relation.

By fringe amplitude, we call the term in front of the variable part (cosine) of the I. The objective of the setup is to measure this amplitude, as it contains information about backscattering (will be shown later). In this case, the fringe amplitude is equal to $I_L/2$.

b The asymmetric Michelson interferometer

In the case where an attenuator with single-pass transmission T is inserted in arm II (see Fig. 5.2), only limited interference will be observable:

$$I = \frac{I_L}{4} + \frac{I_L}{4}T^2 \pm \frac{I_L}{2}T \times \cos(\frac{2\pi}{\lambda}2\Delta L). \tag{5.3}$$

The intensity I_2 senses T^2 transmission, as light reflected from arm II passes a second time through the attenuator. It is a general rule that interference effects are proportional to the product of the amplitudes of the two beams that interfere. In our case, the fringe term is proportional to the single-pass attenuator transmission in power T. The amplitude of the interferometric signal as a function of the path length difference ΔL for three values of double-pass transmission (0 dB, -3 dB, -30 dB) is given in Fig. 5.3. Amplitude of the interferometric signal is $\frac{T}{2}I_L$ (see Eq. 5.3) and it is a linear function of the single-pass transmission T.

However, in the real setup, the losses in the components should be taken into account. For this, let us consider a setup, as shown in Fig. 5.4. The transmission coefficient in power from port n to port p of the beamsplitter is noted t_{np}. The ports of the components (1, 2, 3, 4, in, out, rej) are defined in Fig. 5.4. R and r are the reflectances in power of the mirrors in the arms
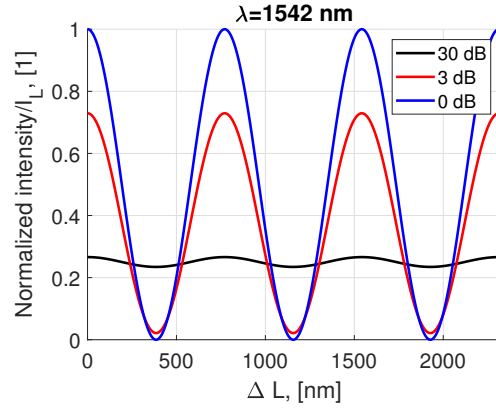
Figure 5.3: Expected dependance of the intensity on the photodiode II as a function of the arms-length difference ΔL for several values of the double pass T^2 attenuation.
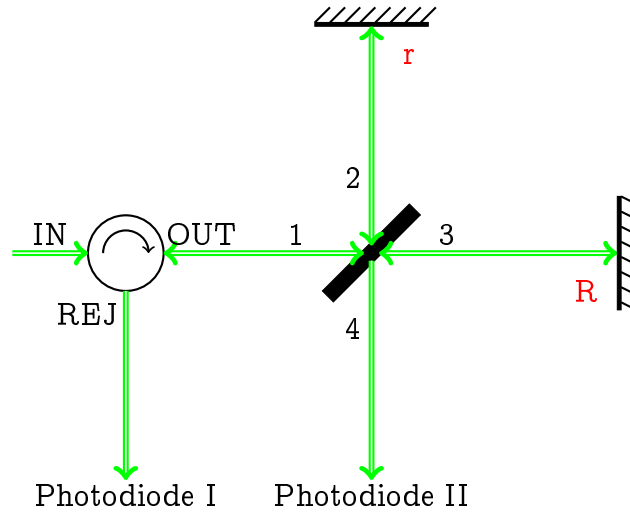
Figure 5.4: Schema of the interferometric setup for the loss analysis.

of the interferometer. E_L is the complex amplitude of the input laser beam $(I_L = E_L^2)$.

The field on the photodiode II connected to the beam splitter is (up to a global phase factor):

$$E = E_L\sqrt{t_{in-out}t_{12}t_{24}r} + E_L\sqrt{t_{in-out}t_{13}t_{34}R}e^{j(\frac{2\pi}{\lambda}2\Delta L)}. \tag{5.4}$$

So the intensity of the light on the same photodiode is:

$$I = EE^* = E_L^2 t_{in-out}(t_{12}t_{24}r + t_{13}t_{34}R + 2\sqrt{(t_{12}t_{24}rt_{13}t_{34}R)} \times \cos(\frac{2\pi}{\lambda}2\Delta L)). \tag{5.5}$$

In the ideal case, when $t_{in-out} = t_{out-rej} = 1$, $t_{12} = t_{24} = t_{13} = t_{34} = \frac{1}{2}$, $r = R = 1$ the equation reduces to Eq. 5.2. The measured values of the transmission and reflection (including insertion loss) are given in the Tab. 5.1. Transmission coefficients were measured with a fibered power meter and a RIO

laser. For the test of the beam splitter, free ends of it were terminated by the beam dumps. The reflectance of the mirror was measured with an optical circulator. The value of reflectance also includes losses on the connectors.

Table 5.1: Measurered values of transmittance and reflectance of the the components, which were used in the setup

t_{13}	t_{12}	t_{31}	t_{34}	t_{24}	t_{21}	r	R	t_{in-out}	$t_{out-rej}$
0.4875	0.4395	0.4102	0.3334	0.4808	0.4436	0.6455	0.64	0.8913	0.8974

So the Eq. 5.5 with coefficients from Tab. 5.1 transforms to:

$$I = I_L(0.2143 + 0.2123 \times \cos(\frac{2\pi}{\lambda} 2\Delta L)). \qquad (5.6)$$

And the Eq. 5.3 will be:

$$I = I_L(0.1216 + 0.0927 \times T^2 + 0.2123 \times T \times \cos(\frac{2\pi}{\lambda} 2\Delta L)). \qquad (5.7)$$

The expression for the interference intensity on photodiode connected to the optical circulator can be derived in the same way, but the transmission $t_{out-rej}$ should be considered as well (except for the sign and energy conservation).

These expressions will be used for calibration purposes.

In the case of low transmission, the extraction of the fringe amplitude is complicated due to the noise issues in the system. A convenient way to extract small fringe amplitudes is to use a modulation-demodulation schema based on lock-in amplification.

Effect of beam path modulation

An interferometric signal with an optical length modulation of ΔL over 3λ is shown in Fig. 5.3. In this case, the extraction of the fringe amplitude does not cause a problem. However, it is not simple to extract the amplitude, when only part of the wavelength is occupied by the modulation (see Fig. 5.5, modulation depth is $\lambda/8$). Depending on the precise value of ΔL, the amplitude and shape of the modulation curve, the signal on the photodiode will be different. The position is determined by the thermal and acoustic variations in the fiber medium, so it is changing with time.

The modulation depth is regulated by the amplitude of the voltage applied to the phase shifter. I use 10 V of a peak to peak positive voltage modulation, as this is the maximum provided by the HF2LI lock-in amplifier used for the modulation and demodulation on the experimental set-up. As discussed later, this voltage does not cause any significant acoustic crosstalk in the setup.

Another problem, which arises in the measurements is the hysteresis of the piezo crystal of the phase shifter. This causes the response to be slightly different when the modulation signal increases and decreases (see Fig. 5.6). Measured hysteresis for this phase shifter is 4.7%. This limits the usage of high modulation amplitudes.
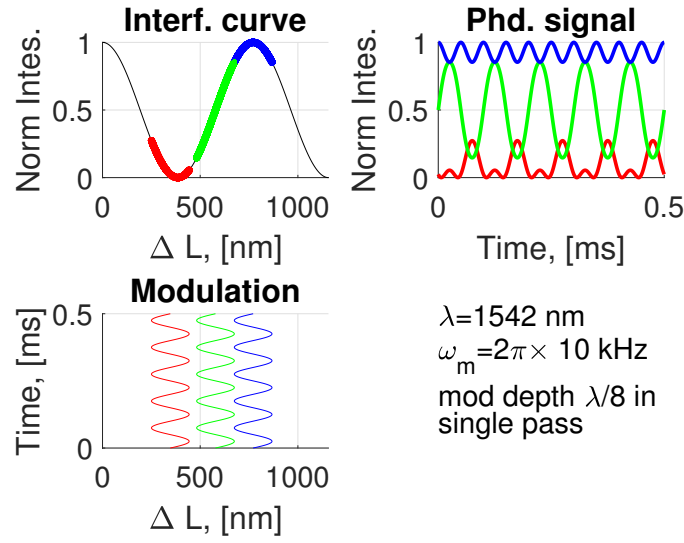
Figure 5.5: *The modeling of the response of the system. The modulation depth is λ/8 at frequency 10 kHz and wavelength of 1542 nm. The shape of the signal on the photodiode (Phd. signal) is dependent on the modulation offset (the exact value of ΔL, affected by the thermal conditions in the room).*
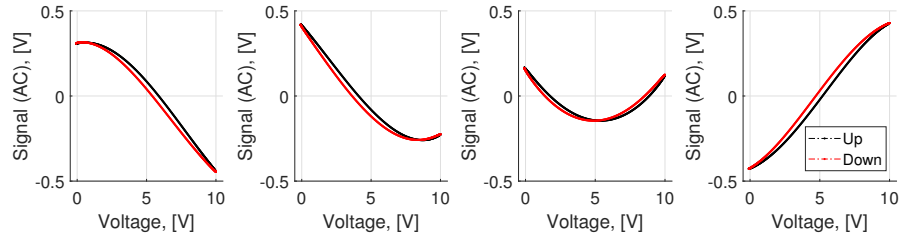
Figure 5.6: *The measured photodiode signal as a function of the applied voltage for different ambient temperature values (25-50 mK difference) in the fiber of Arm I. Due to hysteresis in the phase-shifter pass up (voltage increase) and pass down (voltage decrease) signals are not the same (red and black curves respectively).*

The properties of the modulator mostly define the choice of the modulation frequency. Due to strong mechanical resonances, the maximum frequency is limited to 5-7 kHz. Moreover, the usage of complex modulation curves, spread over a wide spectrum, causes parasitic feedback of the interferometric curve. So more preferable is the usage of a single sine wave reasonably far from the resonance of the modulator.

The frequency and amplitude of modulation are limited by the physical properties of the modulator (phase shifter). In the case of partial (less than λ) modulation of the optical path, on the photodiode will be a complex observable signal with a waveform strongly affected by ambient temperature changes. This signal needs to be analyzed in order to recover the fringe amplitude. The most convenient way to do this is to use spectral analysis.

Spectrum of the modulated interferometric signal

The arm II of the interferometer contains a modulator (see Fig. 5.2). The beam in this arm will be modulated at frequency $\omega_m/2\pi$ and with amplitude δL of the path length modulation . The functional form of the modulating can be a sine, a triangle, or any other. The most simple for analytical calculation is linear modulation (a triangle). However, as the spectrum of a triangle spreads over frequencies much larger than the fundamental frequency, it can produce a distortion of the interferometric curve due to the excitation of the resonances in the phase shifter.

Let us calculate the spectrum of the interferometric function $f(x)$:

$$f(t) = I_1 + I_2 + 2\sqrt{I_1 I_2} cos(\frac{2\pi n_r}{\lambda} 2 \Delta L(t)), \tag{5.8}$$

where the path length difference is:

$$\Delta L(t) = \delta L \sin(\omega_m t) + L_0. \tag{5.9}$$

Here $2\delta L = \frac{\lambda}{N}$ is the peak-to-peak amplitude of the fiber length (single pass). In other words, $\frac{1}{N}$ is the fraction of laser wavelength occupied by the modulation, L_0 − is some initial position on the interferometric curve.

To avoid the tracking of the constant coefficients in the experession, I will simplify the notation:

$$f(t) = C + A \cos(\frac{2\pi n_r}{\lambda} 2 \Delta L(t)), \tag{5.10}$$

where $A = 2\sqrt{I_1 I_2} = \frac{I_L}{2}T$ is an fringe amplitude and $C = I_1 + I_2 = \frac{I_L}{4}(1 + T^2)$ is a constant contribution to the photodiode signal.

To calculate the spectrum, we use the trigonometric Fourier series:

$$f(x) = \frac{a_0}{2} + \sum_{n=1}^{\infty} \Big[a_n \cos(nx) + b_n \sin(nx) \Big]. \tag{5.11}$$

Here the constants a_0, a_n, b_n ($n \in \mathbb{N}$) are called coefficients of the trigonometric series:

$$a_n = \frac{1}{\pi} \int_{-\pi}^{\pi} f(x) \cos(nx) dx, \qquad b_n = \frac{1}{\pi} \int_{-\pi}^{\pi} f(x) \sin(nx) dx. \tag{5.12}$$

To calculate the spectrum of sine wave modulation, we need to perform the integrals:

$$a_n = \frac{2A}{T} \int_{-T/2}^{T/2} sin(\frac{2\pi n_r}{N} sin(\omega t) + \phi) \cos(n\omega t) dt, \tag{5.13}$$

$$b_n = \frac{2A}{T} \int_{-T/2}^{T/2} sin(\frac{2\pi n_r}{N} sin(\omega t) + \phi) \sin(n\omega t) dt, \tag{5.14}$$

where ϕ is a constant phase, which is induced by the offset voltage of the signal generator, the difference in arm length, the thermal change of refractive index of the fiber, the mechanical stretch of the fiber, etc.

The result of the computation for the first harmonic ($n = 1$) is:

$$a_1 = 0, \tag{5.15}$$

$$b_1 = \frac{2A}{T}\Big(cos(\phi) \int_{-T/2}^{T/2} sin(\frac{2\pi n_r}{N} sin(\omega t)) \sin(\omega t) dt +$$

$$+ sin(\phi) \int_{-T/2}^{T/2} cos(\frac{2\pi n_r}{N} sin(\omega t)) \sin(\omega t) dt \Big) =$$

$$= \frac{2A}{T}\Big(cos(\phi) \times T J_1(\frac{2\pi n_r}{N}) + sin(\phi) \times 0 \Big) = 2A cos(\phi) J_1(\frac{2\pi n_r}{N}), \tag{5.16}$$

where J_1 is a Bessel function of the first kind.

For the second harmonic:

$$a_2 = \frac{2A}{T}\Big(cos(\phi) \int_{-T/2}^{T/2} sin(\frac{2\pi n_r}{N} sin(\omega t)) \cos(2\omega t) dt +$$

$$+ sin(\phi) \int_{-T/2}^{T/2} cos(\frac{2\pi n_r}{N} sin(\omega t)) \cos(2\omega t) dt \Big) = 2A sin(\phi) J_2(\frac{2\pi n_r}{N}), \tag{5.17}$$

$$b_2 = 0. \tag{5.18}$$

The value N can be obtained from the data analysis, from other measurements, or from the datasheet of the modulator.

To reject the influence of the thermal phase ϕ, we combine the first and second harmonics, using the identity:

$$sin^2(\phi) + cos^2(\phi) = 1, \tag{5.19}$$

so we have been able to obtain the amplitude, in a way that is independent of the exact value of the path difference offset of the two arms.

$$A = \sqrt{\Big(\frac{b_1}{2J_1(\frac{2\pi n_r}{N})}\Big)^2 + \Big(\frac{a_2}{2J_2(\frac{2\pi n_r}{N})}\Big)^2}. \tag{5.20}$$

So we can compute the fringe amplitude A if the first and second harmonics of the interferometric signal are measured simultaneously. Such a function is now available with the advent of lock-in amplifiers based on the analog-to-digital acquisition of the signal, followed by numerical demodulation.

In the case of the presence of a significant hysteresis of a nonnegligible hysteresis presence in a phase shifter, the signal treatment becomes complicated. However, we could represent it as a constant phase delay of ψ. In this case :

$$b_1 = 2A cos(\phi + \psi/2) cos(\psi/2) J_1(\frac{2\pi n_r}{N}), \tag{5.21}$$

$$a_2 = 2A sin(\phi + \psi/2) cos(\psi/2) J_2\left(\frac{2\pi n_r}{N}\right), \tag{5.22}$$

and

$$A = \frac{1}{2cos(\psi/2)} \sqrt{\left(\frac{b_1}{J_1\left(\frac{2\pi n_r}{N}\right)}\right)^2 + \left(\frac{a_2}{J_2\left(\frac{2\pi n_r}{N}\right)}\right)^2}. \tag{5.23}$$

The impact of hysteresis on the measured returned fraction can be removed by separately calibrating the phase delay in a separate measurement, using a large signal. This parameter is inherent to the piezo actuator of the modulator, and is not expected to change.

Conclusion

The fringe amplitude has a linear dependence on the backscattering fraction in amplitude. The signal should be modulated to measure low fringe amplitudes. The modulated signal has a complex waveform and requires spectrum analysis. The combination of the first and second harmonics allows us to extract the fringe amplitude independently of the thermally induced phase offset.

5.1.3 Signal processing

To measure the fringe amplitude A for any phase offset ϕ, the first and the second harmonic of the signal should be measured simultaneously (see Eq. 5.20). A convenient way to do this with sufficient precision is to use a lock-in amplifier. Before demodulation, the signal should be appropriately treated (converted, amplified, filtered). And after demodulation, the signal should be analyzed and processed. This section will describe the signal path from the photodiode to the lock-in amplifier. I will introduce the basics of lock-in detection and how digital signal processing with MATLAB is performed.

Electronic signal processing

An electrical schema of signal processing is given in Fig. 5.7. The 1.55 μm power, which arrives at the photodiode, is converted to the current with responsivity equal to 1.02 A/W for 5V reverse bias voltage. The first stage of the amplification is a current-voltage converter ($V = I \times 4.7k\Omega$), based on an OP467 operational amplifier, followed by a repeater. The OP467 operational amplifier is low noise ($6nV/\sqrt{Hz}$) 28 MHz bandwidth device. The output current of the amplifier is not sufficient to drive the 50 Ohm load, so the amplifier output is protected by a 470 Ohm resistor. When attenuation in the arm II is high, the signal level (AC) is minimal, but not the DC component of the interferometric signal. So it will prevent from using a high gain for amplification by a lock-in amplifier. For this purpose, a high pass RC=23.5 ms filter was installed at the R=50 Ohm input of an HF2LI lock-in amplifier from Zurich Instruments. At the next stage, the signal is amplified inside the lock-in amplifier. The input range was varied together with the level of optical attenuation

to achieve the best measurement performance. The FPGA-based lock-in detection performs the acquisition of the signal and the mixing with the reference signal of amplitude $\sqrt{2}$.
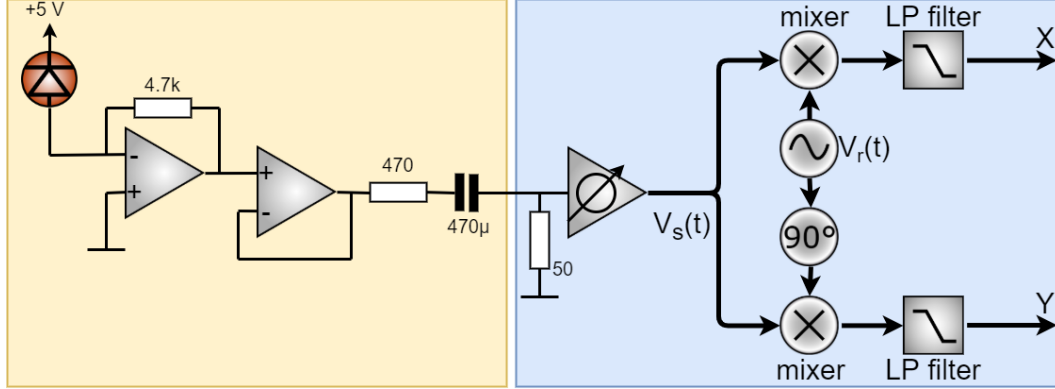
Figure 5.7: Schema of the electrical signal path. Yellow is the amplification part. Blue is the lock-in amplifier part. The operation of the lock-in amplifiers considered in Sec. 5.1.3 below.

So using the values listed above, we get that the conversion V/W coefficient of the photodiode and amplifier is $4700 \times 1.02 \times \frac{50}{470+50} = 461\ V/W$ when driving a 50 Ohm load. As the values of the resistors are not precise, and due to the losses, the real value is a little different and equal to $403.3\ V/W$. To check that interferometer works correctly, I blocked the light in arm II of the interferometer by the beam dump. In this case, only the DC component $I = 0.1216 \times I_L$ (see Eq. 5.7) on the photodiode is expected. The level of the DC voltage is 484 mV, which is equivalent to the laser power of $0.484/0.1216/403.3 = 9.87\ mW$. From the other side, the power measured with a fibered power meter in the place of a photodiode is 1.2 mW, which gives $1.2/0.1216 = 9.87\ mW$ of laser power. These two values are in agreement with the real laser power of 9.87 mW.

To find the calibration coefficient I unblocked the arm II of the interferometer ($T = 1$). Using Eq. 5.6 and the fact that in lock-in amplifier signal is mixed with reference one with amplitude $\sqrt{2}$, I find that the link between reconstructed fringe amplitude A and measured power is:

$$I_L = (A\ [V])/0.2123 \times \sqrt{2} \times /(403.3\ [V/W])\ [W]. \tag{5.24}$$

The amplitude measured with the LI amplifier is in this case $A = 0.559\ V$. Taking into account losses in phase shifter ($0.3dB = 0.966$) so $I_L = 0.559/(0.966)^2/0.2123 \times \sqrt{2}/403.3 = 9.89\ mW$. And finally, the calibration coefficient is equal to $1/0.2123 \times \sqrt{2}/403 = 0.0165\ [W/V]$.

So the electronics stage of the signal processing works correctly, and the calibration coefficient was found.

Lock-in detection

Let us suppose a signal $V_s(t) = A_s cos(\omega_s t + \Theta_s)$ at the input of lock-in amplifier (see Fig. 5.7). The signal and the reference $V_r(t) = \sqrt{2}e^{-j\omega_r t}$ are multiplied in

the mixer:

$$V_s(t)V_r(t) = \frac{A_s}{\sqrt{2}}e^{+j[(\omega_s-\omega_r)t+\Theta_s]} + \frac{A_s}{\sqrt{2}}e^{-j[(\omega_s+\omega_r)t+\Theta_s]}. \quad (5.25)$$

Frequency response of filter of n-th order is defined by the formula:

$$H_n(\omega) = \frac{1}{(1+j\omega\tau_N)^n}, \quad (5.26)$$

where time constant τ_N is

$$\tau_N = \frac{FO_N}{2\pi f_{cut-off}}. \quad (5.27)$$

Here FO_N is a factor that depends on the filter slope, and $f_{cut-off}$ is the -3dB cut-off frequency.

The product of multiplication and further filtering gives the X component of the demodulated signal. The Y component of the demodulated signal is achieved when the input signal is mixed with a 90° shifted reference signal. The output of the demodulation is a signal in the complex plane:

$$X + jY \approx H(\omega_s - \omega_r)\frac{A_s}{\sqrt{2}}e^{j[(\omega_s-\omega_r)t+\Theta_s]}, \quad (5.28)$$

or in the other representation:

$$X + jY = Re^{j\Theta}, \quad (5.29)$$

where R is a modulus and where the phase $\Theta = (\omega_s - \omega_r)t + \Theta_s$ is constant when the signal used for the modulation and for the demodulation are at the same frequency.

The setting of the Lock-in amplifier is given in Fig. 5.8. Demodulation is performed at first ($f_1 = 500\ Hz$) and second harmonics. The amplitude of the phase shifter modulation is $V_{pp} = 10\ V$ with an offset of $V_{offset} = 5\ V$. Signal is mixed with 0 phase delay of the reference signal. Low pass filter of 4 orders (3dB attenuation of 6.8 Hz) is used. The sinc filter is used for deep filtering of the effects caused by presence of residual DC component in the input signal. The output data are the complex demodulated amplitude $X_1 + jY_1$, at
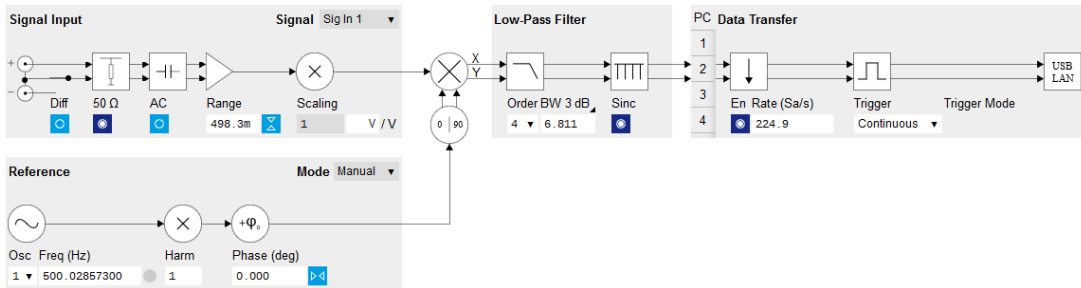
Figure 5.8: Zurich Instruments LabOne settings panel at the fundamental frequency ("Harm"=1). Settings are valid for present measurements.

the fundamental frequency (Fig. 5.9a), and $X_2 + jY_2$, at the second harmonic. These results are recorded on the computer and analyzed with MATLAB.

Software signal processing

The first step is to check that XY signals do not contain offsets. This can arise in the presence of electrical cross-talk. As an example, we observed a contribution due to the crosstalk between channels of the oscilloscope, which was used to tune the setup. The crosstalk will cause a constant offset in XY data. To be sure, that in the data are no offsets, we scan the ϕ phase by heating the fiber. In this case, we scan many fringes, and in the ideal situation, at minimum, the modulus R_1 and R_2 should reach 0. The best would be to check the system for the presence of crosstalk and remove the crosstalks in hardware. If it is not possible, the offsets should be removed in post-processing. The offset can be measured when the piezo modulator is disconnected from the driving cable, and replaced by a capacitor of equivalent capacitance (163 pF).

The next step is to process the complex demodulated amplitude X+jY, either by taking the modulus

$$R = \sqrt{X^2 + Y^2},$$ (5.30)

or by first performing the rotation

$$\begin{pmatrix} X' \\ Y' \end{pmatrix} = \begin{pmatrix} \cos(\Theta_1) & \sin(\Theta_1) \\ -\sin(\Theta_1) & \cos(\Theta_1) \end{pmatrix} \begin{pmatrix} X \\ Y \end{pmatrix},$$ (5.31)

that removes the phase lag due to hysteresis in the piezo, and to propagation in the cables. The two methods differ by their sensitivity to the noise. The appropriate rotation angle $\Theta_1 = -atan(Y/X)$ can be measured at the fundamental frequency, in conditions where the signals are large, and noise is low. The measurement is valid for the second and third harmonics with the relations $\Theta_2 = 2\Theta_1 + \pi/2$ and $\Theta_3 = 3\Theta_1$.

Two harmonics are recorded to retrieve the signal amplitude A, as shown in Fig. 5.9b where the value of A shows very little dependence on the phase offset. So at this stage of the signal processing, the offsets from XY can be removed (if needed). For each measured harmonic, the modulus is computed. A combination of these moduli gives a fringe amplitude of A, and the backscattering fraction (or transmission in case of the fibered setup).

Conclusion

In this section was given the principles of the signal processing at different stages: electronics, digital, software. The calibration of the setup was done. The method for the treatment of fringe amplitude was proposed.

The achieved results are sufficient for the preliminary operation and the first measurements. The last check to do is to examine the measurement floor and the sources of noise.

5.1.4   Results & discussion

On our experimental set-up (Fig. 5.2), the role of the attenuator is to implement increasing attenuation so as to simulate increasingly weak backscattering, down to the level where the signal remains buried in the noise. With the

(a)

(b)
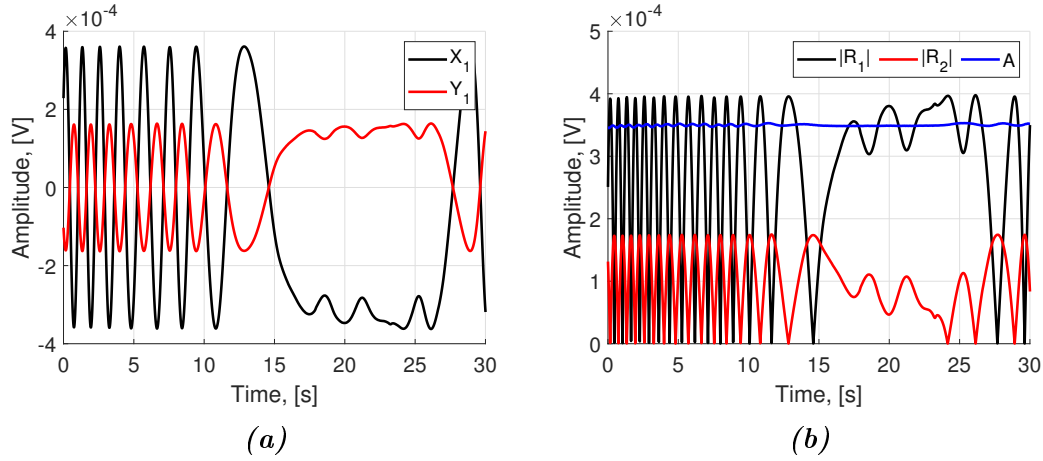
Figure 5.9: Measured values of in-phase and quadrature components (a) for the first harmonic. Modulus for the first and second harmonics (b) with the reconstructed amplitude A. Attenuation is -65.56 dB

method described in the previous sections, I measure the fringe amplitude for multiple values of attenuation. If recorded data are correct, moduli R_1 and R_2 draw ellipses, when the offset phase is scanned (see Fig. 5.10). For small values, the ellipse does not show up above the noise (see Fig. 5.10b). In R_1^2 vs. R_2^2 space data, create a line, the slope of which can be expressed through modulation depth. I use this property to find the modulation depth coefficient from recorded data. In the setup was used two photodiodes: one connected to

(a) R_1 vs. R_2 space.

(b) R_1 vs. R_2 space. Zoom
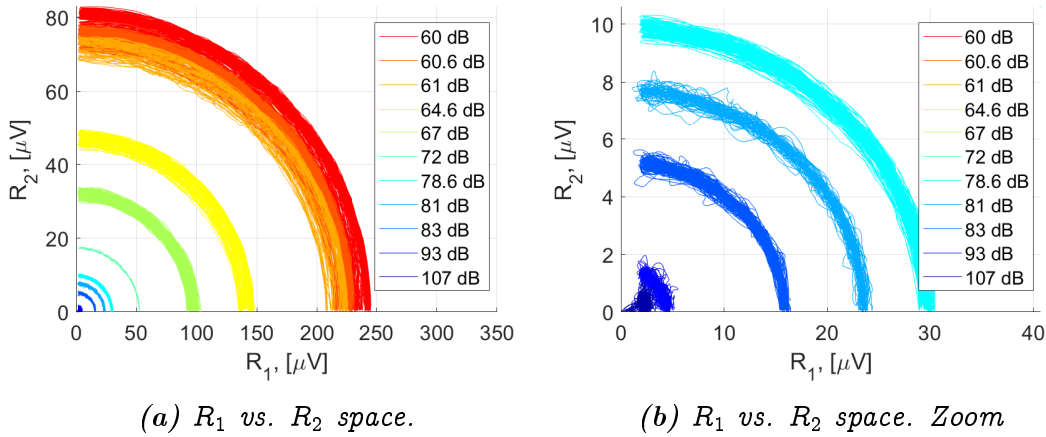
Figure 5.10: Measured values of the modulus for different levels of the transmission.

the beam splitter (transmission output) and the other to the optical circulator. The signal on both photodiodes is the same in amplitude (up to transmission losses in the optical circulator and amplification factor) and opposite in sign. The reconstructed fringe amplitude with both photodiodes ($A_t \pm \sigma_t$ and $A_r \pm \sigma_r$)

was united with an expression for weighted mean and weighed error:

$$\bar{A} = (w_t A_t + w_r A_r)/(w_t + w_r)$$
$$\sigma(A) = \sqrt{1/(w_t + w_r)},$$

(5.32)

where $w_t = 1/\sigma_t^2$ and $w_r = 1/\sigma_r^2$. The reconstructed amplitude as a function of attenuation is given in Fig. 5.11a (black circles). The red curve is an expected linear dependence with the slope coefficient computed in the previous section. The green line corresponds to the electronics and laser noise of the system. The noise level was measured when the modulator was turned off, and the output of the signal generator was shortened on the equivalent load. The cross of the two lines is at ≈ -130 dB, giving the maximum value of attenuation, at which we still could observe the interference.

At some point in attenuation, near the threshold of the detection, it will raise the question if the reconstructed amplitude is reasonable or meaningless. So to find the importance of the data for a certain dataset, I develop a method, which can evaluate the significance of the dataset and provide a numerical value to evaluate it. For this, I calculate the correlation of the moduli of first and second harmonics. When the noise dominates in the system, two signals will not correlate anymore, as noise is random so that correlation will be equal to 0 or close to this. The result of this data processing is summarized in Fig. 5.11b. We see a clear threshold of measurements. So we can use this correlation coefficient for data processing in the future.
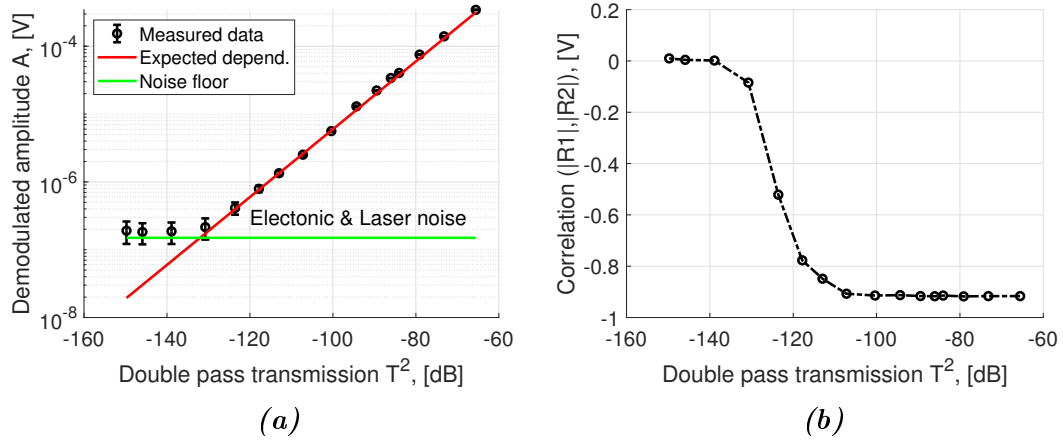
Figure 5.11: *Result of data processing for lock-in amplification data extraction scheme, constant attenuators, fiber heating (a) (offset removal was applied). Dependence of spectrum correlation coefficient vs. double pass transmission (b).*

Should be mentioned that the setup contains different noise sources:

1 Laser frequency and intensity noise.

2 Parasitic cavities: back-reflection in the attenuator creates a parasitic cavity with the imbalanced arms

3 Electronics noise: photodiode, transimpedance amplifier, lock-in amplifier

4 Backreflection in connectors and components of the interferometer and modulation of the resulting interference due to acoustic cross-talk.

The first three are white noise sources when the last one has clear interferometric features. This interference amplitude does not depend on transmission in arm II and, in the case of zero acoustic cross talk, it would not be visible by a lock-in amplifier (thermal frequencies are much lower than the 0.5 kHz modulation frequency). But as vibration caused by piezo movement in phase shifter generates acoustic waves, the fibers in other arms of the interferometer respond at these vibrations by phase modulation at the same frequency as the nominal. So this parasitic effect in case of bad acoustic shielding of the phase shifter may cause the limit of the measurements far above electronics and laser noise.

Conclusion

The measured floor is ≈ -125 dB in double-pass transmission, which is sufficient for the experiment of backscattering measurements. A method to estimate the significance of the data at low levels of the backscattering was proposed. The limiting factor of the measurements is electronic and laser noises.

5.2 Characterization of the free space setup

To measure coherent backscattering from the free-space optics, the setup described in the Sec. 5.1 require modifications. The arm of the interferometer, which contains attenuators and a modulator, is now replaced by the free space part (see. Fig. 5.12), which includes the collimating optics to illuminate the surface under test, and collect the backscattered light. It also includes a piezo-actuated mirror, the equivalent of the piezo fibered modulator in Sec. 5.1

The detailed schema of the setup is shown in Fig. 5.12 [31]. As in Sec. 5.1, the basis of this setup is a Fibered Michelson interferometer. We use the same narrow linewidth Orion RIO infrared laser diode of 1.542 μm wavelength and 9.87 mW power. An optical circulator, inserted between the laser source and the beam splitter, prevents the laser from receiving the fraction of the light, which is rejected by the Michelson interferometer and could otherwise cause amplitude and frequency modulation in the laser. Instead, the reflected beam is sent to a second photodiode (PD I), to increase the gain and precision of the measurements. Then the light is divided by the fibered 50/50 beam splitter and follows the two arms of the interferometer. Arm I is fully fibered, with a fibered 100% reflector and, if a scan of the optical phase difference is useful, a thermal ramp can be applied. Arm II is partially fibered, up to a collimator (see. Sec. 5.2.1), which emits a collimated beam for the free space part. All the optical fibers are polarization-maintaining. To eliminate the laser frequency noise, we equalize the length of the interferometer arms. The length of the
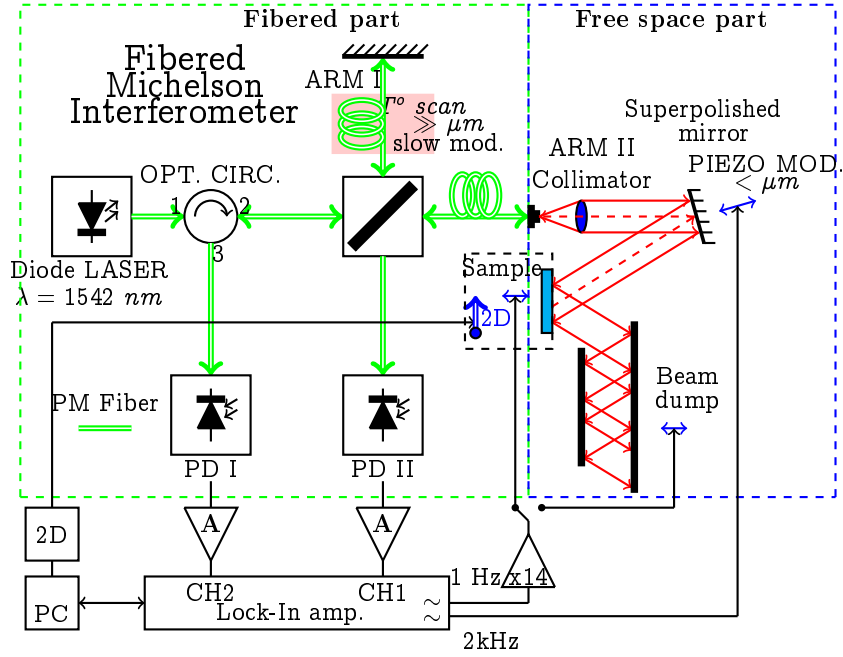
Figure 5.12: *Coherent backscattering measurement setup. Green: optical fibers. Red: free-space beams. Dashed red: backscattered light from the sample.*

ARM I is 341.7 cm, and the length of the ARM II is 261.7 cm in fiber and $80 \times 1.44 = 116 \ cm$ in air. So the residual light path length difference is a few centimeters .

The fibered components are assembled in a compact volume (see Fig. 5.13a), and the assembly is installed in a thermo-acoustical shield (see Fig. 5.13b).
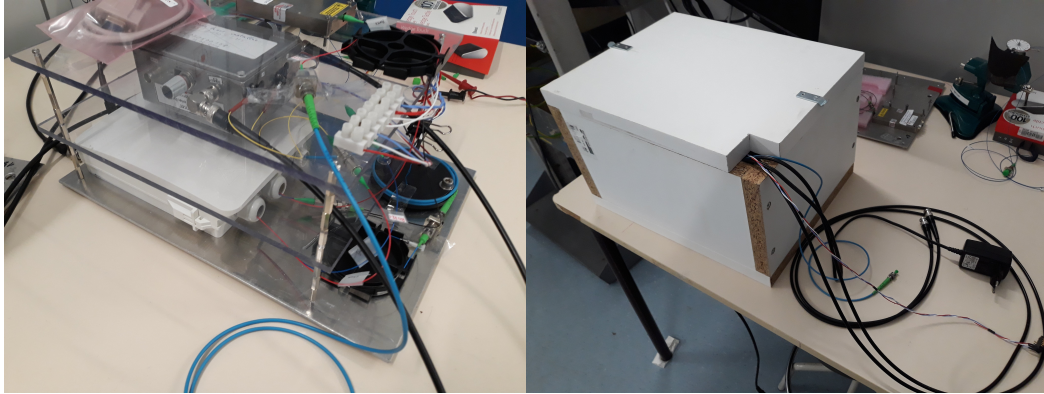
(a) Fibered setup assembly   *(b) Fibered setup assembly in the shield*

Figure 5.13: *Fibered interferometer is installed in compact shelves assembly. Full assembly is shielded (thermally, acoustically, vibrationally) by a wooden box*

The free space setup is shown in Fig. 5.14. The collimated beam (see Sec. 5.2.1) in the free space propagates to a super polished mirror with a

piezo actuator (see Sec. 5.2.2) for rapid modulation of the optical phase. The piezo is powered by a 2 kHz sine from the internal signal generator of the lock-in amplifier. From the piezo mirror, the collimated, phase-modulated beam propagates to the sample under test (see Sec. 5.2.3). The fraction of the backscattered light, which is collected by the collimator, and re-coupled into the fiber, with the beam from Arm I. A beam dump (see Sec. 5.2.4), is placed in such a way to attenuate efficiently the specularly reflected beam from the sample. In the presence of the backscattering, the interference between ARM I and ARM II beams gives rise to a modulation in the photodiode signals. The modulated signal is amplified and then demodulated by the lock-in amplifier. To make 2D maps of the backscattering amplitude, we use a 2D translation
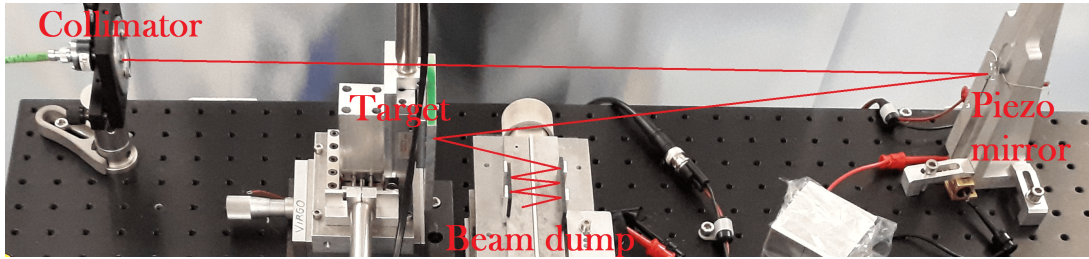
Figure 5.14: Free space part of the setup. The red line indicates the approximate beam path. Incidence angle is $\approx 14^o$.

stage (see Sec. 5.4.2) controlled from a PC to move the sample parallel to its surface. For the angular study of the backscattered light, we use a Picomotor rotational stage (see Sec. 5.2.6).

To take into account all the losses presented in the free space setup, we perform a calibration with specular reflection. For this, instead of the sample, a mirror at 0° incidence is installed. The value of the reconstructed fringe amplitude is used for calibration purposes in further data analysis procedures.

The next sections will be dedicated to the characterization and adjustment of the components in the free space.

5.2.1 Collimator

The first component in the free space part of the setup is the fiber collimator HPUCO-23A-1300/1550-S-18AS from Oz Optics with a focal length of $f = 18\ mm$. This component has no adjustment (all degrees of freedom are frozen), but the beam waist should be measured, as the beam properties on the target location may be different from that, which are at the immediate output of the collimator.

To measure the beam waist, we use a power meter and a blade installed on the translation stage.

The fit of the curve power vs. blade position allows reconstructing the beam waist and the beam divergence. The result of the measurements is presented in Fig. 5.15. From the fit result we get $\omega = 1.717 \pm 0.078\ mm$.

This measurement agrees with the estimate (1.71 mm) that can be made using the collimator's focal length and the numerical aperture $NA = \frac{\lambda}{\pi\omega_0}$ where
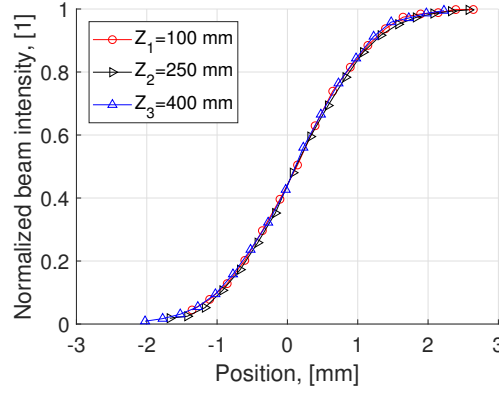
Figure 5.15: Beam waist measurements at different location Z from the collimator

$\omega_0 = a/2$, obtained from $a = 10.4 \ \mu m$, the mode field diameter of the fiber. From a simple geometrical consideration, the beam diameter after the lens is:

$$BD(mm) = 2 \times f(mm) \times NA = 3.42mm. \tag{5.33}$$

So the beam waist is $3.42/2 = 1.71 \ mm$, which agrees with the measurements.

The beam divergence is impossible to recover from the data in Fig. 5.15 due to the limited distance between the extreme data points, but it is linked to the beam diameter (Gaussian beam) for this optical system:

$$\theta = \frac{\lambda}{\pi n \omega_0}. \tag{5.34}$$

The beam in the free space part of the setup has a full-beam divergence angle of $2\theta = 0.58 \ mrad$.

5.2.2   Modulation mirror

The collimated beam in the free space propagates to a super polished mirror, and it is modulated there. The modulator consists of three parts: mirror, piezo and massive base (see Fig. 5.16a).

Average polishing quality mirror (see Fig. 5.16c) contributes to the signal by scattering (mainly by surface roughness), and so it makes the interpretation of the measured interferometric signal difficult. In our setup, we switched to the super-polished mirrors as they contribute less to the scattering in the system. The scattering from them is mainly due to particle contamination (see Fig. 5.16b), and they can be efficiently removed with the "First contact" polymer. A massive base prevents propagation of the vibrations of the modulation system to the rest of the setup. Piezo modulator is glued with cyanoacrylate to the backside of the mirror by one end and to the massive base by the other. The amplitude of modulation linearly depends on the applied voltage. However, the driving signal should be positive.

The high modulation frequency is preferable, as the electronics noise is high at low frequencies. From the other side, at some frequency, the resonance of

(a)   *(b)*   *(c)*
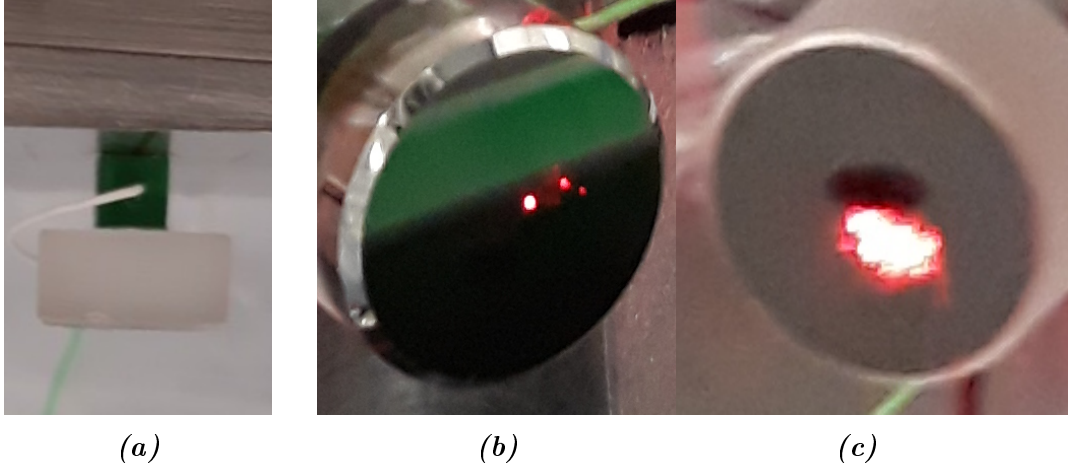
Figure 5.16: Modulation mirror (a) system: mirror, piezo, massive base. Super polished mirror with dominant particle scattering (b). Super polished mirror with dominant surface scattering (c).

the piezo will arise, which is not desirable. The optimal frequency is in the kHz range. In the experiment, the piezo is powered by a sine wave of 2 kHz and positive (peak to peak) amplitude 10V by the internal signal generator of the lock-in amplifier.

The amplitude of the modulation should maximize performance. This amplitude can be found from the following considerations:

1. A function of the type $cos(\phi_0 + \phi_m sin(\omega_m t))$ (the same as measured function) can be represented as series (see Sec. 5.1.2):

$$J_0(\phi_m)cos(\phi_0) + 2\sum_{n=1} J_{2n}(\phi_m)cos(2n\omega_m t)cos(\phi_0)-$$

$$- 2\sum_{n=1} J_{2n-1}(\phi_m)sin((2n-1)\omega_m t)sin(\phi_0), \quad (5.35)$$

where ϕ_m is the modulation depth. In the figure 5.17a is shown the absolute value of the Bessel functions of the first kind with the applied voltage to the piezo mirror (scaling will be discussed later in this section).

2. The first and the second harmonics are used in signal processing, and they are proportional to J_1 and J_2 correspondently. It is impossible to reconstruct the fringe amplitude with only one of them, so when one of the harmonics falls below the noise level, the measurements will be impossible. For this reason, both of them should have a high and equal amplitude for the best performance.

So the optimal value of the modulation voltage is the first intersection of the first and second Bessel functions.

To find the intersection point in units of voltage, I will use the fact that the argument of the Bessel function is $\phi_m = \frac{2\pi n}{N}$ is proportional to the applied to piezo voltage V. In this expression, n is the refractive index of air, and

$N = p/V$ is the inverse value of the modulation depth. The parameter p of the piezo I had found experimentally, by the measurements of the ratio of the Bessel functions (J_3/J_1 and J_1^2/J_2^2) as a function of the applied voltage V (see Fig. 5.17b) for two photodiodes (Ph_1 and Ph_2). From this, I found that the coefficient of proportionality is $p = 40.6 \pm 0.1$ V for the current geometry of the setup and for the chosen piezo actuator, the Thorlabs PC4FL.

(a)   *(b)*
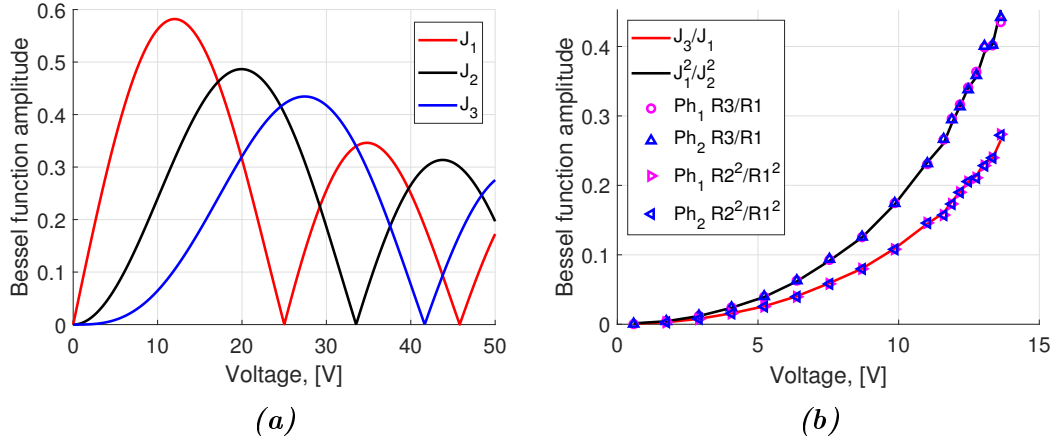
Figure 5.17: Optimization of the phase modulation amplitude and calibration of setup. The absolute value of the Bessel function as a function of the applied to the piezo mirror voltage (a). Illustration for piezo calibration method (b): solid lines are analytical curves, and dotes are measured values.

So the optimal value of the modulation voltage is around 16V. However, this is out of the modulation range of the signal generator of the Lock-in amplifier (10 V). The attempt to use an external amplifier cause an increase of noise of the demodulated signal and unstable offsets in all the harmonics, so we kept the value of 10 V for which the optimum is not perfect but acceptable.

5.2.3 Sample

To demonstrate the functionality of the set-up it has been useful to operate the set-up first with a mirror of moderate roughness. We followed the suggestion of Hevé Bénard (Thales Alenia Space) to purchase an "infra-red mirror" as a sample. The mirrors for the IR range are less demanding on surface polishing, and so they can serve as a moderately rough sample.

For the first tests we used a 1 inch mirror from Edmund optics (Ref. number 47113) with protected aluminum coating. The thickness of the protective coating is approximately 1400 Å made of SiO2.

The RMS roughness of the mirror is specified to be less than 175 Å. This value is large. However, it is small enough that scattering is still in the "small roughness" regime. A map of the roughness profile of the mirror was performed at Institut Fresnel (see Fig. 5.18). In confirms that the mirror complies to the specification.

(a) *RMS=11.32 nm*   (b) *RMS=7.98 nm*   (c) *RMS=7.98 nm*
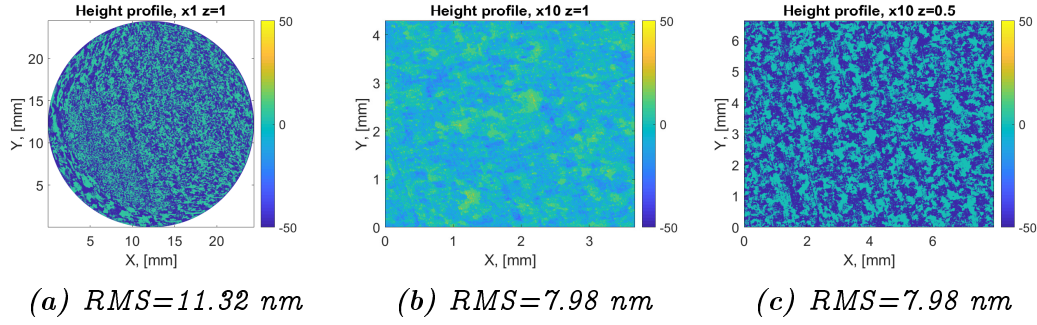
Figure 5.18: Measured surface roughness map. We thank Myriam Zerrad, Institut Fresnel, for providing these measurements.

The example of BRDF calculation from the height maps in Fig. 5.18 is given in Appendix B.

5.2.4 Beam dump

The beam reflected by the mirror will hit a wall or any other surface. In any case, this will give rise to backscattering that will also interfere and bring a systematic error, or at least a noise, and complicate the measurements. For this reason, the beam must be dumped to a level well below the measurement considered. This is particularly true when having in mind the statistics of the backscattered light distribution.

To dump the specularly reflected beam, a beam dump is built. The main requirement for the beam dump in this experiment is low backscattering. Nothing can prevent light backscattered by the beam dump to be collected by the collimator. The beam dump [36] is made from two black HOYA RT-830 glass plates polished by Coastline Optics (see Fig. 5.19a). The two absorbing glass plates are placed parallel to each other so that the laser beam bounces five times and is attenuated (see Fig. 5.19c). For the updated version of the beam dump, I designed and 3D-printed a plastic holder (see Fig. 5.19b).

(a)   (b)   (c)
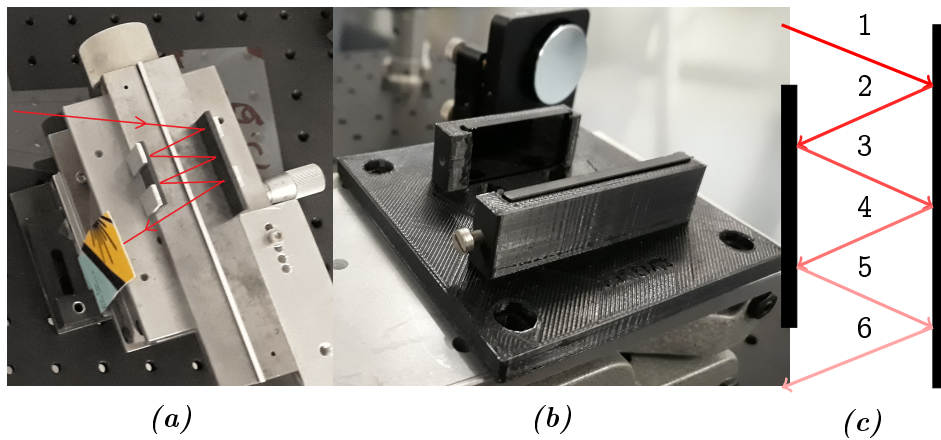
Figure 5.19: The beam dumps used in the setup (a,b) and schema of beam reflection in between beam dump glasses (c)

Glass plates have size of $50 \times 15 \times 2.5$ *mm* and $32 \times 15 \times 2.5$ *mm*. The distance between glass plates is 20 *mm*, and the incidence angle is 15.5^o from normal. The transmission is 3.6×10^{-4} at 1550 *nm* after 2.5 mm propagation, so the beam which will reflect or scatter from the surface behind the glass will be highly attenuated. Strong absorption is the main criterion for the choice of the glass, together with the absence of bubbles in the volume. The reflection of the beam is 4.74%, so from the beam dump will exit the beam with fractional power equal to 2.4×10^{-7} from incident.

We had tested different polishing and different glass for the beam dumps. The results of the measurements are summarized in Table 5.2. The value of backscattering given in the table is the lowest achieved value of backscattering (not an average). The lowest backscattering is the one we get with Coastline polishing, and it has been used in the setup.

Table 5.2: Backscattering from the different beam dumps.

Polishing	Backscattering	Glass
Default	-118.7 $\pm$ 0.7 dB	HOYA RT-830
Optoprim	-117 $\pm$ 0.7 dB	Schott RG9
Coastline	-130.9 $\pm$ 0.9 dB	HOYA

To separate the contribution of the beam dump from other contributions to backscattering (see Sec. 5.3.1), we modulate the position of the beam dump at the frequency of 1 Hz and identify the corresponding contribution in the fringe signal. With a properly adjusted amplitude of the piezo, we completely discriminate the contribution of the backscattering of the beam dump against other contributions (details are discussed in Sec. 5.3.1). As will be shown in the following, the scattered light has a speckle behavior as a function of the incidence angle and spot position, so it is possible to adjust the position and the incidence angle at the beam dump to minimize its backscattering. When the incidence at the beam dump is well adjusted, we switch the 1 Hz signal to modulate the sample position. The minimal backscattering, which we had measured from this beam dump, is -130.9 ± 0.9 *dB* in optical power.

5.2.5   Translation stage

Due to the speckle structure of the scattered light, measurement in a single point is not sufficient to characterize scattering amplitude for a given incidence angle. For the correct estimation of the value of the scattering from an optical surface, a 2D scan of the spot position is required. At first, we used a home-made 2D stage, but we noticed that the 2D scans failed to be repeatable, which prevented from drawing conclusions from the measured data.

To check repeatability, we scanned 25 times the same line on the sample surface. The scanning step is 1 *mm*. The movement of the translation stage (TS) was performed by Newport stepper motors controlled with a MATLAB script. The scanning was performed in a way that, first, the motor was pushing the TS, then the spring was pushing the TS. If the repeatability were good,

we would record the same backscattering signal each time we scan the line once again, and the final pattern should be a collection of vertical lines. But it was obvious that the reproducibility was not satisfactory (see Fig. 5.20a): "even" and "odd" rows did not show the same signal. This was a consequence of an angular wobble of the translation stage. By replacing the home-made translation stage by a high-quality M-461-XY-M "Ultralign" Newport 2D stage, we obtained a pattern (see Fig. 5.30) showing perfect repeatability. As will be shown in Sec. 5.4.4, the sensitivity of the backscattering on the incidence angle is very high and explains that even a moderate angular wobble induces strong changes in the backscattering.
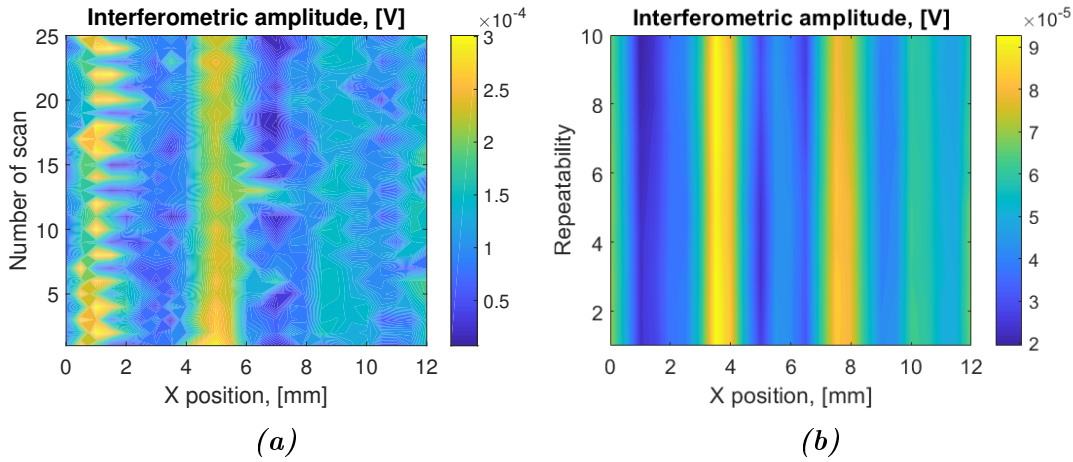
Figure 5.20: The results of the repetitive scan of the same line (a) with home-made 2D stage, b) with a translation stage with an angular repeatability much better than 100 micro-radian.

5.2.6 Tilt stage

To study the angular dependence of coherent scattering, I used a Picomotor motorized mirror mount: the New Focus 8821 mode. As this is an open-loop version, the steps are not repeatable, and hysteresis is present. The hysteresis also makes impossible the mapping of backscattered light with this stage. The calibration of the stage in necessary.

To calibrate the stage, I use the setup, as shown in Fig. 5.21. On the beam path between the mirror and the power meter, I had installed the translation stage with a sharp blade, which, knowing the mirror-blade distance, provided the calibration. Distance from the blade to a mirror is $L = 1205 \ mm$. With this information, I can calculate the incremental step $R_+ = 0,63 \mu rad/step$ in the positive direction ($0.57 \mu rad/step$ in the negative direction) resolution R_+ of the stage in a positive direction, which is approximately equal to the average resolution $0.7 \ \mu rad/step$ specified in the datasheet of the stage.
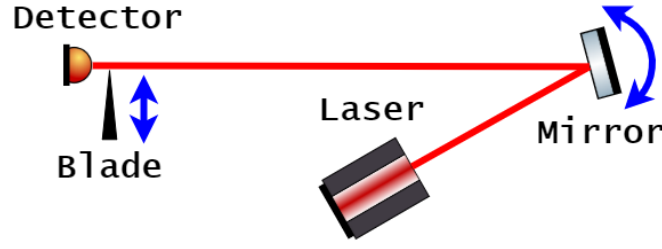
Figure 5.21: Schema of the calibration setup for the Picomotor motorized mirror mount.

5.3 Signal processing for the case of multi-beam interference

I now address the case of the real set-up, where various optical components may give rise to optical return, and complicate the measurement of the backscattering from the sample. In this "multiple-beam interference signal" the target signal must be given a clear, unequivocal signature.

Ideally, after the recombination at the 50/50 beam splitter, the fraction b_s of the power backscattered from the sample surface, with a complex amplitude of $\sqrt{I_L/4}\sqrt{b_s}\times exp(i\phi_{II,s})$ interferes, with the light of amplitude $\sqrt{I_L/4}\times exp(i\phi_I)$. At the PD 1 (resp. PD 2) output ports of the interferometer (see Fig. 5.12), the detected intensity is similar to Eq. 5.3 except for the replacement of T^2 by the backscattering fraction b_s:

$$I = I_L/4 + b_s I_L/4 + \frac{I_L}{2}\sqrt{b_s}cos(\Delta\phi_s).$$ (5.36)

So the interference signal is:

$$I_{AC} = \frac{I_L}{2}\sqrt{b_s}cos(\Delta\phi_s),$$ (5.37)

(resp. is $-I_L/2\sqrt{b_s}\cos(\Delta\phi_s)$). In this expression, I_L is the laser intensity, $\Delta\phi_s = \phi_{II,s} - \phi_I$ is the difference of the propagation phase between arm II (up to the sample), including the 2 kHz modulation by the piezo actuator, and arm I, including a possible thermal ramp. Then extracting the backscattered power fraction b_s by demodulation looks trivial.

However, the processing of demodulated signals is complicated, because multiple contributions from different backscattering sources (e.g., fibers, fiber connectors, collimator, piezo mirror, beam dump, and sample) are presented in the measured signal. First, one could consider separately the three sources located before the piezo mirror, from which backscattering signal should not be modulated, and discard them. But the acoustic crosstalk between the fibered part and the piezo actuator is not negligible, as we observe the corresponding contribution in the demodulated signal. Other stray contributions to backscattering come from the modulated mirror itself, and the beam dump. An additional effort is required to discriminate the different contributions, and I have

implemented a dedicated procedure, giving to the sample's contribution a clear
signature, and processing the recorded data in a way to isolate and extract the
sample's backscattering.

To facilitate the presentation, I divide it into two parts. First, I consider
interference with three beams (reference one, measured, and one stray light
beam). In the second part of the section, I generalize the solution to any
number of stray light beams.

5.3.1 One stray contribution: the three-beam interference

Let us consider a simplified setup (see Fig. 5.22) where a modulated beam
goes directly to the beam dump: this set-up is devoted to measuring and
characterizing the backscattering from the beam dump b_{BD}. As the latter is
and has to be very small, the backscattering from the modulating mirror is
obviously a possible source of error in the measurement.
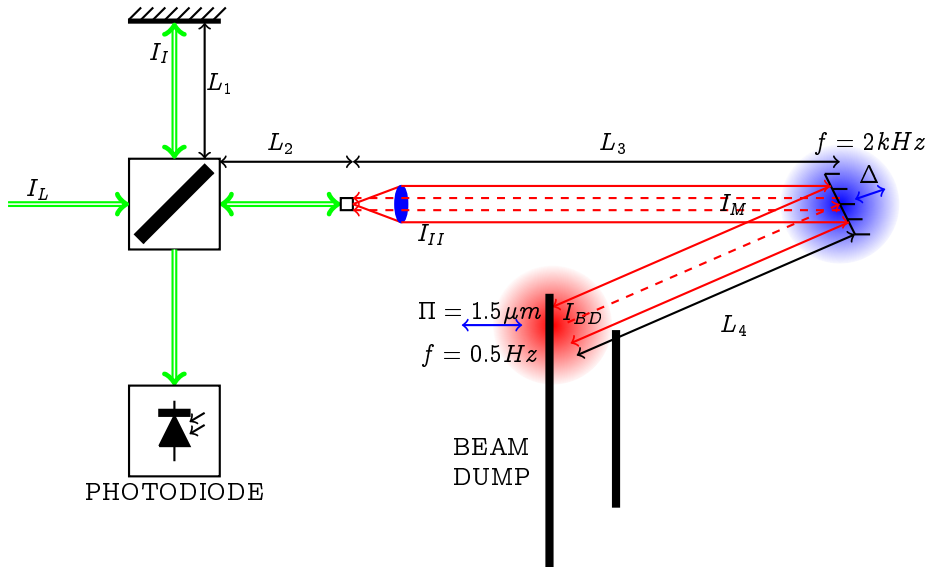
*Figure 5.22: Simplified schema of the experimental setup. The backscattered intensity from the mirror I_M superposes with backscattered intensity
from beam dump I_{BD}. The positions of the mirror and beam dump are
modulated with a displacement of Δ and Π respectively.*

The laser beam of intensity I_L is divided by the beam splitter in two parts.
The beam in arm I with intensity $I_I = I_L/2$ is confined in the fiber when
the other beam propagates in the free space part, and then it attenuates in
the beam dump. Some parts of light scatter in the backward direction from
the beam dump I_{BD} and couples back into the fibered setup. At the same
time, some parts of light backscatter from the modulation mirror I_M and can
also couple in the interferometer. These two beams interfere with the beam
confined in the fibered arm I, and produce a three beam interference signal
at the photodiodes. Due to the low level of backscattering intensities, the
interference between two backscattered beams is negligible. In this setup is

implemented the fast, $\omega_M/2\pi = 2\ kHz$ modulation applied to the modulation
mirror, but also a slow, $\omega_S/2\pi = 0.5\ Hz$ modulation applied, also via a piezo
actuator, to the whole beam dump assembly.

In this case, the variable (AC) part of the interference is given by the
expression:

$$I_i = 2\sqrt{I_I I_M}cos(\phi_{IM}) + 2\sqrt{I_I I_{BD}}cos(\phi_{IBD}), \tag{5.38}$$

where the interferometric phase ϕ_{IM} consists of two parts:

$$\phi_{IM} = \phi_{0M} + \phi_{MM} = \frac{2\pi}{\lambda}2\Big(n_f(L_2 - L_1) + n_a L_3\Big) + 2\pi\delta_M sin(\omega_M t). \tag{5.39}$$

Here slow drifts in ϕ_{0M} are caused mainly by thermal effects in the optical fibers
and ϕ_{MM} is due to fast modualtion with modulation mirror, $\lambda = 1550\ nm$
is laser wavelength, lengths L_1, L_2, L_3, Δ and Π are defined in Fig. 5.22,
$n_f = 1.45586$ is the refractive index of the fiber and $n_a = 1.000293$ is refractive
index of air at normal condition, δ_M is path modulation (in units of wavelength)
by piezo mirror along beam direction.

Phase ϕ_{IBD} consists of three parts:

$$\phi_{IBD} = \phi_{0BD} + \phi_{MBD} + \phi_{MBD}^*. \tag{5.40}$$

The first term is:

$$\phi_{0BD} = \frac{4\pi}{\lambda}\Big(n_f(L_2 - L_1) + n_a(L_3 + L_4)\Big). \tag{5.41}$$

It is caused by the optical path difference of beams propagation in two arms of
the interferometer. The second term is due to the modulation by the mirror:

$$\phi_{MBD} = 4\pi\delta_M sin(\omega_M t). \tag{5.42}$$

The backscattered light from the beam dump is two times modulated by the
piezo mirror ($\delta_{BD} = 2n_a\Delta/\lambda cos(\alpha)$) unlike light backscattered from the mirror
($\delta_M = n_a\Delta/\lambda cos(\alpha)$; see Fig. 5.23). The angle α is the angle between beam
propagation and mirror modulation directions. Similarly $\delta_M^* = 2n_a\Pi/\lambda cos(\beta)$,
where β is angle between beam propagation and beam dump modulation di-
rections.

The last phase contribution is due to the slow modulation of the beam
dump:

$$\phi_{MBD}^* = 2\pi\delta_M^* sin(\omega_S t), \tag{5.43}$$

where δ_M^* is modulated path of the beam dump along beam propagation axis
(in units of wavelength).

To simplify the manipulation with interferometric Eq. 5.38, I will express
the backscattering intensity in terms of input laser intensity I_L, backscatter-
ing fraction from the beam dump b_{BD} and backscattering fraction from the
modulation mirror b_M. In this case, the Eq. 5.38 can be rewritten as:

$$I_i = \frac{I_L}{2}\Big(\sqrt{b_M}cos(\phi_{0M} + \phi_{MM}) + \sqrt{b_{BD}}cos(\phi_{0BD} + \phi_{MBD} + \phi_{MBD}^*)\Big). \tag{5.44}$$
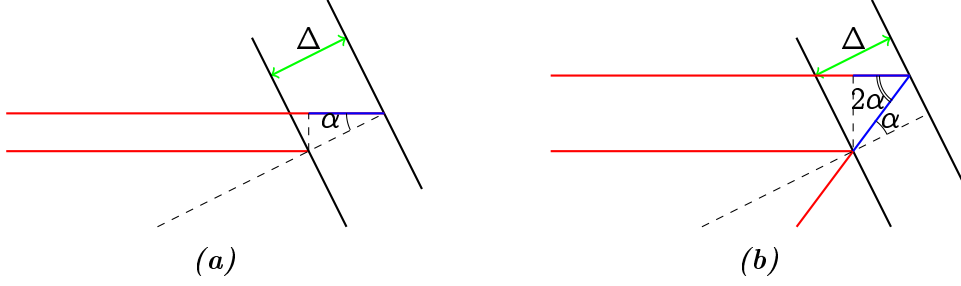
Figure 5.23: Path modulation for the case of backscattering from the mirror (a) and the beam dump (b). With PC4FL piezo (Thorlabs), which is used for the mirror modulation, 10 volts amplitude corresponds to $\Delta = 0.2\mu m$ (green line).

In the following I deal with demodulated amplitude X ($|X| = R$, $\Theta = 0$). The first harmonic of the demodulated interferometric signal is

$$X_1 = I_L\left(\sqrt{b_M}\,J_1(2\pi\delta_M)cos(\phi_{0M}) + \sqrt{b_{BD}}\,J_1(4\pi\delta_M)cos(\phi_{0BD} + \phi^*_{MBD})\right). \quad (5.45)$$

And the second harmonic is:

$$X_2 = I_L\left(\sqrt{b_M}\,J_2(2\pi\delta_M)sin(\phi_{0M}) + \sqrt{b_{BD}}\,J_2(4\pi\delta_M)sin(\phi_{0BD} + \phi^*_{MBD})\right). \quad (5.46)$$

If $b_{BD} \gg b_M$, the solution for b_{BD} is easy to retreave with Eq. 5.20. If not, mathematically the problem is that for the four unknown values ($\sqrt{b_M}$, $\sqrt{b_{BD}}$, ϕ_{0M}, ϕ_{0BD}) exists only two equations. However, as the time series of both harmonics are measured, Fourier spectrum analysis can be used to separate contributions of scattering from the mirror and from the beam dump, taking advantage of the slow modulation of the beam dump.

The spectrum of $X_1(t)$ and $X_2(t)$ will contains multiple peaks at the beam dump modulation frequency ω_S and harmonics, according to:

$$cos(\phi + 2\pi\delta\,sin(\omega_S t)) = J_0(2\pi\delta)cos(\phi)+$$
$$+ 2\sum_{n=1} J_{2n}(2\pi\delta)cos(2n\omega_S t)cos(\phi) - 2\sum_{n=1} J_{2n-1}(2\pi\delta)sin((2n-1)\omega_S t)sin(\phi).$$
$$\quad (5.47)$$

The distribution of the power over harmonics depends on the initial phase ϕ and the modulation parameter δ and are given by Bessel functions of the first kind J_0, J_1, J_2, etc.

In the case of a constant thermal drift with frequency ω_T, each spectrum line splits on two equidistant from ω_S lines. The position of the lines in the spectrum for the harmonic m is $m \times \omega_S \pm \omega_T$.

However, this spectrum also will have a contribution, at or near zero frequency, proportional to $J_0(2\pi\delta^*_M)$. This spectral component will mix with the backscattering contribution from the modulation mirror with no possible way to identify separately the two contributions.

To eliminate this problem, the modulation voltage V^* (and thus modulation path δ_M^*) of the beam dump should be adjusted in a way that J_0 turns out to be zero, which is obtained for the values 2.405, 5.520, 8.654, etc. of the argument.

To find this zero, I had performed a calibration. For this, I recorded the amplitudes of the first three harmonics of ω_S (see Fig. 5.24b), as a function of the voltage modulation applied to the piezo driving the beam dump assembly I found that the second zero of the Bessel function of zero-order J_0 is at 37.1 V of modulation voltage of the beam dump (or 16.2 V for the first zero).

With that choice of the modulation voltage, only the mirror modulation contributes to the zero frequency amplitude $(J_0(2\pi\delta_M^*) = 0)$, which allows to disentagle the two contributions to the interferometric signal (see Fig. 5.24a). The black curve is the precalculated spectrum with correctly chosen parameters: thermal frequency ω_T, modulation frequency ω_S, and the modulation path δ_M^* .

(a)   (b)
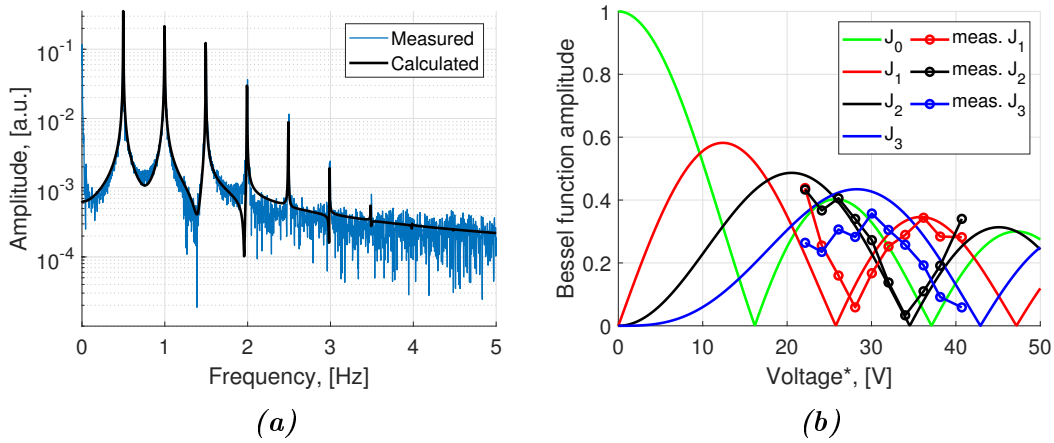
Figure 5.24: A spectrum of the in-phase output of the demodulator X1 with adjusted modulation voltage ($J_0 = 0$) for 0.5 Hz modulation frequency (a). The Bessel functions and the measured values (data 1,2,3) of harmonics ω_S in the demodulated signal (b).

So by proper choice of the modulation voltage amplitude to the beam dump, we stabilize the signal and have the possibility to process and identify two interferometric components mixed up in the signal. To test the idea, I built an experimental setup, as shown in Fig. 5.25.

An example of the recorded data (in-phase component X, first harmonic) is shown in Fig. 5.26b. Contribution from the mirror is not affected by 0.5 Hz modulation and changes only slowly with time. The component which evolves at the 1 s time scale is the beam dump contribution. The spectrum of this signal is shown in Fig. 5.27. The modulated signal on fundamental frequency and its harmonics are highlighted in red.

When the separation in the frequency domain is done, I perform the inverse Fourier transform of spectrum data highlighted in red and in black separately. The phase for both spectrums is the same. The result of this computation is shown in Fig. 5.26c.
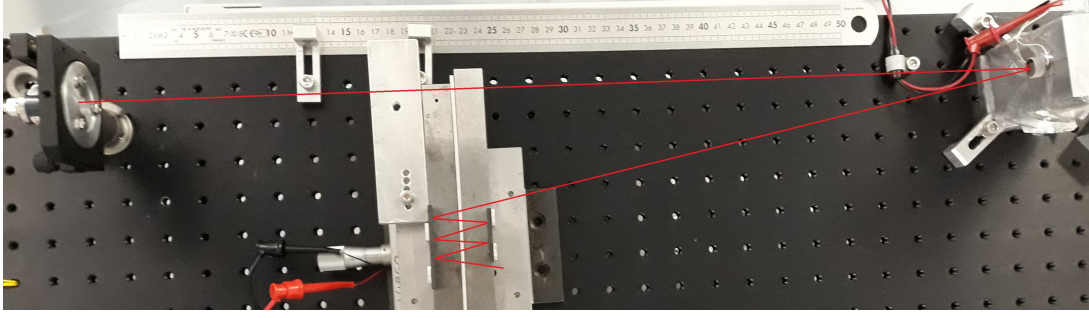
Figure 5.25: A free-space part of the experimental setup. The beam is modulated by the piezo mirror and is attenuated in the beam dump. The beam dump position is modulated at a frequency of $0.5\ Hz$. The red line is an approximate beam pass.

<div align="center">(a)   (b)   (c)</div>
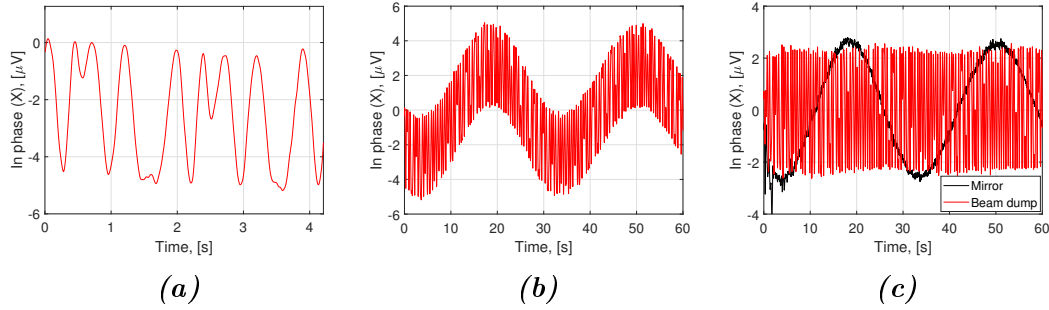
Figure 5.26: Signal before (a), (b) and after (c) the processing for the data recorded with the set-up shown in Fig. 5.25. The signal (a) is a zoom of (b) with an evident slow modulation effect. The amplitude of the slow modulation is 37.1 V. The retrieved backscattering fraction in power from the modulation mirror is $6.7 \pm 0.8 \times 10^{-11}$ and from the beam dump is $1.3 \pm 0.1 \times 10^{-11}$. The signal is the in-phase component (X) of the output of the demodulator at the 1st harmonic for the photodiode 2.

In Fig. 5.26c the black curve is the slow changing component which is associated with the backscattering contribution from the mirror:

$$X_{1M} = I_L \left(\sqrt{b_M} J_1(2\pi\delta_M) cos(\phi_{0M}) \right), \tag{5.48}$$

and the red curve in Fig. 5.26c is the contribution from the beam dump:

$$X_{1BD} = I_L \left(\sqrt{b_{BD}} J_1(4\pi\delta_M) cos(\phi_{0BD} + \phi^*_{MBD}) \right). \tag{5.49}$$

After this stage, each backscattering component is processed independently, using the method (Eq. 5.20), I combine the data recorded at the first and second harmonics of $omega_M$, to give the corresponding backscattering fraction b_{BD} or b_M. As before, the combination of the first and second harmonics for each contribution gives fringe amplitude and so, the backscattering fraction. Here should be taken into account that the modulation path for the backscattering component from the mirror is $\delta_M = 0.094$, and it is about twice smaller than
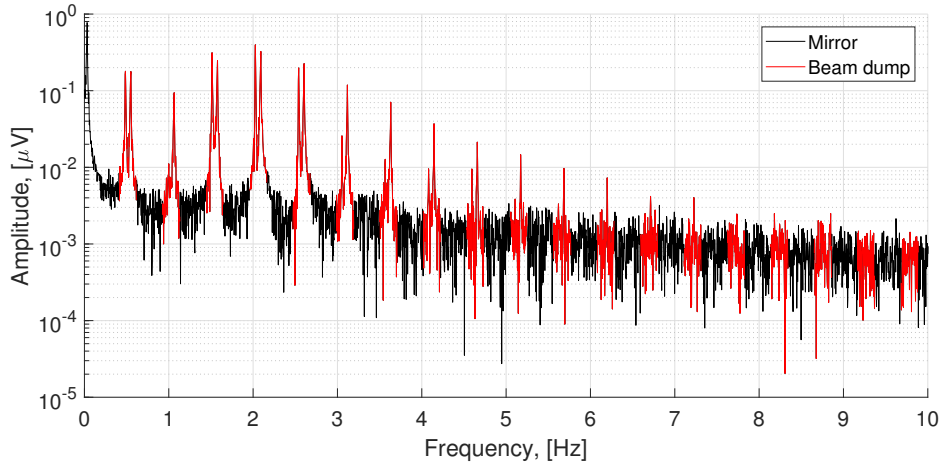
Figure 5.27: The spectrum of the demodulator output signal presented in Fig. 5.26. The red peaks correspond to the harmonics of the beam dump modulation frequency ω_S (doublet structure). Split of the lines is due to thermal drift in the system.

the backscattering component from the beam dump $2\delta_M = 0.23$, which is in agreement with given above considerations.

5.3.2 General case

The total fringe signal at PD 1 (see Fig. 5.2) has to be written as following:

$$I = I_L/2 \Big(\sum_i \sqrt{b_i} cos(\Delta\phi_i) + \sqrt{b_s} cos(\Delta\phi_s) \Big), \qquad (5.50)$$

where all stray contributions to backscattering (power ratio b_i and phase ϕ_i) are under the sum sign. Demodulation is done at the first harmonic (frequency 2 kHz) with a bandwidth of 6 Hz (8th order). After demodulation of the signal using the lock-in amplifier, we get 224 times per second, in-phase X and quadrature Y components. The combination we need is:

$$R \equiv X \times cos(\Theta) + Y \times sin(\Theta), \qquad (5.51)$$

where Θ is the phase of the fringe signal modulation with respect to the voltage applied to the piezo actuator. It differs from zero due partly to the electronic signal propagation delay and mainly to the hysteresis in the piezo actuator. As Θ does not change during data taking, we first determine the value of Θ in conditions where the signal is large. Later we use this value to determine R from Eq. 5.51, and exploit the time series of R, particularly the dependence of R on the thermal drift of the fibered path length and/or on the modulations we apply to the position of the sample.

Then the demodulated signal of the measured signal at the first and second harmonics of piezo mirror modulation frequency (2 kHz) will be:

$$R_1 = I_L(\sum_i \sqrt{b_i} J_1(2\pi\delta_{Mi})cos(\phi) + \sqrt{b_s} J_1(4\pi\delta_M)cos(\phi_s)), \qquad (5.52)$$

$$R_2 = I_L(\sum_i \sqrt{b_i} J_2(2\pi\delta_{Mi})sin(\phi) + \sqrt{b_s} J_1(4\pi\delta_M)sin(\phi_s)), \qquad (5.53)$$

where J_1 is Bessel function of the first order and δ_M is the modulation depth of the piezo mirror (note that for each component modulation depth can be different). Separation of the contributions from all backscattering sources is an unnecessary and challenging task. What we need is to give a specific signature to the $\sqrt{b_s}$ contribution, to identify and record it with the highest precision. For this, we modulate the position of the sample at $\omega_s/2\pi = 1~Hz$. Using the Fast Fourier Transform (FFT), we can easily extract all harmonics of the modulated signal from R_1. When modulation of the sample is applied, we have an additional term in phase ϕ_s for the sample and beam dump components:

$$R_1 = I_L(\sum_i \sqrt{b_i} J_i(2\pi\delta_{Mi})cos(\phi_i) + \sqrt{b_s} J_1(4\pi\delta_M)cos(\phi_s + \delta_1 cos(\omega_s t)) +$$

$$+ \sqrt{b_{BD}} J_1(4\pi\delta_M)cos(\phi_{BD} + 2\pi\delta_1 cos(\omega_s t + \phi_0)). \quad (5.54)$$

A similar expansion holds for the second harmonics. Here δ_1 is the sample frequency modulation depth, and $\phi_0 \approx 0$ is a propagation delay (sample - beam dump $-$ sample). The factor two in front of the modulation depth considers that the backscattered light from the beam dump is twice modulated. In Fig. 5.28 is presented the FFT of R_1 in different measurement conditions, but for the same scattering point of the sample under test. In red is the FFT of R_1 when 1 Hz modulation is applied to the sample. At very low frequency (below 1 Hz) are spectral components of the stray backscattering contributions. They are mainly due to thermal drifts and are not modulated. They contribute only to frequencies $< 1~Hz$. At higher frequencies, we find at 1 Hz and harmonics the sample, useful signal, mixed with the beam dump backscattering contribution.

The distribution of the power between harmonics is given by the Bessel functions of the first kind (see Eq. 5.47). The argument of these functions is proportional to the modulation depth of δ_1. By adjusting δ_1, we can control the way the power is distributed over the spectrum. As we did in Sec. 5.3.1, we adjust delta1 so that $J_0(2\pi\delta_1) = 0$. Then we have the useful signals appearing only at frequency $\omega_S/2\pi$ and harmonics, while the stray contributions are at zero frequency, and so can be discarded in the reconstruction of the signal.

At this stage, we had separated the useful signal from the stray contribution. But it's still mixed with backscattering from the beam dump. To lower the contribution from the beam dump, we adjust its position and incidence, to reach the minimum possible scattering. This is made possible because scattered light has speckle behavior (as will be shown later). The Fig. 5.28 shows the FFT of R_1 when slow modulation is applied to the beam dump and not to the sample (black color). The contribution from the beam dump is approximately one order of magnitude lower than the backscattering amplitude measured from the sample. The position and incidence of the beam dump can be adjusted to minimize the backscattering from it, and so, this contribution can be neglected.

However, even in case of modulation are applied to the sample (red color in Fig. 5.28), it is possible to estimate the contribution from the beam dump. The
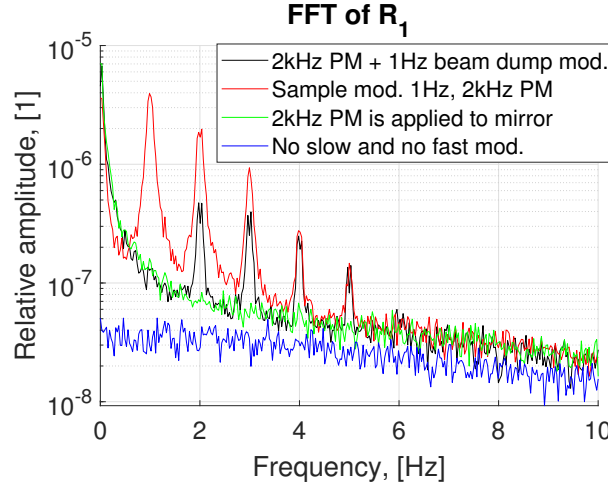
Figure 5.28: FFT of R_1 when slow (1 Hz) modulation is applied to the beam dump (black), and the case without slow modulation (green). For the sample modulation (red), we had adjusted the voltage to reach the condition $J_0(\delta) = 0$. The case when neither the fast nor the slow is applied gives electronics plus laser noise level (blue).

modulation depth of the backscattered light from the beam dump is twice larger than from the target, so modulation spectrums for these two contributions will be different. Distortion of the spectrum fit at higher harmonics will indicate the significance of the problem.

Figure 5.28 also shows the FFT of R_1 when slow modulation is not applied (green color). In this case, the contributions of backscattering are not separable, and any precise measurements are not possible. In blue in the same figure is shown the spectrum when neither slow nor fast modulation is applied to the setup. So, this displays the contributions to the noise floor from the laser power noise and electronic noise of the detection system.

After all these adjustments and assumptions, we will have:

$$R_1 = I_L \sqrt{b_s} J_1(4\pi\delta_M) cos(\phi_s), \tag{5.55}$$

$$R_2 = I_L \sqrt{b_s} J_2(4\pi\delta_M) sin(\phi_s). \tag{5.56}$$

Recalling that $sin^2(\phi_s) + cos^2(\phi_s) = 1$, the combination with the second harmonic contribution will allow getting rid of the impact of thermal variations of the phase ϕ_s

$$\sqrt{b_s} = \frac{1}{I_L/2} \sqrt{\left(\frac{R_1}{2J_1(4\pi\delta_M)}\right)^2 + \left(\frac{R_2}{2J_2(4\pi\delta_M)}\right)^2}. \tag{5.57}$$

The calibration coefficient $I_L/2$ is measured when in the ARM II the sample is replaced by a metal mirror at normal incidence. To reduce statistical error, we combine the measured values from the two photodiodes (weighted mean).

The listing of the MatLab script for basic data processing is given in Appendix C. The algorithms consist of four main steps:

1 Read the recorded data of XY for the first and second harmonics.

2 Rotate the XY vector for the first and second harmonics to align the signal along the X axis. If the angle of rotation for the first harmonic is Θ_1, so for the second one is $\Theta_2 = 2\Theta_1 + \pi/2$.

3 Separate the slow (at the thermal frequency), and fast active component (on the frequency of slow modulation ω_s and harmonics) of the signal with Fourier transform.

4 Combine two harmonics with Eq. 5.57 to eliminate the impact of the thermal phase and calculate the backscattering in amplitude and power using the calibration coefficient.

After these steps, the result of backscattering measurement by two photodiodes can be combined and analyzed.

In result, the current method suggests:

- modulating the position of the phase modulating mirror at kHz frequency, with a depth chosen such that both the fundamental and first harmonic terms of the spectral decomposition are large, and simultaneous recording of the result of the two demodulations $X_1 + jY_1$ and $X_2 + jY_2$ of the photodiode signal

- modulating the sample's position slowly with a depth such that the DC of the spectral decomposition cancels

- in post-processing, eliminating possible DC contributions (as they originate from stray contributions) to retrieve the sample contribution to $X_1 + jY_1$ and $X_2 + jY_2$

- Perform the quadratic sum of R_1 and R_2 to calculate the amplitude of the optical return at the sample

In this section, we have shown that, since different backscattering sources contaminate the measured signal, a specific data processing algorithm (Eq. 5.57) has to be developed, which, with few adjustments in the setup, allows extracting the useful data from the measured signal. The current method allows the measurement of the backscattering from the sample down to the level of $\approx -130dB$ in optical power, limited by the backscattering from the beam dump.

5.4 Measurements

At this stage, the setup is ready for the measurements. In this section, I would like to study the main properties of the coherent scattering – speckle. Speckle is a random interference pattern. First, I would like to show that speckle is observable in our interferometric setup (see Sec. 5.4.1). Then I will study the spatial properties of the speckle in the experiment (see Sec. 5.4.2),

and I will examine amplitude and intensity distribution (see Sec. 7.4), the angular distribution of mean speckle intensity (see Sec. 5.4.4) of the coherent backscattering pattern.

5.4.1   Speckle mapping

Speckle behavior of scattered light is observable when the sample is moved parallel to its optical surface, using the setup shown in Fig. 5.12. For the sample surface, an IR mirror from Edmund Optics has been used (see Sec. 5.2.3). The mirror roughness is probed by a collimated Gaussian beam with size $\omega_0 = 1.71\ mm$ and a full-beam divergence angle of $0.58\ mrad$ (see Sec. 5.2.1). The 2D translation of the sample is carried out by the Newport translation stage (see Sec. 5.2.5) with a scanning step $0.5\ mm$ over a travel distance of $12\ mm$.

The three 2D maps of Fig. 5.29 were recorded with slightly different incidence angles at the sample, explaining why this experiment requires a 2D translation stage with very good angular accuracy and repeatability. Because the change of incidence is small compared to the beam divergence 4, one can follow the correlation between successive scattering maps.
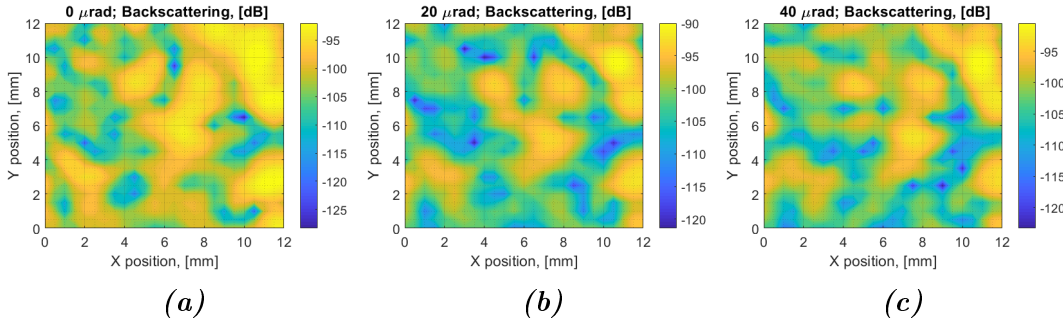
Figure 5.29: 2D maps of the backscattered power (in dB) of the same $12\ mm \times 12\ mm$ area of the sample, an Edmund Optics "infra-red mirror", ref. 47113. The scans differ due to small changes (20 µrad steps) of the $\approx 14^o$ tilt of the sample with respect to the beam. The horizontal and vertical scan step is $0.5\ mm$. The colour scale is indicated at the right of each image, indicating the fraction of power detected by the interferometer.

The ratio between the maximum and minimum scattering points in each of these maps exceeds three orders of magnitude in optical power. On the other hand, the RMS average value of the backscattering fraction for each map changes by a fraction of a dB (98.4, 98, and 98.6 dB, respectively). Backscattering fraction is a fraction of measured power to measured by the normal incidence mirror (retro-reflected).

5.4.2   Dynamical properties of the speckle

If no redistribution of the phase in the random phasor sum is introduced, the resulting (speckle) amplitude of the sum would be constant. In this case, for

LISA, scattering would cause a simple shift of the phase measurements and would be subtracted by the post-processing. But redistribution of the phases in the phasor sum of speckle may be caused by a tilt of the optical surfaces (see Fig. 5.29) can easily arise due to thermal changes in the system, or vibrations.

To study the size of the speckle grain under translation, we perform an experiment described in subsection A. Subsection B is devoted to a complete study of how speckle changes under a tilt of the sample.

A. Speckle grain size under a translation of the sample

As can be noticed in Fig. 5.29, the change of scattering intensity in the map has smooth behavior with a speckle grain size. This grain diameter is compatible with the beam diameter on the sample surface (see Fig. 5.30c). In this setup, the beam diameter is defined by the optical collimator. After replacing the collimator, the beam waist changes from $w_0 = 1.71$ mm to $w_0 = 0.65mm$ (and the divergence increases from 0.58 to 1.51 milliradian). Map measured with $0.25\ mm$ step size and $12 \times 12\ mm^2$ scanning area, shown in Fig. 5.30b, confirms that the grain size is compatible with the spot size at the sample. This is, of course, expected as the beam "samples" an area of the target surface, which is of diameter w_0.

B. Variations of the speckle pattern under a tilt of the sample

The dependence of the measured b_s with the incidence angle also displays a speckle structure. To study the change rate of the speckle intensity under the tilt of the sample, a Picomotors rotational stage was used (see Sec. 5.2.6). The measured speckle amplitude as a function of the tilt angle is given in Fig. 5.31. In this study were used the same two collimators with beam waists 0.65 mm and $1.72mm$.

In Sec. 4.1.3, we had derived that under the tilt of the sample, the speckle grain is $\lambda \cos(\theta_i)/2w$, where θ_i is the incidence angle and $2w$ is the diameter of the beam spot on the sample. If the divergence of the beam is small, $w \approx w_0$. Observations confirm the dependence of the angular grain size as inversely proportional to the beam waist w_0.

Scanning the speckle by the tilt of the surface changes the incidence angle only on a few 10s mrad. It allows us to measure various independent speckle amplitudes (intensities) with about the same experimental parameters. This is essential when the surface of the sample is small, and the translation is impossible. The tilt of the sample will be used in the next experimental setup for the acquisition of the data.

5.4.3   Statistical properties of the speckle

The statistical properties of the speckle were well studied by Goodman in Ref. [23]. He states that the probability density function (PDF) in the ampli-

(a) $\omega_0 = 1.72 \ mm$

(b) $\omega_0 = 0.65 \ mm$

(c)

(d)
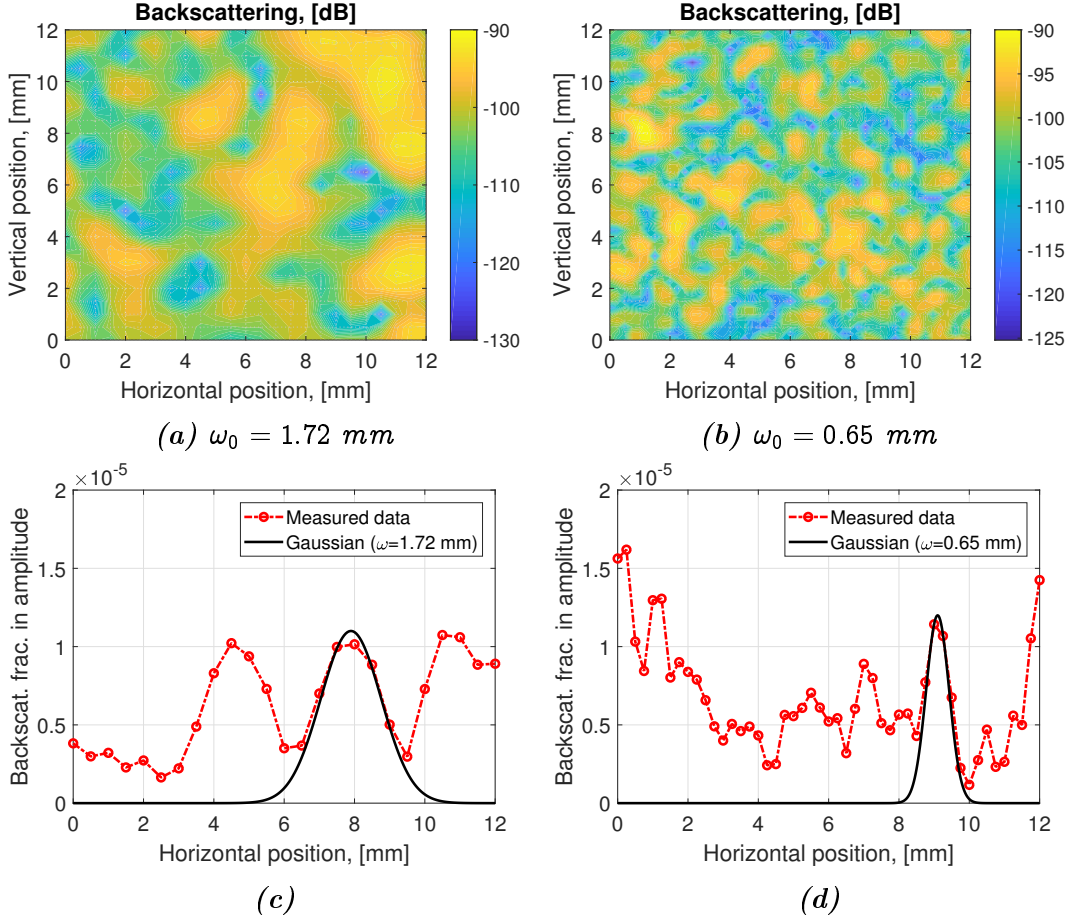
Figure 5.30: *Map of backscattered light with a collimator of 18 mm focal length (a) and 8 mm focal length (b). Profiles of backscattered light from a moderately scattering target (c and d) for the two types of collimator. Black curve (arbitrary units): plotted for comparison, a Gaussian beam profile of the same beam waist (ω_0) as the incident beam. The size of the speckle grain corresponds to the size of the beam.*

tude of the random phasor sum is given by the Rayleigh. distribution:

$$p_A(A) = \frac{A}{\sigma^2} exp\left(-\frac{A^2}{2\sigma^2} \right), \tag{5.58}$$

where σ is a parameter of the distribution. Note that this expression is valid only if the data points are uncorrelated, that is, if the data points are taken with coordinate increments larger than the speckle grain size.

For analysis, we took the backscattering x-y map measured when the collimator provides a beam with a waist of $\omega_0 = 0.65 \ mm$. We assume uniform roughness properties of the sample along with all the surface under test. We sample the measured map (see Fig. 5.32a) with a step of $1mm$. The sampled points are in red circles. The normalized histogram of the sampled amplitudes is given in Fig. 5.32b. The obtained distribution (see Fig. 5.32b) can be described by Eq. 5.58. The parameter σ can be found from mean $\overline{A}$ of the
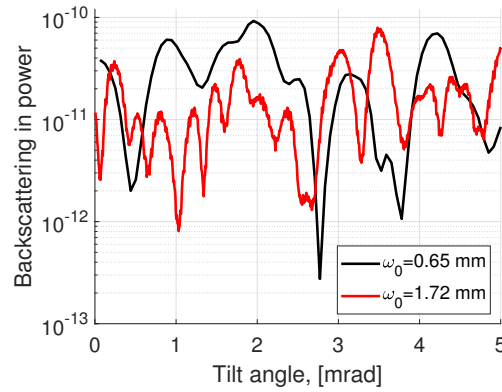
Figure 5.31: Dependence of the coherent backscattering intensity with the tilt angle for two collimators (different beam waist ω_0) used in the experiment.

distribution:

$$\sigma = \sqrt{\frac{2}{\pi}}\overline{A}. \tag{5.59}$$

So, we confirm with experimental data that it's possible to describe the PDF of the speckle amplitudes by a Rayleigh distribution with a single parameter σ. The same result was obtained with the numerical model (see Sec. 4.4.4).
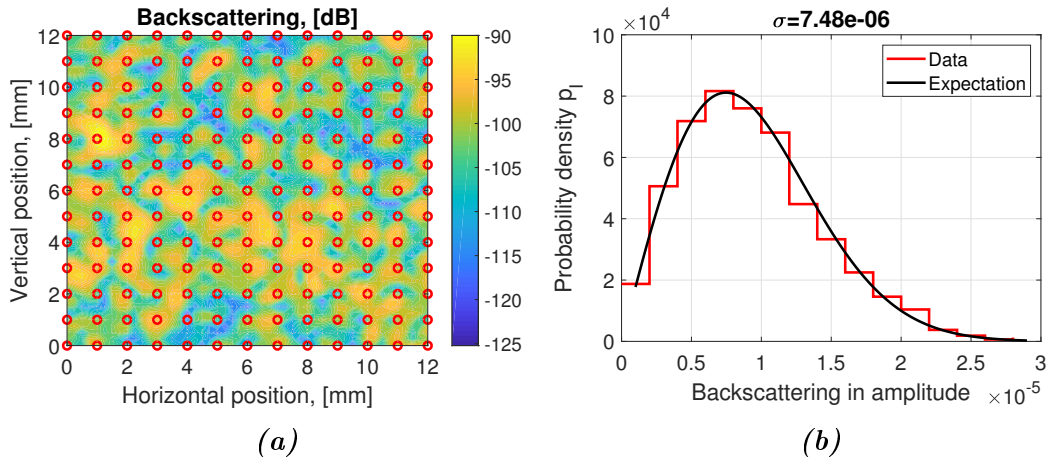
Figure 5.32: In red circles of the backscattering map (a) are sampled points, which were used in the analysis. The histogram of amplitudes of these points (b) with Rayleigh PDF

In Ref. [23] is also given the intensity distribution in the speckle amplitudes:

$$p_I(I) = \frac{1}{\overline{I}}exp\left(-\frac{I}{\overline{I}}\right), \tag{5.60}$$

where intensity $I = A^2$, and $\overline{I} = 2\sigma^2$. In a similar way we found that the measured data (see. Fig. 5.33) confirmed the expectation (Eq. 5.60 and black curve in Fig. 5.33).
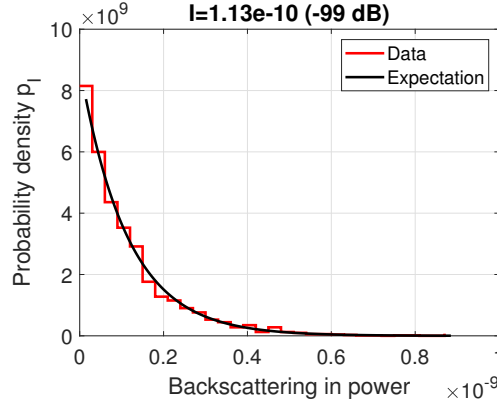
Figure 5.33: Distribution of backscattering intensities in the map and negative exponential distribution (see Eq. 5.60). The black curve is not a fit, but an expected dependency with parameter $\overline{I} = -99$ dB.

Compared to the BRDF approach, which provides only one value for the backscattering, the random phasor approach, with the distribution of possible values, provides a complete description via the probability distribution function. The two approaches agree, as we will show later, in that the scattering intensity obtained under the BRDF approach agrees with the mean value obtained under the random phasor sum approach. Note that the latter predicts a probability of ≈ 0.368 of getting an intensity larger than the mean value of $\overline{I}$.

5.4.4 Angular distribution of the coherent scattering

The common way to describe scattering from a rough surface is to use BRDF. In this study, I used the measurement of the back-scattered power provided by the interferometric set-up to compare with conventional scattered power measurements in directions close to backward. The schema of the setup is given in Fig. 5.34.

The laser beam with wavelength $\lambda = 1.55$ μm, power $P_L = 3.789$ mW, and beam waist $\omega_0 = 0.65$ mm illuminates the sample mirror. In these measurements, I use a 25.4 mm silver coated mirror from Thorlabs (PF10-03-P01). Before the measurements, the mirror was cleaned with "First contact" polymer and acetone.

To perform the measurements of backscattered light, I install the sample with a translation stage on a rotation stage, as shown in Fig. 5.34a. To find the normal incidence, the stage was rotated until the interferometer received maximum reflected power.

For each angle of incidence, the position of the beam dump was individually adjusted to minimize backscattering from it. To measure a speckle-averaged value of b_s, the sample was translated over 12 mm by steps of 0.25 mm in the horizontal direction. For each angle of incidence, the measured backscattering fraction in power b_s was normalized on the detection solid angle Ω_I and cosine
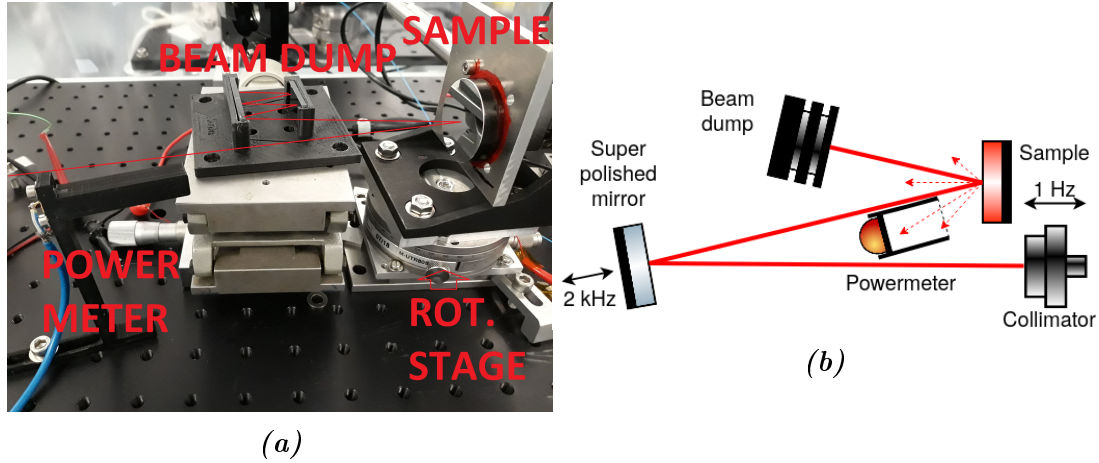
Figure 5.34: Image (a) and schema (b) of the free space part of the setup for the angular distribution study of coherent backscattering. The beam (red line) goes to the sample and is attenuated in the beam dump. Close to the incident beam is the installed sensor of the power meter. To control the angle of incidence, a rotational setup was installed under the sample 2D mount.

of scattering angle θ_s:

$$BRDF = \frac{\overline{b_s}}{cos(\theta_s)d\Omega_I}. \tag{5.61}$$

For the case of backscattering, the incidence angle in absolute value equal to the scattering angle. The solid angle Ω_I, in which the interferometer receives the backscattered light, is:

$$\Omega_I = \pi(BD)^2 = 1.8 \times 10^{-6} \ srad, \tag{5.62}$$

where $BD = 0.76 \ mrad$ is the beam half-divergence. Simultaneously, a power-meter was measuring, close to backward, the scattered light without attenuation or focusing optics. The detector of the power meter was installed in a plastic 3D printed holder (see Fig. 5.34a). This allows installing the power meter close to the laser beam. The aim of the long squared tube in front of the detector is to reduce the background light down to 0.21 nW. This value was stable enough that the subtraction could be made with confidence. The active area of the detector is a circle with a $d = 3 \ mm$ diameter. The distance to the sensor is $L = 190 \ mm$. This distance was chosen for the reason to be close to the scattering object without obstructing the beam. Before the measurements, the power meter was aligned on the beam spot on the sample.

BRDF of power meter measurements was calculated as:

$$BRDF = \frac{P_{PM}}{P_L cos(\theta_s)\Omega_{PM}}, \tag{5.63}$$

where P_{PM} is power measured with the power meter, and $d\Omega_{PM}$ is the solid angle of the detection for the power meter. Then solid angle Ω_{PM} in which

detector of power meter receive scattered light is:

$$\Omega_{PM} = \frac{\pi d^2/4}{L^2} = 195.8 \times 10^{-6} \ srad. \tag{5.64}$$

To calibrate the power meter, I had used surface and volume scattering targets. The surface scattering target is the UIRT-94-020 Diffuse reflectance panel for calibrating NIR-MIR instruments. Volume scattering target SRS-99-010 is Lambertian scatterer with reflectance 99% (white). Back-scattering from volume scattering target almost don't depend on the angle. The measured BRDF for these two targets is given in Fig. 5.35. The measured scattering for volume scatterer is in agreement with expected dependence (blue dashed in Fig. 5.35). Slightly higher measured level maybe be caused be rescattering from other surfaces, as it is hard to efficiently dump a diffused beam.
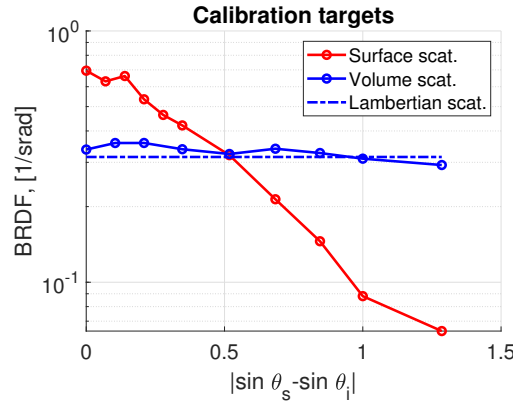
Figure 5.35: BRDF of the surface and volume scattering targets measured with the power meter.

The result of the measurements for two methods is given in Fig. 5.36b. The values of BRDF measured with the two approaches are about the same, as was expected (see Sec. 4.4.3). The difference for some points may be explained by the fact that the power meter is installed under $\approx 5^o$ angle from the exact backscattering direction.

From this, we can conclude that the value of scattering measured with a power meter is approximately the same as the average value of the backscattering intensity measured with an interferometer. This is expected in the case the power meter measurement is made with a relatively large sensor: here, the solid angle of the power meter sensor (2×10^{-4} steradian) is large enough that it averages many speckle grains.

5.5   Conclusion

We have developed a setup and data processing for the measurements of the backscattered light from an imperfect surface with a view at the scattered light issues in the LISA mission. The setup is capable of measuring backscattering fraction in power down to $-130 \ dB$ at 1.55 μm wavelength.
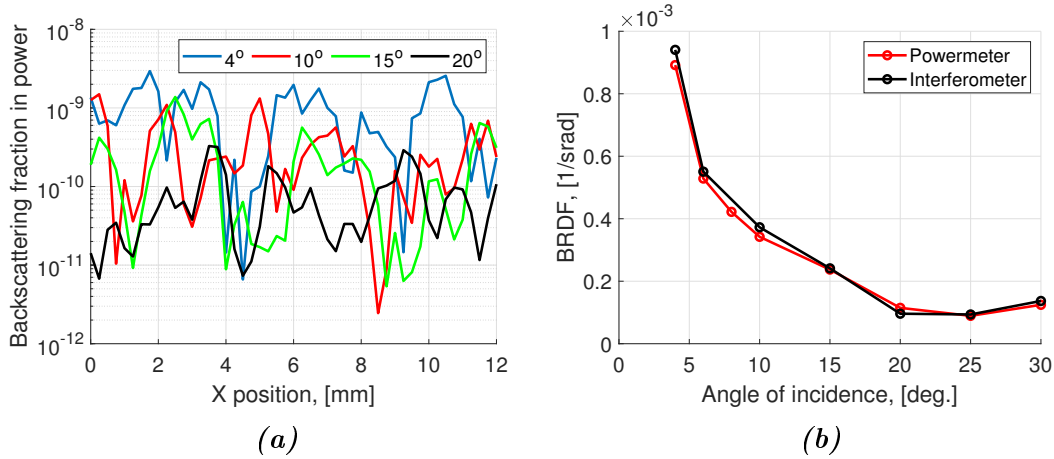
Figure 5.36: The backscattering fraction in power b_s measured with an interferometer by scanning one row of the sample mirror for different incidence angles (a). Angular distribution (BRDF) measured with interferometer and power meter (b).

We have studied scattered light from an IR mirror with intermediate roughness. We have observed that:

1. Speckle is observable with an interferometric setup.

2. Speckle size, in the case of sample translation and tilt, are expected from the optical properties of the system.

3. Amplitude and intensity distribution can be described by Rayleigh and negative exponential distribution, respectively.

4. BRDF measured with an interferometer converges to the conventional BRDF when taking averages.

So basically, a BRDF is a simplified case of coherent scattering. Only in case of some averaging: over detector surface, long exposure time in unstable setup, multiple wavelengths, or polarization, the mean intensity of the speckle reduces the value given by the conventional roughness. Speckle behavior can be observable in narrowband optical measurements (interferometric, high spectral, or angular resolution), fast measurements (when any averaging have no time to be performed), or in one with relatively small detector area, with low nominal intensity, etc. The usage of BRDF for interferometric systems with narrow laser bandwidth and single polarization maybe be inappropriate. It cannot describe rapid changes of intensity in the system caused by speckle. These rapid changes are caused by the reconfiguration of phases in a random phasor sum. In turn, this reconfiguration is caused by displacement (mechanical, thermal, vibrational) or other changes in the optical system, and it has a specific change rate.

The setup was a preliminary version of backscattering measurements setup at 1.06 μm (the wavelength of LISA). The experience and data processing

routines obtained during the development of this device will be used in the next setup.

Chapter 6

Experimental setup at 1.06 μm

The setup of coherent backscattering measurements at 1.55 μm (see Chapter 5) was a forerunner of an improved setup at 1.064 μm. The motivation to build a new setup at 1.064 μm is caused by the LISA instrument. As was mentioned in the previous chapters, the working optical frequency of LISA is 1.064 μm, so it is necessary to measure and describe the coherent effects of scattering at this wavelength as well. Moreover, components that have very different behavior at 1.06 μm and 1.55 μm (multilayer mirrors, for instance) must obviously be tested at their design wavelength.

The schema of the new setup at 1.064 μm (see Sec. 6.1) is identical to the one described in Chapter 5, except that the laser source and all fibered components are at the 1.064 μm wavelength. The very first step of the development was to measure and check the transmission and reflection of all components before the assembly of the setup. A number of other tests and verification was performed to achieve the best performance of the setup: measurements of the beam waist and laser noise, calibration. Numerous mechanical components were designed and manufactured for the free space part of the setup. Some of the elements (holders, interfaces) were 3D printed. Amplifiers for photodiodes were made in the ARTEMIS laboratory as well.

During the test and verification phase, we have found that some of the devices do not satisfy the requirements. A home-made power-meter, not good enough for the low fluxes of the scattered light, had to be redesigned. The driver of the laser diode, not stable enough, had to be replaced by a stable current driver. One problem, however, deserves attention. I explain in Sec. 6.14 that no solution could be found to the polarization imperfections on the setup. I will present the discussion I made of the polarization problem, with the hope that it could apply to other situations.

In the final section 6.3, I discuss the main results achieved with this setup. The first and second-order statistical analysis was performed to analyze the measured data. The BRDF of our test sample, an "infra-red mirror" (see Sec. 5.2.3), measured with the interferometric method was compared and verified with conventional power meter measurements. The noise floor of backscattering measurements was studied.

6.1 Description of the setup

The schema of the setup (see Fig. 6.1) is similar to the setup at 1.55 μm. However, the configuration of some of the components was improved. The basis
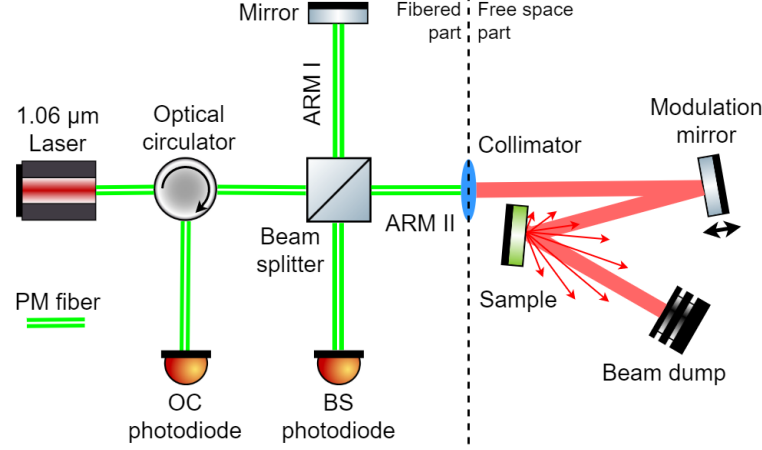
Figure 6.1: Schema of the interferometric setup for coherent backscattering measurements. Green: PM optical fibers. Red: free-space beams. Thin red arrows: scattered light from the sample.

for the setup is the fibered Michelson interferometer. All the fibers used in the setup are polarization-maintaining (PM) fibers. The laser beam at wavelength 1.064 μm passes through an optical circulator and then is divided into two by a fibered beam splitter. One arm of the interferometer is terminated by a PM fiber mirror. Another arm of the setup contains a free space part. The collimated beam in the free space part is modulated by a super polished mirror and then is directed to the reflective surface under test. The reflected beam is absorbed by the beam dump, while a small fraction of backscattered light couples back into the fiber, and then it interferes with the reference beam in ARM I on the two photodiodes connected to the optical circulator and the beam splitter. The photodiodes signals are demodulated by the same lock-in detector (see Sec. 5.1.3) as with the 1.55 setup. The signal is recorded on the PC and analyzed with the same procedure as described in Sec 5.3.

The image of the free space setup is shown in Fig. 6.2. The length of the beam path from the collimator end to the sample is 82 cm. The position of the collimator can be adjusted to minimize the frequency noise. The distance between the sample and the power meter photodiode is 20 cm. This is the minimal distance that still allows installing the beam dump in front of the sample. The incidence angle on the modulation mirror is 10 deg. This angle is minimized to increase the modulation depth. The height of the beam is mainly defined by the stage on which the sample is installed. This stage has a complex structure, as it requires: translation stage with a piezo for slow modulation; rotation stage for wide incidence angle measurements; Picomotor tilt stage (for one and 2-inch samples) and the axis of rotation should be in the plane of the mirror. All the mechanical support and interfaces were manufactured in the ARTEMIS workshop by the author of the thesis.
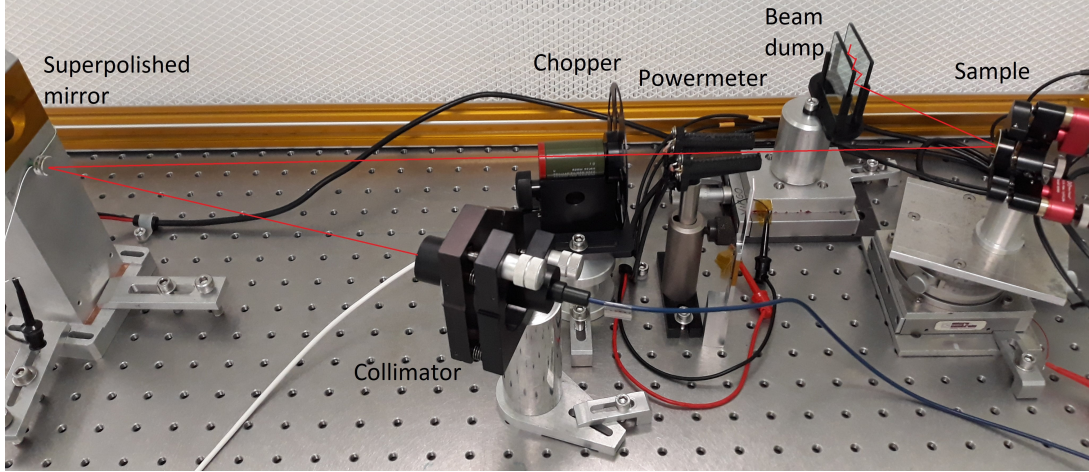
Figure 6.2: The free space part. The red line indicates the approximate beam path. The collimated beam is modulated on the super-polished mirror and then illuminates the sample. The beam reflected from the sample is directed to the beam dump where it is absorbed. The two-sensor power-meter is used to measure backscattering in two directions symmetric with respect to back-ward.

6.1.1 Laser

Contrary to the 1.55 μm laser, which is a self-contained RIO Orion diode laser with a very stable current source, hence very good frequency noise characteristics, the 1.064 μm is an RIO Planex laser, which requires an external laser driver. In the setup, we use RIO Planex 1064.4 laser with the Vescent D2-105[1] driver. During operation, the temperature of the laser is stabilized on 28.5 $°C$ using the Peltier module provided in the Planex package. The output power is not a smooth function of the input pump current, but it has mode jumps, as shown in Fig. 6.3. On the same plot is given a photocurrent of the built-in photodiode. In the figure are present two-mode jumps at 38 mA and 104 mA. The next mode jump is at 152.5 mA.

The study of the laser diode characteristics was done up to 120 mA. The first attempt was to use a working point at 90 mA. This point is a dozen milliamperes away from the nearest mode jump, in order to allow for a stable regime of operation. However, at 90 mA, the laser intensity noise is not yet dominant with respect to the electronics noise and that I can get a better noise floor by increasing the laser power even more. The new working point was set at 150 mA, which is also sufficiently far away from a mode hop, and provides a better noise floor in the measurements, as compared to 90 mA.

In the frame of interferometric measurements, the frequency and intensity noises of the laser diode are important. Below, I describe the method for the frequency noise power spectrum density (PSD) measurements and present the

---

[1]The Vescent D2-105 is based on the Libbrecht-Hall circuit, and it is a precision diode laser current source, with noise $< 100~pA/\sqrt{Hz}$.
https://www.vescent.com/products/electronics/d2-105-laser-controller/
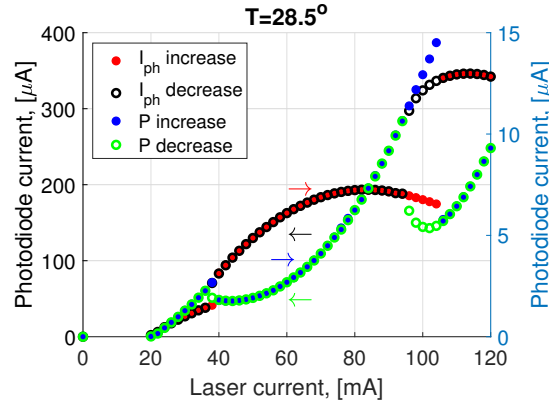
Figure 6.3: Output laser power as a function of the pump current

obtained results.

Method of the frequency noise PSD measurements

For the measurements of the frequency noise of the laser, an interferometric setup is required. We built an interferometric setup as shown in Fig. 6.4. The imbalance of the arms of the interferometer is $\Delta L = 25\ m$. The setup is fully fibered in it is thermally isolated.
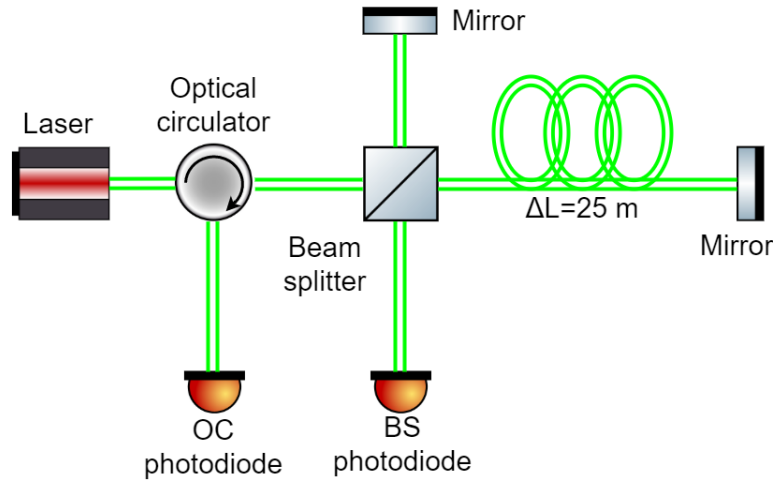
Figure 6.4: Fully fibered setup for laser optical frequency noise measurements. Double green line is a PM fiber.

Let us consider AC part of the interferometric signal measured with this setup:

$$V = \frac{A}{2} \cos\left(2\pi\nu\frac{2n\Delta L}{c} + \phi\right), \tag{6.1}$$

where A is amplitude of the signal, ν is optical frequency, ΔL is the path difference between the two arms of the interferometer, n is refractive index of the fiber. The free spectral range (FSR) is $\frac{c}{2n\Delta L}$, where c is the speed of light.

The derivative of the interferometric signal gives:

$$\frac{dV}{d\nu} = \frac{A}{2}\frac{2\pi}{FSR}\sin\left(2\pi\nu\frac{2n\Delta L}{c} + \phi\right). \tag{6.2}$$

If the setup is stable, we chose the phase ϕ such that $2\pi\nu\frac{2n\Delta L}{c} + \phi \approx \pi/2$. Then $dV = A\pi/FSR \cdot d\nu$ or in other form:

$$d\nu = \frac{dV}{A\pi} \times FSR, \tag{6.3}$$

so using this expression we can link the measured PSD in $[V/\sqrt{Hz}]$ and the Laser Frequency noise expressed in $[Hz/\sqrt{Hz}]$.

Frequency noise measurement

At first, let us calculate the free spectral range. The FSR for arms disbalance of $\Delta L = 25\ m$ is $FSR = \frac{c}{2 \cdot n \cdot \Delta L} = 4.17\ [MHz]$. Here was used that the refractive index of the PM fiber, which was used in the setup, is $n = 1.44$.

The noise in the laser optical frequency was observed to be excessive when the current driver used to power the laser was the Wieserlabs current driver.The reason for this was the bad settings of the PID temperature controller of the previously used Wieserlabs laser driver. That was the reason to switch on Vescent D2105 driver.

We have used several methods to measure PSD of the photodiode interferometric signal. One is with spectrum analyzed, and the other is with an oscilloscope and periodogram calculation with a Hamming window in Matlab. The two methods converge (see Fig. 6.5). The RSM value of noise at 2 kHz
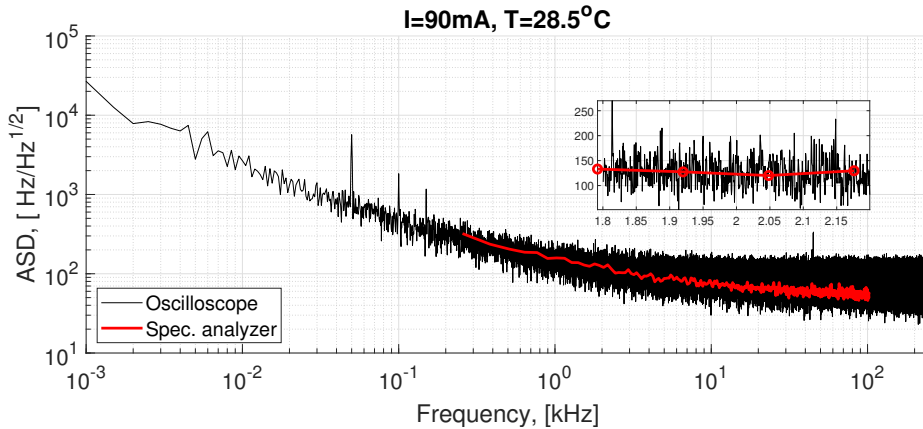
Figure 6.5: Laser frequency noise measured by two methods

in the bandwidth of 10 Hz is 403.25 Hz. Using this, we can estimate laser frequency noise for a 1 cm imbalance in the air (for example) in the setup. In this case, $FSR = 15\ GHz$, so $403.25\ Hz/15\ GHz \times \pi = 8.45e - 8$ is sufficient for the measurements.

Intensity noise

The laser intensity noise will directly add to the noise in the measurements, so we need to assess its importance. The RIN (relative intensity noise) was measured with a photodiode connected to the output of the laser diode. An attenuator of 12 dB was used to prevent saturation in the photodiode. The signal was measured with an oscilloscope, and the analysis of it was performed in MATLAB. Laser intensity noise was measured for the different currents of the laser diode. The noise at high frequencies may be dominated by the oscilloscope noise. In Fig. 6.6 is shown relative intensity noise (normalized by power).
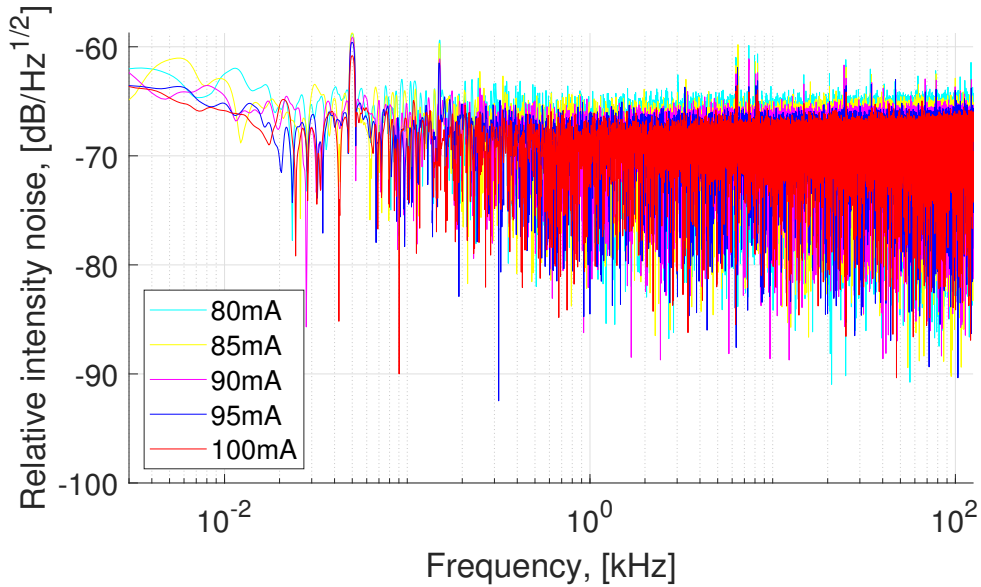
Figure 6.6: Relative intensity noise of the laser diode. The noise of the amplifier was subtracted.

Part of this noise came from the current noise of the Vescent D2-105 driver. At 2 kHz it have noise of $8 \times 10^{-11} A/\sqrt{Hz}$. With bandwidth 10 Hz and pump current 90 mA, we have the relative intensity noise due to current noise is $\frac{8 \cdot 10^{-11} \times \sqrt{10}}{90 \cdot 10^{-3}} = 2.7 \cdot 10^{-9}$. While the current noise contribution is relatively small, the measured relative intensity noise at 90 mA in the bandwidth of 10 Hz is $5.7 \cdot 10^{-7}$ One of the possible explanations can be frequency to intensity noise coupling. The more probable is the domination of input oscilloscope noise in the measured spectrum.

The measured values of the frequency and intensity noises are sufficient for precise interferometric measurements of backscattering because the level of the lowest backscattering amplitude, which is desired to be measure is $10^{-6} - 10^{-7}$.

6.1.2 Collimators tests

Collimators are a crucial component of the setup. It is essential to check the divergence of the collimated beam all along the double path to the target, when

measuring the specular reflection from the target, for calibration of the measurement chain. For the 1.064 μm setup, we have ordered the manufacturing of two collimators at Anylink with beam waist 1 mm and 2 mm at approximate working distance 0.9 m. Specified in the datasheet beam diameter at 0.9 m working distance was 1.2 mm and 2.3 mm for collimator S/N 1718176 and S/N 1718177, respectively. We ordered pigtailed collimators, for better repeatability, rather than receptacle collimators.

To measure the beam waist, I use a WinCamD UCD12 camera. The camera was equipped with DataRay software, which determines the size of the beam in the two transverse directions (major and minor axes) and effective diameter (diameter of a circle that contains 86.5% of the total power of the laser beam). Laser settings were 45 mA at 22° C. The measurement was performed for several collimators - camera separation (see Fig. 6.7. The measured values of the effective beam diameters are 1.11 mm and 2.28 mm, respectively. The
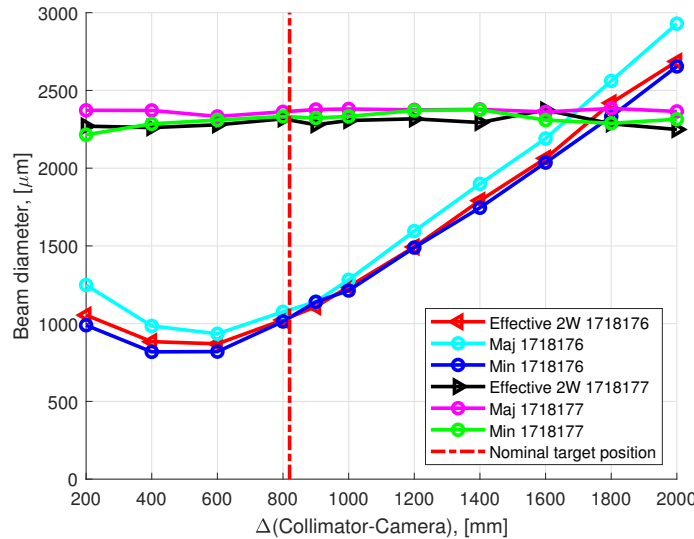
Figure 6.7: The result of the effective beam diameter measurements.

collimator S/N 1718176 has a focus at 504 mm and effective beam diameter 0.88 mm at this point. The collimator S/N 1718177 has low beam divergence and is the most suitable for backscattering measurements. Low divergence also allows acquiring sufficient speckle statistics in a small tilt angle (see. Sec 6.3.1).

6.1.3 Calibration

As in the previous setup, the calibration is a necessary part of the system validation.

The schema of the signal pick-up is shown in Fig. 6.8, and it is essentially the same as before. For calibration purposes, a mirror at normal incidence was installed in the free space part of the setup. The interference signal is measured by biased +5V photodiodes connected to the outputs of the optical circulator and beam splitter. I assume that the two photodiodes are identical,
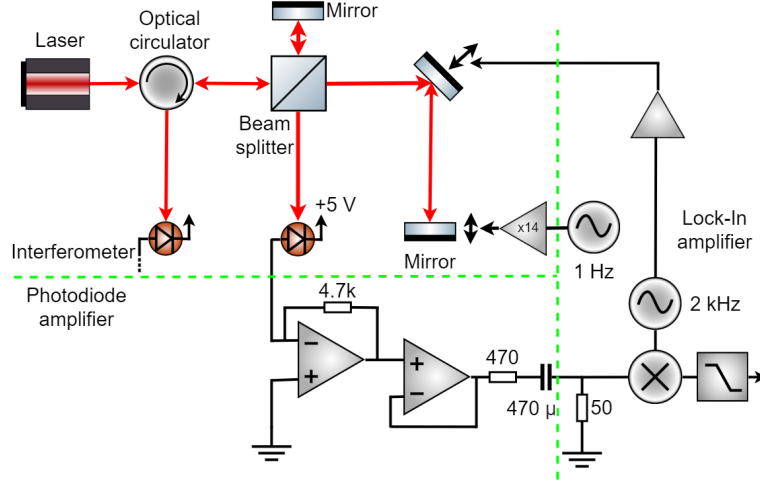
Figure 6.8: The schema of the optical and electrical signal path for calibration of the setup. Three main parts are separated by the dashed green line. The optical part of the setup (interferometer) conserves full optical power inside the setup. The optical power on the photodiode is transformed into an electrical signal by the amplifier. The signal is analyzed with the lock-in amplifier.

and the two signal paths as well. So I will describe only one of them. The received optical power is converted to the photocurrent with a coefficient of 0.567 A/W. The first stage of the amplifier converts the current to voltage $V = 4.7$ $k\Omega \times photocurrent$. The converter is made on the OP470 operational amplifier. The second stage is voltage repeater with a limiting resistor of 470 Ω to drive a 50 Ω load. The unused amplifiers of the chip were shortened to reduce noise. The capacitor on the input of the lock-in amplifier blocks the DC component of the signal. The interferometric signal is mixed with a reference signal with an amplitude $\sqrt{2}$ of the lock-in amplifier. The mixed-signal passes through low pass filter and so demodulated. The frequency of the demodulation is equal to the modulation frequency of the piezo modulation mirror (2 kHz). Having this information, we can calculate that the calibration coefficient of the demodulated amplitude to input optical power is:

$$0.567 \left[\frac{A}{W}\right] \times 47000 \left[\frac{V}{A}\right] \times \frac{50}{470 + 50} \times \frac{1}{\sqrt{2}} = 181.16 \frac{V}{W}. \qquad (6.4)$$

This allows performing crosscheck of the measured amplitude with a lock-in amplifier under full reflection condition and optical power measured with a fiber power meter.

Optical power measured with a fiber power meter before the collimator is 3.3 mW. Taking account losses and coupling ratio in the beam splitter, then the optical power at the input of the beam splitter is $I_{in} = 3.3$ $mW/0.416 = 7.93$ mW.

From the other side, the photodiode signal is measured with the lock-in amplifier. To exploit this number, we need to take into account the reflection coefficient of the aluminum mirror at 1.06 μm is 0.85 (measured value).

The beam performs three reflections in the free space part. The demodulated amplitude is 0.3682 V, so the power at the input of the beam splitter is:

$$P_{in} = \frac{0.3682 \ V}{181.16 \ V/W \times 2 \times 0.416^2 \times \sqrt{0.85^3}} = 7.49 \ mW. \tag{6.5}$$

This value is in agreement with the previous method. The small difference is caused by losses in the collimator, which was not taken into account.

6.1.4 Modulation voltage adjustments

Apart from the sample, other components in the beamline scatter as well. This causes difficulties in interpreting the measured signal. To solve this problem, in section 5.3 was proposed a method of Fourier analysis of the demodulated signal. To make this method works, the sample should be modulated at low frequency with a certain amplitude. The goal of this section is to correctly adjust this amplitude to achieve the best performance.

The modulation depth is $\frac{2\pi}{\lambda}\Delta\cos\alpha$, where λ is the optical wavelength, α is the incidence angle, and Δ is path modulation of the used piezo modulator (Thorlabs PA44LEW). The path of modulation δ is proportional to the value of the voltage V applied to the piezo, choosen such that $J_0(x(V)) = 0$ (see Sec. 5.3). So calibration (Bessel value vs. amplitude of the modulation voltage) is required.

For the experiment, I use the same configuration of the setup as in Fig. 6.8. The sample is at normal incidence, so $\alpha = 0$. The spectrum of the first harmonic of the demodulated amplitude is given in Fig. 6.9a. The shape of the
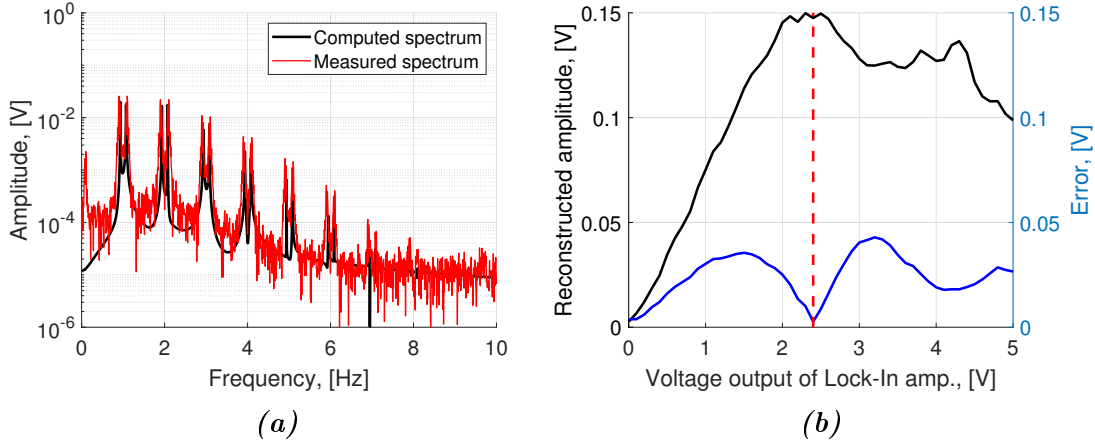
Figure 6.9: The optimal Fourier spectrum of the demodulated signal for the first harmonic and for the optimal modulation volatge (a) and the reconstructed demodulated amplitude with the error as a function of the applied modulation voltage (b).

spectrum is well known, and it can be described with three parameters: reconstructed amplitude, thermal change rate, and slow modulation depth δ. The computed spectrum with well-adjusted parameters is given in black in

Fig. 6.9a. At very low frequencies, there is a peak that was not described by the computed spectrum because it has different nature (stray light of the other components in the interferometer, placed before the sample). As was discussed in section 5.3, the idea of this spectrum analysis is to cut this contribution. In this particular case, it is straightforward, because all the spectral contribution which comes from the sample are at higher frequencies and stray light contributions are at low frequency. The demodulated amplitude of the signal with a removed low-frequency part (below 0.5 Hz) is given in black in Fig. 6.9b as a function of the applied modulation voltage. When the modulation voltage is well adjusted, the spectral component is distributed over high harmonics, and all the amplitude is reconstructed (maximum on the curve). This also corresponds to the minimum of the error of the reconstructed amplitude (blue in Fig. 6.9b). When the modulation voltage is not well adjusted, there is some contribution at zero frequency, which is not separable from stray light and so it is removed by the algorithm. Based on these data, I found that the optimal modulation voltage at the output of the lock-in amplifier is 2.4 V.

6.1.5   Beam dump

As the new setup works at 1.064 μm, so new efficient beam dump is required. For this setup, we have developed two beam dumps. As before, they consist of two plates with proper polishing. However, the plates are not parallel anymore. An angle of 3 deg between them was used to increase the number of interaction points and so increase the incident angle. A higher incident angle causes lower backscattering (see Sec. 5.4.4). The designed incident angle is 45 deg instead of 15 deg for the first versions. The material of the plates to the first beam dump is HA15 (heat absorbing) Hoya glass, and for the other is a silicon wafer (super-polished Si wafers are mass-produced for the electronics industry). The measured backscattering of the HA15 beam dump is lower that -125 dB (will be discussed later). And the measured backscattering of Si beam dump is -115 dB. Later in the experiment, we will use only the HA15 beam dump.

The measurement of a faint backscattering signal requires some confidence that the measured signal still has optical nature. In Sec. 5.1.4, I have proposed a method based on correlation function to verify the validity of the data. To measure the backscattering of the beam dumps, I used the setup, as shown in Fig. 6.1. In Fig. 6.10a is the example of the backscattered fraction (BSF) in amplitude measured for a certain tilt range of the sample (mirror). The red line in Fig. 6.10a corresponded to the case when the sample was modulated, and the black line corresponds to the case when the beam dump was modulated. In the same conditions, I plot the correlation of first and second demodulated amplitudes as a function of the BSF in amplitude(see Fig. 6.10b). If the data is good, the correlation is high and vice versa. If the data is dominated by noise, the correlation is 0 or even negative. In Fig. 6.10b, the data follows a step function and has a turn below 10^{-6} (-120 dB), so the backscattering from the beam dump is lower than instrumental noise of the system. It's to say that the measured signal interpreted as backscattering from the HA15 beam dump
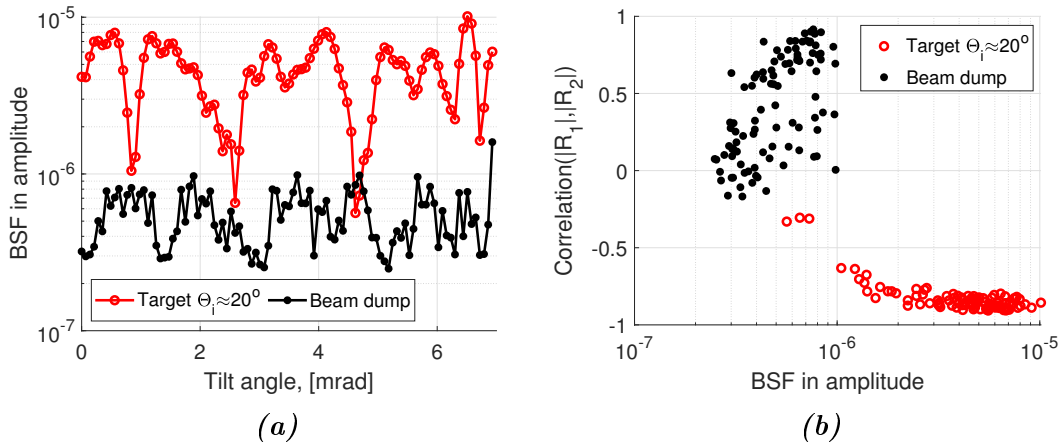
Figure 6.10: *The measured backscattering from the sample (in red) and beam dump (in black) as a function of sample tilt angle (a) and the same data plotted with correlation coefficient (b) to verify the optical properties of the measured signal.*

has not the signature of backscattering, and it is rather noisy. So the value of backscattering given at the top of the section is on the upper value of the real backscattering from the beam dump. That means that the HA15 beam dump is very efficient in terms of backscattering, despite the fact that we use it as delivered, without super-polishing.

6.1.6 The noise in the measurements

The last step is to identify the limiting factor of the measurements. To do this, I compare the spectra of the demodulated amplitude under different conditions. Each of the spectrum presented in Fig. 6.11 is an average of more than ten Fourier spectra. This was done to reduce data noise. Also, each spectrum was taken at working point (28.5 $°C$, 150 mA) of the laser and normalized by a calibration value of full retroreflectance.

Four cases were considered. The first case is when the laser beam is reflected from the sample into the beam dump, and the sample position is modulated (green in Fig. 6.11). This spectrum contains all the contributions (stray light signal from the components of the setup, modulated scattered signal from the sample, laser, and electronics noise). The second case is similar, except the beam dump is modulated and not the sample (black in Fig. 6.11). The modulated peaks are not visible, so the backscattering contribution from the beam dump is minimal. The third case is when the laser beam is terminated in the beam dump (red in Fig. 6.11), the spectrum of the signal contains laser noise and backscattering from components in the beamline. The backscattering is at low (thermal drift) frequencies. The fourth case is when the laser is turned off, and the spectrum represents electronics noise only (blue in Fig. 6.11). The spectrum at high frequencies (1 Hz and higher) of the third and fourth cases is about the same; the contribution of the laser noise is small.
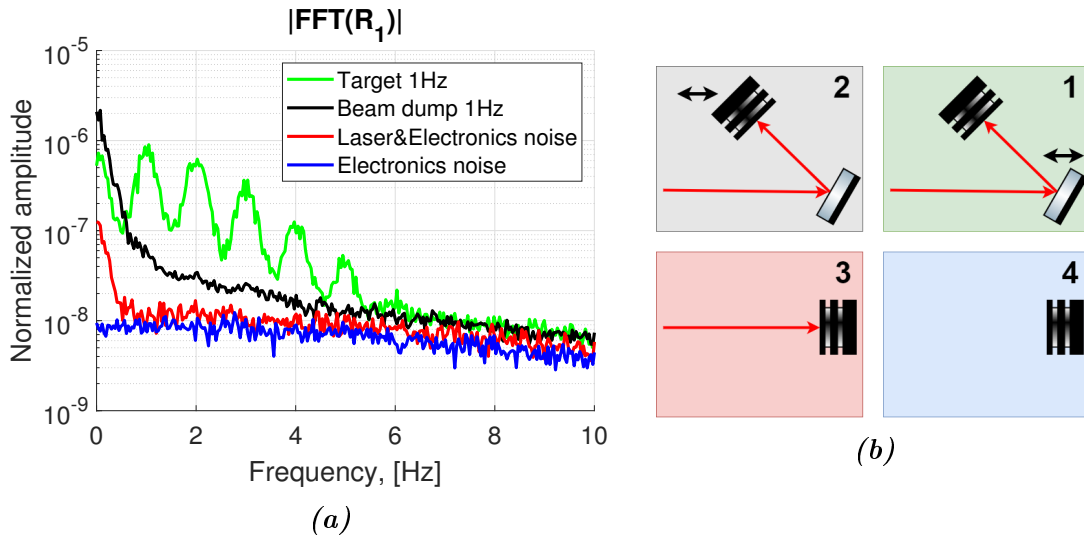
Figure 6.11: The noise spectra (a) measured under various condition (b): blue − no laser beam (Electronics is on); red − beam goes directly to HA15 beam dump (no reflection or back-scattering from the target); black − beam reflects from the target and goes to the beam dump (BD modulated at 1 Hz); green − target mirror slow modulation at 1 Hz.

So the floor of the measurements is close to the electronics and laser noise of the system.

6.2 Polarization problem

As was described in chapter 2, the transmitted and received beams in the LISA telescope will be in crossed polarization. This allows us to improve the signature of the measurement of the science interferometer heterodyne beat note using a polarization beam splitter (PBS), which rejects, to a large extent, backscattered Tx light. However, if the transmitted beam scatters in the crossed polarization, it can spoil phase measurements. So the measurements of backscattering in crossed polarization are desirable. In principle, it can be realized with the interferometric setup described above. The only change to do is to replace the fibered mirror in one of the arms of the interferometer by a 90° Faraday mirror (see Fig. 6.12).

The polarization vector of the light reflected from the normal mirror is turned on 180°. As opposed to an ordinary mirror, the polarization of light reflected by a Faraday mirror is turned by 90° (blue line in Fig. 6.12) with respect to light incident on the sample (red in Fig. 6.12). This beam will interfere with backscattered light in crossed polarization and will be measured by the photodiode. In the proposed setup with the Faraday mirror, the backscattered light in the incident polarization will not cause any interferometric effect.

However, if mixing of the polarization appears in the setup, the results of the measurements are hard to interpret. This can happen as a result of polarization
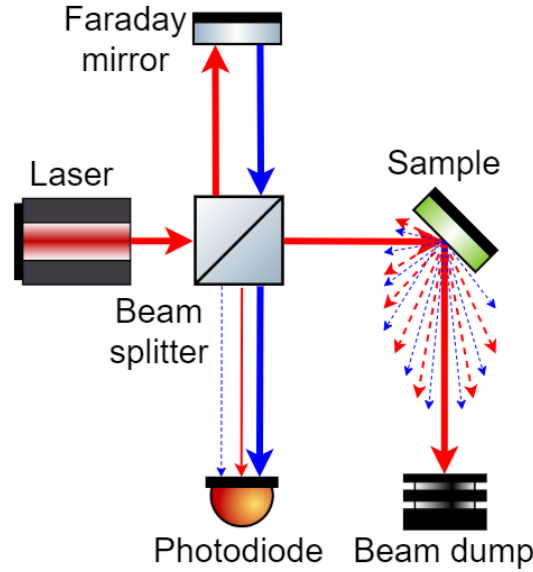
Figure 6.12: Interferometric setup for measurements of backscattering in crossed polarization. Blue and red colors represent crossed and straight polarizations respectively.

vector rotation in the optical components of the setup or the optical fibers.

As an example, we use the setup as in Fig. 6.12, except the beam dump, replaced by a mirror at normal incidence. The demodulated amplitude of the two photodiodes, recorded with the lock-in amplifier, is given in Fig. 6.13. The demodulated amplitude of the OC (optical circulator) photodiode is quite
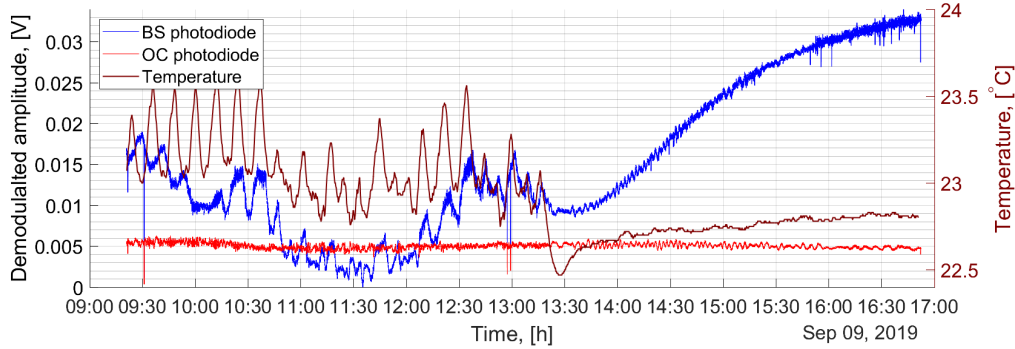
Figure 6.13: Illustration of the polarization problem. The demodulated signal of the OC photodiode (red curve) is stable in time. However, the demodulated signal from the BS photodiode (blue curve) is temperature-sensitive (brown curve).

stable in time, as expected. However, the amplitude of the BS photodiode is changing in a wide range of amplitudes. These changes are quite correlated with temperature recorded near the setup. This phenomena makes impossible backscattering measurements in crossed polarization and need to be investigated.

To study the polarization mixing problem, few simple checks can be done.

For these checks, we use a fully fibered setup, as shown in Fig. 6.14. It turns
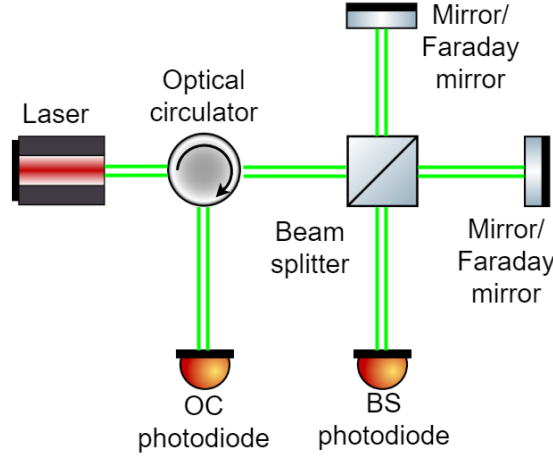
Figure 6.14: Setup for the investigation of the polarization mixing problem. The double green line is a PM optical fiber

out that the optical circulator is of the "fast axis blocked" type. It means that only light with polarization aligned along the slow axis can propagate in it. It has two consequences: the light, which exits the optical circulator, has a polarization aligned along the slow axis, and the interference measured by the photodiode connected to the optical circulator is in single-polarization too and cannot observe the crossed-polarization interference. Of course, the beam splitter has no blocked axis and can measure interference in both polarizations.

The possible configurations of the setup to investigate the problem are:

1. Both arms of the interferometer are terminated by ordinary mirrors. In this case, strong interferometric signals are observed on both photodiodes (see Sec. 6.2.1).

2. Both arms of the interferometer are terminated by the Faraday mirrors. In this case, full interference is observed only on the photodiode connected to the beam splitter, and on the OC photodiode, the signal is 0 (see Sec. 6.2.2).

3. The Faraday mirror terminates one of the arms, and the normal mirror terminates the other. In this case, if everything is nominal, no interference is expected, on any of the two photodiodes: no photocurrent in the OC photodiode, a constant photocurrent in the BS should be strictly constant even in the presence of thermal drifts (see Sec. 6.2.3).

As we work with mirror reflections, the signal is going to be strong. So we would not use a modulator, and the signal would be observed with an oscilloscope, which gives an advantage of measurements of the DC component of the signal.

6.2.1   Case 1: two normal mirrors

Let us consider the case when two of the interferometer arms are terminated by the normal mirrors (see Fig. 6.15a). In this case, the polarization vector before and after reflection is mainly aligned along the slow axis of the optical fiber. The recorded signal of both photodiodes in this configuration is given in Fig. 6.15b.

(a)	(b)
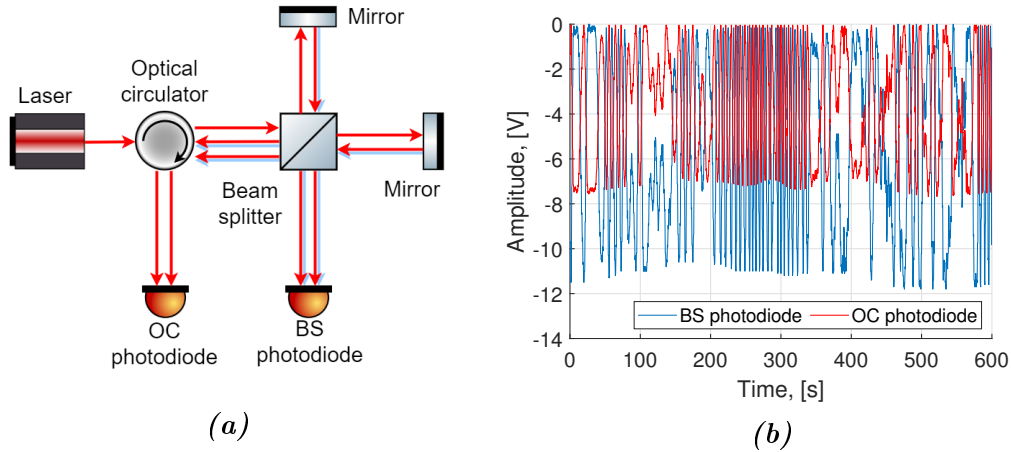
Figure 6.15: Schema of experimental setup # 1. (a). Red arrows correspond to the polarization vector aligned along the slow axis and blue – along the fast axis. The recorded signal of the two photodiodes during 10 minutes (b).

The signal on the OC photodiode (red in Fig. 6.15b) is lower in amplitude due to losses in the optical circulator. The sign of both signals is opposite due to energy conservation law. However the fluctuation of the amplitudes is out of frame of a simple two beam interference model. Also the observed signal of the OC photodiode always reaches zero, while the signal of the BS photodiode (blue in Fig. 6.15b) does not.

To explain this phenomena I will introduce a model with following assumptions:

- The phenomena is caused by addition of two interference patterns on the photodiode surface corresponding to the two polarizations.

- Optical circulator completely blocks that component of the polarization which is aligned along the fast axis.

- Laser emits only in one polarization (or, equivalent: at the output of the optical circulator, only one polarization, slow axis, is launched towards the beam splitter).

- Presence of the other polarization component on the photodiode is caused by rotation of the polarization vector in the setup (the exact place of rotation will be suggested later in this section).

- The system is symmetrical (two arms of the interferometer are the same).

Based on these assumptions, let us consider a small tilt in the polarization in the beam reflected by the mirror (however, I assume that polarization happens inside the fiber and not in the mirror):

$$\frac{A}{2}\cos(\alpha)\hat{s} + \frac{A}{2}\sin(\alpha)\hat{f}, \tag{6.6}$$

where $\hat{s}$ is slow axis and $\hat{f}$ is fast axis, A is amplitude of the input beam and α is angle of deviation from the slow axis. This angle is supposed to be small.

As the system is symmetrical, the two reflected beams are the same (except for the optical propagation delay). To calculate the interferometric intensity on each photodiode, first let us write the recombined field from the two arms. As optical circulator has fast axis blocked, the field which arrives on the photodiode connected to it is:

$$\sqrt{a}\frac{A}{2}\cos(\alpha)\hat{s} + \sqrt{a}\frac{A}{2}\cos(\alpha)\hat{s}e^{-j\phi}, \tag{6.7}$$

where ϕ is the phase difference resulting from propagation in $\hat{s}$ polarisation, and a is the transmission in the optical circulator. So, the intensity at the OC photodiode is:

$$2a\left(\frac{A}{2}\right)^2\cos^2(\alpha) - 2a\left(\frac{A}{2}\right)^2\cos^2(\alpha)\cos(\phi). \tag{6.8}$$

From Eq. 6.8 we expect a DC term plus a term which oscillates when the phase ϕ evolves with temperature, as observed in the red curve of Fig. 6.15b.

On the BS photodiode the interference is possible in both polarizations, so the interferometric intensity on it is:

$$2\left(\frac{A}{2}\right)^2 + 2\left(\frac{A}{2}\right)^2\cos^2(\alpha)\cos(\phi) + 2\left(\frac{A}{2}\right)^2\sin^2(\alpha)\cos(\psi), \tag{6.9}$$

where ψ is the phase difference resulting from propagation in $\hat{f}$ polarisation, and we used $\cos^2\alpha + \sin^2\alpha = 1$.

From the DC component of the signal on the BS photodiode (see Fig. 6.15b and Eq. 6.9), I find that:

$$\left(\frac{A}{2}\right)^2 = 2.95 \ V. \tag{6.10}$$

Its also possible to verify that in maximum ($\cos(\phi) = \sin(\psi) = 1$), the AC part of the interferometric signal is equal to the DC part. So using Eq. 6.10, Eq. 6.8 and data in Fig. 6.15b, I also find that:

$$a\cos^2(\alpha) = 0.6508, \tag{6.11}$$

this equation will be used in Sec. 6.2.3.

Phases ϕ and ψ have different thermal coefficient of the refractive index $\frac{\partial n}{\partial T}$ and refractive index n due to birefringence of the PM fiber. The difference

between dn/dT for the two polarisations is of the order of 5% of 8×10^{-6} $1/K$, about 4×10^{-7} $1/K$ (see reference [45]). So, in this case, the variations in amplitude can be explained by different change rate of phases ϕ and ψ. For example, the fast changes in Fig. 6.15b are caused by temperature drift, and a $\phi - \psi$ phase difference causes slow changes in the envelope.

We can also conclude that signal on BS photodiodes does not reach zero because it is a mixture of two interference signals with different phases in different polarization. This model will be applied consistently for case 2 and 3.

6.2.2 Case 2: two Faraday mirrors

Now, let us consider the case when the two arms are terminated by the Faraday mirrors (see Fig. 6.16a). The recorded signal of the photodiodes in this configuration is given in Fig. 6.16b. The signal on the OC photodiode is close to zero as expected. In this case the reflected beam from the Faraday mirror

(a) (b)
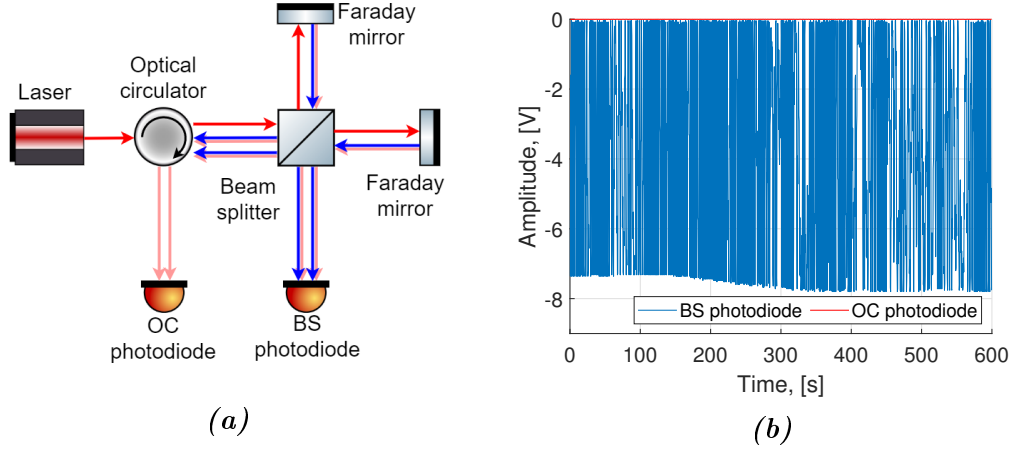
Figure 6.16: The recorded signal of the two photodiodes during 10 minutes (b) when the interferometer is obtained with two Faraday mirrors (a). Red arrows: light with slow axis polarization. Blue: light with fast axis polarization.

is:

$$r\frac{A}{2}\sin(\beta)\hat{s} + r\frac{A}{2}\cos(\beta)\hat{f}, \tag{6.12}$$

where $1 - r^2$ is insertion loss of the Faraday mirror and β is angle of deviation of the polarization vector from the fast axis of the optical fiber. This angle is supposed to be small, as observed from the very small signal on the OC photodiode (see Fig. 6.16b). In this case the intensity at the OC photodiode is:

$$2ar^2\left(\frac{A}{2}\right)^2\sin^2(\beta) - 2a\left(\frac{A}{2}\right)^2\sin^2(\beta)\cos(\phi). \tag{6.13}$$

And on the BS photodiode:

$$2r^2\left(\frac{A}{2}\right)^2 + 2r^2\left(\frac{A}{2}\right)^2\sin^2(\beta)\cos(\phi) + 2r^2\left(\frac{A}{2}\right)^2\cos^2(\beta)\cos(\psi). \tag{6.14}$$

From the DC component of the BS photodiode signal (see Fig. 6.16b) and Eq. 6.10 we get that $r^2 = 0.661$ and $r = 0.813$.

6.2.3 Case 3: Faraday mirror and normal mirror

The last case to consider is to use a Faraday mirror together with normal mirror (see Fig. 6.17a). The record of the signal of both photodiodes is given in Fig. 6.17b. The behaviour of the two signal is more complex. I will use the

(a)   (b)
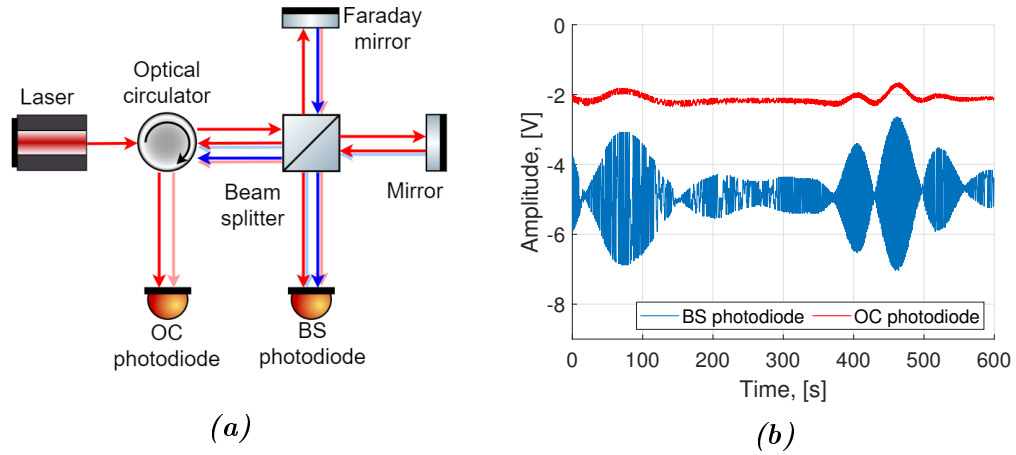
Figure 6.17: The recorded signal of the two photodiodes during 10 minutes.

same approach as in the two previous configurations to describe the phenomena. Let us consider a small tilt in polarization in the reflected from the Faraday mirror beam:

$$r\frac{A}{2}\sin(\beta)\hat{s} + r\frac{A}{2}\cos(\beta)\hat{f}. \tag{6.15}$$

In the other arm, the beam reflected from the normal mirror is:

$$\frac{A}{2}\cos(\alpha)\hat{s} + \frac{A}{2}\sin(\alpha)\hat{f}. \tag{6.16}$$

The intensity on the OC photodiode is:

$$a\left(\frac{A}{2}\right)^2 (r^2 \sin^2(\beta) + \cos^2(\alpha)) - 2ar\left(\frac{A}{2}\right)^2 \sin(\beta)\cos(\alpha)\cos(\phi). \tag{6.17}$$

The intensity on the BS photodiode is:

$$\left(\frac{A}{2}\right)^2 (1 + r^2) + 2r\left(\frac{A}{2}\right)^2 \sin(\beta)\cos(\alpha)\cos(\phi) + 2r\left(\frac{A}{2}\right)^2 \cos(\beta)\sin(\alpha)\cos(\psi). \tag{6.18}$$

Using DC and AC parts of the Eq. 6.17 and Eq. 6.18, data in Fig. 6.17b and result of the previous sections, we can write the system of equation:

$$\begin{cases} (A/2)^2(1+r^2) = 4.9 \ V \\ a(A/2)^2(r^2\sin^2(\beta)+\cos^2(\alpha)) = 1.74 \ V \\ 2ar(A/2)^2\sin(\beta)\cos(\alpha) = 0.08 \ V \\ (A/2)^2(1+r^2) = 4.9 \ V \\ 2r(A/2)^2\sin(\alpha+\beta) = 2.16 \ V \end{cases} \qquad (6.19)$$

Using result from Sec. 6.2.1 we can check that first equation is satisfied. Another four equations can be rewritten in form:

$$\begin{cases} a\sin(\beta)\cos(\alpha) = 0.0167 \\ \sin(\alpha+\beta) = 0.4503 \\ ar^2\sin^2(\beta)+\cos^2(\alpha) = 0.5898 \\ a\cos^2(\alpha) = 0.6508 \end{cases} \qquad (6.20)$$

For three unknown variables, we have four equations, so to solve the system, I use only 3 of them. Using 2,3,4 equations, we get that solution $\alpha = 0.3886$, $\beta = 0.0262$ and $a = 0.68$ and using 1,3,4 equations, we get that solution $\alpha = 0.391$, $\beta = 0.02376$ and $a = 0.7614$. Two solutions are quite close numerically to each other. However, in both solutions, the value α is quite big.

So the proposed model can explain the behavior of the interferometric signals for different combinations of the normal and Faraday mirrors in the interferometer. The next step is to identify the component, where the polarization rotation happens and, if possible, to eliminate the problem. Also, I did measurements of coherent backscattering in crossed polarization at 1.55 μm that vaguely looked reasonnable, but that I do not trust these measurements anymore after I found the problem at 1.06 μm.

6.2.4 Discussion and conclusion

One of the possible solutions that can eliminate the problem is to use the polarizer or polarizing (PZ) fiber. I had used a 2 m long HB1060Z polarizing fiber in two experiments. The experimental setup was the same as described in Sec. 6.2.3, but the PZ fiber was inserted in different places of the setup.

In the first experiment the PZ fiber was installed in between beam splitter and the mirror. In this case no qualitative change (see Fig. 6.18) was observed in comparison to Case 3 (see Sec. 6.2.3). Another problem of this setup is that PZ fiber disbalance arms of the interferometer.

A minor improvement was observed in the second experiment, when PZ fiber was installed before the BS photodiode. This partially cuts the other polarization component, but the interferometric amplitude was still fluctuating (see Fig. 6.19). Another idea to eliminate the problem was to identify the component in the interferometric setup, which is responsible for this polarization rotation. I have tried different mirrors and Faraday mirrors, try beam splitters
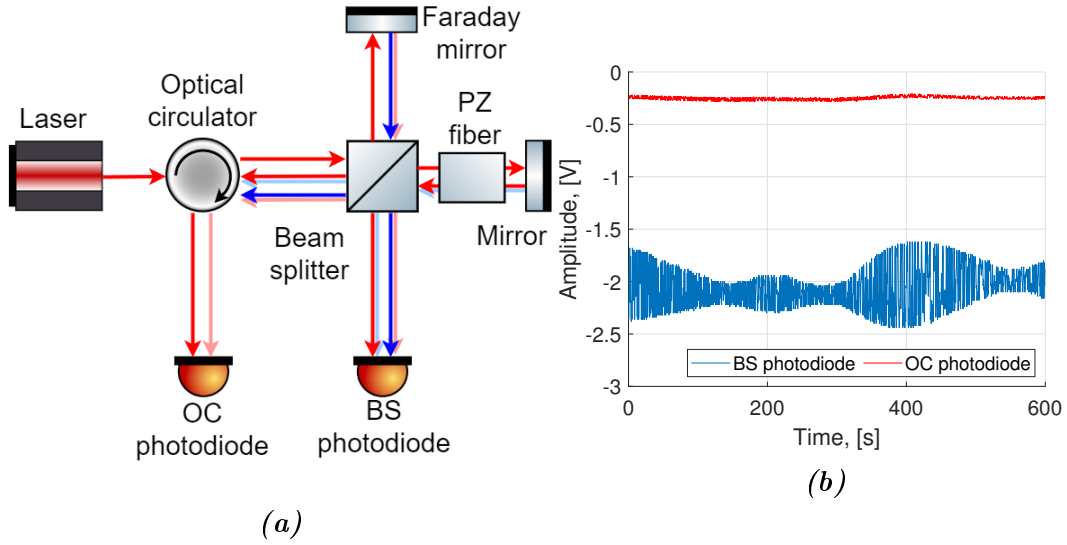
Figure 6.18: The schema of the setup, when a polarizing (PZ) fiber was installed in between beam splitter and PM fiber mirror (a) and the recorded signal of both photodiodes during 10 minutes.
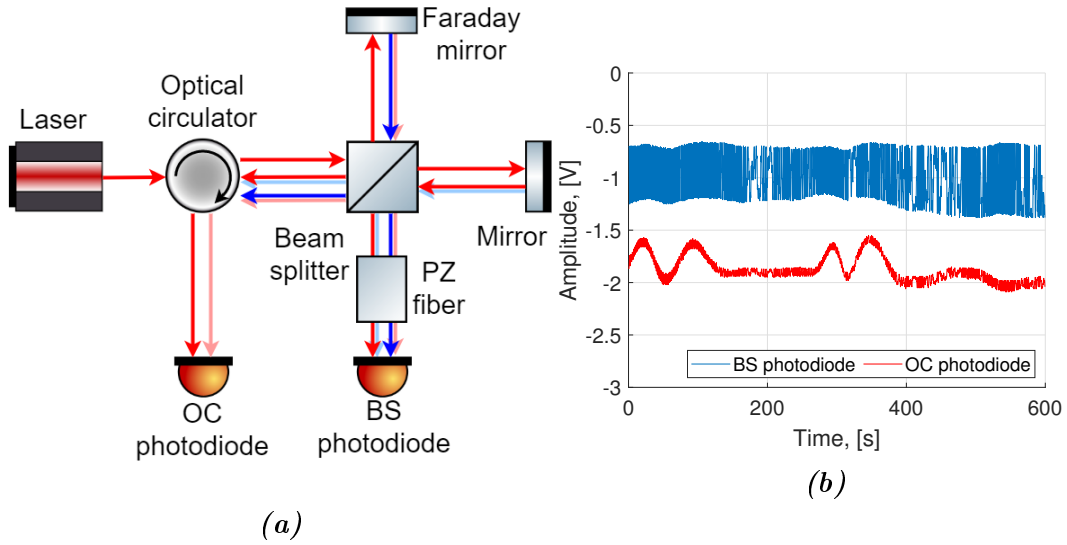
Figure 6.19: The schema of the setup, when a polarizing (PZ) fiber was installed in between beam splitter and photodiode (a) and the recorded signal of both photodiodes during 10 minutes.

of different manufacturers, check and replace all the fiber connectors, I have tried beam splitter in different configurations of the input/output ports, but the problem was always present. A series of experiments of heating of the bodies of the mirrors and beam splitter didn't give evidence that the polarization rotation happens in it.

From all this, we conclude that polarization rotation happens rather in the optical fibers than on the components. The given above model can well describe the behavior of the interferometric signal under different conditions. The real

situating way is even more complex, as not only ϕ and ψ phases change but also polarization rotation angles α and β rotates because they are temperature sensitive. (temperature coefficient is given by Verdet constant, and it is about $10^{-4}~K^{-1}$).

6.3 Results & Discussion

In this section, I will describe the results of the measurements of two samples: IR aluminum mirror (see Sec. 6.3.1) and the super-polished side of Si wafer (see Sec. 6.3.2).

6.3.1 Backscattering measurements of IR mirror

The sample mirror is Infra-Red Edmund optics mirror. Before the measurement, the mirror was cleaned with the First contact polymer, and the rotation stage was set to zero (normal incidence angle). The measurements of backscattering were performed for multiple incidence angles. For each angle, the position of the beam pump was adjusted to minimize back-scattering. For each incidence angle, a speckle scan was performed. That means the Picomotor stage of the mirror performed a series of angular increments of 17.5 μrad, in a range of a few milliradians. Under these conditions, several speckle grains are observed, allowing a reasonnable estimate of the speckle mean. An example of speckle patterns recorded at several incidence angles is given in Fig. 6.20a. The amplitude distribution of this amplitudes follow Rayleigh distribution (see Fig. 6.20b) as was expected (see Sec. 4.4.4).
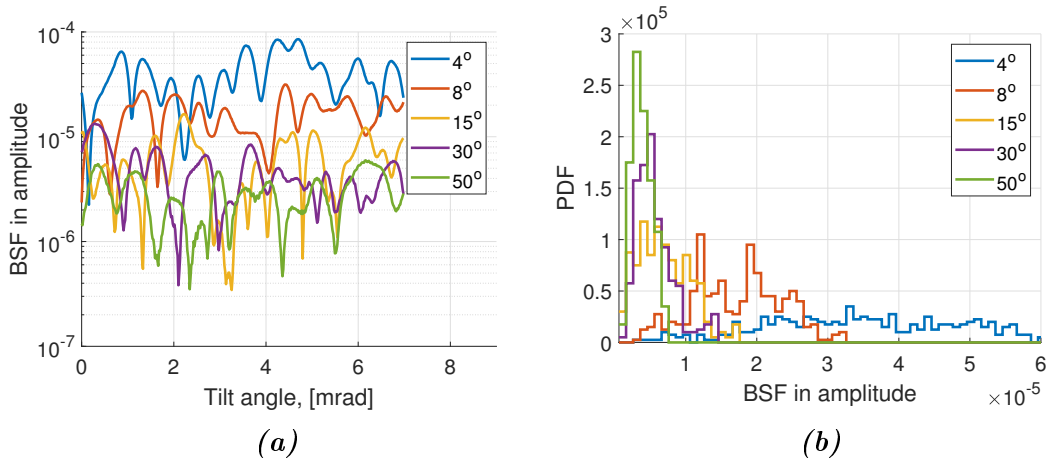
Figure 6.20: Measured speckle (a) and its amplitude distribution (b) for several incidence angles. The laser beam at the sample surface is 2.3 mm in diameter, and it has s polarization.

To find how speckle size changes with the incidence angle, I calculate the autocorrelation of the measured speckles in amplitude (see Fig. 6.21a). I calculate the width of the autocorrelation function at 90% of the maximum. The

width is compatible with beam divergence (see Fig. 6.21b) but there is no obvious sign of the change of the speckle grain with incidence angle.

Figure 6.21: Autocorrelation function (a) and its width as a function of the incidence angle (b).

At the last step, I express the measured data in the form of BRDF of the IR mirror (see Fig. 6.22a). At the same time, the scattering was measured with a power meter on the left and right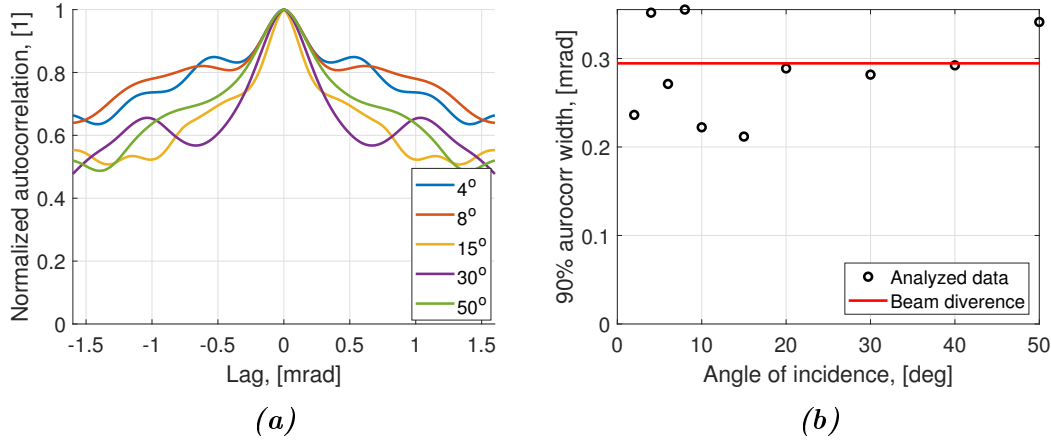 side from the incident beam. Each of the photodiodes is tilted from the exact backscattering direction on 3.7 deg. To hold the precise orientation of the detector, I design and print a photodiode holder of the Newport power meter. The output signal of the power meter was averaged during 200s (10kSps) with the built-in function of an oscilloscope. The result of the power meter measurements is in Fig. 6.22a. The values measured with power meter don't coincide with interferometer measurements as the two of the photodiodes are shifted (by 3.7 deg) in opposite directions from the exact backscattering axis. The values measured with the power meter have higher significance at lower incidence angles as the measured scattering power is higher. As a result, we have a good agreement of backscattering measurement with two methods, as expected in Sec. 4.4.4.

Besides this, I calculate the contrast of the speckle (see Fig. 6.22b) and find that it varies about unity, which corresponds to fully developed speckle (see Sec. 4.1).

6.3.2 Si wafer measurements

A more challenging task is to measure the scattering from super-polished surfaces. To demonstrate the possibilities of the setup, I have measured the scattering from super-polished undoped Si wafers purchased from Siltronix[2], specified with <3 Å roughness.

The first step before the measurement is the alignment of the rotational stage to the normal incidence angle. This also allows us to measure the reflectance from the Si wafer and make one more check.

[2]sil-tronix-st.com
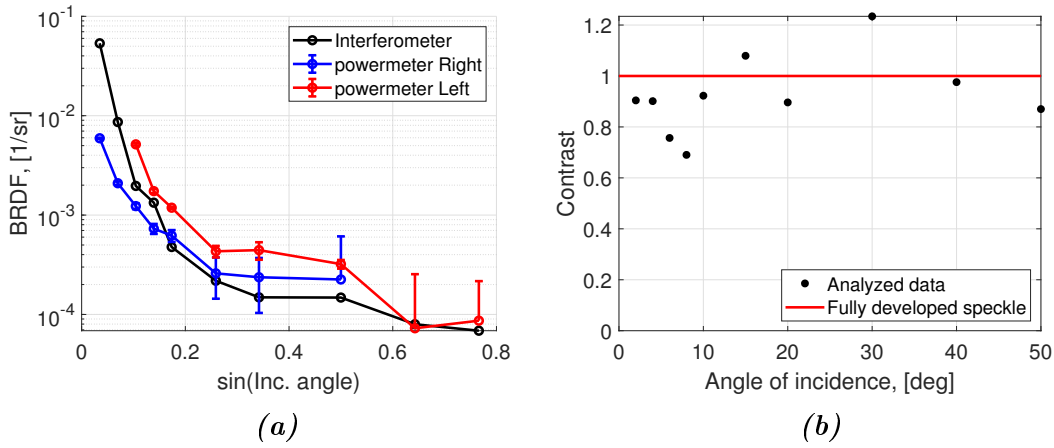
Figure 6.22: *BRDF (a) of the IR mirror and contrast (b) as a function of the incidence angle*

In reference [49] is specified that at 1.064 μm Si has a reflectance coefficient of $r_{Si} = 0.31461$ at zero incidence angle. The measured interferometric amplitude with lock-in amplifier is 0.2239 ± 0.0018 V. So taking into account reflection losses r_T, we have that $r_{Si} = (0.2239/0.36982)^2 \cdot 0.8571 = 0.317$. The reflection coefficient measured with power meter is $r_{Si} = 0.318$. So the agreement is achieved. I recall that silicon is strongly absorbing at 1.064 μm: with our wafers, of thickness 1 mm, the transmission is measured to be 6×10^{-4} which prevents contribution from the rear side.

To perform the speckle scan, I used a 2" Picomotor stage. The speckle amplitudes were averaged and normalized to achieve BRDF values. The final BRDF of the super-polished side of the Si wafer is given in Fig. 6.23a. The lowest measured value of the BRDF is lower than 10^{-5} $1/sr$. This is an excellent result for low cost, home-made setup. For example, minimum measurable BDRF for High Specular bench from LightTech[3] is 10^{-5} in IR.

As well as with scattering of the beam dumps, certain precautions should be taken. One of the main points to check is if the measured signal still has optical properties. Same as in the case with beam dumps, I use a correlation method. The correlation as a function of backscattering fraction in amplitude is shown in Fig. 6.23b. A definite step function is observed. For high backscattering fractions, the correlation is high. When the correlation is lower than 0.5, the measured values are wiggly valid.

This demonstrates the possibility to measure BRDF at levels down to 10^{-5} $1/sr$. This is extremely useful for the BRDF measurement of low scattering LISA optics.

---

[3]http://www.lighttec.fr/scattering-measurements/
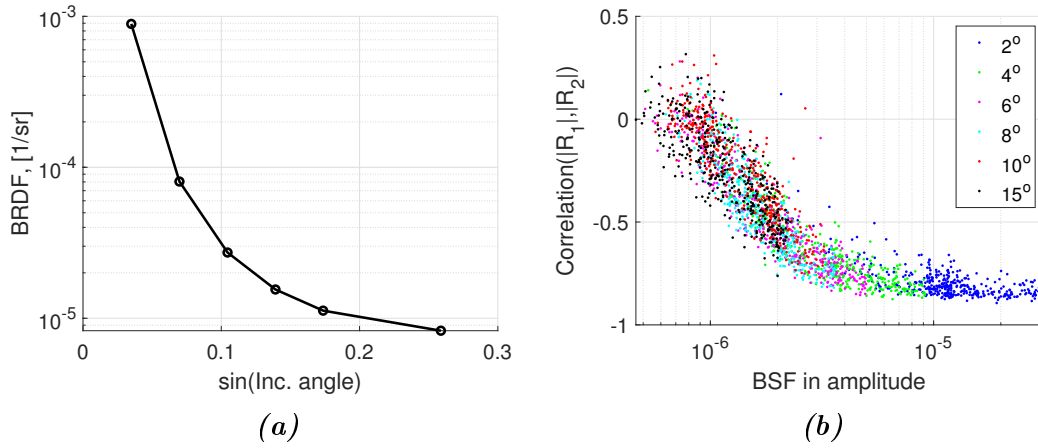
Figure 6.23: *BRDF of the Si wafer (a) and a correlation test method (b). Each point in Fig. (a) is an averaged value of cloud of points in Fig. (b). The correspondence between BRDF and BSF is* $BRDF = 3.67 \times 10^6 BSF^2 / \cos(\theta_i)$.

6.4 Conclusion

We built a new setup for backscattering measurements at 1.064 μm. Each component and the setup in assembly was tested and validated. In classical BRDF meter, the limit of measurements is due to the presence of air (Rayleigh scattering) or dust which give rise to a measurement floor or noise: these contributions are absent in measurements with 1.06 experimental setup, as the corresponding contributions fall out of the bandwidth of the measurement. The possibility of backscattering measurements was demonstrated at two samples. As before, with the 1.55 μm setup, the coherent properties of scattering were observed.

The setup can measure BRDF below 10^{-5} $1/sr$, which is the level of state-of-art of modern BRDF meters. The setup is validated to be used for low backscattering measurements of LISA optics.

Chapter 7

CBS in optical fibers

Up to now, we considered only scattering at the optical surfaces. However, scattering in the bulk of a medium is also possible, and it will take place in the LISA instrument. The particularly sensitive part of LISA to internal scattering is an optical fiber (see Sec. 1.2), which will link the two MOSAs in the satellite. The fibers are susceptible to the thermal change, so we expect that the evolution of the backscattering amplitude may happen. This change will cause a shift in the clock phase and thus the error in total phase measurements.

In this chapter, I develop a model of Coherent backscattering (see Sec. 7.2) based on the widely used models of scattering in the optical fiber (see Sec. 7.1). The basis of the model is the random phasor sum. This idea has already been used to describe the coherent features of scattering in optical fibers (see Ref. [38]). However, I complete the model by deriving the change rate of the backscattering power as a function of temperature (see Sec. 7.2.1). Also, I show the link of coherent backscattering in fiber with other models of fiber scattering (see Sec. 7.2.2). The obtained results of the model are verified with experimental results (see Sec. 7.3).

7.1 Scattering in optical fiber

Optical fiber light scattering is caused by micro-heterogeneities in the permeability index [40]. The classical description of the scattering in a fiber uses the approach given in Ref. [35]. Let us consider a fiber of length L_f. We divide the fiber into small pieces with length dL, small enough that we can neglect attenuation. Backscattered power on each of the pieces is:

$$dP_{bs}(L_f) = P_{in}\frac{\alpha_R S}{2}\exp(-2\alpha L_f)dL, \tag{7.1}$$

where P_{in} is the input power, α_R is the Rayleigh-scattering coefficient, α is the total attenuation coefficient of scattering and absorption ($\alpha = \alpha_R + \alpha_{abs}$) in units of inverse length $[m^{-1}]$, S is the recapture factor [40] in single mode fibers:

$$S = \frac{3}{2n^2W_0^2(\omega/c)^2} \approx 10^{-3}, \tag{7.2}$$

132

where $2W_0$ is the mode field diameter of the field propagating in the fiber and n the index of the fiber core. To get the total backscattering at the fiber end, we integrate Eq. 7.1 all along the fiber length L_f:

$$P_{bs} = P_{in} \frac{\alpha_R S}{2} \frac{1}{2\alpha} (1 - \exp(-2\alpha L_f)). \qquad (7.3)$$

So we see, that by increasing the fiber length to infinity, backscattered power reaches the limit of $P_{in} \frac{\alpha_R S}{2} \frac{1}{2\alpha}$. This effect is due to attenuation in the fiber of the transmitted and the backscattered beams.

7.2 Coherent model of fiber backscattering

To describe coherent backscattering in the optical fiber, we will use the approach of a random phasor sum [23, 38]. It is to say, that the total scattering at the fiber end is given by the complex sum of N backscattering contributions equidistantly placed all along the fiber. The backscattering sum in this case is:

$$E_{bs} = \frac{1}{\sqrt{N}} \sum_{i=1}^{N} E_s(z_i). \qquad (7.4)$$

The factor $\frac{1}{\sqrt{N}}$ is used for normalization. Each element $E_s(z_i)$ in the sum is a complex vector which represents the backscattering amplitude and phase of an elementary fiber piece of a length ΔL placed at a distance $z_i = \Delta L \cdot i = i \cdot L_f / N$ from the fiber end (see Fig. 7.1). We consider that each of these fiber pieces has the absorption and thermal effects inside of it. Moreover, we consider that the properties of the different fiber pieces are independent of each other, and do not change over the time.
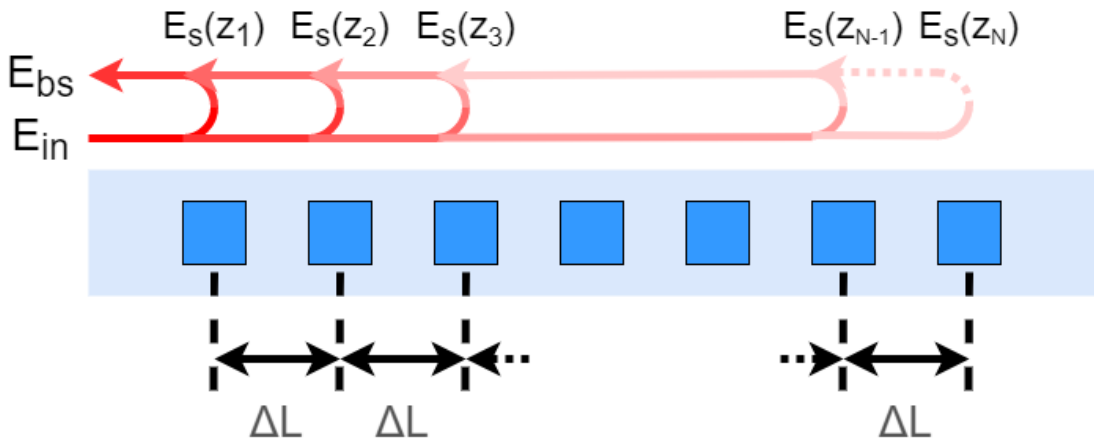
Figure 7.1: An illustration to the backscattering model. The blue squares are equidistant scattering centers placed all along the fiber. Each center is separated from other at distance ΔL from another and scatter with complex amplitude $E_s(z_i)$.

The complex backscattering amplitude of the scattering center at point z_i is:

$$E_s(z_i) = E_{in} \times b \times exp\Big[-\alpha z_i + j2\phi(z_i)\Big], \qquad (7.5)$$

where $E_{in} = \sqrt{P_{in}}$ is the modulus of the input laser field and I define a backscattering coefficient as $b = \sqrt{5/3 \cdot \alpha_R S L_f / 2}$. The coefficient 2 near the phase $\phi(z_i)$ indicates double pass in the fiber (to the scattering center and back).

The backscattering phase contains two contributions: one is phase change due to propagation in the fiber and the other is due to fluctuation of the fiber index:

$$\phi(z_i) = \frac{2\pi}{\lambda}(n\Delta L \cdot i + \Delta n_i \Delta L), \qquad (7.6)$$

where λ is optical wavelength, n is the average refractive index of the fiber material (between the input and the output of the fiber) and Δn_i is local index variation. In this model, the phase $\frac{2\pi}{\lambda}\Delta n_i \Delta L$ is independent of the time or temperature and has random uniform distribution on $[-\pi, \pi]$.

The refractive index is:

$$n(T) = n_0 + \kappa T = n_0 + \left(\frac{dn}{dT} + \frac{n}{L_f}\frac{dL}{dT}\right)T = 1.47219 + 17 \cdot 10^{-6} \cdot T. \qquad (7.7)$$

The κ coefficient expresses the change of the refractive index due to heating and expansion of the fiber by thermal impact.

So the sum E_{bs} (see Eq. 7.4) is a function of temperature T. In Fig. 7.2 I plot the backscattering amplitude and phase of the sum for temperature variation $\Delta T = 1^o\ K$ for two fiber lengths (1 m and 10 m).
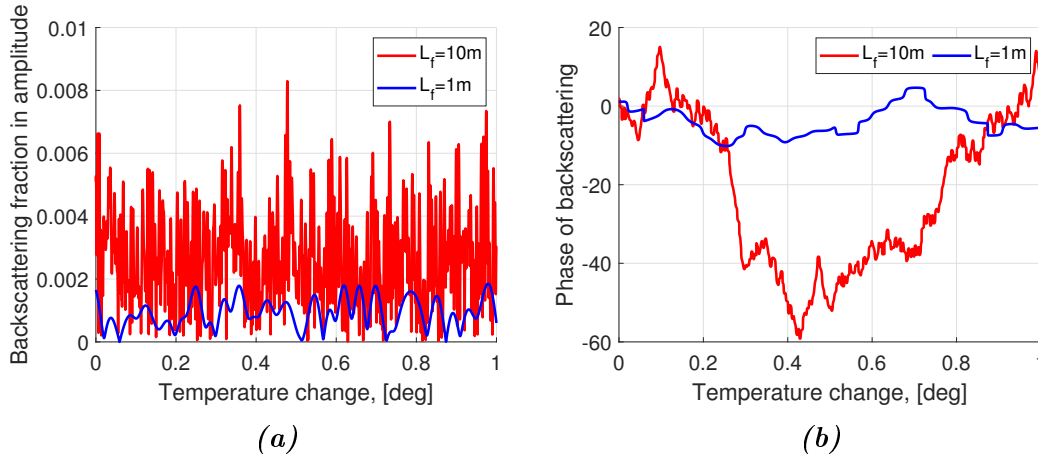
Figure 7.2: Backscattering amplitude (a) and phase (b − deviation from linear $2\pi \cdot \kappa L_f / \lambda \times T$) of the backscattering phasor sum, as a function of temperature. Parameters of the model: $\frac{\alpha_R S}{2} = 10^{-6}$ 1/m, $P_{in} = 1\ W$, $\lambda = 1.064\ \mu m$, $n_0 = 1.47219$, $\kappa = 17\ \frac{\mu m}{m\ K}$, $N = 10000$, $\alpha = 10^{-3}$ 1/m, Temperature increments $\Delta T = 1\ mK$

The computed amplitude of E_{bs} is random. As a function of the temperature change, it displays a "speckle", with "speckle grains", reminiscent of the speckle

structure observed on the X-Y or theta-phi maps, here, in one dimension. Comparing the average amplitude for $L_f = 1\ m$ and $L_f = 10\ m$ shows that the average of the modulus is larger for longer fibers. This is expected (see Eq. 7.1). However, the temperature dependence also changes when the fiber length changes. The rate of change increases with the fiber length. This dependence will be figured out in the next section.

It should also be mentioned that as the model is numerical (with a discrete step), it would be preferable to avoid reaching the "aliasing temperature" region $\Omega_T = \lambda/(2\kappa\Delta L)$. Its to say that working temperature T should always be lower than Ω_T. This is achievable by increasing the number of scattering centers N in the fiber.

7.2.1   Typical change rate in temperature

To derive how fast the BS amplitude changes as a function of temperature, I use the autocorrelation function (see Fig. 7.3). If the dependence of the amplitude, close to the top of a speckle grain can be approximated by a gaussian dependence $exp\left(-\frac{(T-T_0)^2}{\Delta_T^2}\right)$, then the typical temperature change rate is:

$$\Delta_T = \frac{\lambda}{2\sqrt{2}\kappa L_f}.\qquad(7.8)$$

This expression is approximate, and it is obtained from an analysis of numerous modeling data. So, it is proportional to the optical wavelength λ and inversely proportional to the thermal index coefficient κ and the fiber length L_f.
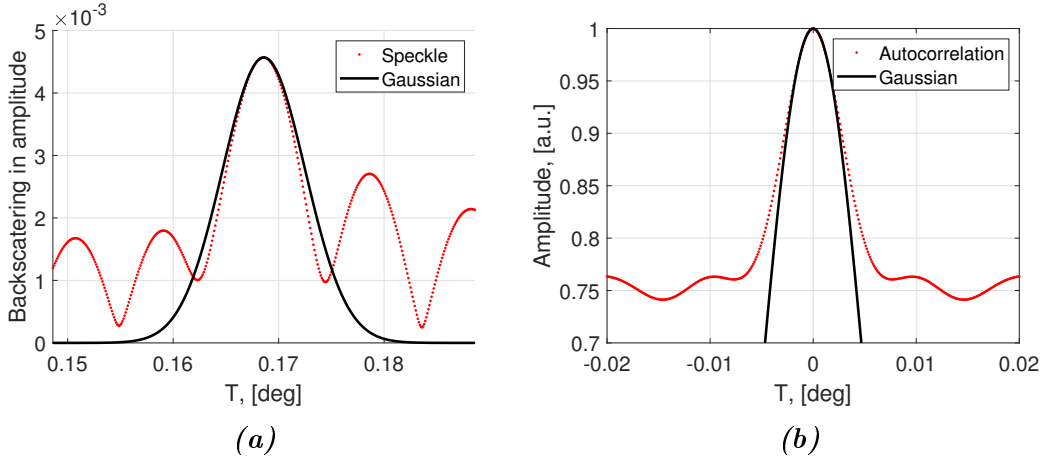
Figure 7.3: Backscattering in amplitude (a) as function of the temperature and an autocorrelation funtion (b) of it with the same parameter $\Delta_T = 5.5\ mK$ for both plots. Parameters of the model are the same as in Fig. 7.2, except: $L_f = 4\ m$

From the other side, the functional dependence (up to constant coefficient) can be found analytically.

In order to proceed, we simplify the sum 7.4 a little bit:

- first we consider only the real part (in heterodyne phase contamination by stray light, only one quadrature of stray light matters; the other one only affects the amplitude of the signal);

- we consider that absorption in the fiber is negligible: $\alpha = 0$;

- and randomness is absent ($\Delta n_i = 0$).

So:

$$\Re E_{bs} = \Re \frac{1}{\sqrt{N}} \sum_{i=1}^{N} E_{in} \cdot r \cdot exp(j(4\pi \frac{n\Delta L}{\lambda} \cdot (i-1) + \frac{4\pi n}{\lambda} \Delta L)) =$$

$$= \frac{E_{in} r}{\sqrt{N}} \cdot \sum_{i=1}^{N} cos(\psi(i-1) + \frac{4\pi n}{\lambda} \Delta L) \equiv \frac{E_{in} r}{\sqrt{N}} \cdot \frac{sin(\frac{N}{2}\psi)}{sin(\frac{\psi}{2})} cos(\frac{4\pi n}{\lambda} \Delta L + \frac{N-1}{2}\psi)$$

$$\tag{7.9}$$

where $\psi = 4\pi \frac{n\Delta L}{\lambda}$. The function $\frac{sin(\frac{N}{2}\psi)}{sin(\frac{\psi}{2})}$ has main lobe near $\psi = 0$. Similarly as in diffraction problem, we determine the typical temperature change rate as:

$$sin(\frac{N}{2}\psi) = 0, \tag{7.10}$$

which implies $\frac{N}{2}\psi = \pi$ or the same $\frac{N}{2}4\pi \frac{n\Delta L}{\lambda} = \pi$. Usiang the fact that t $N\Delta L = L_f$ and $n = n_0 + \kappa \Delta_T$, we have:

$$2(n_0 + \kappa \Delta_T^*)L_f/\lambda = 1. \tag{7.11}$$

As refractive index n_0 set just a constant shift, but does not determine the speckle size, so

$$\Delta_T^* = \frac{\lambda}{2\kappa L_f}, \tag{7.12}$$

what is up factor $\sqrt{2}$ is equal to Δ_T. I will verify the obtained result with the experimental data in Sec. 7.3.1.

7.2.2 Amplitude and Intensity distribution

Amplitude and intensity distributions have typical speckle properties and can be described by Rayleigh and negative exponential distribution correspondently [23] (see Fig. 7.4). Data set in Fig. 7.4a and in Fig. 7.4b are the same. The black curve in Fig. 7.4 is not a fit, but an expected distribution with a parameter derived from the mean of the data.

The mean of the scattering intensity of the model as a function of fiber length (red circles in Fig. 7.5) can be compared with the classical approach (see Eq. 7.3). In black in Fig. 7.5 is the expected dependence. This is not a fit, but the parameters of the curve were calculated from the input parameters of the model.

So we get a perfect agreement with widely used models. At the same time, our model give a predictions on distribution of amplitudes and intensities and typical temperature change rate. This new features will be verified in the next section.
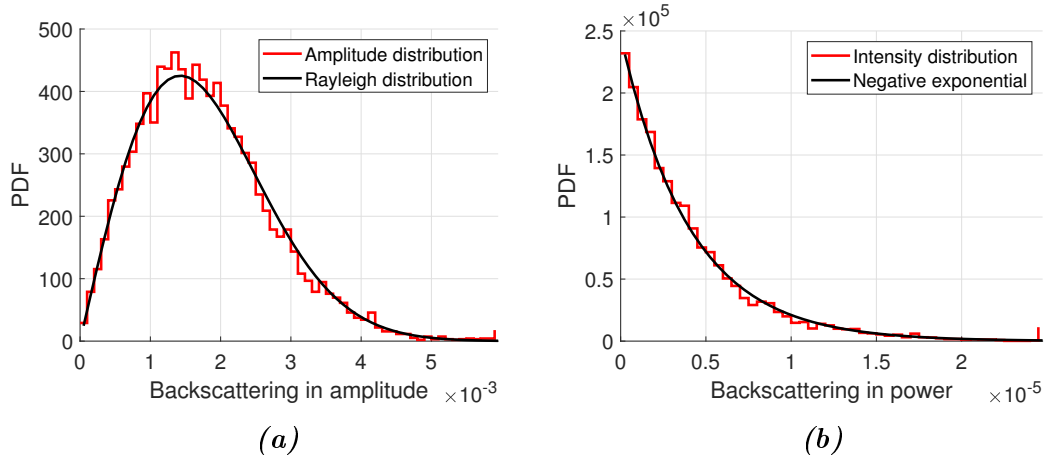
Figure 7.4: Amplitude (a) and intensity (b) distribution of the CBS in fiber.
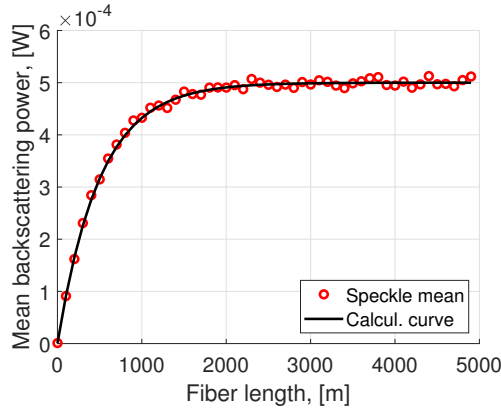
Figure 7.5: Comparison of mean CBS intensity (red circles) and classical, incoherent approach (black line – see Sec. 7.1). Parameters of the model: $P_{in}\frac{\alpha_R S}{2} = 10^{-6}$ W/m, $\lambda = 1.064$ μm, $n_0 = 1.47219$, $\kappa = 17$ $\frac{\mu m}{m\ K}$, $N = 10000$, $\alpha = 10^{-3}$ $1/m$, $L_f = 4$ m, $\Delta T \in [0, 10]^\circ$ K

7.3 Analysis of the experimental data

To prove the validity of the model of CBS in the optical fiber, I use data kindly provided by Johann Max Zwetz (AEI, Hanover). In their work [21] was used a heterodyne setup for measurements of backscattering from irradiated fibers. The fiber under test was winded on an aluminum cylinder of 10 cm diameter. To the cylinder was applied sinusoidal thermal modulation around 21° C with peak-to-peak amplitude 1° C at frequency 0.02 Hz (a blue line in Fig. 7.6). Recorded temperature change is not synchronized with backscattering measurements: not in start time, not in sampling frequency (10 Hz for temperature and 25 Hz for backscattering data). The measurements were performed at 1.064 μm wavelength. Each tested fiber had a length of 4 m. The measured optical fiber path length thermal coefficient is $\kappa = 17$ $\mu m/(m \times K)$. This value may be overvalued, as the aluminum coil thermal expansion can

contribute.

Four sets of measurements were provided. The data for the first set of provided measurements are shown in figure 7.6. I analyze parts of the sample data ("cuts" in red on Fig. 7.6), which correspond to a linear temperature scan. Each sample contains three such regions. The rate of temperature increase was used to plot the backscattering as a function of the temperature (see Fig. 7.7a).
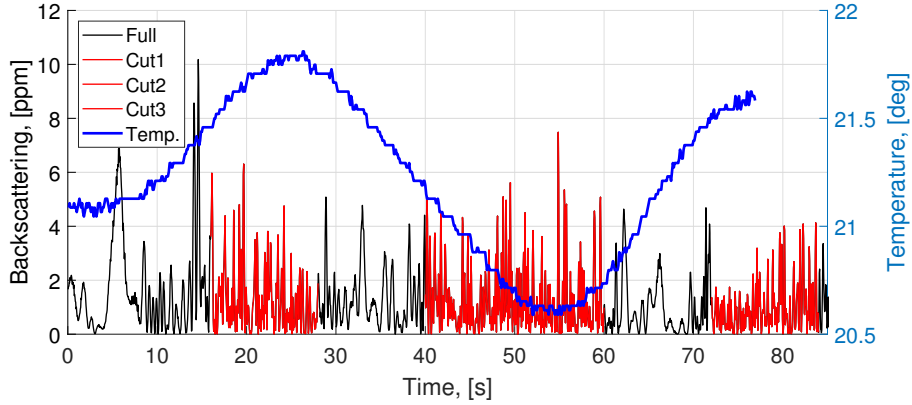
Figure 7.6: Example (meas1, PM07) of the analyzed data set: "Full" is a complete data set of measured backscattering in ppm, "Temp" is the measured temperature change. In red are data cuts on the approximately linear range of the temperature change.

For each of the data sets, I analyze the typical temperature change rate of the speckle and intensity distribution.

7.3.1 Change rate in temperature

To extract the change rate of the backscattering intensity, I use the autocorrelation function. If a single "speckle grain" in intensity can be approximated by a Gaussian $exp(-2T^2/\Delta_T^2)$, so the autocorelation functional form is $exp(-T^2/\Delta_T^2)$. To extract Δ_T from the data, I fit the autocorrelation function (see Fig. 7.7b). The parameters Δ_T of the fit are summarized in the Table 7.1. The united result for all the measurements is 7.1 ± 0.1 $[mK]$.

On the other size, by prediction of the model, the speckle size should be $\Delta_T = \lambda/(2\sqrt{2}\kappa L_f) = 5.5$ $[mK]$. The value is slightly lower than the obtained from the experiment. This can be explained by the fact that the refractive index change coefficient κ was measured in conditions that may be different from the backscattering measurements. In addition to that, the expansion of the aluminum cylinders under the temperature increase may have added mechanical stresses.

7.3.2 Distribution of the backscattering intensity

It is expected that distribution of the backscattering intensities in speckle will follow negative exponential distribution [23].

(a) Piece of the data sample (in blue) with a Gaussian of speckle size (in red).

(b) Autocorrelation of 3 "cuts" for the first measurements data set and Gaussian of appropriate speckle width (in green)
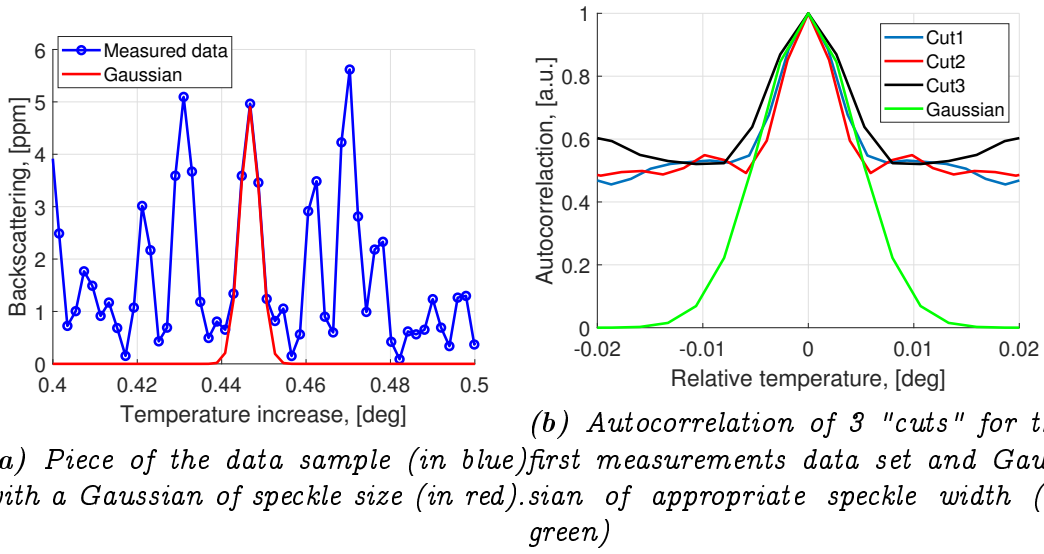
Figure 7.7: Illustrations for the data analysis procedure

However, in two data sets (PM08, PZ08), I observe a deviation from this law. This can be explained by:

- Presence of constant contribution together with backscattering sum.

- Sum of several independent speckle patterns in case of different wavelengths of interfering components.

- Sum of two independent speckle patterns in case of polarization diversity of interfering components.

I assume that the observed effect is due to reflection on the fiber end (first case above). Corresponding probability density function [23] is:

$$p_I(I) = \frac{1}{\bar{I}} exp\Big\{ - \Big(\frac{I}{\bar{I}} + \rho\Big)\Big\} I_0 \Big(2\sqrt{\frac{I}{\bar{I}}\rho}\Big), \qquad (7.13)$$

where $\bar{I}$ is mean intensity of scattering, ρ is the ratio of the intensity of the reflection to the average intensity of the random phasor sum $\bar{I}$ (beam ratio).

Fit of intensity distribution is shown in Fig. 7.8 and summarized in Table 7.1 in columns "CBS fit, [ppm]" and "Beam ratio ρ".

Except this, in Table 7.1 is given mean of intensity distribution ("CBS mean, [ppm]"). This value is quite close to the values achieved from the fit. However, there is a difference in the datasets with a constant contribution (PM08, PZ08). So if the data would not be analyzed properly (if only mean value of CBS would be computed), it is possible to misinterpret and overvalue the measured data CBS from a fiber. The measurements of the CBS in fiber should be done for multiple connection-disconnection of the fiber from the setup. In this case, the value of the CBS intensity in fiber should be the same from measurement to measurement, but the value of back-reflection each time would be different.

Table 7.1: Result of data analysis. CBS mean is a result of intensity averaging, CBS fit and beam ratio ρ are obtained by the fit of the intensity distribution. Reflection is value in [ppm] of reflected intensity on the fiber end ($\rho \times \bar{I}$).Δ_T, [mK] is the change rate in temperature obtained with the method described in Sec. 7.3.1. The errorbars of Δ_T are obtained from the fit.

Fiber	CBS mean, [ppm]	CBS fit $\bar{I}$, [ppm]	Beam ratio ρ	Reflection, [ppm]	Δ_T, [mK]
PM07	1.22	1.22	0	0	6.5 ± 1.3
PM08	4.34	1.19	2.64	3.14	7.2 ± 1
PZ07	7.	6.99	0	0	7.0 ± 0.1
PZ08	5.41	1.33	3.06	4.07	10.2 ± 0.5

(a) PM datasets distributions fit *(b) PZ datasets distributions fit*
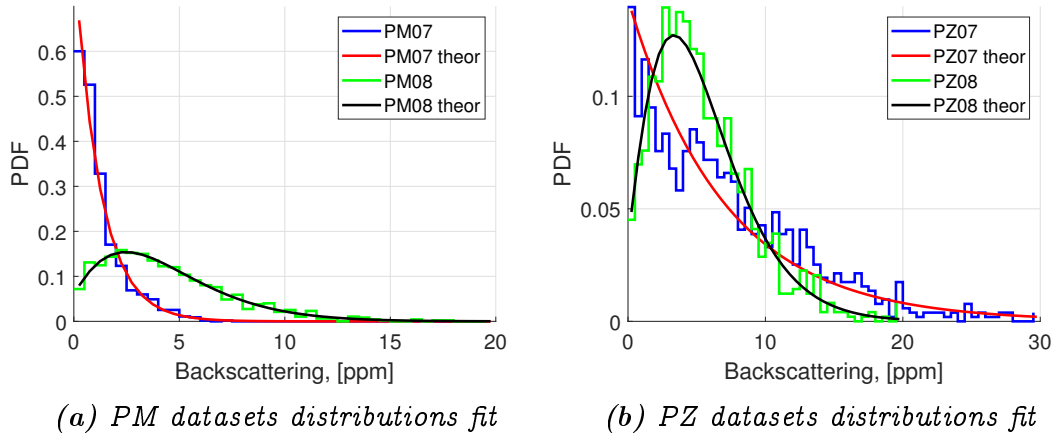
Figure 7.8: Analysis of the intensity distribution

7.4 Conclusion

So using classical formulas given in [35, 40], and few additional assumptions, we can describe coherent backscattering in an optical fiber of length L_f. We see during a temperature ramp, speckle behavior will show up. The typical change rate of the "speckle grain" in temperature space is given by $\lambda/(2\sqrt{2}\kappa L_f)$ where κ is the effective thermal coefficient for the optical path. The distribution of amplitudes and intensities fits the expected behavior [23] and can be described with simple Rayleigh and negative exponential distributions, respectively.

At the same time, the behavior of the mean backscattered intensity as a function of fiber length can be described by the classical approach [35]. So, the model agrees with previous works [35, 40], but also provides new information about the thermal speckle change in optical fiber.

Experimental verification of the model was done with datasets provided by Albert Einstein Institute [21]. The measured typical change rate is compatible with the value predicted by the model. The measured intensity distribution was analyzed. I found that, out of the four backscattered intensity records provided by AEI, two showed an intensity distribution differing from the ex-

pected negative exponential. Among the possible reasons, a likely one is an optical reflection at one of the two input ends. However, I find a possible reason, describe the effect and also, I propose a possible improvement for CBS measurements in the optical fiber.

The results presented in this chapter generally apply for coherent backscattering in fibered systems, particularly in interferometers such as the LISA instrument.

Chapter 8

Scattering due to particulate contamination

The scattering due to surface roughness was discussed before in this thesis. However, as observed in the estimates presented in Ref. [41], the scattering in the LISA instrument due to particulate contamination is significant and can be even dominant. Like the scattering from a rough surface, the laser source's coherence will give rise to specific features in the scattering at a contaminated surface. The measured (in LISA and this experiment) scattering is coherent, but the models, which describe the scattering from particles, are classical. A quantitative description of the particulate contamination of a surface is much less accurate than the description of roughness and does not include its coherent features. Consequently, there is considerable uncertainty in the description of the scattering of light from a surface contaminated by dust. The aim is to verify on experiment convergence of conventional model (Mie theory) and averaged coherent backscattering intensity measured in experiment.

To arrive at this aim, I have implemented an experiment (see Sec 8.1), which consists of three systems: particle deposition, particle counting, and interferometric setup for backscattering measurements. With lessons learned during this study, I built an improved experimental setup (see Sec. 8.2). As a result, the backscattering measurements from particulate contamination at 1.06 μm were compared with Mie theory.

Besides this, and to help reach reproducible conditions in the experimental room, I made a cleanroom contamination control system based on the IoT (Internet of Things) concept. The idea of this system was to check the possibility of using general-purpose air particle counting sensors for cleanroom monitoring. The implementation and results of this experiment are discussed in Sec. 8.3.1.

8.1 Particulate coherent backscattering experiment at 1.55 micron

The experiment's idea is to correlate the backscattering measured in an interferometer with the sequential increase of the number of particles on the surface. These measurements should give an idea of the increased rate of backscattering for the LISA mission (assuming that the rate of contamination is known to some extent during the various phases of the mission: assembly/integration, launch, etc.). To facilitate the problem, the particles will be monodisperse spheres.

The experiment consists of:

- Particle deposition system (see Sec. 8.1.1), which is used to deposit particles on a mirror surface in a controlled way.

- Particle counting system, which is based on a general-purpose camera and image processing software (see Sec. 8.1.2).

- Interferometric 1.55 μm setup for backscattering measurements (see Sec. 8.1.3).

Based on the lesson learned, I improved image processing (see Sec. 8.1.4), and in Sec. 8.1.4, I suggest some possible improvements in the experiment.

8.1.1 Particle deposition system

The design of the particle deposition system significantly relies on the type of particles considered to be used. In this case, we are going to use monodisperse SiO_2 spheres from granuloshop.com. The available sizes are $1.93 \pm 0.05 \mu m$, $3.97 \pm 0.12 \mu m$, $7.87 \pm 0.23 \mu m$ and $16.04 \pm 0.35 \mu m$. These particles are in a solution of pure water, with a concentration of 5% in mass. Each bottle (15ml) contains a number of silica spheres of diameter D of approximately

$$N_{part} \approx 10^{12}/(D \ [\mu m])^3, \tag{8.1}$$

where I used the value of $\rho_{H_2O} = 1 \ g/ml$ for the specific mass of water, and the value of $\rho_p = 1.9 \ g/ml$ for silica spheres, given by the provider. We have about 2.4×10^8 spheres in the solution with 16 μm particulates.

We considered two different ways to deposit these particles on the surface. The first one is to use the liquid form of the solution and use a spray system. Another approach is to allow the solution to dry and use a powder of these particles.

The usage of liquid form has the advantage of controlling the number of deposited particles by changing the concentration of the solution.

To deposit the particles on the mirror surface, I have built a liquid spray system (see Fig. 8.1). The principle is the following: the flow of air produced by a compressor creates a low pressure at the outlet of the volume with a particle
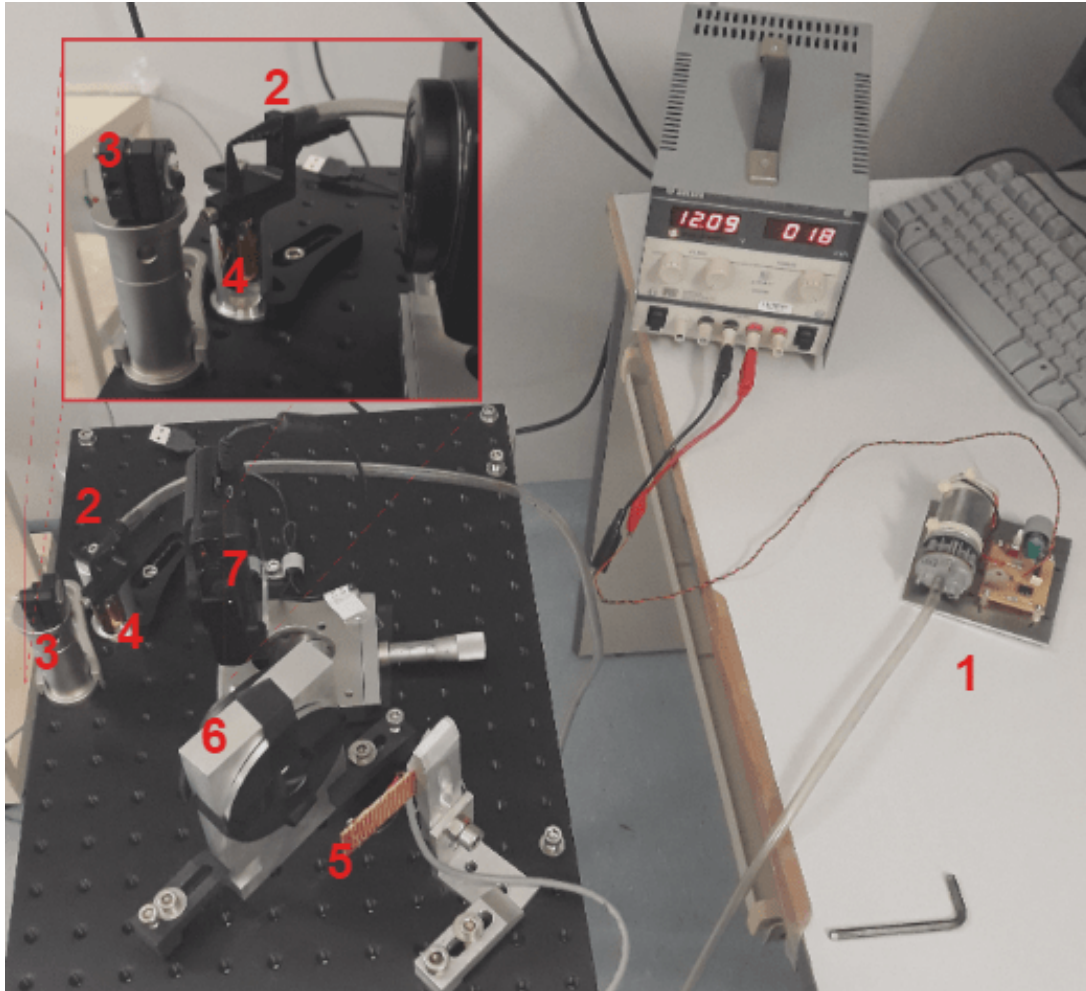
Figure 8.1: Liquid spray system, which was built to test the particle de-position system. The compressor with a control circuit is on the right side of the image (1). The compressed air moves through the transparent tube to the small optical table. The tube is connected to the "spray head" (2) (see a zoom of the area in the red frame). The container with the required concentration of particles (4) is placed under the exit of the spray head nozzle. The system deposits the droplets of liquid with spheres on the mirror surface (3). The illumination system of a single lens (6) and LED diode (5) is used to create uniform illumination of the mirror surface. The images are taken with a well-focused camera (7) installed on a translation stage for accurate focusing.

mixture. The liquid moves up and is captured by the airflow, which spreads the droplets towards the mirror.

Laboratoire ARTEMIS recently purchased a 3D printing device, and I could design and 3D print the nozzle of the spray head (the part of the system, where the mixing of the air and liquid happens). The structure also holds clean container with a mixture of particle solution and propanol (99% clean), to reduce the concentration of particles and helps better control the particle

deposition rate. The liquid (propanol in our case) which is mixed with particles should be clean, should not dissolve components (acetone, for example, can dissolve PLA (Polylactic acid) plastic) and should have low viscosity.

The last property we need is to create small droplets. Each droplet contains multiple particles. If the droplet is big, the deposition of particles may give rise to "dots," while the experiment requires uniform spraying of individual spheres. Aggregates of several spheres should remain exceptional, as the modeling for individual spheres cannot account for the behavior of an aggregate of spheres.

The amount of spray can also be controlled by the time when compressor works. The control circuit is based on the monostable NE555 timer and MOSFET transistor. The button triggers a pulse of a controlled duration. The compressor is connected to the spray head through a tube. At the end of the tube is installed a filter to prevent contamination of the sprayed liquid by uncontrolled, foreign dust particles.

The images of the mirror taken with Panasonic camera, after five sequential depositions, are shown in Fig. 8.2.

| (a) | (b) | (c) |
| (d) | (e) | (f) |
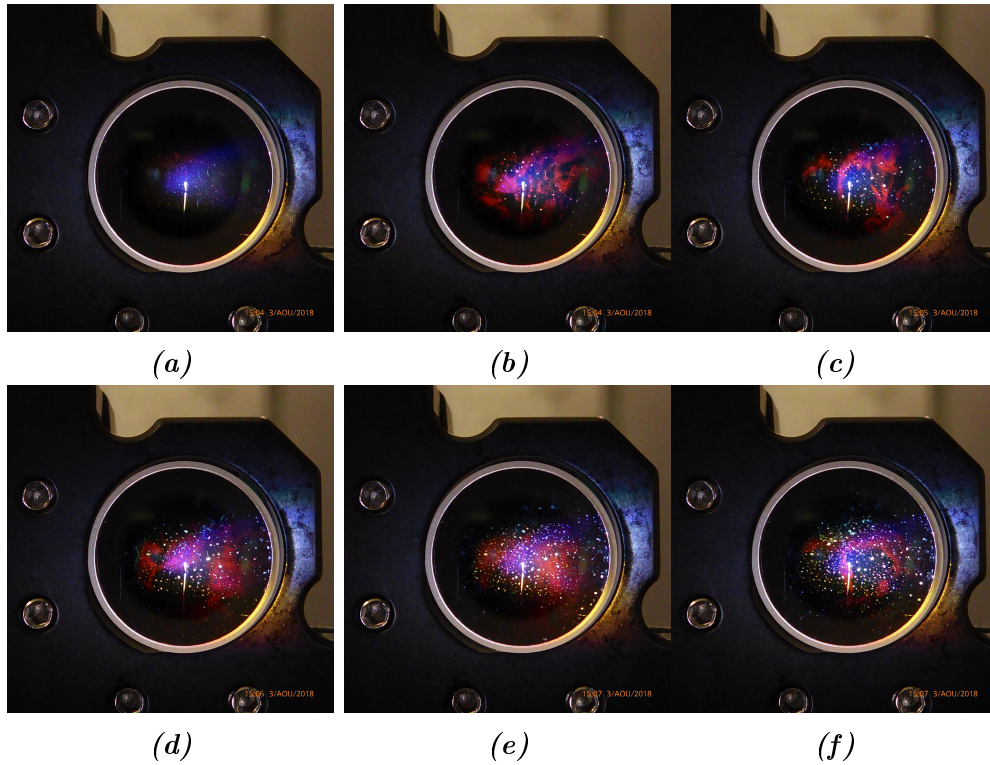
Figure 8.2: Images of the mirror after five sequential depositions. The image (a) is an image of the mirror before deposition. After each deposition steps, the particulate contamination increases.

The colorful patterns of the mirror indicate the potential presence of a film of chemical contamination. This effect is undesired as it can contribute to or modify the scattering signal. As the liquid of spheres mixture is clean at a high level, the only explanation can be the partial dissolving of the PLA plastic of the spray head. The problem of chemical contamination was completely solved

only after we switched to the dry powder deposition method (see Sec. 8.2).

Moreover, it can be observed that often the spots are not point-like but
have a finite extension, which is the indication of liquid droplets arriving at
the mirror and leading to non-uniform deposition of spheres. The liquid depo-
sition method was not continued, as improvement of this method is technically
challenging to improve.

8.1.2   Image processing

The image of the mirror with particles is captured with a Panasonic camera.
The next step is to count the number of particles of the mirror surface. For this
purpose, I have used a classical stars search algorithm[1] and I have prepared a
specific background rejection procedure.

The beam size limits the analysis area, as only that part of the mirror,
which is illuminated by the laser beam, would be observable on the signal.
The raw image in the area of interest is shown in Fig. 8.3a. Each of the
pictures is in three colors; however, for the analysis, it is not required. To
increase the contrast, I sum up the color layers and obtain a monochrome
image (see Fig. 8.3b). Background rejection is necessary to reduce the amount
of incorrectly reconstructed particles. The background is mainly caused by
the non-uniformity of the illumination. So the background is considered to
be a smooth change of the brightness. For each of the captured images, the
background is computed individually from the raw image. To calculate the
background, I average the image pixel brightness in the neighborhood area if
their intensity is lower than a certain level. This level should be higher than the
background and smaller than typical scattering amplitudes from the particles.
For the best performance, the level is adjusted manually for each image. Then,
the background is subtracted from the raw image (see the result in Fig. 8.3c).

(a)   (b)   (c)
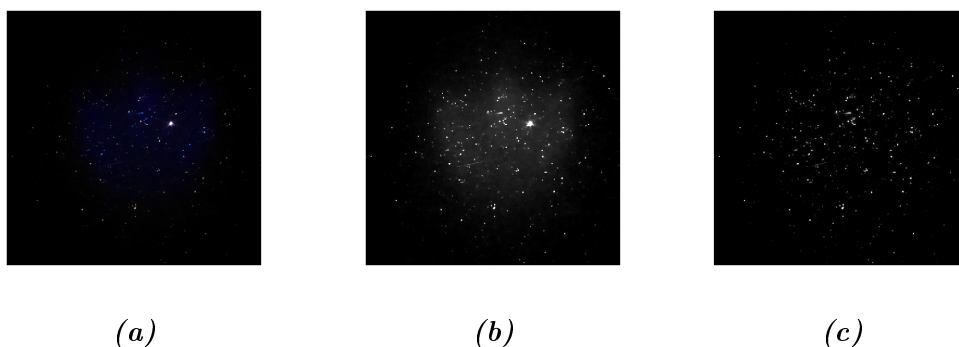
*Figure 8.3: Image processing. Illustration of the background rejection.
A raw image in the region of interest (a), Sum of 3 colors (to increase
contrast) (b), After background rejection (c). The background is removed
from the image as Gaussian smoothing of the image down a certain level
of amplitude.*

---

[1]http://www.astro.umd.edu/~bolatto/teaching/ASTR310/MATLAB/Lab03/

After the background is removed, for each image, the star's search algorithm is applied. The algorithm works in a loop. It finds the maximum peak on the image and then fits the peak with a 2D Gaussian. The output for each peak (particle) consists of the amplitude, the sizes along the major and minor axes (see the distribution of them in Fig. 8.4b), and the position of the peak. After the fit is complete, the peak is replaced by a constant value, which is estimated from the mean of the surrounding values, and the iterations continue until a certain level of peak amplitude.

Ideally, the limit is caused by scattering of the mirror surface. All the reconstructed particles in the image area in the center of the circles in Fig. 8.4a.

(a)	*(b)*
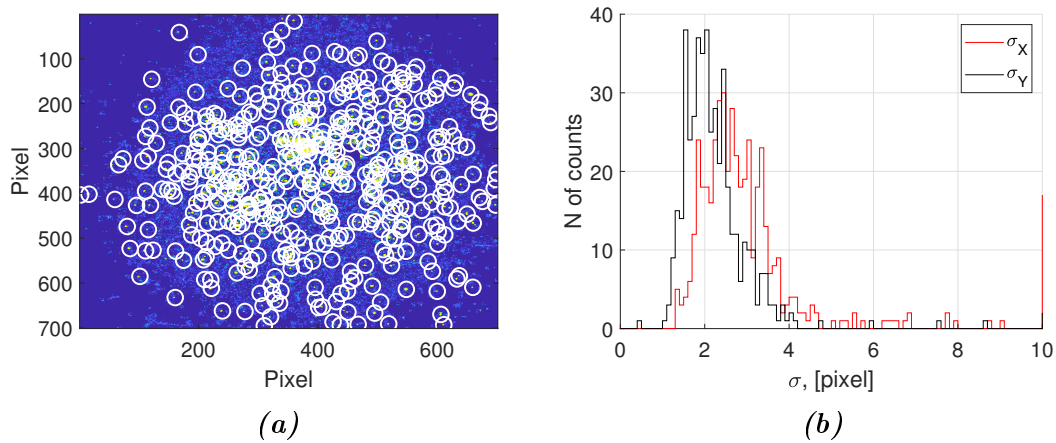
Figure 8.4: An illustration of the star search algorithm. A map with retrieved particles (a) and distribution of the size of these particles (b). Pixel size is 5.4 μm.

The disadvantage of this method is that only simple particle shape can correctly be described. In case of scratches on the mirror or in the case of particles of complicated or irregular shape, the result is biased. The achieved distribution of the particles (see Fig. 8.4b) does not signify the presence of only one sort of particles. Partial improvements can be achieved with the improvement of the camera system (see Sec. 8.1.4).

8.1.3 Preliminary coherent backscattering experiment

The idea of the experiment is to simultaneously measure the backscattering signal, capture the images of the mirror, and sequentially deposit particles on the surface. For this, we built a new free space part of the interferometric setup at 1.55 μm (see Chap. 5). The image of the installation is shown in Fig. 8.5. The layout of the interferometric part of the free space part of the setup is quite the same as before: the collimated beam is phase-modulated on a super-polished mirror, which is also used to direct the beam to a contaminated surface. The beam reflected by the contaminated surface is absorbed by a beam dump. The part of the setup with clean optics and with the contaminated surface is placed on different optical tables and are separated by a plastic film
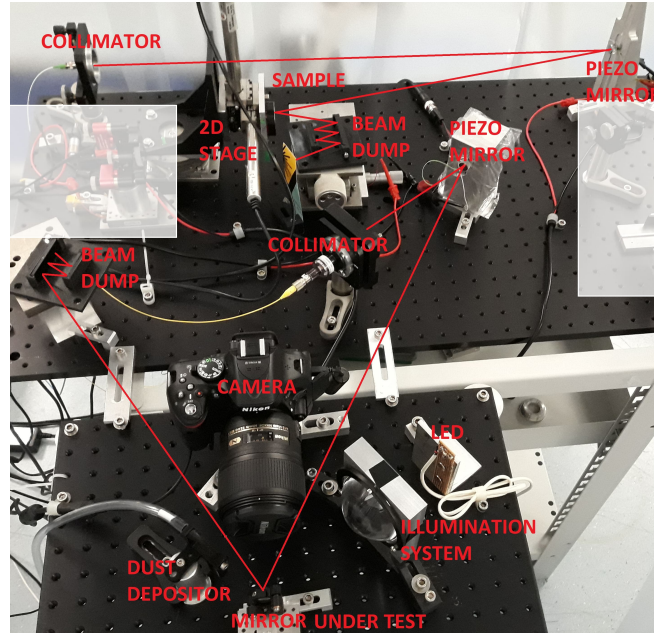
Figure 8.5: The image of the free space part of the setup for backscattering measurements due to surface roughness (top of the picture) and due to particle contamination (bottom of the image).

(not shown on the figure) to help prevent silica particles from reaching the clean part of the setup. Except this, in the setup is present a particle deposition system, a Nikon camera with a 60 mm lens, and a white-light illumination system. For the fine focusing of the camera, the mirror is installed on the translation stage.

To identify the region of interest for image processing, I highlight the area on the mirror with a red laser. For this, I connect a red, pigtails laser diode to the collimator. The red beam propagates by the same path as an interferometric beam. The red beam spot on the test mirror is captured by the camera and used later in the analysis.

The results of the experiment were presented in the ICSO 2018 conference [31]. However, there is a huge space for misinterpretation and error in this experiment. The main problems are divided into four groups:

1. Interferometric signal measurements. The backscattered light from the mirror with particles should be modulated at frequency 1 Hz to reduce the stray light contribution from other components. Beside of this, the mirror should be tilted to achieve an average value of the speckle (see Sec. 5.4.2). In this way, the conventional measurements of scattering may be more appropriate than interferometric. Another problem is that during modulation and tilt, some of the particles would move or fall off from the mirror if it is not turned upwards, so the orientation of the mirror plane should be horizontal.

2. The idea of using a camera instead of a microscope does not work in this case. The image quality may not be sufficient to observe individual

particles, with good enough reliability (see Sec. 8.1.4). So the amount of the identified particles significantly depends on the parameters of the image processing routine.

3. Substrate quality. The mirror for particle depositions may not be the best surface. Nevertheless, this surface should be super polished.

4. As discussed in Sec. 8.1.1, the liquid deposition system of particles is not acceptable due to the introduced contamination.

The first problem is somewhat technical, and it is easy to solve. Also, we switch to dry particle deposition with powder and a brush and use only super polished mirror surfaces for the experiment. A vertical setup was built as an upgrade of the experiment (optical table is vertical, and the surface under test is horizontal). The last problem to solve is particle recognition. In the Sec. 8.1.4 I will introduce an improved technique of image processing.

8.1.4 Improved image processing

Certain improvements in particle recognition can be made by the use of a raw format of images in image processing. The image processing of five steps:

1. Conversion of the raw image to a format readable under Matlab[2].

2. Linearization. Nikon camera saves a nonlinear quantization of the original 14-bit signal. The linearization curve is in Fig. 8.6a. For example, in Fig. 8.6b is an arbitrary pixel value as a function of exposition time (measured in experiment) with corrected in MatLab (black) and uncorrected (red) linearization.

(a)   (b)
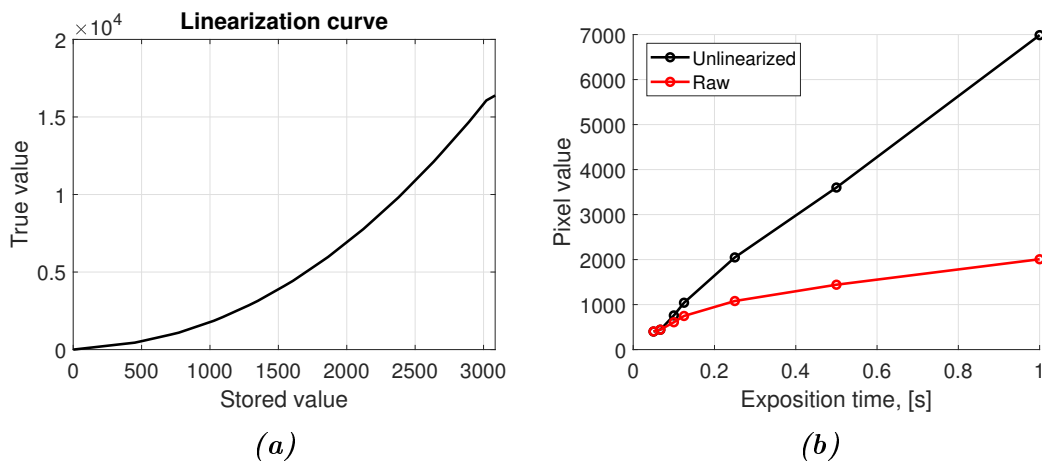
Figure 8.6: Linearization curve for Nikon D5200 (a) and Pixel value as a function of exposition time (b).

---

[2] www.blogs.mathworks.com/steve/

3. Background rejection. The background is defined as the initial picture
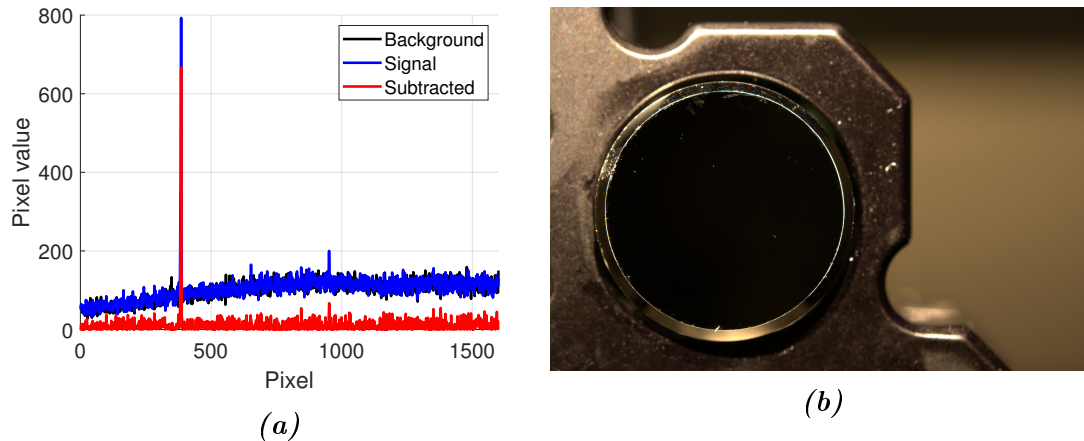   of the clean mirror (ideally without deposited particles), as shown in
   Fig. 8.7b.

(a)

(b)

*Figure 8.7: Illustration for background rejection technique (a) and image
of the mirror (b) which was used as a background reference. Exposition
time is 1/8 s. A peak in (a) corresponds to a particle.*

4. Demosaic of Bayer array. The image is organized in the Bayer filter ar-
   ray (BGGR for Nikon). To process demosaicing, I used the corresponding
   Matlab function. "Demosaic"[3] converts the Bayer pattern encoded image
   to the true-color image, RGB, using gradient-corrected linear interpola-
   tion for a specific Bayer pattern.

5. The same as before, star search algorithm[4] was used to find the particles
   in the image.

Ten sequential depositions of the 16 μm particles were performed. After
each deposition, a picture was taken. The amount of recovered particles as a
function of picture number is given in Fig. 8.8a. The most probable size of
the particles corresponds to the size of the deposited particles of 16 μm (see
Fig. 8.8b).

So with a dry method of deposition, we succeed to deposit small quantities
of the particles of the mirror surface. The dominant size of the reconstructed
particle corresponds to the expected one. However, significant uncertainty in
size distribution and lousy image quality does not allow us to be sure about
the quality of particle distribution and identification. So, we conclude that
imaging of the contaminated surface with a microscope would be preferable.
This idea is realized in the next section.

The idea of using a camera instead of a microscope does not work well
enough with good reliability since the size of the sphere is close to the point
spread function of the camera system. However, imaging of the optical surface

---

[3]https://fr.mathworks.com/help/images/ref/demosaic.html
[4]http://www.astro.umd.edu/~bolatto/teaching/ASTR310/MATLAB/Lab03/
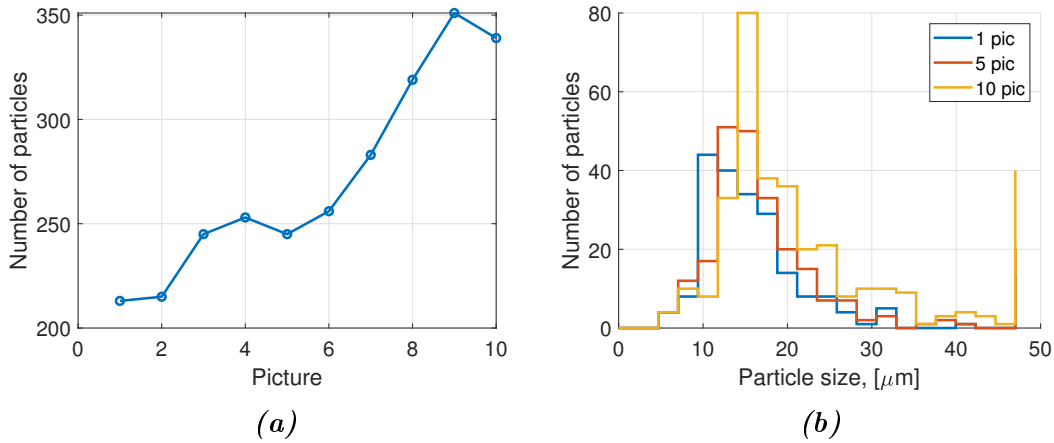
*Figure 8.8: The number of recovered particles as a function of the picture
number (a) and histogram of the particle size (b). Pic 1 is the first picture
after deposition, Pic 5 is after five depositions, 10 after ten depositions.*

can work in stray light analysis for visual inspection and identification of big
particles.

8.2 Particulate coherent experiment at 1.06 micron

A significant improvement of the experiment was made by reconsidering all the
aspects of the measurement procedure. The main improvements which were
done in comparison to the initial idea are dry deposition of the spheres, the
horizontal orientation of the surface with spheres, multiple interferometric mea-
surements of the backscattered light under slightly different conditions (speckle
scan), particle recognition with an optical microscope instead of camera.

The biggest challenge of the experiment was to measure the correct amount
of particles on the mirror. We conclude from Sec. 8.1.4 that with a camera, it
is impossible to identify with sufficient confidence, even the 16 μm deposited
spheres. So we changed the approach of the experiment. Instead of sequential
deposition of spheres on the same sample, we had prepared four samples with
a sufficient amount of calibrated spheres for convenient detection with inter-
ferometric backscattering setup. It is to say that amount of spheres should be
so much that backscattering from them will be at least one order higher than
the backscattering from a substrate. Only one type of spheres (2 μm, 4 μm,
8 μm, 16 μm) was deposited on each sample. Back-scattering from the sam-
ples was measured with the interferometric setup (see Sec. 8.2.2) in Artemis
laboratory, and then observation and counting of the spheres were made at
Thales Alenia Space with an optical microscope (see Sec. 8.2.1). The results of
the measurements were analyzed and compared with Mie's theory predictions
(see Sec. 8.2.3).

We had also changed the test surface. Instead of the super-polished mirrors,

we have used a Si wafer. The super polished side of them has a low scattering, and so it is appropriate for the interferometric measurements, and the contrast between white spheres and dark Si wafer surface should improve the image quality.

8.2.1 Processing of the images

To take the pictures of the Si wafer with spheres, we use Olympus BX53M[5] microscope. The objective of the microscope was changed for each sample to achieve the best quality of the image.

The picture of the full Si wafer (2 inch diameter) with deposited 16 μm spheres is shown in Fig. 8.9a. The image obtained with a microscope is shown in Fig. 8.9b. The 16 μm spheres are clustered in the center. Around the center is a dust cloud. We suppose that the residual of the humidity caused this effect during the deposition process. A droplet of liquid with spheres dries on the surface and leave the dust. The droplet dries from the sides, so the spheres concentrate in the center. This effect is not intuitive, and it is not visible without a microscope. That is why excellent imaging of the surface is necessary for the experiment. Definitely, the uniform deposition of the particles is always challenging, and the next try on spheres deposition was far better (based on image comparison).

(a)

(b)
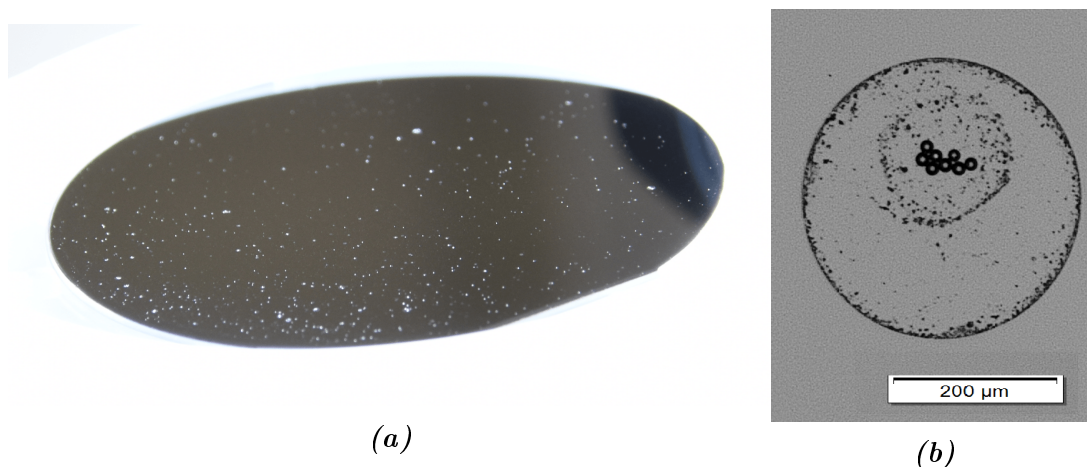
Figure 8.9: The picture of the 2 inch Si wafer with 16 μm spheres under grazing light (a) and a microscope image of a dried droplet on the same sample (b). The picture of the Si wafer was made by Séverine BLANC. The illumination of the microscope is from the top. The colors of the microscope image are inverted.

The physical interpretation of scattering from this cluster is difficult. However, the images can be used to build the image processing routines. As the images are of high quality, the simple image format conversion with built-in *imfindcircles* function of the MatLab image processing toolbox was used. The

---

[5]https://www.olympus-europa.com/ssd/de/BX53M.html

result of the image processing is summarized in the Tab. 8.1 and Fig. 8.10. For each of the samples, more than a hundred images were taken (column four in Tab. 8.1). Each of the images was taken on the independent area of the sample. Each sample was observed with an appropriate objective (Image scale in Tab. 8.1). The goal of the changing objectives is not only to improve the image quality but also to increase the analyzed area per image (column 3 in Tab. 8.1). The total amount of spheres recovered in all images for each sample is given in the last column of the Tab. 8.1.

Table 8.1: The result of the image processing. Each row corresponds to the sample with the deposited spheres of diameter given in the first column. The second column corresponds to the used objective and so the image scale. The third column is the square of the analyzed area per image, and the fourth column is the number of analyzed images. The last column is the total number of spheres that were found on all the images of the sample.

Sphere diam.	Im. scale	Square/image	Num. images	Tot. numb. of spheres
2 μm	50 μm	0.22977 mm^2	130	8599
4 μm	50 μm	0.22977 mm^2	141	3936
8 μm	100 μm	0.91909 mm^2	143	517
16 μm	200 μm	3.6764 mm^2	88	129

The distribution of the diameter of the sphere for each of the samples is given in Fig. 8.10. From this, I conclude that the spheres are well reconstructed in images, and the acquisition of the images with a microscope is an appropriate method.
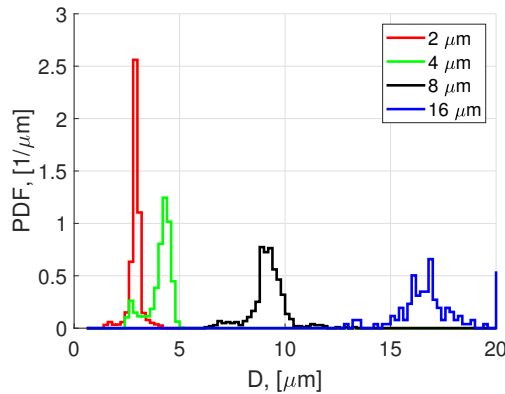
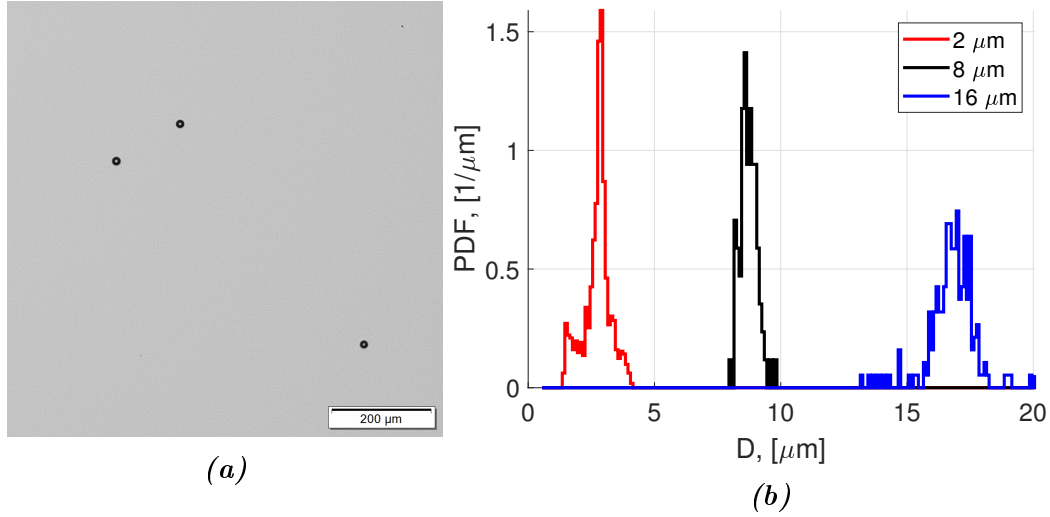*Figure 8.10: Distribution of the size of the reconstructed spheres for each sample.*

However, the clustering of the spheres on the samples is not a desired effect and the experiment should be repeated.

The second time I had used the well-dried powder of the calibrated spheres. The deposition was performed with clean brushes without contact with the surface. The aim was to deposit small quantities of the spheres, so they were

basically invisible on the surface. The disadvantage of this was that control
of the deposition could not be performed. It turns out that optical control
of the sample with 4 μm spheres didn't recognize any of them on the optical
surface. However, with 2, 8, and 16 μm spheres, the distribution of spheres
was perfectly uniformly random and without any clustering (see Fig. 8.11a).
The distribution of the spheres after image processing is given in Fig. 8.11b.
The result of the image processing is summarized in the Tab. 8.2. So the

(a)

(b)

Figure 8.11: Microscope image of 16 μm spheres at the second try (a)
and distribution of the size of the reconstructed spheres for each sample
(b).

Table 8.2: The result of the image processing for the second try of dry
sphere deposition. Each row corresponds to the sample with the deposited
spheres of diameter given in the first column. The second column cor-
responds to the used objective and so the image scale. The third column
is the square of the analyzed area per image, and the fourth column is
the number of analyzed images. The last column is the total number of
spheres that were found on all the images of the sample.

Sphere diam.	Im. scale	Square/image	Num. images	Tot. numb. of spheres
2 μm	50 μm	0.22977 mm^2	113	1623
8 μm	100 μm	0.91909 mm^2	116	85
16 μm	200 μm	3.6764 mm^2	109	188

samples are well prepared. The spheres on each of the samples have the same
diameter, as shown in Fig. 8.11b. The distribution of the spheres on the surface
is statistically uniform. These samples are well suitable for the backscattering
measurements.

8.2.2 Interferometric measurements

For the interferometric measurements, I used the set-up at 1.06 μm (see Chapter 6) with reconfigured free space part of the setup. All the components are placed on a small optical table (see Fig. 8.12a) in vertical orientation. The

(a) The setup seen from above

(b)

(c)
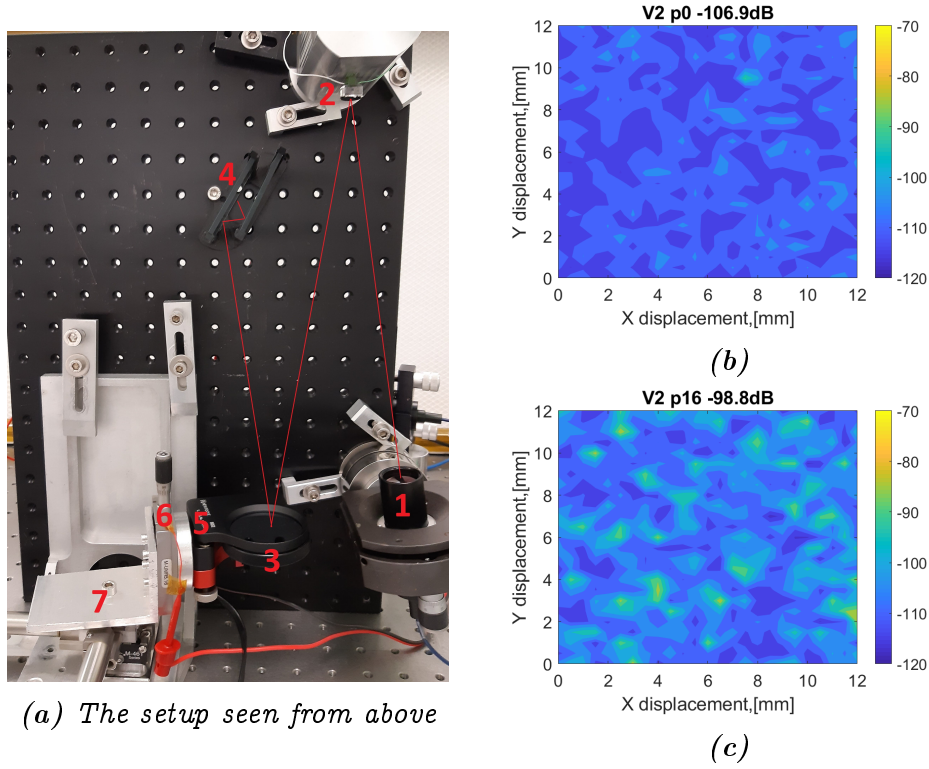
Figure 8.12: The free space part of the interferometric setup for the backscattering measurements of the contaminated samples (a). The map of the interferometric scan of the clean Si wafer (b) and after 16 µm spheres deposition (c).

red line is an approximate beam path. The beam from the collimator (1) is modulated by the super-polished mirror (2) and then falls on the sample under test (3). The reflected beam from the sample is directed to the beam dump (4). The sample is a 2-inch diameter Si wafer installed in the Picomotor rotational stage (5). The latter is placed on the small translation stage with installed piezo for the slow modulation of the sample (6). This construction is installed on the 2D translation stage (7) to scan the surface of the sample.

In this configuration, the optical table is vertical, so that the surface under test is horizontal. This allows holding the particles on the surface during the measurements. The sample was placed in the focus of the beam. For the setup, we use a 1718176 collimator with a small focal distance (see Fig. 6.7). The beam dump has the same structure as in 1.06 μm setup (see Sec. 6.1.5). The HA15 glass holder was designed, and 3D printed for this setup in Artemis laboratory. The scanning area of the translation stage is 12x12 mm^2 with a step of 0.5 mm. Each point is measured during 20 s. It takes about 6 hours to

make the full scattering map. Besides this, we change the incidence angle by a small fraction with the Picomotor stage. For each of the samples, from 3 to 4 maps was taken (under slightly different incident angles). The necessity of taking so much data is caused by the speckle behavior of the scattered light. To achieve reasonable mean value, averaging over big data samples should be taken. This is one of the reasons why interferometric measurements are not widely used for contamination measurements.

The backscattering fraction for each measured point was extracted following the procedure described in Chapter 5. The examples of the measured map for a clean sample and sample with deposited spheres are given in Fig. 8.12b and Fig. 8.12c correspondingly. The measured backscattering fractions are 5.8e-10, 2.9e-10, 2.5e-10 for 2, 8, and 16 μm spheres correspondently.

8.2.3 Results and discussion

In this section, I compare the measured backscattering with estimates obtained from the Mie theory [6]. The calculations in this theory are difficult, but codes have been implemented already long ago, and are available on the web. To calculate the backscattering in this theory, I use a BHMIE code[6]. This is one of the most used codes for scattering calculation. It is based on the ancient version of the code listed in the Ref. [6]. The input of the Mie calculation requires size parameter $x = 2\pi a/\lambda$, where λ is the wavelength, and a is the radius of the sphere. Another parameter is the complex refractive index of the sphere material ($n = 1.4496 + j \times 0$ was used), and the number of computational points between 0 and $\pi/2$ (here was used 100, but it does not affect the result).

Let us consider a particle illuminated with irradiance I_i. According to the theory, the amount of energy scattered in the unit solid angle in direction (θ, ϕ) is

$$\frac{I_i |\vec{X}(\theta, \phi)|^2}{k^2},$$ (8.2)

where k is wave vector and $\vec{X}$ is vector scattering amplitude.

For the backscattering direction ($\theta = 180^o$), the square modulus of scattering amplitude is:

$$|\vec{X}(180^o)| = |S_2(180^o)|^2 \cos(\phi)^2 + |S_1(180^o)|^2 \sin(\phi)^2,$$ (8.3)

where elements of scattering matrix $S_2(180^o) = -S_1(180^o)$ and can be computed. The value of $|\vec{X}(180^o)|$ for each sphere diameter is given in the third column in Tab. 8.3. It should be mentioned here, that to calculate this quantity, the sphere was considered isolated, without the proximity of the surface. This may affect the precision of the prediction.

The backscattering of the surface with spheres has two contributions: backscattering from the spheres and the surface.

$$b_{total} = b_{Mie} + b_{surface},$$ (8.4)

---

[6]http://scatterlib.wdfiles.com/local--files/codes/bhmie-matlab.zip

where b_{Mie} is backscattering contribution from the deposited spheres. It is proportional to the averaged number of particles N_p:

$$b_{Mie} = \frac{N_p}{\pi(b_r)^2} \Omega \frac{|\vec{X}(180°)|^2}{k^2}. \tag{8.5}$$

Here was taken into account that, if under the illumination of the beam are N_p particles of radius a and $b_r = 0.44$ mm is beam radius on the surface. The capturing solid angle is $\Omega = \pi(\lambda/(\pi 2 b_r))^2$. The wavelength is $\lambda = 1.06$ μm. The computed value of the Mie backscattering is given in the fourth column in the Tab. 8.3.

The N_p value represents the number of particles seen by the beam. To compute this value, first, I compute the averaged number of particles on the surface. It is the total number of all particles on all the images divided by the total area under test. The number of backscattering particles seen by the beam is the illumination square occupied by the beam on the sample multiplied by the averaged number of the particles on the sample. This computed quantity is given in the second column in the Tab. 8.3.

The backscattering by the surface was measured when the surface was clean (without particles). The measured backscattering over all the map and all tilt angles is averaged, and then the value of surface roughness (-106.4 dB) is subtracted. This result for each sample is summarized in Tab. 8.3 in the last column.

Table 8.3: The result of the interferometric measurements and comparison with the Mie theory.

Sphere diam.	Aver. Number part	$|\vec{X}(180°)|$, $[1/m^2]$	b_{Mie}	BSF meas.
2 μm	37.16	10.2	0.35e-10	5.8e-10
8 μm	0.47	799.1	0.35e-10	2.9e-10
16 μm	0.28	813.9	0.21e-10	2.5e-10

The computed values of the backscattering with Mie theory are about one order lower than the measured values. The possible explanation of this can be the effect of surface on spheres backscattering and partial reflection of the amplitudes scattered from the spheres. From an experimental point of view, the most significant disadvantage of the experiment is the lack of a microscope in the neighborhood of the interferometric setup. The transportation of the samples to TAS and back definitely cause the release or redeposition of the spheres and bias the measurements. The lesson learned is that the camera-based counting system is not well suitable for this experiment.

The possible improvement of the experiment can be by performing two experiments in the same experimental room (ideally without touching the sample). Multiple measurements should be done to see the trend between the number of deposited spheres and the backscattering signal. As the full measurements of one sample took almost 24 hours, the conventional setup based on inherent scattering may be considered instead. Due to the complexity of the

scattering in the case of complex geometry, some theoretical research should be performed.

8.3 Contamination control

During the AIVT phase of the space satellite construction, the primary source of contamination on the optical surface is the particles present in the volume of the cleanroom. It is practically impossible to eliminate the deposition of the particles. However, it is possible to reduce them to a sufficient level. For this, certain precautions are made: the air circulation in the cleanroom, high-quality filters on the input airflow, overpressure of the volume of the cleanroom, regular cleaning of the cleanroom, and of all the parts inserted in it. The appropriate cleanroom class will depend on the contamination requirements for the units to be integrated. However, the most significant source of particles in the air of the cleanroom is working personal. Certain precautions are required for operation in the cleanroom: hair cover, booties, lab coat, face masks, gloves, etc. The last but not least system is a particle counting system. This is required to certify that operation in the cleanroom is performed at a satisfactory cleanliness level. The particle counting may be conducted continuously or occasionally. Labs that work on satellite assembly is required continuous measurements of particles in the cleanroom. For example, for ISO5 clean room, the level of contamination for optical surfaces should not exceed one-two ppm/day (may vary).

The systems of continuous particle counting are expensive and not always required for less demanding projects. Nevertheless, it is good to have a particle monitoring system in the cleanroom. An alternative to expensive particle counters is provided by the widely available SPS30 counters (see Fig. 8.16) for air control. In this way, we can perform continuous measurements of particles

Figure 8.13: Image of a SPS30 sensor

in several positions of the cleanroom and increase the cleanliness performance of it.

In this section, I describe a cleanroom contamination control system (see Sec. 8.3.1), which I built for the cleanroom that hosts the LISA stray light experiments at ARTEMIS laboratory. The building block of the system is a sensor module with SPS30 particle counter on board. It is a Particulate

Matter Sensor for Air Quality Monitoring and Control. The measurement principle of the particle counter is based on laser scattering. This sensor is not designed for operation in the cleanroom and is not calibrated according to ISO standard. SPS30 counter can perform simultaneous measurements in four mass (PM1.0, PM2.5, PM4, PM10) and five number (PM0.5, PM1.0, PM2.5, PM4, PM10) concentration channels. PM here indicates particulate matter and will be explained in detail in Sec. 8.3.2. Besides this, the sensor provides a typical particle size. The sensor's acoustic noise does not perturb the interferometric measurements. The results of the particle monitoring are compared with the MetOne particle counter. The sensor channels are calibrated in accordance with it. The measurement floor of the sensor will be studied in section 8.3.2.

8.3.1 Clean room contamination control system (CRCCS)

The basic block of the CRCCS is a sensor module. It is shown in Fig. 8.14a without enclosure. The green block in it is an SPS30 particle sensor. Besides this, it has a temperature, humidity, and pressure sensors (HIH8000 and MS5837-02BA). They all are connected to a WiFi module based on ESP8266m, which works like a webserver. This web server has two HTML accessible, for example, from an internet browser. The root HTML page (IP/) contains all the data from all the sensors, and the page (IP/clean) is used for cleaning of the particle sensor (for this, the fan of the sensor is operated at the maximum speed for 10s).

(a)   (b)
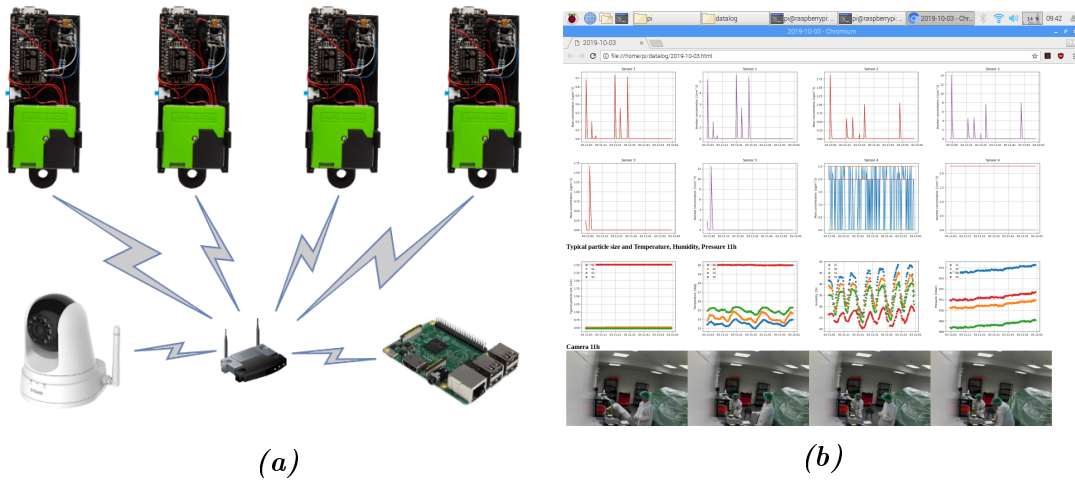
Figure 8.14: The network of the CRCCS (a) and typical 1h report of the automatically generated webpage (b).

Each sensor requires only one standard power supply of 5V. The powering of the device is done by USB and can be provided by power-bank or wall-plug power supply. No additional cables are required. This makes the sensor module highly mobile, and it allows providing measurements at any place in the cleanroom.

CRCCS is based on the IoT (Internet of Things) concept (see Fig. 8.14a). It manages all the sensors, collects, and analyzes the data. In our CRCCS,

we implement only four sensors. However, the system is easily scalable, and any of the sensors can be used. The data collection and analysis center is Raspberry Pi (single-board computer). Besides this, the system also contains a WebCamera. It takes pictures if a certain level of contamination is exceeded. This was done to determine the source of the highest contamination income.

The data are visualized in the form of plots on a dedicated HTML webpage (see Fig. 8.14b). For each day, a new webpage is created. The page is updated each hour. The data acquisition and visualization were made on Python and Bash scripts, which run on the Raspberry Pi.

Under the regular operation of the cleanroom, only a few particles are detected per hour. However, in case of emergency (for example, when air circulation in the cleanroom is stopped), the CRCCS is very useful. The example of the output data of one of the sensors of the CRCCS is shown in Fig. 8.15. During this day, the interferometric measurement was performed at 1.06 setup. The noise of the air circulation perturbs the measurements, so it must be off during the measurements. Of course, during the period with not working air circulation, the amount of particles highly increases. This is well seen on mass the same as on number concentration channels (see Fig. 8.15b and Fig. 8.15c). Except for the air circulation, this system causes overpressure in the cleanroom and temperature control (see Fig. 8.15a). The period of turned off air circulation is well seen in this data as well. In a time when the air circulation is on, only a few particles are detected, and the temperature in the cleanroom is quite stable.

(a)   *(b)*   *(c)*
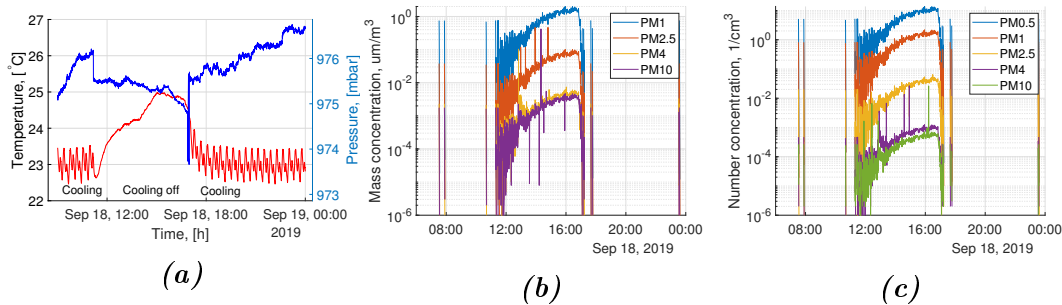
Figure 8.15: Data collected with CRCCS during shut down of air circulation in the cleanroom: temperature and pressure (a), mass concentration (b), number concentration (c).

The system is easy to use, and it worked without any crash during the test period of about eight months. The data recorded by the system are particularly useful when an incident happens with consequences on the cleanroom cleanliness.

## 8.3.2   Comparison of SPS30 and MetOne particle counters

To check the validity of the measured data with the SPS30 sensor, I perform a calibration with certified MET ONE HHPC 3+ particle counter. For compari-

son of the two counters, I launch simultaneous measurements for a duration of 62.5 hours.

The comparison of the measured data requires some analysis. The Met One counter provides data in ISO standard. In this standard, a discrete-particle-counting instrument is used to determine the concentration of airborne particles, equal to and greater than specified sizes, at designated sampling locations [27]. However, SPS30 counted measures in PMXX format, i. e. the number of particles which diameters are XX micrometers and smaller. So first of all, the data from PM need to be converted to ISO standard. For example, PM10 is the concentration of all particles smaller or equal 10 μm, and the value of concentration in 0.3 μm channel is the number of all particles bigger and equal to 0.3 μm. So PM10 and 0.3 μm is approximately equal. For the channel 0.5 μm, we need to take a difference between PM10 and PM0.5 and for channel 1 μm between PM10 and PM1.

An example of the acquired and converted data from the SPS30 sensor is given in Fig. 8.16. The ISO8 levels shown in Fig. 8.16 are given as maximum
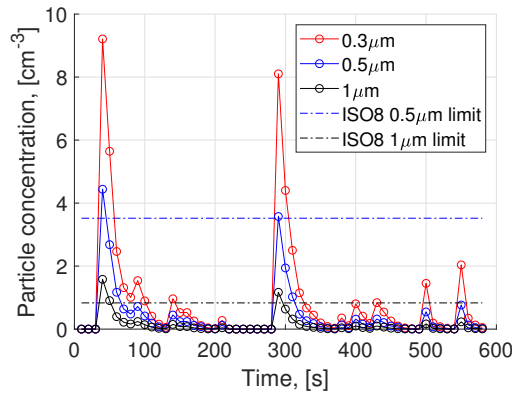
Figure 8.16: Measured dust evolution with a time step of 10s with Sensor 1.

particle concentration levels in the ISO8 class clean room, and it is specified in the ISO14644 standard [27]. This standard specifies the procedure of the cleanroom certification. The CRCCS goal is not to certify the cleanroom, but rather to monitor a problem and send an alarm. The acquired data of the system need a human eye to identify and eliminate the problem. To simplify the task, the webcam takes a picture each time, each time a given particle level is exceeded. Usually, the increase of particles in the cleanroom is caused by human activity.

For the comparison of the two sensors, I perform the measurements in all available channels of SPS30 and in three channels (maximum possible) of MetOne: 0.3 0.5 and 1 μm. MetOne measures one minute (2.83 L of air pumped) every 15 minutes when SPS30 performs measurement during 1 s each 1 minute. The values measured with SPS30 have averaged over 15 points for better comparison. The result of the comparison in three number concentration channels is presented in Fig. 8.18. A good agreement of all sensors is observed.
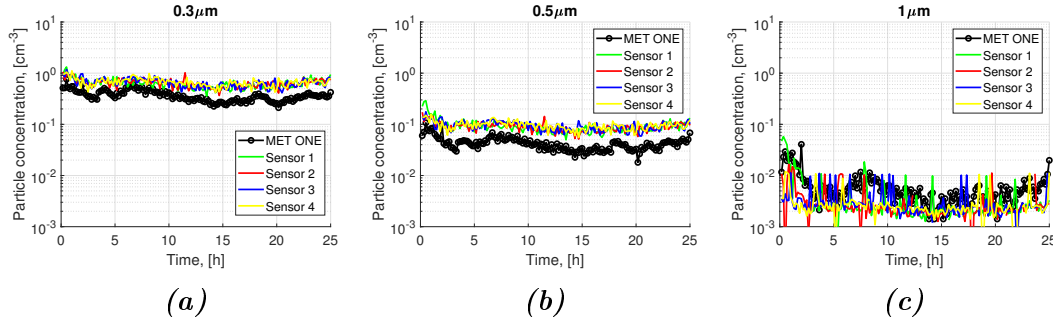
*Figure 8.17: Comparison of data from a MetOne counter and four SPS30 counters, for the three different channels of the MetOne counter.*

The number of particles in 0.3, 0.5 channels is slightly over-evaluated comparing to Met One HHPC3+ counter. We see that the noise floor of SPS30 does not allow to go down to lower levels of dust, but it is sufficient for ISO8 cleanroom [27].

Calibration

By simultaneous measurements of MetOne HHPC3+ and SPS30 counters the calibration of the sensor was performed. MetOne performs one measurement (volume 2.84 L) every 10 minutes and the SPS30 measures during 1 s, every 10 s. For each MetOne point, the corresponding mean of 60 measurements with SPS30 is estimated. Achieved relation (see Fig. 8.18) was fitted by a linear curve of type $ax + b$, where x is the measurement with MetOne, a is a calibration coefficient, b – "noise floor" in cm^{-3}.

(a) $0.3\mu m$=PM10   (b) $0.5\mu m$=PM10-PM0.5   (c) $1\mu m$=PM10-PM1
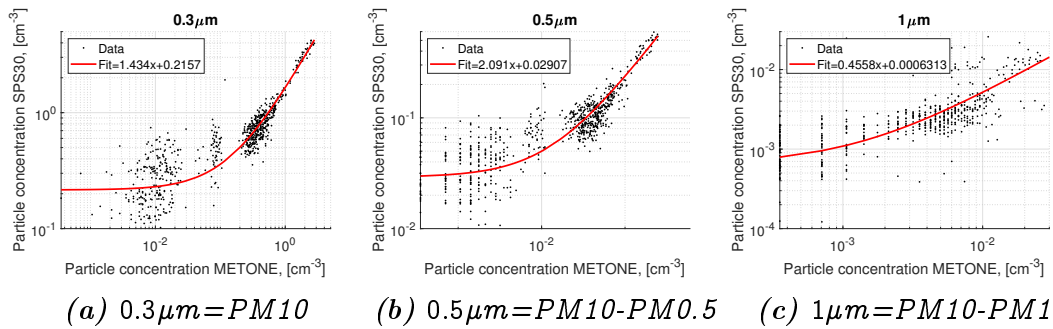
Figure 8.18: Calibration curves for the three channels

The results of the fit for the three channels are summarized in Tab. 8.4.

The data were measured in ISO6, ISO7, ISO8 clean rooms. SPS30 counter somewhat over evaluates the number of particles at $0.3\mu m$ and $0.5\mu m$ and under evaluates at $1\mu m$. Nevertheless, the achieved results show that the sensor can be used to monitor contamination in an ISO8 cleanroom.

So I have created a clean room cleanliness control system, which is able to operate in ISO8 clean room and to give a reasonable estimate of the number of particles in the cleanroom. The system is cheap and very flexible; it is

Table 8.4: The summary of of the calibration coefficient and Noise coefficients. The calibration coefficient has no dimension and that the noise floor parameter has the dimension of cm^{-3}.

	Calibration coefficient			Noise coefficient		
Sensor	$0.3\mu m$	$0.5\mu m$	$1\mu m$	$0.3\mu m$	$0.5\mu m$	$1\mu m$
1	1.4332	2.1128	0.6037	0.2027	0.0265	0.0009
2	1.4848	2.1708	0.4487	0.2131	0.0274	0.0017
3	1.5077	2.2370	0.2426	0.2284	0.0282	0.0015
4	1.5752	2.3389	0.3585	0.4702	0.0627	0.0020

easy to operate and modify. I hope that the idea of using multiple general-purpose particle counters in the cleanroom will be widely used and improve the cleanliness performance and practice of low budget laboratories.

8.4 Conclusion

The scattering due to contamination is an essential part of the stray-light analysis. In this chapter, I had described the experiments conducted in this field. A new, original experimental setup was built from an idea to hardware implementation and final data analysis. Especially for this experiment was built a particle deposition system, designed image processing routines, built a compact free space part of the interferometric setup, etc. Almost all the components of the setup were home-made in the Artemis workshop, all the software was written from zero, and much time was invested. However, significant technical difficulties caused the reconsideration of the initial experiment (see Sec. 8.1). All the main problems were solved in the new significantly improved setup (see Sec. 8.2). This time was used as a microscope imaging, speckle scan over multiple locations, vertical stage for interferometric measurements. The obtained experimental result was compared with Mie theory.

However, I must claim that the difficulty of the interferometric measurements due to speckle properties of scattered light push to the idea to switch on conventional measurements of the scattering. Indeed, the studies on the contamination impact should be performed. Nevertheless, for these systems, the interferometric setup brings in a significant complexification of the studies. Let us hope that the experimental results and difficulties raised during this study and, what is more important, the proposed solutions listed in the chapter will be useful in the development of similar experiments.

Besides this, I have developed a cleanroom contamination control system (see Sec. 8.3). It is a cheap system to control the air cleanliness in the cleanroom. This is a budget solution for the small labs with clean rooms of class ISO8 or similar. The system was designed, built, and is used and progressively improving in the Artemis laboratory.

Chapter 9

Conclusions and Perspectives

The LISA is a space-based GW observatory now in Phase A. The measurements of GW are performed by heterodyne interferometric phase measurements. In the case of the presence of any light which was not intended into the design (stray light), the precise phase measurements can be perturbed. The stray light can have a different origins (see Chapter 2), but one of the most contributing is scattering. This thesis considers different sources of scattered light: micrometeoroids (Chapter 3), microroughness (Chapters 4, 5, 6), contamination (Chapter 8) and scattering inside optical fibers (Chapter 7).

Indeed, the scattering in classical understanding assumes that the incident light is incoherent and predicts a smooth angular dependence. However, interferometers are operated with coherent, collimated beams, and "coherent scattering" generates an optical field with a grainy structure called speckle. This type of scattering can depend rapidly on parameters such as angles of incidence and, for that reason, can degrade the noise floor of the instrument. This thesis is dedicated to experimental and modeling studies of the influence of the coherent scattering on interferometric measurements.

9.1 Main contributions

To mitigate the problem of stray light related noise in LISA, specific methods have been used: heterodyne measurement, polarization-based method, and thermal stability. Optical modeling has used conventional methods based on the BRDF approach. In my thesis, I also used a BRDF approach to study scattering due to micrometeoroids, but I also developed new models, instruments, and methods to describe and study coherent scattering from optical surfaces.
.

- In section Chapter 3, I propose a method of the stray light estimate due to micrometeoroid damage. The method can be applied for any piece of optics exposed to the space environment, but in my study, I apply it to the damage of the primary M1 mirror of the LISA telescope. The method consists of four steps: calculation of flux of micrometeoroids, which arrives on the optical surface, calculation of damage crater diameter

and corresponding ejected mass, calculation of the corresponding BRDF with Peterson model, and 1246C standard and the last step is an optical simulation in FRED. With this study, I find that, under the assumption that ejected matter can contaminate the M1 mirror itself, contamination due to mass ejection gives a significant contribution to stray light (BSF$\approx$ 10^{-12}) in comparison to crater damage (BSF$\approx 10^{-14}$). The method is straightforward to apply, and it can be used for any optical instrument with minor parameter changes.

- To model coherent scattering, I have developed a model of coherent backscattering. The model is based on the Fraunhofer solution of the wave propagation equation. The scattering is represented as a complex aperture, where the amplitude part is given by the properties of an illuminating beam, and the phase part contains information about surface height distribution. This model converges to the conventional Harvey-Schack model from one side and correctly describes the dimensional and statistical properties of coherent scattering from the other. It is used to explain the experimental results, and potentially it can be used to study the properties of coherent scattering.

- To measure the coherent scattering. I built two homodyne interferometric setups, at 1.55 μm (Chapter 5) and 1.06 μm (Chapter 6). These fibered interferometers allowed me to measure back-scattering down to $< 10^{-13}$ in fractional power. I could study the speckle properties of backscattering: dependence on the spot position or the sample orientation, intensity, and amplitude distributions. The average properties have been compared with the BRDF approach of the optical surfaces (mirror, super-polished Si wafer). Besides this, I check the convergence of the coherent scattering to the incoherent, classical one in simulation (Chapter 4) and in experiments (Chapter 5, 6). The floor of the backscattering measurements of the setup is at the level of modern state-of-art BRDF meters. This would not be possible without a dedicated signal processing associated with specific modulations applied to the different elements of the setup and the experimentalist's hard work.

- A model of coherent backscattering in optical fibers was made to demonstrate the presence of speckle in this case and to explain the experimental results. The model converges to the classical, incoherent models of fiber backscattering, but more of this, it reasonably predicts the observed features of the Rayleigh backscattering of a 1.064 μm laser beam from optical fibers. The predictions of the model were verified with experimental data.

- Contamination studies were made as well. Except for the experimental work to measure the coherent backscattering from silica spheres, I built a contamination control cleanroom system based on the IoT concept (Chapter 8).

9.2 Future work

This research has made significant progress in the understanding of the impact of coherent scattering on interferometric measurements. Moreover, some specific aspects of component level coherent scattering in LISA would deserve further studies:

- A general model of stray light in LISA is required at the system level. It is necessary to write a detailled account of the PSDs of the contributions to the noise in the phase measurement, as soon as the vibrational and thermal spectra of the LISA Optical Metrology System are known. Coherent features of scattering presented in this thesis should be taken into account and included in the model. This is the first step before setting up measures to mitigate the noise in the instrument.

- A profound modeling of ejected mass transfer is required to precise the estimates of stray light due to micrometeoroids. In my study (Chapter 3), I assume that all ejected mass is back-directed to the M1 mirror. This allows me to draw an upper value of the M1 contamination. But it deserves more work to understand the fraction that goes back to the cratered mirror, and what is the fraction ejected, than can contaminate other mirrors in the telescope, such as M2. For the same level of cleanliness, the M2 mirror causes much more backscattered light in the system, and it is more sensitive to contamination.

- Study of the speckle size on the at the CAS (Constellation Acquisition Sensor). Depending on where the scattering surface is, it can give rise to a speckle grain size that is as small as the point spread function of the imaging system. This point deserves a study, as it can raise critical constraints on the constellation acquisition procedure.

- A profound studies of contamination at different levels are required: experimental and modeling. Each space optical instrument keeps tracking a particle counter recording during the AIVT phase in a cleanroom. Still, so far, to the best of my knowledge, there has been no meta-analysis of the collected data. Modeling of complex contamination effect in LISA is required, particularly the degradation of optical properties in an intense radiation and laser field and the resulting stray light.

- Finally, the issues observed with the polarization tagging should be studied and explained in order to provide reliable measurement of crossed-polarisation back-scattering.

The presented work is a step forward to understanding coherent scattering. The achieved results are valuable not only for LISA applications but for any state-of-art optical interferometers.

Appendices

Appendix A

Coupling to the fiber

In this appendix we justify Eq. 4.41 in Sec. 4.3.4, where we consider the incoming field arrives at the plane, where the fiber end is placed. The goal is to calculate the coupled power into the fiber. For this, let us rewrite the incoming field amplitude U_{foc} as:

$$U_{foc}(u,v) = \left[U_{foc}(u,v) - AG_{00}(u,v) \right] + AG_{00}(u,v). \qquad (A.1)$$

There is value of A for which the first term in square brackets corresponds to higher-order modes, which do not propagate in the fiber, and the second term corresponds to fundamental mode, which propagates in the fiber. At the output of the fiber, only propagating (guided) mode remains, with intensity

$$\int \int |AG_{00}|^2 dudv = A^2 \int \int |G_{00}(u,v)|^2 dudv. \qquad (A.2)$$

But from equation A.1 we can obtain:

$$\int \int U_f(u,v)G_{00}^*(u,v)dudv = A \int \int G_{00}(u,v)G_{00}^*(u,v)dudv, \qquad (A.3)$$

the rest is zero (orthogonality of the modes), so the power coupled into the fiber is:

$$A = \frac{\int \int U_f(u,v)G_{00}^*(u,v)dudv}{\int \int G_{00}(u,v)G_{00}^*(u,v)dudv}. \qquad (A.4)$$

This result is used in a numerical model of coherent scattering.

Appendix B

# Calculation of the BRDF from a surface height map

The measured maps of height distribution of a 1 inch IR mirror from Edmund optics (Ref. number 47113) coated with aluminum are shown in Fig. 5.18. To calculate the BRDF from the PSD of the surface profile, I use the two-step method:

1. At first, I calculate radially averaged 2D power spectrum with function psd_2D[1]. Examples of computed PSD for maps (b) and (c) in Fig. 5.18 are in red and blue in Fig. B.1a. The difference between the two maps is a different scanning step ($2.2\mu m$ and $1.1~\mu m$) and analyzed area, which affects maximal and minimal accessible frequencies. The two PSD are quite the same, except for the very beginning and the very end, which was probably caused by the measurement instrument. The computed PSD was fitted with the ABC curve (see Eq. 2.23). The curve is given in black in Fig. B.1a.

2. The next step is the computation of the BRDF with Eq. 2.19. Here I calculate the BRDF for the case of backscattering ($\theta_i = -\theta_s$). The computed BRDF for the two maps and their PSD fit is given in Fig. B.1b.

This result is ready to use in the stray light analysis.

---

[1]fr.mathworks.com
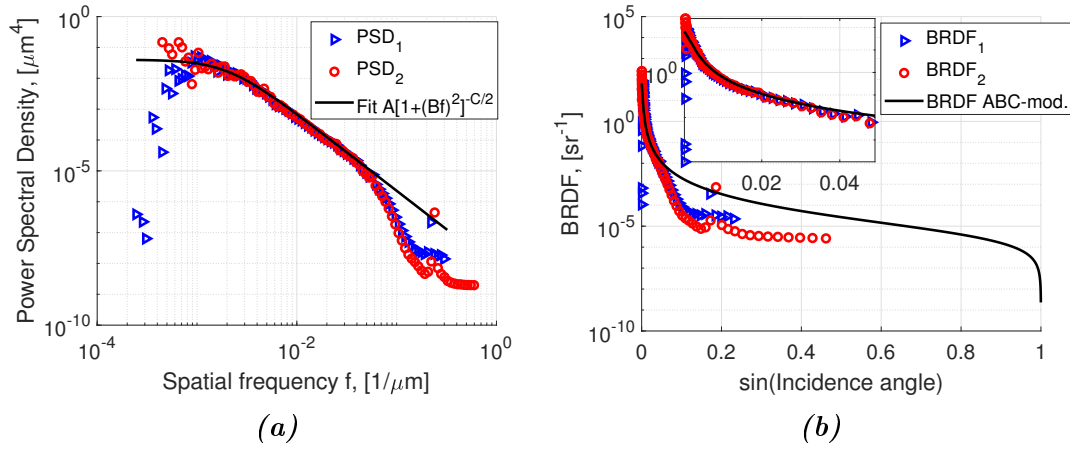
Figure B.1: *The computed PSD (a) and corresponding BRDFs (b) for maps (b,c) given in Fig. 5.18 (PSD_2 and PSD_1 respectively). The fit coefficients are $A = 4 \times 10^{-2}$ μm^4, $B = 5 \times 10^2$ μm, $C = 2.5$ (same for both figures). In the box of the figure (b) is zoom of near-normal incidence part of the BRDF.*

Appendix C

Basic signal processign script

```
close all; clear all; clc
%% Parameters
Th1=−0.078;%rotation angle
N=3.195;%modulation depth
Ac=0.3682;%calibration
omega_s=1.00;% slow modulation frequency 1Hz

%% Read Lock−in amplifier file
load(['../data/dataX1Y1.mat']);

%First harmonic
X1primary=device.demods(1).sample.x;
Y1primary=device.demods(1).sample.y;
%Second harmonic
X2primary=device.demods(2).sample.x;
Y2primary=device.demods(2).sample.y;

%% Rotation
X1=X1primary.*cos(Th1)+Y1primary.*sin(Th1); % modulus

Th2=2*Th1+pi/2;
X2=X2primary.*cos(Th2)+Y2primary.*sin(Th2); % modulus

%% Spectrum cleaning
%frequency array of demodulated signal
f=2.248663651315789e+02*((1:length(X1))−1)/length(X1);


Spectr1=fft(X1);
Phase1=angle(Spectr1);
Modul1=abs(Spectr1);

Spectr2=fft(X2);
```

```matlab
Phase2=angle(Spectr2);
Modul2=abs(Spectr2);

freq=omega_s:omega_s:10*omega_s;% 10 harmonics
llm=freq-omega_s/2; % lower limit : half of harmonic freq down
hlm=freq+omega_s/2; % ligher limit : half of harmonic freq up

%spectrum cut
tmp1=0;
tmp2=0;
for c=1:length(freq)
tmp=Modul1;
tmp(~(f>llm(c)&f<hlm(c)))=0;
tmp1=tmp1+tmp;

tmp=Modul2;
tmp(~(f>llm(c)&f<hlm(c)))=0;
tmp2=tmp2+tmp;
end

%fast component of spectrum
X1fast=real(ifft(2*tmp1.*exp(1i.*Phase1)));
X2fast=real(ifft(2*tmp2.*exp(1i.*Phase2)));

%% phase offset elimination
A=sqrt((X1fast/(2*besselj(1,2*pi/N))).^2+ ...
        (X2fast/(2*besselj(2,2*pi/N))).^2);

%% backscattering calculation
b=mean(A)/Ac;
b_err=std(A)/Ac;

% check on correlation
CRR=corr(abs(X1fast'),abs(X2fast'));
```

Bibliography

[1] B. P. Abbott, R. Abbott, T. D. Abbott, M. R. Abernathy, F. Acernese, K. Ackley, et al. "Observation of Gravitational Waves from a Binary Black Hole Merger". In: *Phys. Rev. Lett.* **116** (6 Feb. 2016), p. 061102. DOI: 10.1103/PhysRevLett.116.061102. URL: https://link.aps.org/doi/10.1103/PhysRevLett.116.061102.

[2] E. Akkermans, P. E. Wolf, and R. Maynard. "Coherent Backscattering of Light by Disordered Media: Analysis of the Peak Line Shape". In: *Phys. Rev. Lett.* **56** (14 Apr. 1986), pp. 1471–1474. DOI: 10.1103/PhysRevLett.56.1471. URL: https://link.aps.org/doi/10.1103/PhysRevLett.56.1471.

[3] M. Armano, H. Audley, G. Auger, J. Baird, M. Bassan, P. Binetruy, et al. "Sub-Femto-g Free Fall for Space-Based Gravitational Wave Observatories: LISA Pathfinder Results". In: *Phys. Rev. Lett.* **116** (June 2016). DOI: 10.1103/PhysRevLett.116.231101.

[4] L. L. BARBIER. *Etude théorique de l'interférométrie à rétro-injection optique en vued'applications en dynamique des matériaux.* Thèse de l'université Paul Sabatier, Toulouse, 2017.

[5] M. Bass et al. *Handbook of Optics: Devices, measurements, and properties. Chap. 7: Surface scattering.* Handbook of Optics. McGraw-Hill, 1995. URL: https://books.google.fr/books?id=owg6AQAAIAAJ.

[6] C. F. Bohren and D. R. Huffman. "Absorption and Scattering by a Sphere". In: *Absorption and Scattering of Light by Small Particles.* John Wiley & Sons, Ltd, 2007. Chap. 4, pp. 82–129. DOI: 10.1002/9783527618156.ch4. URL: https://onlinelibrary.wiley.com/doi/abs/10.1002/9783527618156.ch4.

[7] C. Buy. *Straylight at the CAS position using FRED and Zemax, LISA-APC-INST-TN-007 (unpublished).* Tech. rep. APC, 2019.

[8] B. G. Cour-Palais. "Meteoroid Environment Model-1969". In: *NASA-SP-8013* (1969). URL: https://ntrs.nasa.gov/search.jsp?R=19690030941.

[9] E. Grün and H.A. Zook and H. Fechtig and R.H. Giese. "Collisional balance of the meteoritic complex". In: *Icarus* **62** (1985), pp. 244–272. DOI: https://doi.org/10.1016/0019-1035(85)90121-6. URL: http://www.sciencedirect.com/science/article/pii/0019103585901216.

[10] "ECSS-Q-ST-70-01C: Space product assurance Cleanliness and contamination control". ECSS Secretariat ESA-ESTEC, Requirements & Standards Division, Noordwijk, The Netherlands, 2008. URL: https : / / escies.org/download/webDocumentFile?id=62823.

[11] Einstein Albert. "Näherungsweise Integration der Feldgleichungen der Gravitation". In: *Sitzungsberichte der Königlich Preussischen Akademie der Wissenschaften* (1916), pp. 688–696.

[12] *Einstein Gravitational Wave Telescope Conceptual Design Study: ET-0106C-10*. 2011. URL: https : / / books . google . fr / books ? id = FGPCnQAACAAJ.

[13] *ESA's Space Environment Information System's webpage*. URL: https : / / www . spenvis . oma . be / help / background / metdeb / metdeb . html#METFLUX.

[14] F. Hörz and D.E. Brownlee and H. Fechtig and J.B. Hartung and D.A. Morrison and G. Neukum and E. Schneider and J.F. Vedder and D.E. Gault. "Lunar microcraters: Implications for the micrometeoroid complex". In: *Planetary and Space Science* **23** (1975), pp. 151–172. DOI: https : / / doi . org / 10 . 1016 / 0032 - 0633(75) 90076 - 8. URL: http : //www.sciencedirect.com/science/article/pii/0032063375900768.

[15] D. FAYE. "Contamination issues for space hardware. How to mitigate the risks?" CNES stray light workshop Toulouse Nov. 14-15th 2017.

[16] E. Fest. *Stray Light Analysis and Control*. SPIE Digital Library. SPIE Press, 2013. URL: https://books.google.fr/books?id=8-ZEmAEACAAJ.

[17] S. Fineschi, P. Sandri, F. Landini, M. Romoli, V. DaDeppo, F. Frassetto, et al. "Stray-light analyses of the METIS coronagraph on Solar Orbiter". In: *Solar Physics and Space Weather Instrumentation VI*. Ed. by S. Fineschi and J. Fennelly. International Society for Optics and Photonics. SPIE, 2015. DOI: 10 . 1117 / 12 . 2203629. URL: https : / / doi . org / 10 . 1117/12.2203629.

[18] S. Fischer, P. Meyrueis, and W. W. Schroeder. "Brillouin backscattering in fiber optic gyroscope". In: *Fiber Optic and Laser Sensors XIII*. Ed. by R. P. DePaula and J. W. B. III. Vol. **2510**. International Society for Optics and Photonics. SPIE, 1995, pp. 49–58. DOI: 10.1117/12.221717. URL: https://doi.org/10.1117/12.221717.

[19] R. Fleddermann. *Interferometry for a Space-based Gravitational Wave Observatory: Reciprocity of an Optical Fiber*. PhD thesis, Leibniz Universität Hannover, 2012. URL: https://books.google.fr/books?id=DUKZMwEACAAJ.

[20] D. Gault. "Displaced mass, depth, diameter, and effects of oblique trajectories for impact craters formed in dense crystalline rocks". In: *The Moon* **6** (Apr. 1973), pp. 32–44. DOI: 10.1007/BF02630651.

[21] O. Gerberding et al. "TN 1: Design Report Prepared in response to ESA ITT AO/1-8586/16/NL/BW (unpublished)". May 2019.

[22] J. W. Goodman. *Introduction to Fourier optics, 3rd ed.* Englewood, CO: Roberts & Co. Publishers, 2005.

[23] J. W. Goodman. *Speckle phenomena in optics : theory and applications.* Englewood, Colorado : Roberts & Company, 2007.

[24] H. Halloin. *Stray light to phase coupling, LISA-APC-INST-TN-005 (unpublished).* Tech. rep. APC, 2019.

[25] G. S. Hawkins. "The Harvard radio meteor project". In: *Smithsonian Contributions to Astrophysics* **7** (Jan. 1963), p. 53.

[26] J. B. Heaney. "MLCD micrometeoroid optical damage analysis – solar window (unpublished) ". In: (2005).

[27] "ISO14644-1:2015(E) standard: Cleanrooms and associated controlled environments". URL: https://www.iso.org/standard/53394.html.

[28] V. E. Johansen. "Preparing the generalized Harvey-Shack rough surface scattering method for use with the discrete ordinates method". In: *J. Opt. Soc. Am. A* **32** (Feb. 2015), pp. 186–194. DOI: 10.1364/JOSAA.32.000186. URL: http://josaa.osa.org/abstract.cfm?URI=josaa-32-2-186.

[29] Y. Khmou. *2D Autocorrelation function.* Tech. rep. MATLAB Central File Exchange, 2020. URL: https://www.mathworks.com/matlabcentral/fileexchange/37624-2d-autocorrelation-function.

[30] V. Khodnevych, M. Lintz, N. Dinu-Jaeger, and N. Christensen. "Stray light estimates due to micrometeoroid damage in space optics, application to the LISA telescope (Submitted to Journal of Astronomical Telescopes, Instruments, and Systems)". In: (2019).

[31] V. Khodnevych, S. D. Pace, J.-Y. Vinet, N. Dinu-Jaeger, and M. Lintz. "Study of the coherent perturbation of a Michelson interferometer due to the return from a scattering surface". In: *International Conference on Space Optics — ICSO 2018.* Ed. by Z. Sodnik, N. Karafolas, and B. Cugny. Vol. **11180**. International Society for Optics and Photonics. SPIE, 2019, pp. 2802–2811. DOI: 10.1117/12.2536200. URL: https://doi.org/10.1117/12.2536200.

[32] A. Krywonos, J. Harvey, and N. Choi. "Linear systems formulation of scattering theory for rough surfaces with arbitrary incident and scattering angles". In: *Journal of the Optical Society of America. A, Optics, image science, and vision* **28** (June 2011), pp. 1121–38. DOI: 10.1364/JOSAA.28.001121.

[33] M. Lequime, V. Khodnevych, M. Zerrad, M. Lintz, and C. Amra. "Coherent detection of the light back-scattered by a rough surface". In: *Optical Interference Coatings Conference (OIC) 2019.* Optical Society of America, 2019, TE.7. DOI: 10.1364/OIC.2019.TE.7. URL: http://www.osapublishing.org/abstract.cfm?URI=OIC-2019-TE.7.

[34] P. Lightsey, C. Atkinson, M. Clampin, and L. Feinberg. "James Webb Space Telescope: Large deployable cryogenic telescope in space". In: *Optical Engineering* **51** (Feb. 2012), pp. 1003–. DOI: 10.1117/1.OE.51.1.011003.

[35] S. Lin and T. Giallorenzi. "Sensitivity analysis of the Sagnac-effect optical-fiber ring interferometer". In: *Applied optics* **18** (Mar. 1979), pp. 915–31. DOI: 10.1364/AO.18.000915.

[36] M. Lintz and A. Papoyan. "A simple and efficient laser beam trap using a highly absorbing glass plate at Brewster incidence". In: *Review of Scientific Instruments - REV SCI INSTR* **71** (Dec. 2000), pp. 4681–4682. DOI: 10.1063/1.1324733.

[37] "LISA Mission Proposal for L3 submitted to ESA, https://www.lisamission.org/?q=articles/lisa-mission/lisa-mission-proposal-l3 ". In: (2017). URL: https://www.lisamission.org/?q=articles/lisa-mission/lisa-mission-proposal-l3.

[38] X. LU. *Coherent Rayleigh time domain reflectometry: novel applications for optical fibre sensing*. PhD thesis in physics, EPFL, 2016.

[39] M. Millinger and P. Jiggens. "LISA Environment Specification". In: *ESA-L3-EST-MIS-SP-001, ESA-TEC-SP-006666, (unpublished)* (2017).

[40] M. Nakazawa. "Rayleigh backscattering theory for single-mode optical fibers". In: *Journal of The Optical Society of America* **73** (Sept. 1983), pp. 1175–1180. DOI: 10.1364/JOSA.73.001175.

[41] C. Nguyen. "Calculation of the back-scattered light from telescope in the long-arm interferometer using FRED and Zemax, LISA-APC-INST-TN-006 (unpublished)". In: (2019).

[42] J. O'Keefe and T. Ahrens. "The size distribution of fragments ejected at a given velocity from impact craters". In: *International Journal of Impact Engineering* **5** (Feb. 1987), pp. 493–499. DOI: 10.1016/0734-743X(87)90064-9.

[43] G. Peterson. "A BRDF model for scratches and digs". In: *Proceedings of SPIE - The International Society for Optical Engineering* **8495** (Oct. 2012). DOI: 10.1117/12.930860.

[44] R. Pfisterer. "Approximated scatter models for: Stray light Analysis". In: *OPN Optics & Photonics News* (Oct. 2011), pp. 16–17.

[45] D. H. Phung, J. P. Coulon, M. Lintz, and T. Lévèque. "Temperature control of a PM ring fiber cavity for long-term laser frequency stabilization". In: *International Conference on Space Optics — ICSO 2018*. Ed. by Z. Sodnik, N. Karafolas, and B. Cugny. Vol. **11180**. International Society for Optics and Photonics. SPIE, 2019, pp. 1907–1919. DOI: 10.1117/12.2536103. URL: https://doi.org/10.1117/12.2536103.

[46] *Product cleanliness levels and contamination control program*. Military Standard (MIL STD) 1246C, U.S. Department of Defense, Washington, DC, 1994.

[47] H. Rabal and R. Braga. *Dynamic Laser Speckle and Applications*. Optical Science and Engineering. CRC Press, 2009. URL: https://books.google.fr/books?id=T4MA%5C_XtWAwMC.

[48] P. R. Saulson. *Fundamentals of Interferometric Gravitational Wave Detectors*. WORLD SCIENTIFIC, 2017. DOI: 10.1142/10116. URL: https://www.worldscientific.com/doi/abs/10.1142/10116.

[49] C. Schinke, C. Peest, J. Schmidt, R. Brendel, M. R. Vogt, I. Kröger, et al. "Uncertainty analysis for the coefficient of band-to-band absorption of crystalline silicon". In: *AIP Advances* 5 (June 2015), p. 067168. DOI: 10.1063/1.4923379.

[50] B. Scott. *Stray light analysis and control*. Bellingham, Washington, USA: SPIE press, 2017.

[51] L. Seals. "FRED Divot Analysis". In: *(unpublished technical note)* (2019).

[52] A. Sharma, S. Xie, R. Zeltner, and P. Russell. "On-the-fly particle metrology in hollow-core photonic crystal fibre". In: *Optics Express* 27 (Nov. 2019), p. 34496. DOI: 10.1364/OE.27.034496.

[53] J.-M. Siguier and J.-C. Mandeville. "Test procedures to evaluate spacecraft materials ejecta upon hypervelocity impact". In: *Proceedings of The Institution of Mechanical Engineers Part G-journal of Aerospace Engineering - PROC INST MECH ENG G-J A E* 221 (June 2007), pp. 969–974. DOI: 10.1243/09544100JAERO236.

[54] A. Taylor. "The Harvard Radio Meteor Project Meteor Velocity Distribution Reappraised". In: *Icarus* 116 (1995), pp. 154–158. DOI: https://doi.org/10.1006/icar.1995.1117. URL: http://www.sciencedirect.com/science/article/pii/S0019103585711177.

[55] *U.S. General Services Administration Federal Government computer system: LISA telescope design*. URL: https://beta.sam.gov/opp/72d6f9eaf7308681d44a4391e73ad57b/view?keywords=80GSFC19R0032%5C&sort=-relevance%5C&index=%5C&is%5C_active=false%5C&page=1.

[56] P.-E. Wolf and G. Maret. "Weak Localization and Coherent Backscattering of Photons in Disordered Media". In: *Phys. Rev. Lett.* 55 (24 Dec. 1985), pp. 2696–2699. DOI: 10.1103/PhysRevLett.55.2696. URL: https://link.aps.org/doi/10.1103/PhysRevLett.55.2696.

Abreviations list

GW . . . . Gravitational wave

LISA . . . . Laser interferometer space antenna

CAS . . . . Constellation acquisition sensor

MOSA . . . . Moving optical subassembly

AIVT . . . . Assembly integration verification test

BSDF . . . . Biridectional scattering distribution function

BRDF . . . . Biridectional reflectance distribution function

BTDF . . . . Biridectional transmittance distribution function

CBS . . . . Coherent backscattering

BSF . . . . Backscattering fraction

OPD . . . . Optical path difference

PDF . . . . Probability density function

PSD . . . . Power spectrum density

ASD . . . . Amplitude spectrum density

IoT . . . . Internet of Things

DCD . . . . Damage crater diameter

CL . . . . Cleanliness level

CRCCS . . . . Clean room contamination control system

Publications

Journal papers:

- Vitalii Khodnevych, Michel Lintz, Nicoleta Dinu-Jaeger and Nelson Christensen *Stray light estimates due to micrometeoroid damage in space optics, application to the LISA telescope*, Submitted to Journal of Astronomical Telescopes, Instruments, and Systems, 2020.

Conference papers:

- Vitalii Khodnevych, Sibilla Di Pace, Jean-Yves Vinet, Nicoleta Dinu-Jaeger and Michel Lintz *Study of the coherent perturbation of a Michelson interferometer due to the return from a scattering surface*, International Conference on Space Optics — ICSO 2018, 2019.

- Sibilla Di Pace, Arwa Dabbech, Vitalii Khodnevych, Michel Lintz and Nicoleta Dinu-Jaeger *Particle contamination monitoring in the backscattering light experiment for LISA*, NANOP 2018, Open Material Sciences, 2019.

- Nicolas Delerue, Jean-Paul Berthet, Stéphane Jenzer, Nicolas Jestin, Vitalii Khodnevych, Alexandre Migayron, Jean-Michel Ortega, Rui Prazeres *Bunch Length Measurements Using Coherent Smith-Purcell Radiation With Several Gratings at CLIO*, IPAC 2018.

- Vitalii Khodnevych , Michel Lintz , Nicoleta Dinu-Jaeger, Dominique Huet, Sibilla Di Pace *Coherent characterization of backscattering in the LISA instrument*, Optro2020.

- Michel Lequime, Vitalii Khodnevych, Myriam Zerrad, Michel Lintz, and Claude Amra *Coherent detection of the light back-scattered by a rough surface* Optical Interference Coatings 2019, Santa Ana Pueblo, New Mexico United States, 2–7 June 2019, ISBN: 978-1-943580-58-3